

NEW MID-IR-CRD SPECTROMETER FOR
ORGANOHALOGEN DETECTION AND INNOVATIVE
APPLICATIONS OF SATURATION SPECTROSCOPY

DISSERTATION

IN FULFILLMENT OF THE REQUIREMENTS

FOR THE DEGREE

“DR. RER. NAT.”

OF THE FACULTY OF MATHEMATICS AND NATURAL SCIENCES

AT UNIVERSITY OF KIEL

SUBMITTED BY

IBRAHIM SADIEK

KIEL, 2017

Ibrahim Sadiek: *New Mid-IR-CRD Spectrometer for Organohalogen Detection and Innovative Applications of Saturation Spectroscopy*, © 2017.

FIRST REFEREE: Prof. Dr. Gernot Friedrichs

SECOND REFEREE: Prof. Dr. Friedrich Temps

DATE OF THE ORAL EXAMINATION: 02.11.2017

APPROVED FOR PUBLICATION: 02.11.2017

SIGNED: Prof. Dr. Natascha Oppelt, Dean

This Page Intentionally Left Blank

Acknowledgments

In front of you a thesis of almost four years of scientific research culminated into one volume. But really, there is far more than four years of work that has gone into this thesis. And most of it has not mentioned in this tome—the wonderful people in my life who have shaped everything that you will read about here. In the following I spend few lines thanking people who helped making this thesis possible.

- The first person who I would like to thank is my advisor—Prof. Dr. Gernot Friedrichs has been incredible advisor. I learned from him how to do more precise, high-impact and integrated science. But perhaps most importantly, Gernot is a wonderful person, and have made positive working environment. This thesis would not have been possible without Gernot’s expert guidance, and I thank him for shaping my future as a scientist.
- It has been a joy to come into work each day and see the members of the AK Friedrichs. Thank you to the graduate students, postdocs, and staff scientists who I have had the good fortune to work with: Dr. Kristian Lass, Saira Raiz, Dr. Nancy Fassheber, Michael Stuhr, Alexandra Dabrowski, Sebastian Hesse, Florian Lange, Dr. Inga Piller, Dr. Joscha Kleber, and Christian Smets. I would like to single out a few of my co-workers. Kristian and Saira were my office mates for more than two and half years, many family and scientific related issues that I have learned came from our office chats. Kristian and Saira are two of the kindest persons that I have met. Christian Smets did part of his undergraduate studies with me (PCF3), I hope he enjoyed working in the lab as much as I enjoyed working with him.
- Thanks to the Helmholtz Research School for Ocean System Science and Technology (HOSST) and all HOSSTers, I am really grateful for spending the first three years of my Ph.D. as a HOSST fellow. Thank you to the representatives of HOSST, Profs. Wolf-Christian Dullo and Colin Devey. Thanks to Dr. Christel van den Bogaard, coordinator of HOSST, for her time, effort, and patience. Thanks to the Integrated School of Ocean Science (ISOS) and thank you to PD Dr. Avan Antia and the entire ISOS team for the diverse, and informative soft skills and events. Thanks to the Kiel cluster of excellence “Future Ocean” for the financial support.
- I was lucky enough to have many collaborations with Prof. Dr. Arne Körtzinger (GEOMAR, Kiel), Prof. Dr. Doug Wallace (University of Dalhousie, Canada), and Prof. Dr. Yasuyuki Sakai (University of Fukui, Japan). Thanks, Anne, for the stimulating discussions during the several meetings and retreats. Big thanks to you Doug for your time, effort, for hosting me in your lab, for pushing our collaborations forward, and most importantly, being a great person to work with. Thanks to Yasuyuki for learning me how to do RRKM/master equation analysis.
- It takes a lot to make a new experiment running, especially when it is being started from scratch. I still remember the first days for me in the lab when I was trying to float our new NEWPORT optical table. Thanks to Klaus Warns for fixing and providing many electronic components, Tanja Stojsic introduced a lot of support to keep paperwork in line, packages and mail flowing, and smiles to go around. The employee of the institute workshop for providing advices, being patient and making available many hardware components. Thank you to Dr. Joachim Gripp for

being in the lab many times for introducing advice and making available many chemicals and vacuum components. They deserve my most sincere thanks.

- My good fortune extends past CAU: I have had many great research mentors, professors, and teachers who have helped shape me into a chemist. I thank Professors B. El-Anadouli, M. S. El-Deab, M. Elshakre, and A. M. Mohammad for the research opportunities that they extended to me. My time at the University of Cairo helped develop my passion for teaching.
- They say that you are saving the best for last. In this case, I saved my largest thanks for my wife, Lamis Afify and my two little daughters, Masa and Hana. I am really happy to have you in my life. My parents Mohammed Sadiek and Samia Fath-Allah, you have been always pushing me to follow my dreams wherever they may take me. I am happy every day because of you. This thesis may satisfy the requirements for a Ph.D. at CAU, but it was written for you.

Abstract

Cavity Ringdown Spectroscopy (CRDS) has proven successful for industrial process monitoring as well as for trace gas detection in the environment. Halogenated Volatile Organic Compounds (HVOCs) are a very important class of atmospheric molecules, with a wide spectrum of agricultural and industrial applications. HVOCs are currently detected by gas chromatography (GC) based techniques, which are bulky instruments, require considerable calibration efforts and offer low sampling frequencies. CRDS holds the potential to overcome these limitations. The main challenges for implementing CRDS for HVOCs detection are their low absorption cross-sections in combination with very low atmospheric mixing ratio levels (< 1 ppb) as well as the scarcity of their high-resolution spectra.

In this study, a new mid-IR cw-CRD spectrometer has been setup as a *development platform* for trace gas sensors and field going instruments. In addition, novel approaches based on optical saturation have been developed to further enhance the attainable limit of detection (LOD) and to overcome the issue of cross-sensitivity. Quantitative measurements on two HVOCs, CH_2Br_2 and CH_3I , have been performed to assess the potential of mid-IR CRDS for HVOCs detection. The high-resolution spectra of symmetric and asymmetric CH stretch vibrations of CH_2Br_2 have been measured and assigned for the first time. Spectral assignment has been accomplished by combination of microwave ground state data with excited state parameters derived from anharmonic quantum chemical calculations using the second-order vibrational perturbation theory (VPT2). In addition, all quantitative spectroscopic parameters needed for the detection of CH_3I at the ${}^{\text{R}}\text{R}_2(15)$ transition at $\tilde{\nu}=3090.4289\text{ cm}^{-1}$ have been determined. The attainable LOD for CH_3I using a standard CRDS approach corresponds to a mixing ratio of 15 ppb (at 100 s averaging). This is sensitive enough with regard to CH_3I exposure limits, but direct detection of CH_3I at atmospheric mixing ratio levels is not possible. Nevertheless, a designed tank-purging experiment revealed that calibration-free quantitative detection of CH_3I by mid-IR CRDS is possible with a time-resolution of several seconds and with high reproducibility.

Furthermore, a novel approach for quantitative detection of trace gases based on saturation absorption spectroscopy has been implemented to enhance the attainable LOD. The dynamics of the absorption saturation evolution within the ringdown transients and the working limits of the new saturated-absorption CRDS approach (Sat-CRDS) have been investigated using CH_4 as a test molecule. The simultaneous extraction of multiple parameters from a single ringdown transient results in strong parameter correlation, hence the achieved sensitivity was comparable to that of standard CRDS measurements. However, the Sat-CRDS approach is advantageous when it is difficult to determine empty cavity decay constant due to baseline instabilities or broad absorption features.

Moreover, by exploiting the different optical saturation behavior of two interfering absorptions, a novel “Two-species One-wavelength” detection scheme has been developed as a new technique to reduce the limitations of absorption spectroscopy with respect to cross-sensitivity. In a successful proof-of-concept experiments, the individual absorption of CH_4 and CH_3Cl have been quantitatively retrieved from their overlapping transitions using CRDS and direct laser absorption spectroscopy. The utilization of optical saturation effect for multi-species detection holds the potential to significantly expand the capabilities of absorption based trace gas detection by adding the absorption saturation as a new spectral dimension.

Kurzzusammenfassung

Die Cavity-Ringdown-Spektroskopie (CRDS) hat sich als erfolgreiche Methode zur industriellen Prozesskontrolle und zur Detektion von umweltrelevanten Spurengasen erwiesen. Halogenierte flüchtige organische Verbindungen (Halogenated Volatile Organic Compounds, HVOCs) stellen eine wichtige Klasse atmosphärischer Moleküle dar, die ein breites Anwendungsspektrum in Landwirtschaft und Industrie besitzen. HVOCs werden für gewöhnlich mit gaschromatographischen Techniken nachgewiesen, welche auf großen Instrumenten mit erheblichem Kalibrationsaufwand und geringer Messfrequenz basieren. CRDS birgt das Potenzial, diese Einschränkungen zu überwinden. Das Hauptproblem bei der Implementierung der CRDS für den Nachweis von HVOCs besteht in ihren geringen Absorptionsquerschnitten, den sehr geringen atmosphärischen Konzentrationen (< 1 ppb) sowie im Mangel an vorhandenen hochaufgelösten Spektren.

Im Zuge dieser Arbeit wurde ein neues Mid-IR-cw-CRD-Spektrometer als Entwicklungsplattform für Spurengassensorik aufgebaut. Zudem wurde ein neuer Ansatz zur Verbesserung der Nachweisgrenze und zur Vermeidung von Querempfindlichkeiten verfolgt, der auf dem Effekt der optischen Sättigung basiert. Quantitative Messungen an CH_2Br_2 und CH_3I dienten zur Erprobung des neuen Spektrometers. Hierbei wurden erstmalig hochaufgelöste Spektren der CH-Streckschwingungen von CH_2Br_2 aufgenommen. Deren Zuordnung erfolgte mithilfe von Grundzustands-Daten und Parametern für angeregte Zustände, die mittels anharmonischer quantenmechanischer VPT2-Rechnungen (second-order vibrational perturbation theory) gewonnen wurden. Außerdem wurden alle für den quantitativen Nachweis von CH_3I auf dem ${}^R\text{R}_2(15)$ -Übergang ($\tilde{\nu} = 3090,4289 \text{ cm}^{-1}$) benötigten spektroskopischen Parameter bestimmt. Die erreichte Nachweisgrenze von 15 ppb bei 100 s Mittelungszeit ist für Anwendungen im Bereich der Arbeitsplatzsicherheit ausreichend, der direkte Nachweis von CH_3I in der Atmosphäre ist jedoch nicht möglich. Allerdings konnte durch ein Entgasungsexperiment mit wässrigen Proben gezeigt werden, dass die quantitative und kalibrationsfreie Detektion von CH_3I mit einer Zeitauflösung von einigen Sekunden möglich ist.

Des Weiteren wurde eine neue Messtechnik zur Verbesserung des Detektionslimits auf Basis der optischen Sättigung durch Absorption verwirklicht. Die Sättigungsdynamik während des Intensitätsabfalls im Resonator und die Anwendungsgrenzen der neuen Sättigungs-CRDS-Methode (Sat-CRDS) wurden mit CH_4 als Testsubstanz eingehend untersucht. Bei der notwendigen simultanen Anpassung mehrerer Parameter wurde eine ausgeprägte Korrelation der erhaltenen Parameter beobachtet, so dass die erreichte Empfindlichkeit in etwa mit der von konventioneller CRDS vergleichbar ist. Allerdings ist die Sat-CRDS-Methode überlegen, wenn die Bestimmung der Abklingkonstanten durch Basislinienschwankungen oder breite Absorptionsbanden erschwert wird.

Darüber hinaus wurde unter Ausnutzung des unterschiedlichen Sättigungsverhaltens zweier Moleküle mit überlagerten Absorptionslinien ein neues „Zwei-Spezies-eine-Wellenlänge“-Detektionsschema entwickelt, mit dem das Problem der Querempfindlichkeit reduziert werden kann. In einer Machbarkeitsstudie mit CH_4 und CH_3Cl konnte gezeigt werden, dass es durch selektive transiente Sättigung einer der beiden Spezies gelingt, die individuelle Absorptionen beider Spezies zu ermitteln. Die Methode hat das Potenzial, durch die Einführung der Sättigung als zusätzliche spektroskopische Messvariable, signifikant zur Verbesserung von absorptionsbasierten Spurengas-Spektrometern beizutragen.

Contents

1	Introduction	1
1.1	Humans and Earth’s Ocean-Atmosphere	1
1.2	Halogenated Volatile Organic Compounds	2
1.2.1	Very Short-Lived Substances	3
1.3	Laser-Based Trace Gas Sensing	4
1.4	Objectives and Research Milestones	7
2	Theoretical Background	13
2.1	Cavity Enhanced Absorption Techniques	13
2.1.1	Standard Cavity Ringdown Spectroscopy	13
2.1.2	Theory of Cavity Ringdown Spectroscopy	15
2.2	Saturated-Absorption Cavity Ringdown Spectroscopy	17
2.2.1	Modeling Sat-CRDS Signal	18
2.3	Energy Transfer Dynamics	23
2.4	Vibrational-Rotational Spectroscopy	26
2.4.1	Rotational Assignment	27
2.4.2	Quantum-Chemically Assisted Spectrum Simulations	29
2.4.3	Spectral Line Intensities	31
3	Experimental	37
3.1	Sample Preparation and Chemicals	37
3.2	cw Mid-IR Cavity Ringdown Spectrometer	38
3.2.1	Light Source	38
3.2.2	CRD Spectrometer	40
3.2.3	Signal Processing	41
3.3	Laser Absorption Spectroscopy	41
3.4	Computational Tools	42
3.4.1	Numerical Fitting	42
3.4.2	Quantum Chemical Calculations	44
3.4.3	PGOPHER Simulations	44
4	Quantitative Mid-Infrared Cavity Ringdown Detection of Methyl Iodide for Monitoring Applications	49
4.1	Experimental Section	51
4.1.1	CRD Spectrometer	52
4.1.2	GC-MS/ECD Analysis	53
4.1.3	Purge Tank Experiments	54
4.2	Results and Discussion	54

4.2.1	CRDS Measurement Performance	54
4.2.2	The High-Resolution Spectrum of CH ₃ I	55
4.2.3	Quantitative Analysis of ν_4 -R ₂ (15) Absorption Line	57
4.2.4	Purge-Tank Experiment	58
4.2.5	Potential of CRDS Analyzers for CH ₃ I Monitoring	60
4.3	Conclusions	62
5	Doppler-Limited High-Resolution Spectrum and VPT2 Assisted Assignment of the C-H Stretch of CH₂Br₂	67
5.1	Introduction	68
5.2	Experimental	70
5.2.1	Cavity Ringdown Spectrometer	70
5.2.2	Computations	72
5.3	Results and Discussion	73
5.3.1	Absorption Saturation	73
5.3.2	High-Resolution Spectrum	74
5.3.3	Computational Results	76
5.3.4	Spectrum Simulation	79
5.3.5	Spectrum Assignment	80
5.3.6	Choice of Density Functional	84
5.4	Conclusions	86
5.5	Supplementary Material	92
6	Saturation Dynamics and Working Limits of Saturated Absorption Cavity Ring-down Spectroscopy	97
6.1	Introduction	98
6.2	Sat-CRDS Model	100
6.2.1	Saturation and Relaxation Dynamics	100
6.2.2	Ringdown Equation	101
6.3	Experimental	102
6.4	Results and Discussion	105
6.4.1	Ringdown Characteristics	105
6.4.2	Working Limits	110
6.4.3	Standard Error Analysis	112
6.5	Conclusion	115
7	Two-Species One-Wavelength Detection Based on Selective Optical Saturation	120
7.1	Supplementary Material	132
8	Summary and Outlook	146

List of Figures

1.1	Some of the oceanic emissions and its impact on the atmosphere.	2
1.2	Simulated absorption spectra of several atmospheric molecules in the mid-IR.	6
2.1	Schematic of pulsed and cw-CRDS.	14
2.2	Working principle of Sat-CRDS.	18
2.3	Lennard-Jones potential of CH ₄ and Stockmayer potential of CH ₃ Cl.	24
3.1	Schematic of the all-in-fiber cw-SR-OPO laser.	38
3.2	Wavelength tuning in the cw-SR-OPO.	39
3.3	Schematic of the new mid-IR cw-CRD spectrometer.	40
3.4	Schematic of the direct LAS setup	41
4.1	Schematic of the mid-IR cw-CRD spectrometer.	53
4.2	Schematic of the purge vessel.	54
4.3	Allan plots of the collected empty cavity decay constants.	55
4.4	Selection of interference absorption line for monitoring applications.	56
4.5	Quantitative spectroscopic data for the ^R R ₂ (15) line of CH ₃ I.	58
4.6	CH ₃ I concentration-time profiles of the purge-tank experiment.	60
4.7	Simulated absorption spectra of CH ₃ I main interfering gases.	61
5.1	Schematic of the mid-IR cw-CRD spectrometer.	71
5.2	CH ₂ Br ₂ absorption saturation as a function of total cell pressure.	74
5.3	High-resolution absorption spectra of ν_1 and ν_6 bands of CH ₂ Br ₂	75
5.4	Molecular structure of CH ₂ Br ₂	79
5.5	Comparison of measured and VPT2 assisted simulations.	81
5.6	Comparison of measured and simulated spectrum of ν_6 band of CH ₂ Br ₂	82
5.7	Difference in peak positions (observed - simulated) for different theoretical models.	85
6.1	Schematic of the new mid-IR cw-CRD spectrometer.	104
6.2	Experimental characterization of Sat-CRD signals.	106
6.3	Single-exponential fit residuals of the Sat-CRDS.	107
6.4	Saturation intensity as a function of argon buffer gas pressure.	109
6.5	Working limits of Sat-CRDS model.	111
6.6	Concentration linearity response of Sat-CRDS.	112
6.7	Standard error analysis of Sat-CRDS as a function of degree of sample saturation.	114
7.1	Direct LAS double-banded absorbance-input power profile.	123
7.2	Realization of the Two-species One-wavelength approach by Sat-CRDS.	126
7.3	Concentration linearity response of the Two-species One-wavelength approach.	127

7.4	Working limits of Two-species One-wavelength approach.	128
7.S1	Schematic of the direct LAS and Sat-CRDS used for two-species detection.	134
7.S2	Absorption profiles of overlapping transitions at different input laser power.	134
7.S3	Characterization of Sat-CRD transients for overlapping transitions.	138
7.S4	Complete individual spectra retrieved from their overlapping transitions using Sat-CRDS.	139
7.S5	Allan standard deviation analysis for the Two-species One-wavelength approach.	140
7.S6	Extracted CH ₃ Cl and CH ₄ absorption spectra for variable species partial pressures.	141
7.S7	Extracted CH ₃ Cl and CH ₄ at variable total cell pressure.	142
7.S8	Schematic for vibrational energy transfer pathways in two excited molecules.	144

List of Tables

1.1	MBL mixing ratios of common brominated, chlorinated, and iodinated VSLS.	4
3.1	MATLAB main code as well as objective and cost functions for fitting Sat-CRD transients.	43
4.1	Model parameters extracted from CH ₃ I concentration-time profiles.	60
5.1	Calculated molecular structures of ground state CH ₂ ⁷⁹ Br ⁸¹ Br at different levels of theory.	77
5.2	Calculated harmonic and anharmonic vibrational frequencies of CH ₂ ⁷⁹ Br ⁸¹ Br.	78
5.3	Anharmonic rotational constants of CH ₂ ⁸¹ Br ₂ at vibrational ground and excited states.	79
5.4	Band origin and rotational constants of ν_6 band of CH ₂ ⁷⁹ Br ⁸¹ Br.	83
5.5	Band origin and rotational constants of the ν_6 band of CH ₂ ⁸¹ Br ₂ and CH ₂ ⁷⁹ Br ₂	83
5.6	Weighted mean average error $\overline{\text{Err}}\%$ of the simulated intensity of the $p/rQ_{K_a}(J)$ clusters.	85
5.S1	Fundamental bands, overtones, and combination bands of CH ₂ ⁷⁹ Br ⁸¹ Br.	93
5.S2	Comparison of structural parameters of the three isotopologues of CH ₂ Br ₂	93
5.S3	Anharmonic rotational constants of CH ₂ ⁷⁹ Br ⁸¹ Br at vibrational ground and excited states.	94
5.S4	Anharmonic rotational constants of CH ₂ ⁷⁹ Br ₂ at vibrational ground and excited states.	94
5.S5	Inertia, Coriolis, and anharmonicity correction terms of CH ₂ ⁷⁹ Br ⁸¹ Br.	95
7.S1	List of atmospheric molecules grouped in terms of their relaxation times.	144

Acronyms

AOM	acousto-optical modulator
BO	Born–Oppenheimer
cw	continuous wave
CEAS	cavity enhanced absorption spectroscopy
CRDS	cavity ringdown spectroscopy
DFB	distributed feedback
ECD	electron capture detection
FMS	frequency modulation spectroscopy
FSR	free spectral range
FTIR	Fourier transform infrared
GC	gas chromatography
HVOCs	halogenated volatile organic compounds
ICE	intracavity etalon
ITCZ	intertropical convergence zone
LAS	laser absorption spectroscopy
LOD	limit of detection
MBL	marine boundary layer
MS	mass spectrometry
OPO	optical parametric oscillator
PZT	piezoelectric transducer
Sat-CRDS	saturated-absorption cavity ringdown spectroscopy
SNR	signal-to-noise ratio
SSA	sea salt aerosol
SR	single resonant
TTL	tropical tropopause layer
VOCs	volatile organic compounds
VPT2	second-order vibrational perturbation theory
VSLs	very short-lived substances
WMO	World Meteorological Organization
WMS	wavelength modulation spectroscopy

Introduction

1.1 Humans and Earth's Ocean-Atmosphere

The Earth's system as a whole with its four major components—the atmosphere, oceans, land, and associated living beings including humans—are inevitably intertwined. In fact, understanding of the dynamics driving changes in the global environment must surpass the classical academic disciplines. Fortunately, scientists are ever-aware that the sciences of the oceans, atmosphere, and land are interconnected in a countless ways (i.e., a change in one part of the Earth's system has reflections for other parts). That is why the term *Ocean-Atmosphere* is preferred in this context to emphasize the strong interactions between these two large components of our Earth's system. Human activities such as energy and food production, since the beginning of industrialization in the 19th century, have profoundly forced many of the global environmental changes. Many of these changes are of chemical origin. Examples of such changes include the formation of ozone hole in the Antarctica since the late 1970s, the global spread of air pollution resulting from industrial combustion and biomass burning, and global warming with the related ocean acidification issues resulting from increasing anthropogenic CO₂ emissions and other greenhouse gases [1].

Our understanding to the Earth's atmosphere has greatly evolved with time. Actually, he was Aristotle (384 - 322 BC), who wrote the first scientific treatise recognizing water as a distinct component of the air and its continuous recycling between the atmosphere and the ocean. As chemistry evolved over two millennia—as Khem became Khemia, then Alchemy and eventually Chemistry¹ [2]—the study of the chemistry of the atmosphere has become a multidisciplinary approach that draws on environmental chemistry, physics, meteorology, computer modeling, oceanography and other disciplines. The earlier view of the atmosphere in 1950 has been changed dramatically—it was viewed as a chemically inert fluid that moved moisture, heat, and momentum. Progress since then has revealed the current picture of the Earth's atmosphere as a complex chemical and dynamical system interacting internally (within the troposphere and stratosphere) and externally (with oceans, lands and living beings). As new observation methods with impressive sensitivity and selectivity became available, less abundant chemical constituents (so-called trace gases) were discovered, and time series measurements have discovered their temporal trends. For example, halocarbons were first detected in the atmosphere in 1970 after the invention of electron-capture-detector that is very sensitivity to electron-absorbing components such as halogenated compounds [1]. New related chemical reactions and mechanisms have been proposed and investigated—the stratospheric ozone formation by UV dissociation of O₂ is now well-known to be counterbalanced by the very efficient ozone-depleting catalytic chain reactions involving HO_x, NO_x, BrO_x, and ClO_x.

The ocean is coupled physically and biogeochemically to the atmosphere and thus contributes sig-

¹It should be noted that the etymology of the word chemistry is debatable and the ultimate origin of the root word *chem* is uncertain.

nificantly to the global budget of a number of atmospherically relevant trace gases, including those compounds that contain sulfur, nitrogen and halogens [3]. The oceans can be a source or a sink of these trace gases, depending on the concentration gradient across the ocean-atmosphere interface and the possible photochemical reactions taking place at or near the surface seawater. These trace gases play critical roles in the global biogeochemical cycles and are involved in several atmospheric processes including marine aerosol formation and aging, tropospheric ozone formation and destruction, stratospheric ozone loss and cycling process of the photo-oxidants. Fig. 1.1 presents some of the ocean-atmosphere interactions that take place at the marine boundary layer (MBL), where biological processes in the water and photochemical reactions at the interface produce volatile organic compounds (VOCs), dimethyl sulfide (DMS), and halocarbons (R-Hal, Hal = Br, Cl, I).

It is a matter-of-fact that changing atmospheric chemical composition can exert strong leverage over climate system, hence, future human life. A significant opportunity to adopt a more comprehensive approaches to combat climate change and its impacts is connected to the 2030 Agenda for Sustainable Development, which was ratified in 2015 by the United Nations. Urgent combating of climate change and conservation of the oceans, seas, and marine resources are addressed in the Sustainable Development Goals 13 *“Take urgent action to combat climate change and its impacts”* and 14 *“Conserve and sustainably use the oceans, seas and marine resources”*.

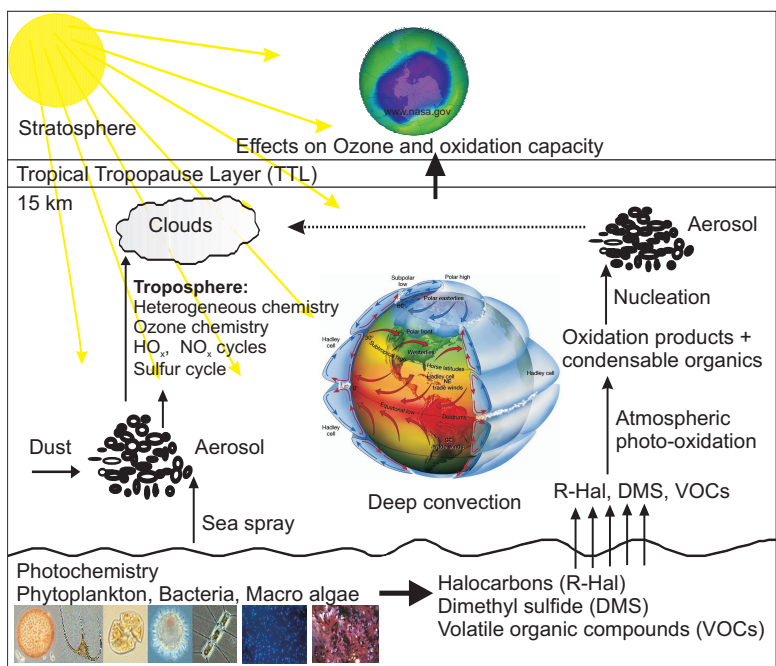


Figure 1.1: Schematic showing some of the oceanic emissions and their impact on the lower and upper atmosphere (picture inspired by B. Quack, GEOMAR, Kiel).

1.2 Halogenated Volatile Organic Compounds

Halogenated volatile organic compounds (HVOCs) are a group of trace gases that play critical roles in atmospheric chemistry—they contribute significantly to stratospheric ozone depletion and change the overall oxidation capacity of the atmosphere [4, 5, 6, 7]. In addition, some of those HVOCs are extensively used in many industrial and agriculture applications. For example, methyl bromide was used as a fumigant for soils, which was banned after the Montreal protocol, promoting the use of

methyl iodide as an alternative pre-plant agriculture pesticide [8]. Methyl iodide is also used for other dispersive applications including decontamination/fumigation of buildings [9].

The anthropogenic sources of HVOCs are quite well known [10] as can be estimated from industrial production data. More challenging are the halogenated compounds of natural origin as their sources and transport to the upper atmosphere remain uncertain. Oceans have been implicated as one of the major natural sources [11, 12, 13, 14], where organisms such as bacteria, fungi, and algae produce large quantities of HVOCs as part of their marine biological activity [15, 16], and photochemical processes occurring at or near the surface produce others [17, 18]. Also, some terrestrial abiotic processes (e.g., volcanic eruptions, biomass burning, and degradation of rotten plant material) [19, 20, 21] have been identified as such sources. For example, it has been reported that halide ions in soils and sediments can be alkylated during the oxidation of organic matter by an electron acceptor such as Fe(III) [22].

Most of the active bromine and chlorine in the MBL are liberated to the atmosphere from sea salt aerosol (SSA). Vogt et al. [23] suggested a mechanism for acid catalysis of halogen release from SSA in the remote MBL (i.e., it is independent of the NO_x -based mechanism as NO_x are not present in the un-polluted air of the remote MBL). In this mechanism the gaseous HOBr is scavenged by the aerosol and converted to slightly soluble BrCl and Br_2 , which are then released into air. Although sea-spray accounts for most of bromine and chlorine in the MBL [24, 25, 26], the sea-air exchange is a dominant source for important very short-lived brominated compounds such as CHBr_3 , CH_2Br_2 [27, 28] and it is the main source of gaseous organic and inorganic iodine [29, 30, 31]. The processing of reactive halogens through gas and aerosol phases of the MBL is believed to have a significant effect on the lifetimes and the budget of many climatically active gases [32]. For example, reactions involving chlorine and bromine change the oxidation capacity of the troposphere in many different ways including the destruction of ozone ($\sim 50\%$ of MBL photochemical O_3 destruction) [29], modification of HO_x and NO_x cycles [33], oxidation of DMS (up to 60% reduction in the DMS column by BrO [28]), and oxidation of sulfur (IV) in acidified SSA (HOBr and HOCl are responsible for 20% and 40%, respectively) [23].

1.2.1 Very Short-Lived Substances

It was generally believed that only HVOCs whose average lifetime in the lower atmosphere exceeds one year are able to contribute to stratosphere ozone depletion (as they remain intact long enough to be transported to the stratosphere). However, there is a discrepancy between the relatively well quantified long-lived HVOCs and the observed amount of stratospheric halogen [34, 35]. It was also suggested that this discrepancy could be displaced when taking into account very short-lived substances (VSLS) as a previously neglected source.

The World Meteorological Organization (WMO) [27] defines VSLS as trace gases whose local tropospheric lifetimes are comparable to, or shorter than, tropospheric transport time scales. Consequently, their spatial tropospheric distributions are non-uniform. In practice, VSLS are considered to have atmospheric lifetimes of less than 6 months. Several studies have demonstrated that VSLS, by being transported to the stratosphere by strong-upwind presents in the intertropical convergence zone (ITCZ), can act as an additional radical source for ozone depletion [27]. Berthet et al. [36] found that the concentrations of VSLS in the tropical tropopause layer (TTL) are strongly dependent on the efficiency of vertical transport. The concentrations tend to be high in areas of vigorous convective activity, such as the West Pacific or the Maritime Continent of localized hot spots.

Table 1.1: Estimated MBL mixing ratios of most common brominated, chlorinated, and iodinated VSLs and their tropospheric lifetimes, adopted from WMO [27].

Species	Mixing ratio, ppt	Lifetime, days
CHBr ₃	1.6 ± 0.9	24
CH ₂ Br ₂	1.1 ± 0.4	123
CHBr ₂ Cl	0.3 ± 0.3	59
CHBrCl ₂	0.3 ± 0.3	78
CH ₂ BrCl	0.5 ± 0.1	137
CH ₂ Cl ₂	17.5 ± 15	140
CHCl ₃	7.8 ± 3.9	150
CH ₃ I	0.8 ± 0.8	7.0

Nowadays, after more than one and half decade of research, the importance of VSLs for stratospheric ozone depletion is generally accepted, with brominated VSLs believed to make the significant contribution to total stratospheric bromine. Most important brominated VSLs are assumed to be CHBr₃ and CH₂Br₂ contributing about 4.5 ± 3.5 parts per trillion (ppt) to stratospheric bromine loading, compared to approximately 15.5 ppt originated from long-lived source gases [27]. The estimated boundary layer mixing ratios and tropospheric lifetimes of the most common VSLs, adopted from the WMO [27], are presented in Table 1.1. This table shows that CH₂Cl₂ and CHCl₃ are the most abundant VSLs, with an average boundary layer mixing ratios of 17.5 ± 15.0 ppt and 7.8 ± 3.9 ppt, respectively. However, for comparison with brominated and iodinated VSLs, it needs to be taken into account that bromine atom is about 40 - 60 times more effective than chlorine for global ozone destruction [37]. The main source of bromine VSLs is considered to be marine microorganisms such as macroalgae and phytoplankton groups. The highest emissions of these species are measured in near-coastal and upwelling areas, especially in the tropics [38, 39, 40], with air mixing ratios as high as 100 ppt [38]. Another important issue is the large uncertainty of the reported mixing ratios, as indicated in Table 1.1. Therefore, in light of the current knowledge, it is difficult to give an accurate large-scale VSLs flux estimates, as there are only few measurements available with very large spatial and temporal variability. For instance, Quack and Wallace [38] measured CHBr₃ in a range from 0.2 to 100 ppt in the MBL. Next to the natural effects, at least part of this large variability may be attributed to inter-instrumental biases immanent to quantification of such very low species concentrations [41].

1.3 Laser-Based Trace Gas Sensing

Laser-based absorption spectroscopy has found widespread use in a multitude of applications including environmental monitoring, industrial process control (e.g., semiconductor fabrication), atmospheric chemistry (e.g., pollutant emission monitoring), remote gas sensing (e.g., toxic environments, explosive compounds, astronomical instrumentations), and medical applications (e.g., breath analysis), to name a few [42, 43, 44]. In addition, it has been widely applied for atomic and molecular physics applications where the use of quantum mechanical models can relate the atomic and the molecular spectra of the gases to their physical properties [45]. The unique capabilities of laser sources—the high monochromaticity and spectral brightness, narrow line width, and the wavelength tunability—are key parameters to achieve high selectivity and sensitivity for trace gas monitoring applications.

Absorption of light is based on quantization of energy states, where only photons that fulfill the res-

onance condition (i.e., the photon energy equals the energy difference between the two connected molecular energy states) are absorbed. Measuring attenuation of a light beam transmitted through a sample as function of the wavelength (i.e., photon energy) yields the absorption spectrum. Since each molecule exhibits its own characteristic absorption spectrum, selective species detection is possible. In addition, quantitative concentration measurements can be performed using Beer-Lambert’s law, assuming known absorption cross-section of the species.

$$I(\nu) = I_0(\nu)e^{-\alpha(\nu)L_{\text{eff}}} = I_0(\nu)e^{-\sigma(\nu)[c]L_{\text{eff}}}. \quad (1.1)$$

Here, $I(\nu)$ is the transmitted intensity, $I_0(\nu)$ is the initial intensity, and L_{eff} is the effective absorption path length. $\alpha = \sigma[c]$ is the absorption coefficient, with σ is the absorption cross-section and $[c]$ is the concentration of species. The absorption coefficient α comprises all individual absorption coefficients in case there are more than one absorbing species. It should be noted that Beer-Lambert’s law is only strictly obeyed when the spectral bandwidth of the detection light is narrower than the spectral width of the absorption feature (i.e., narrow-bandwidth absorption) and when the electric field interacting with the sample is weak (i.e., low intensity). The latter case is termed “linear” absorption spectroscopy in contrast to “non-linear” absorption when a strong electric field is applied². At the non-linear absorption conditions, the measured absorption coefficient α becomes a function of the intensity of the incident laser radiation (more details are introduced in Chapter 2).

In principle, there are two main challenges for optical trace gas sensing based on laser absorption spectroscopy techniques: (i) the attainable limit of detection (LOD), and (ii) the so-called cross-sensitivity or interference issue.

The most common and simple type of laser-based sensing techniques—direct laser absorption spectroscopy (LAS) [46]—is often limited to minimum detectable absorbances of $\sim 10^{-3}$, which is 4 – 5 orders of magnitude worse than the theoretical shot noise level of $10^{-7} - 10^{-8}$ for a single pass direct LAS technique. Basically, the LOD is evaluated by the signal-to-noise ratio (SNR), which can be enhanced by several measures. Some measures improve the SNR by suppressing the noise components (i.e, modulation spectroscopy). Other measures enhance the SNR by increasing the signal. For example, the absorption cross-section can be maximized (e.g., by detecting species in the IR instead of the NIR, where the absorption cross-sections are relatively lower). Also, the absorption path length can be effectively extended (i.e., by using multi-pass absorption cells or optical cavities).

Modulation techniques rely on the fact that $1/f$ noises usually decrease with increasing frequency, hence improving the SNR and the attainable LOD. The most common modulation approaches, wavelength modulation spectroscopy (WMS) [47] and frequency modulation spectroscopy (FMS) [48], provide about two orders of magnitude better sensitivity than direct LAS (i.e., typical sensitivities are in the 10^{-5} range). Optical cavities (in its simplest form consisting of two high reflective mirrors) extend the apparent path length of few cm to an effective path length of few km. Introducing a species inside the cavity in which the light bounces back and forth many times multiplies the measured effective absorption considerably. This cavity advantage has led to a group of techniques referred to as cavity-

²At linear condition of weak electric field $E(\omega)$, the macroscopic electric dipole moment called polarization, $P(\omega)$ is related to the molecular susceptibility $\chi(\omega)$ as: $P(\omega) = \chi(\omega)E(\omega)$ where ω is the angular frequency. At non-linear condition of intense electric field, $P(\omega)$ will include a contribution from the higher order molecular susceptibility as: $P = P^{\text{Linear}} + P^{\text{Non-linear}} = \epsilon_0 [\chi^{(1)} \cdot E + \chi^{(2)} \cdot E^2 + \chi^{(3)} \cdot E^3]$, where ϵ_0 is the permittivity.

enhanced absorption spectroscopy (CEAS). A very common variant of CEAS is called cavity ringdown spectroscopy (CRDS) [49, 50], in which the decay constant of the transmitted light intensity from an excited cavity is measured rather than the absolute intensity (details are introduced in Chapter 2).

Of similar importance to the attainable limit of detection is the cross-sensitivity issue (i.e., the existence of several overlapping absorptions at the same wavelength). In this case, the measured spectrum will be a superposition of the individual spectra of all interfering species. There exist some precautions to bypass this issue including (i) the use of narrow bandwidth light sources that enable absorption features of different molecular species to be discriminated, (ii) the measurement of the high-resolution absorption spectra over a wide range and use spectral fitting routines to retrieve the composition of the mixture, and (iii) the use of upstream separation columns that separate the different species based on their physical and chemical properties.

As an example, Fig. 1.2 presents the simulated absorption spectra of several atmospheric constituents at their typical atmospheric mixing ratios. Except for H₂O, where a 300 ppm mixing ratio has been assumed.³ The simulations cover the accessible range of the mid-IR light source used in this work (2200 to 4000 cm⁻¹) and have been calculated using the HITRAN database [51] assuming an absorption cell pressure of 20 mbar. Although the mixing ratio H₂O has been reduced, H₂O is still the dominant absorbing species, in particular the broad absorption band around 3750 cm⁻¹ that can be assigned to rovibrational OH-stretch transitions. The second strongest absorber is CO₂, which shows a very strong absorption at wavenumbers around 2349 cm⁻¹, corresponding to the ν_3 asymmetric stretch. Given the strong overlap of the absorption spectra, it is astonishing that selective detection of a single trace gas in natural environment is possible at all. However, as will be demonstrated in this thesis as well, high-resolution spectroscopy enables more or less interference free detection—but cross-sensitivity remains a cause of concern.

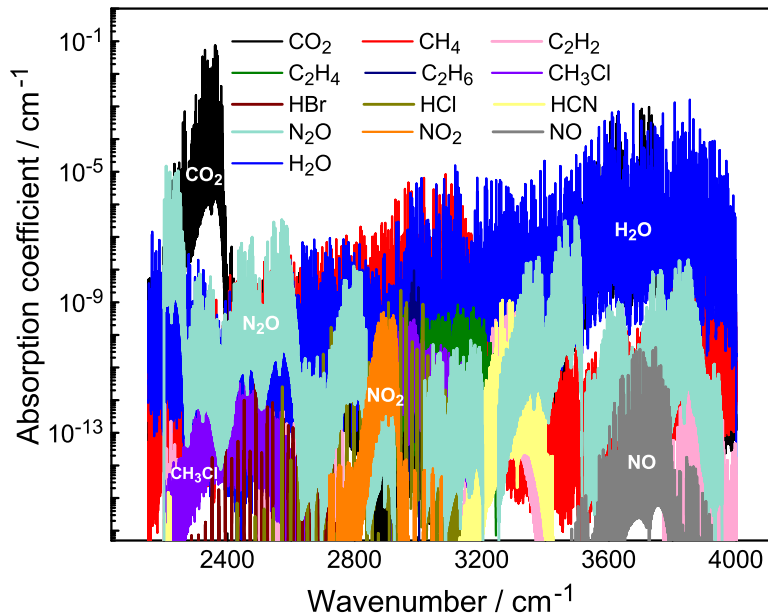


Figure 1.2: Simulated absorption spectra of several atmospheric molecules in the mid-IR window from ~ 2.5 to $4.6 \mu\text{m}$ using HITRAN database [51]. The spectra were calculated for atmospheric mixing ratios and for 20 mbar. H₂O absorption is reported for 300 ppm mixing ratio assuming dry atmospheric samples (see text).

³Such mixing ratios of water can be readily achieved by removing water vapor from gas flow using e.g., desiccants, cryocondensation, adsorbents.

1.4 Objectives and Research Milestones

The detection of HVOCs is mainly based on gas chromatography - mass spectrometry/electron capture detection (GC-MS/ECD) techniques, as yet. Such GC-MS/ECD techniques require considerable calibration efforts and allow for only discrete measurements with low sampling frequency. The discrete measurements together with the time consuming analysis (several tens of minutes for each sample) represent a barrier for field and workplace monitoring applications as well as for leak detection and laboratory process studies. Recent advances in laser absorption-based optical detection schemes such as the state-of-the-art CRDS have proven to overcome these limitations. Unfortunately, commercially available and field-deployable CRDS instruments are limited to the most common atmospheric trace gases (e.g., CO₂, CH₄, and N₂O) [52, 53, 54, 55]. They are mostly based on molecular absorption in the NIR spectral range where light sources with sufficient narrow spectral bandwidth and the required optical equipment are readily available. Due to the low absorption cross-sections in the NIR in combination with their low natural abundance, similar instruments are not available for HVOCs and many other volatile organic compounds.

To add on these issues, the research in this thesis was mainly concerned with two main objectives:

1. Setting up a new mid-IR cavity ringdown spectrometer as a *development platform* for trace gas sensors and field going instrumentation. As a pre-requisite for HVOCs detection, fundamental spectroscopic and analytical work has been performed as well. Following research milestones were achieved:
 - Setting up a CRD spectrometer using a new continuous wave (cw) single-resonant (SR) optical parametric oscillator (OPO) as a light source in the mid-IR range (Chapter 3).
 - In collaboration with Prof. D. Wallace, University of Dalhousie, Canada—a first comparative study for the detection of HVOCs using both GC-MS/ECD and mid-IR CRDS has been performed, CH₃I has been selected as a test case (Chapter 4).
 - A major challenge for environmental monitoring of HVOCs is the scarcity or even lack of the high-resolution spectra that are required for line selection. High-resolution rovibrational spectra of the of the ν_1 and ν_6 vibrational bands of CH₂Br₂ have been recorded and assigned with the help of a new quantum-chemically assisted simulation approach (Chapter 5).
2. Implementation and development of new and innovative approaches for quantitative detection of trace gases based on saturation absorption spectroscopy that holds the potential to further enhance the sensitivity and to overcome the cross-sensitivity issue. In contrast to previous work that often avoided saturation effects, quantitative saturated-absorption CRDS [56] has recently been reported to enhance the measurements sensitivity [57]. Following research milestones were achieved:
 - The dynamics of the absorption saturation evolution within the ringdown transient have been studied in detail allowing to assess the working limits and to perform error analysis of the new saturated-absorption CRDS approach (Chapter 6).
 - In a novel approach, optical saturation was exploited to allow for selective saturation of an individual absorption contribution out of two species absorbing at the same wavelength. In

principle, by adding absorption saturation as a new dimension to the absorption spectra, this approach enables “Two-species One-wavelength” detection and hence holds the potential to overcome, or at least significantly reduce the limitations arising from spectral band overlap (Chapter 7).

References

- [1] G. P. Brasseur, R. G. Prinn, and A. A. P. Pszenny, editors. *Atmospheric Chemistry in a Changing World*. Springer Berlin Heidelberg, Berlin, Heidelberg, 2003.
- [2] C. A. Ronan. *Science: Its history and development among the world's cultures*. Facts on File, New York, 1982.
- [3] P. S. Liss, C. A. Marandino, E. E. Dahl, D. Helmig, E. J. Hints, C. Hughes, M. T. Johnson, R. M. Moore, J. M. C. Plane, and B. Quack *et al.* *Short-Lived Trace Gases in the Surface Ocean and the Atmosphere*. Springer Berlin Heidelberg, Berlin, Heidelberg, 2014.
- [4] P. J. Crutzen and F. Arnold. Nitric acid cloud formation in the cold Antarctic stratosphere: A major cause for the springtime ‘ozone hole’. *Nature*, 324(6098):651–655, 1986.
- [5] S. Solomon. Progress towards a quantitative understanding of Antarctic ozone depletion. *Nature*, 347(6291):347–354, 1990.
- [6] J. G. Anderson, D. W. Toohey, and W. H. Brune. Free radicals within the Antarctic vortex: The role of CFCs in Antarctic ozone loss. *Science*, 251(4989):39–46, 1991.
- [7] G. W. Gribble. *Naturally Occurring Organohalogen Compounds - A Comprehensive Update*, volume 91. Springer Vienna, Vienna, 2010.
- [8] D. J. Ashworth, S. R. Yates, L. Luo, S. R. Lee, and R. Xuan. Coupling of soil solarization and reduced rate fumigation: Effects on methyl iodide emissions from raised beds under field conditions. *J. Agric. Food Chem.*, 61(51):12510–12515, 2013.
- [9] M. Sutton, S. R. Kane, and J. R. Wollard. Methyl iodide fumigation of bacillus anthracis spores. *LLNL-Technical Report-562673*, 2012.
- [10] J. H. Butler, M. Battle, M. L. Bender, S. A. Montzka, A. D. Clarke, E. S. Saltzman, C. M. Sucher, J. P. Severinghaus, and J. W. Elkins. A record of atmospheric halocarbons during the twentieth century from polar firn air. *Nature*, 399(6738):749–755, 1999.
- [11] J. E. Lovelock. Natural halocarbons in the air and in the sea. *Nature*, 256(5514):193–194, 1975.
- [12] H. B. Singh, L. J. Salas, and R. E. Stiles. Methyl halides in and over the eastern Pacific (40°N–32°S). *J. Geophys. Res.*, 88(C6):3684, 1983.
- [13] Th. Class and K. Ballschmiter. Chemistry of organic traces in air. *J. Atmos. Chem.*, 6(1):35–46, 1988.
- [14] R. M. Moore, W. Groszko, and S. J. Niven. Ocean-atmosphere exchange of methyl chloride: Results from NW Atlantic and Pacific ocean studies. *J. Geophys. Res.: Atmos.*, 101(C12):28529–28538, 1996.
- [15] W. T. Sturges, C. W. Sullivan, R. C. Schnell, L. E. Heidt, and W. H. Pollock. Bromoalkane production by Antarctic ice algae. *Tellus B*, 45(2):120–126, 1993.
- [16] F. Laturus, F. C. Adams, and C. Wiencke. Methyl halides from Antarctic macroalgae. *Geophys. Res. Lett.*, 25(6):773–776, 1998.

- [17] N. Bell, L. Hsu, D. J. Jacob, M. G. Schultz, D. R. Blake, J. H. Butler, D. B. King, J. M. Lobert, and E. Maier-Reimer. Methyl iodide: Atmospheric budget and use as a tracer of marine convection in global models. *J. Geophys. Res.*, 107(D17):ACH-8/1–12, 2002.
- [18] R. M. Moore and O. C. Zafiriou. Photochemical production of methyl iodide in seawater. *J. Geophys. Res.: Atmos.*, 99(D8):16415–16420, 1994.
- [19] D. B. Harper. Halomethane from halide ion—a highly efficient fungal conversion of environmental significance. *Nature*, 315(6014):55–57, 1985.
- [20] M. O. Andreae, E. Atlas, G. W. Harris, G. Helas, A. de Kock, R. Koppmann, W. Maenhaut, S. Manø, W. H. Pollock, and J. Rudolph *et al.* Methyl halide emissions from savanna fires in southern Africa. *J. Geophys. Res.: Atmos.*, 101(D19):23603–23613, 1996.
- [21] Y. Yokouchi, Y. Noijiri, L. A. Barrie, D. Toom-Sauntry, T. Machida, Y. Inuzuka, H. Akimoto, H. J. Li, Y. Fujinuma, and S. Aoki. A strong source of methyl chloride to the atmosphere from tropical coastal land. *Nature*, 403(6767):295–298, 2000.
- [22] F. Keppler, R. Eiden, V. Niedan, J. Pracht, and H. F. Scholer. Halocarbons produced by natural oxidation processes during degradation of organic matter. *Nature*, 403(6767):298–301, 2000.
- [23] R. Vogt, P. J. Crutzen, and R. Sander. A mechanism for halogen release from sea-salt aerosol in the remote marine boundary layer. *Nature*, 383(6598):327–330, 1996.
- [24] E. M. Knipping and D. Dabdub. Impact of chlorine emissions from sea-salt aerosol on coastal urban ozone. *Environ. Sci. Technol.*, 37(2):275–284, 2003.
- [25] J. A. Thornton, J. P. Kercher, T. P. Riedel, N. L. Wagner, J. Cozic, J. S. Holloway, W. P. Dube, G. M. Wolfe, P. K. Quinn, and A. M. Middlebrook *et al.* A large atomic chlorine source inferred from mid-continental reactive nitrogen chemistry. *Nature*, 464(7286):271–274, 2010.
- [26] R. Vogt, R. Sander, R. von Glasow, and P. J. Crutzen. Iodine chemistry and its role in halogen activation and ozone loss in the marine boundary layer: A model study. *J. Atmos. Chem.*, 32(3):375–395, 1999.
- [27] S. A. Montzka, S. Reimann, S. O’Doherty, A. Engel, A. K. Kruger, W. T. Sturges, D. Blake, M. Dorf, P. Fraser, and L. Froidevaux *et al.* *Scientific assessment of ozone depletion:2010*. Global Ozone Research and Monitoring Project report: No. 52. World Meteorological Organization, Geneva Switzerland, 2011.
- [28] R. von Glasow, R. von Kuhlmann, M. G. Lawrence, U. Platt, and P. J. Crutzen. Impact of reactive bromine chemistry in the troposphere. *Atmos. Chem. Phys.*, 4(11/12):2481–2497, 2004.
- [29] A. S. Mahajan, J. M. C. Plane, H. Oetjen, L. Mendes, R. W. Saunders, A. Saiz-Lopez, C. E. Jones, L. J. Carpenter, and G. B. McFiggans. Measurement and modelling of tropospheric reactive halogen species over the tropical Atlantic ocean. *Atmos. Chem. Phys.*, 10(10):4611–4624, 2010.
- [30] C. E. Jones, K. E. Hornsby, R. Sommariva, R. M. Dunk, R. von Glasow, G. McFiggans, and L. J. Carpenter. Quantifying the contribution of marine organic gases to atmospheric iodine. *Geophys. Res. Lett.*, 37(18), 2010.

- [31] L. J. Carpenter. Iodine in the marine boundary layer. *Chem. Rev.*, 103(12):4953–4962, 2003.
- [32] L. J. Carpenter, S. D. Archer, and R. Beale. Ocean-atmosphere trace gas exchange. *Chem. Soc. Rev.*, 41(19):6473–6506, 2012.
- [33] W. C. Keene, M. S. Long, A. A. P. Pszenny, R. Sander, J. R. Maben, A. J. Wall, T. L. O’Halloran, A. Kerkweg, E. V. Fischer, and O. Schrems. Latitudinal variation in the multiphase chemical processing of inorganic halogens and related species over the eastern north and south Atlantic oceans. *Atmos. Chem. Phys.*, 9(19):7361–7385, 2009.
- [34] V. L. Dvortsov, M. A. Geller, S. Solomon, S. M. Schauffler, Elliot L. Atlas, and D. R. Blake. Rethinking reactive halogen budgets in the midlatitude lower stratosphere. *Geophys. Res. Lett.*, 26(12):1699–1702, 1999.
- [35] W. T. Sturges, D. E. Oram, L. J. Carpenter, S. A. Penkett, and A. Engel. Bromoform as a source of stratospheric bromine. *Geophys. Res. Lett.*, 27(14):2081–2084, 2000.
- [36] G. Berthet, J. G. Esler, and P. H. Haynes. A lagrangian perspective of the tropopause and the ventilation of the lowermost stratosphere. *J. Geophys. Res.*, 112(D18), 2007.
- [37] J. S. Daniel, S. Solomon, R. W. Portmann, and R. R. Garcia. Stratospheric ozone destruction: The importance of bromine relative to chlorine. *J. Geophys. Res.: Atmos.*, 104(D19):23871–23880, 1999.
- [38] B. Quack and D. W. R. Wallace. Air-sea flux of bromoform: Controls, rates, and implications. *Global Biogeochem. Cycles*, 17(1), 2003.
- [39] Y. Yokouchi, F. Hasebe, M. Fujiwara, H. Takashima, M. Shiotani, N. Nishi, Y. Kanaya, S. Hashimoto, P. Fraser, and D. Toom-Sauntry *et al.* Correlations and emission ratios among bromoform, dibromochloromethane, and dibromomethane in the atmosphere. *J. Geophys. Res.*, 110(D23), 2005.
- [40] L. J. Carpenter and P. S. Liss. On temperate sources of bromoform and other reactive organic bromine gases. *J. Geophys. Res.: Atmos.*, 105(D16):20539–20547, 2000.
- [41] J. H. Butler, T. G. Bell, B. D. Hall, B. Quack, L. J. Carpenter, and J. Williams. Technical note: Ensuring consistent, global measurements of very short-lived halocarbon gases in the ocean and atmosphere. *Atmos. Chem. Phys.*, 10(2):327–330, 2010.
- [42] P. Hering, J. P. Lay, and S. Stry, editors. *Laser in environmental and life sciences: Modern analytical methods*. Springer, Berlin and New York, 2004.
- [43] A. Amann and D. Smith, editors. *Breath analysis for clinical diagnosis and therapeutic monitoring*. World Scientific, Singapore and London, 2005.
- [44] M. Lackner, editor. *Lasers in chemistry*. Wiley-VCH, Weinheim, 2008.
- [45] W. Demtröder. *Laser Spectroscopy: Experimental Techniques*, volume 2. Springer, Berlin, Heidelberg, 2008.

- [46] A. Fried and D. Richter. Infrared absorption spectroscopy. In *Analytical Techniques for Atmospheric Measurement*. Blackwell Publishing, 2007.
- [47] P. Kluczynski, J. Gustafsson, Å. M. Lindberg, and O. Axner. Wavelength modulation absorption spectrometry—an extensive scrutiny of the generation of signals. *Spectrochim. Acta, Part B*, 56(8):1277–1354, 2001.
- [48] G. C. Bjorklund, M. D. Levenson, W. Lenth, and C. Ortiz. Frequency modulation (FM) spectroscopy. *Appl. Phys. B: Photophys. Laser Chem.*, 32(3):145–152, 1983.
- [49] A. O’Keefe and D. A. G. Deacon. Cavity ring-down optical spectrometer for absorption measurements using pulsed laser sources. *Rev. Sci. Instrum.*, 59(12):2544–2551, 1988.
- [50] B. A. Paldus and A. A. Kachanov. A historical overview of cavity-enhanced methods. *Can. J. Phys.*, 83(10):975–999, 2005.
- [51] L. S. Rothman, I. E. Gordon, Y. Babikov, A. Barbe, D. Chris Benner, P. F. Bernath, M. Birk, L. Bizzocchi, V. Boudon, and L. R. Brown *et al.* The HITRAN2012 molecular spectroscopic database. *J. Quant. Spectrosc. Radiat. Transfer*, 130:4–50, 2013.
- [52] G. Friedrichs, J. Bock, F. Temps, P. Fietzek, A. Körtzinger, and D. W. R. Wallace. Toward continuous monitoring of seawater $^{13}\text{CO}_2 / ^{12}\text{CO}_2$ isotope ratio and $p\text{CO}_2$: Performance of cavity ringdown spectroscopy and gas matrix effects. *Limnol. Oceanogr.: Methods*, 8(10):539–551, 2010.
- [53] M. Becker, N. Andersen, B. Fiedler, P. Fietzek, A. Körtzinger, T. Steinhoff, and G. Friedrichs. Using cavity ringdown spectroscopy for continuous monitoring of $\delta^{13}\text{C}(\text{CO}_2)$ and $f\text{CO}_2$ in the surface ocean. *Limnol. Oceanogr.: Methods*, 10(10):752–766, 2012.
- [54] E. R. Crosson. A cavity ring-down analyzer for measuring atmospheric levels of methane, carbon dioxide, and water vapor. *Appl. Phys. B*, 92(3):403–408, 2008.
- [55] C. O’Reilly, I. R. Santos, T. Cyronak, A. McMahon, and D. T. Maher. Nitrous oxide and methane dynamics in a coral reef lagoon driven by pore water exchange: Insights from automated high-frequency observations. *Geophys. Res. Lett.*, 42(8):2885–2892, 2015.
- [56] G. Giusfredi, S. Bartalini, S. Borri, P. Cancio, I. Galli, D. Mazzotti, and P. de Natale. Saturated-absorption cavity ring-down spectroscopy. *Phys. Rev. Lett.*, 104(11):110801/1–4, 2010.
- [57] I. Galli, S. Bartalini, S. Borri, P. Cancio, D. Mazzotti, P. de Natale, and G. Giusfredi. Molecular gas sensing below parts per trillion: Radiocarbon-dioxide optical detection. *Phys. Rev. Lett.*, 108(17):179902, 2012.

Theoretical Background

2.1 Cavity Enhanced Absorption Techniques

Cavity Ringdown Spectroscopy (CRDS), in a broad sense, is one variant of the cavity enhanced absorption spectroscopic methods that exploits the use of high-finesse optical cavities for absorption spectroscopy. Technically speaking, cavity ringdown method refers to experiments when the intracavity absorption is deduced from the decay of the intracavity intensity. The unique feature of the high-finesse optical cavities, which act as optical resonators, is that they support stable resonance frequencies (i.e., cavity modes) based on their physical configuration. Like each resonator, optical cavities are described by their characteristic time response after an impulsive excitation. This time response is very sensitive and selective to any external perturbations, making them ideal for sensitive applications.

As mentioned earlier (cf. Section 1.3), before the exploitation of optical resonators, the sensitivity of laser based absorption measurements was limited by the interaction length of the light beam with the absorbing matter as well as the amplitude and frequency fluctuations of the laser source. Actually, frequency fluctuations are as important as amplitude fluctuations for high-resolution measurements, which are essential for trace gas sensing (vide infra). Cavity ringdown techniques overcome all of these issues simultaneously, where the use of super-reflective mirrors extends the few cm apparent length of the cavity to few km effective interaction length. This enhancement of the absorption length depends on the gain factor $1/(1 - R)$, with R being the mirror reflectivity. In addition, the measurement of the the photon lifetime (i.e., ringdown decay time) rather than the absolute intensity allows for a kind of immunity with respect to amplitude fluctuations of the light source. These two advantages are inherent to all cavity ringdown experiments. Moreover, the cavity resonances can be used to provide a very precise frequency scale for metrology applications.

2.1.1 Standard Cavity Ringdown Spectroscopy

The term *standard* in this thesis is used to refer to an absorption measurement that is conducted at the linear absorption regime with low light field intensity. This is the case for almost all practical implementation of quantitative absorption measurements relying on Beer-Lambert's law. The first paper on standard cavity ringdown measurement clearly stating its advantage of immunity to source intensity noises was published in 1984 by Anderson et al. [1]. Actually, this was four years after Herblin et al. [2] who were able to measure the cavity photon lifetime using a phase shift approach. Much earlier, the spectral properties of optical cavities were investigated starting around 1960 with the invention of the first lasers. Later on, the manufacturing of dielectric mirrors with very high reflectivity stimulated the development of cavity ringdown spectroscopy. In the seminal work of Crawford et al. [3] in 1985, the figurative term *cavity ringdown* was introduced to denote the exponential decay of the intracavity power after impulsive excitation. O'Keefe and Deacon [4] in 1988 used Crawford's experimental scheme and adopted the same term *cavity ringdown* for their measurements of the weak magnetic-dipole allowed

transitions of the atmospheric oxygen. This is what is now commonly considered the first demonstration of CRDS. Figure 2.1 presents a schematic of the basic elements of standard CRDS setup in pulsed (upper panel) and continuous wave, cw (lower panel) configurations. An acousto-optical modulator is commonly used in the cw-CRDS implementation as a fast optical switch.

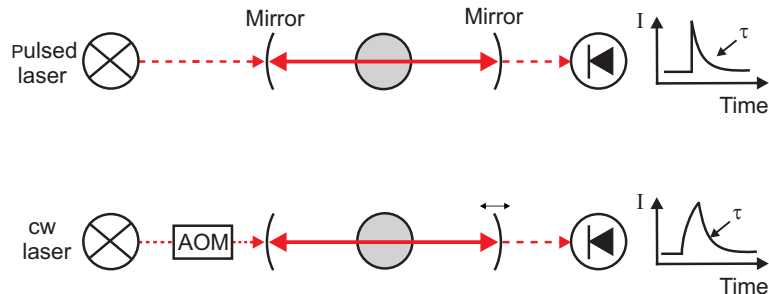


Figure 2.1: Schematic of pulsed (upper panel) and cw (lower panel) CRDS. AOM: acousto-optical modulator.

Indeed, CRDS was first demonstrated using pulsed lasers, covering the spectral range from UV to IR. Using pulsed lasers, no frequency match with the optical cavity is necessary since the pulse linewidth is typically much broader than the cavity mode separation. Several earlier pulsed CRDS measurements were devoted for understanding and avoiding artifacts showing up with the resulting multi-mode excitation (e.g., mode beatings, multi-exponential decay) [5, 6, 7].

With the advent of cw narrow linewidth diode lasers, frequency-stabilized and tunable cw-CRDS became more common. Romanini et al. [8] in 1997 introduced the first cw-CRDS implementation using a single-frequency dye laser. They modulated the cavity length to achieve the mode matching conditions between the cavity modes and the laser frequency. The cw schemes allow for optimal and exclusive excitation of only longitudinal modes. Since different cavity modes exhibit different ringdown times, single mode excitation is advantageous in terms of attainable precision.

The improvement of the resolution and precision of cw-CRDS never stopped since the first measurements by Romanini [8]. Huang and Lehmann performed extensive exploratory work about the remaining excess noise in cw-CRDS due to coupling into higher order modes [9], insufficient excitation by fast optical switching of the excitation source [10], and mirror birefringence and polarization effects [11]. Hodges et al. [12] introduced frequency-stabilized CRDS (FS-CRDS) based on a precise control of cavity length. A huge scientific progress of the method continued in late nineties. This includes, for example, frequency locking to improve the data acquisition rate [13], heterodyne detection to increase the SNR [14], and setup simplifications avoiding optical switches [15]. In the mean time CRDS has become a very mature spectroscopic tool and hence it is very difficult to review both the method developments and applications. A very good overview can be obtained by referring to a series of three books devoted to theoretical, methodological, and practical aspects of CRDS [16, 17, 18].

Interestingly, in contrast to the extensive utilization of CRDS in the linear absorption regime, the use of the high intracavity power build-up inside the ringdown resonators to observe non-linear effects is rather scarce. A detailed description of related non-linear absorption saturation phenomena and its beneficial use for quantitative measurements are given in Section 2.2.

2.1.2 Theory of Cavity Ringdown Spectroscopy

An optical cavity in its simplest form consists of two super reflective mirrors ($R > 99.95\%$). In order to have a stable optical resonator, specific criteria have to be fulfilled, which are related to the radii of curvature r_i and the mirror separation L . The stability condition for a two-mirror cavity is

$$0 < g_1 g_2 < 1, \quad (2.1)$$

where the stability parameter g_i is given by

$$g_i = \left(1 - \frac{L}{r_i}\right). \quad (2.2)$$

A stable optical cavity is capable of confining an electric field inside. However, build-up of the electric field happens only for wavelengths whose multiples coincide with the cavity round-trip distance (i.e., the mode matching condition $n\lambda = 2L$ is fulfilled). Once the mode matching is achieved, the light intensity build-up. Subsequently, switching off the excitation light by an acousto-optical modulator (i.e., the fast optical switch) the light field intensity inside the cavity decays. The characteristic decay time of an empty cavity is related to the mirror reflectivity $1 - R = L/c\tau_0$, with τ_0 being the empty cavity decay time. Another common criterion describing the quality of a resonator related to the mirror reflectivity is the finesse \mathcal{F} .

$$\mathcal{F} = \frac{\pi\sqrt{R}}{1-R}. \quad (2.3)$$

The higher the finesse of the cavity, the sharper and the more pronounced is the mode structure. The spectral line width $\delta\nu$ of the corresponding modes is given by

$$\delta\nu = \frac{c}{2L\mathcal{F}}, \quad (2.4)$$

where c is the speed of light and L is the cavity length. The frequency spectrum of the mode structure is given by the following general equation:

$$\nu_{qnm} = \frac{c}{2L} \left[q + \frac{n+m+1}{2\pi} \times \theta \right]. \quad (2.5)$$

The spacing between frequencies of two allowed modes q_i and q_{i+1} is known as the longitudinal mode spacing of the cavity $\Delta\nu_{\text{long}}$. n and m are the mode indices of the transversal modes (i.e., higher order modes). Here, longitudinal modes of the zero order transversal mode (i.e., TEM₀₀ mode, where $n = m = 0$) are of interest.

Finally,

$$\theta = 2 \arccos(1 - L/r), \quad (2.6)$$

is the round-trip Gouy phase shift corresponding to the cavity length and the mirror radius of curvature. This equation can be adopted for specific cases where the eigenfrequencies are affected by slight astigmatism in the mirrors (see Chapter 6).

In an “ideal” situation the transmitted intensity out of the cavity should be equal to the incident intensity on the entrance mirror. Assuming that the mirror transmission $T = 1 - R$ (i.e., absorption and scattering by the mirror surface and substrate can be neglected), for an empty cavity with identical mirror reflectivity the transmitted intensity I_{out} is given by [7]

$$I_{\text{out}} = I_{\text{inc}} \times \frac{T^2}{(1 - R)^2 + 4R \sin^2\left(\frac{\nu\pi}{\Delta\nu_{\text{long}}}\right)}, \quad (2.7)$$

where I_{inc} is the incident intensity. For that “ideal” situation where the incident frequency perfectly matches the longitudinal mode frequency of the cavity (i.e., $\nu = \nu_{qnm} = q\Delta\nu_{\text{long}}$, with $q = 1, 2, \dots$), maximum transmission is achieved (i.e., $T^2 = (1 - R)^2$). However, in real experiments the transmitted intensity is usually up to orders of magnitude less than the incident intensity. This is partially due to the absorption and scattering of the light on the mirror surface, but more importantly due a poor coupling efficiency. Low coupling efficiencies are due to a mismatch between the laser line width and the cavity mode width (in particularly for high-finesse cavities where the mode width is only a few kHz) as well as the frequency tuning speed of the exciting laser over the cavity modes. Therefore, the narrower line width of cw light sources ensures better efficiency of light injection into an optical cavity compared with the pulsed light sources.

The decay of the intracavity intensity of an empty cavity after switching off the incident light beam can be modeled according to

$$I(t) = I_0 \times \exp\left(\frac{c \ln(R(\nu))}{L} t\right) = I_0 \times \exp\left(\frac{-t}{\tau_0(\nu)}\right) \quad (2.8)$$

and

$$\tau_0 = -\frac{L}{c \ln(R(\nu))} \approx \frac{L}{c (1 - R(\nu))}. \quad (2.9)$$

Suppose that there is an absorber with an absorption coefficient $\alpha(\nu)$ inside the cavity, an additional loss term will be added to the decay of the stored intensity and Eq. 2.8 becomes

$$I(t) = I_0 \times \exp\left(\frac{c [\ln(R(\nu)) - \alpha(\nu) l]}{L} t\right) = I_0 \times \exp\left(\frac{-t}{\tau(\nu)}\right). \quad (2.10)$$

Here, $\tau(\nu)$ is the overall decay time, including the absorber losses, where

$$\tau(\nu) = -\frac{L}{c [\ln(R(\nu)) - \alpha(\nu) l]} \approx \frac{L}{c [1 - R(\nu) + \alpha(\nu) l]}. \quad (2.11)$$

Combining Eq. 2.9 and Eq. 2.11, and assuming that the cavity length L is the same as the absorption path length l , the absorption coefficient $\alpha(\nu)$ can be determined as follows.

$$\alpha(\nu) = \frac{1}{c} \times \left(\frac{1}{\tau(\nu)} - \frac{1}{\tau_0(\nu)} \right) \quad (2.12)$$

To this end, CRDS can provide the absorption coefficient independent of the light intensity. To do so, the time constant of the cavity with and without an absorber need to be determined separately. Typically, this is achieved by scanning the detection laser over the absorption feature of interest and then extracting τ_0 from the off-resonance baseline of the measured spectrum. In practice, etaloning effects causing baseline undulations, spectral interferences, and drift components of the ringdown times often limit the ultimate attainable sensitivity of the detection system. Therefore, the possibility to measure both τ and τ_0 during one single ringdown event would be advantageous.

2.2 Saturated-Absorption Cavity Ringdown Spectroscopy

In saturated-absorption cavity ringdown spectroscopy (Sat-CRDS), the gas absorption decay rate and the empty cavity decay rate are simultaneously retrieved from a single decay transient. In principle, this approach overcomes one of the main limiting factors for achieving the ultimate sensitivity in standard-CRDS measurements, which is the fluctuation of the background signal (i.e., the empty cavity decay rate). The functionality of the Sat-CRDS approach can be intuitively understood from the shape of a saturated decay transient as schematically illustrated in Fig. 2.2. In this figure, simulated CRD transients for the empty cavity (solid/green), and when an absorbing gas is introduced at low laser intensity (i.e., linear absorption regime; dashed/yellow) and at high laser intensity (i.e., non-linear absorption regime; dotted-dashed/red) are presented. The ratio of the saturated to the empty signals is plotted as well (blue/right axis) showing more clearly the absorption saturation evolution over the ringdown transient.

The empty cavity decay is fundamentally independent of the intracavity power level. However, when an absorber exists inside the resonator, this high intracavity power will saturate the resonant absorption transition. The existence of this saturable absorber inside the resonator results in a deviation from the typical mono-exponential behavior of standard-CRD transient. The beginning of the saturated-CRD transient will, temporally, be similar to that of the empty cavity decay signal due to the strong saturation of the sample absorption. With decaying intracavity power, however, the absorbing sample will restore its linear absorption (i.e., it will look similar to the standard-CRD signal at the end of the decay), as can be seen from the tail slopes of the yellow and red curves in Fig. 2.2. Therefore, within one single decay transient, the empty cavity decay rate can be extracted from the beginning of the decay event and the gas absorption can be extracted from the later part of the decay event. However, the ‘‘price’’ of extracting two parameters from a single ringdown event is the possible strong correlation between the two parameters. This may result in a larger standard error as outlined theoretically by Lehmann [19] and supported experimentally in this work [20] (see also Chapter 6).

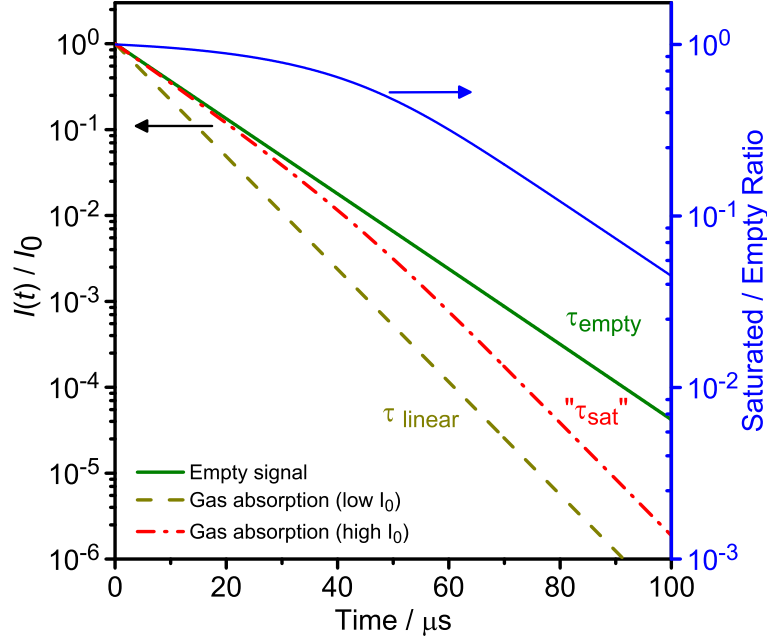


Figure 2.2: Simulated empty (solid/green), linear (dashed/yellow), and saturated (dotted-dashed/red) CRD transients showing the principle of Sat-CRDS. The ratio of Sat-CRD to the empty-CRD (blue/right axis) shows the transition from the saturation regime to linear absorption regime.

Another interesting application of the “non-linear” absorption saturation is to measure, within a single Sat-CRDS shot, two species simultaneously absorbing at the same wavelength. Here, saturation is used to switch off the absorption of one of the species within the beginning of the ringdown transient, while the other species is absorbing. The so-called “Two-species One-wavelength” detection approach will be introduced in Chapter 7.

2.2.1 Modeling Sat-CRDS Signal

There are available several mean-field analyses and studies on the saturation absorption dynamics in high-finesse cavities [21, 22, 23, 24, 25, 26]. Quite recently, Giusfredi et al. [23, 26] reported a fitting routine for Sat-CRDS signals and further demonstrated the decoupling of the empty cavity decay rate and the gas absorption decay rate from a single Sat-CRDS signal.

A main assumption of Sat-CRDS model is that the laser beam has a Gaussian profile for all positions along the propagation direction z (i.e., TEM₀₀). The spatial distribution of the electric field magnitude of a Gaussian beam is given by

$$E(\rho, z) = E_0 \frac{w_0}{w(z)} e^{-\rho/w(z)^2}, \quad (2.13)$$

and its intensity distribution can be expressed as

$$I(\rho, z) = I_0 \left(\frac{w_0}{w(z)} \right)^2 e^{-2\rho/w(z)^2}, \quad (2.14)$$

where $\rho = \sqrt{x^2 + y^2}$ is the radial distance from the z axis, and z is the distance along the propagation direction. The parameter $w(z)$ is the spot size, which is, loosely speaking, the “radius” of the beam, varying along the propagation distance z according to [27]

$$w^2(z) = w_0^2 \left[1 + \left(\frac{z}{z_R} \right)^2 \right]. \quad (2.15)$$

$w(z)$ increases in both directions from its minimum value w_0 at the beam waist (i.e., the radial size of the beam at its narrowest point at $z = 0$), and the parameter $z_R = \pi w_0^2 / \lambda$ is called the *Rayleigh range* (i.e., a range at which the beam radius is $\sqrt{2}$ its values at the beam waist). The peak intensity on the axis I_0 (in Watt per unit area) is related to the total power P (in Watt) propagating in a Gaussian beam. The total power can be found by integrating the intensity over the area A of the beam for a particular z . For a circular symmetric beam profile, the integration can be performed by considering a concentric rings of radius ρ and thickness $d\rho$, so that $dA = 2\pi\rho d\rho$

$$P = \int I(\rho, z) dA = \int_0^\infty I(\rho, z) 2\pi\rho d\rho. \quad (2.16)$$

Using Eq. 2.14 with I_0 specifying peak intensity on the axis, it follows

$$P = 2\pi I_0 \left(\frac{w_0}{w(z)} \right)^2 \int_0^\infty e^{-2(\rho/w(z))^2} \rho d\rho, \quad (2.17)$$

$$P = \frac{\pi w_0^2}{2} I_0. \quad (2.18)$$

For a TEM₀₀ mode that “fits” into an optical cavity, the intensity distribution (Eq. 2.14) and the total power propagation (Eq. 2.18) will have time-dependent expressions:

$$I(\rho, t) = I_0(t) \left(\frac{w_0}{w(z)} \right)^2 e^{-2(\rho/w(z))^2}, \quad (2.19)$$

$$P(t) = \frac{\pi w_0^2}{2} I_0(t). \quad (2.20)$$

where $I_0(t) = I(\rho = 0, t)$ is the peak intensity along the cavity axis z . Further assuming that the beam radius is constant along z (i.e., can be approximated by an average value w), which is valid for most CRDS implementations with mirror separations much below the radius of curvature of the cavity mirrors, the time-dependent intensity and power of the TEM₀₀ mode become

$$I(\rho, t) = I_0(t) e^{-2(\rho/w)^2}, \quad (2.21)$$

$$P(t) = \frac{\pi w^2}{2} I_0(t). \quad (2.22)$$

Now suppose that there is a gas that interacts with the intracavity power radiation in a TEM₀₀ mode of the optical cavity. The power attenuation due to gas absorption, along the z axis, can be expressed as

$$\frac{dP(t)}{dz} = -2\pi \int_0^\infty \alpha(\rho, t) I(\rho, t) \rho d\rho. \quad (2.23)$$

For inhomogeneous broadening, due to the thermal Gaussian distribution of molecular velocities, the absorption coefficient α is affected by saturation and obeys the following relation [28]

$$\alpha(\rho, t) = \frac{\alpha_0}{\sqrt{1 + \mathcal{S}}}. \quad (2.24)$$

Here, α_0 and $\alpha(\rho, t)$ are the non-saturated and saturated absorption coefficients, respectively. The parameter \mathcal{S} is called the saturation parameter, which is a measure of the degree of sample saturation. The saturation parameter corresponds to the ratio of the intensity and the saturation intensity, $\mathcal{S} = I(\rho, t)/I_s$. Hence, for a closed two-level system, for $I(\rho, t) \gg I_s$ (i.e., $\mathcal{S} \rightarrow \infty$), both ground and excited states become saturated and the absorption of the sample vanishes, $\alpha(\mathcal{S} \rightarrow \infty) = 0$.

For a specific transition, the saturation intensity is determined by the relaxation rates of the involved energy states and, as many relaxation processes involve molecular collisions, it is a pressure dependent and collider specific quantity. Theoretically, $I_s \propto \tau^{-1}g(\nu)^{-1}$ (homogeneous broadening) or $I_s \propto \tau^{-1}g(\nu_0)^{-1}$ (inhomogeneous broadening, ν_0 is the line center frequency) [29]. Here, τ corresponds to the pressure dependent inversion lifetime (typically the lifetime of the upper level) with $\tau^{-1} = A + Q(p)$. $Q(p)$ is the overall pressure-dependent quenching rate. Typically $Q(p) \propto p$ and with it $\tau^{-1} \propto p$ holds for a quenching rate that is dominated by collisional processes. $g(\nu)$ corresponds to the normalized Lorentzian line shape function of the underlying *homogeneous* line profile with line width $\Delta\nu_L$. Considering a pressure broadened homogeneous line width with $\Delta\nu_L \propto p$ and using $\Delta\nu_L \times g(\nu_0) = \text{const.}$, it follows that $g(\nu_0)^{-1} \propto p$. Therefore, at not too low pressures, the line center saturation intensity is expected to scale quadratically with pressure, $I_s \propto p^2$. Note that for an inhomogeneously broadened line this holds for all ν . Towards lower pressures, however, $g(\nu_0)$ eventually becomes pressure independent and, more important, diffusion, wall deexcitation and transit-time effects start to prevail the overall quenching. This results in a distinct deviation of I_s from the anticipated p^2 dependence.

Inserting Eq. 2.21 into Eq. 2.23, the power attenuation due to absorption can be obtained by solving the integral

$$\frac{dP}{dz} = -2\pi \int_0^\infty \frac{\alpha_0}{\sqrt{1 + \frac{I_0(t)}{I_s} e^{-2(\rho/w)^2}}} I_0(t) e^{-2(\rho/w)^2} \rho d\rho. \quad (2.25)$$

Since $I_0(t) = 2P(t)/\pi w^2$ (from Eq. 2.22), similarly, $I_s = 2P_s/\pi w^2$, where P_s is the saturation power,

Eq. 2.25 can be rearranged and written in terms of the time-dependent power as

$$\frac{dP}{dz} = -2\pi\alpha_0 \int_0^\infty \rho \frac{2P(t)}{\pi w^2} \frac{e^{-2(\rho/w)^2}}{\sqrt{1 + \frac{P(t)}{P_s} e^{-2(\rho/w)^2}}} d\rho. \quad (2.26)$$

Eq. 2.26 can be further rearranged to satisfy the integration rule $\frac{d}{dx} \sqrt{f(x)} = \frac{1}{2} \frac{f'(x)}{\sqrt{f(x)}}$.¹ It follows with $f(x) = 1 + \frac{P(t)}{P_s} e^{-2(\rho/w)^2}$

$$\begin{aligned} \frac{dP}{dz} &= -2\pi\alpha_0 \int_0^\infty \frac{P_s}{\pi} \frac{1}{2} \frac{4\rho}{w^2} \frac{P(t)}{P_s} \frac{e^{-2(\rho/w)^2}}{\sqrt{1 + \frac{P(t)}{P_s} e^{-2(\rho/w)^2}}} d\rho \\ &= 2P_s\alpha_0 \left[\sqrt{1 + \frac{P(t)}{P_s} e^{-2(\rho/w)^2}} \right]_{\rho=0}^{\rho=\infty} \\ &= 2P_s\alpha_0 \left(1 - \sqrt{1 + \frac{P(t)}{P_s}} \right). \end{aligned} \quad (2.27)$$

Expanded and simplified by means of third binomial formula one gets

$$\begin{aligned} \frac{dP}{dz} &= 2P_s\alpha_0 \frac{\left(1 - \sqrt{1 + \frac{P(t)}{P_s}}\right) \left(1 + \sqrt{1 + \frac{P(t)}{P_s}}\right)}{1 + \sqrt{1 + \frac{P(t)}{P_s}}} \\ &= 2P_s\alpha_0 \frac{1 - 1 - \frac{P(t)}{P_s}}{1 + \sqrt{1 + \frac{P(t)}{P_s}}} \\ &= -\alpha_0 \frac{2P(t)}{1 + \sqrt{1 + \frac{P(t)}{P_s}}}. \end{aligned} \quad (2.28)$$

Using a simplified expression for the gas absorption decay rate $\gamma_g = c\alpha_0$,³ where α_0 is the non-saturated absorption coefficient, together with the speed of light relation $c \frac{d}{dz} = \frac{d}{dt}$, the decay of the intracavity power due to gas absorption can be expressed as

$$\frac{dP}{dt} = c \frac{dP}{dz} = -\gamma_g \frac{2P(t)}{1 + \sqrt{1 + \frac{P(t)}{P_s}}}. \quad (2.29)$$

Eq. 2.29 represents the decay of the intracavity power due to gas absorption and γ_g is the corresponding

¹ The mentioned integration rule is nothing but the simple differentiation $\frac{d}{dx} f(x)^n = n f(x)^{n-1}$ combined with the chain rule, $\frac{d}{dx} g(f(x)) = g'(f(x)) f'(x)$, where $g(f(x))$ is set to $\sqrt{f(x)} = f(x)^{1/2}$. This leads to $\frac{d}{dx} f(x)^{1/2} = \frac{1}{2} \frac{d}{dx} f(x)^{-1/2} f'(x) = \frac{1}{2} \frac{f'(x)}{f(x)^{1/2}} = \frac{1}{2} \frac{f'(x)}{\sqrt{f(x)}}$.

² Remember that $e^{-\infty} = 0$ and $e^0 = 1$.

³ The relation $\gamma_g = c\alpha_0$ is related to the general formula of the absorption coefficient from standard-CRDS measurements $\alpha_0 = \frac{1}{c} \times \left(\frac{1}{\tau_0} - \frac{1}{\tau} \right)$, where $\gamma_g = \left(\frac{1}{\tau_0} - \frac{1}{\tau} \right)$.

decay rate. Of course, there is another loss mechanism mainly attributed to the mirror transmission losses (i.e., $\frac{dP}{dt} = -\gamma_c P(t)$ and $P(t) = P_0 \times \exp(-\gamma_c t)$, where $\gamma_c = 1/\tau_0$ is the empty cavity decay rate). Therefore, the overall power attenuation within an optical resonator can be given by

$$\frac{dP}{dt} = -\gamma_c P(t) - \gamma_g \frac{2P(t)}{1 + \sqrt{1 + \frac{P(t)}{P_s}}} \quad (2.30)$$

The intracavity power $P(t)$ is related to the detector signal $S(t)$ (measured in Volt) by a calibration parameter C , $S(t) = C \times P(t)$. In accordance with the literature [26], we define the fitting parameter $Z^{1V} = 1/(CP_s)$. Z^{1V} is independent of the initial signal amplitude and corresponds to the value of P/P_s for a measured signal amplitude of 1 V. Eq. 2.30 can be rewritten as

$$\frac{dS(t)}{dt} = -\gamma_c S(t) - \frac{2\gamma_g S(t)}{1 + \sqrt{1 + S(t)Z^{1V}}}. \quad (2.31)$$

Eq. 2.31 resembles the Sat-CRDS model that can be fitted to the experimentally observed signal with the adjustable parameters γ_c , γ_g , and Z^{1V} . We also accounted for the detector background signal S_{Bg} , so that the observed signal was fitted to $S(t) + S_{Bg}$. Alternatively, as a numerically more stable variant, the evolution of the signal relative to the empty cavity decay can be described by defining the ratio function $f(t)$ according to

$$f(t, \gamma_c, \gamma_g, Z^{1V}) = S(t)/[S_0 \times \exp(-\gamma_c t)]. \quad (2.32)$$

With a direct substitution in Eq. 2.31 and by using the chain rule

$$\begin{aligned} \frac{dS(t)}{dt} &= \frac{d}{dt} ([S_0 \times \exp(-\gamma_c t)] \times f(t)) \\ &= -\gamma_c [S_0 \times \exp(-\gamma_c t)] \times f(t) + [S_0 \times \exp(-\gamma_c t)] \times \frac{df(t)}{dt} \\ &= -\gamma_c S(t) + [S_0 \times \exp(-\gamma_c t)] \times \frac{df(t)}{dt}. \end{aligned} \quad (2.33)$$

By comparing Eq. 2.31 and Eq. 2.33, it can be identified that

$$[S_0 \times \exp(-\gamma_c t)] \times \frac{df(t)}{dt} = -\frac{2\gamma_g S(t)}{1 + \sqrt{1 + S(t)Z^{1V}}}. \quad (2.34)$$

From Eq. 2.34, it follows that the first derivative of the f function can be given by

$$\frac{df(t)}{dt} = -\gamma_g \frac{2f(t)}{1 + \sqrt{1 + Z^{1V} [S_0 \times \exp(-\gamma_c t)] \times f(t)}}. \quad (2.35)$$

Numerical integration is needed to simulate the observed ringdown transient $S(t)$ using Eqs. 2.32 and 2.35, as further outlined in the experimental section (see Chapter 3).

The real forte of using a “non-linear” saturation approach for extracting “linear” absorption can be seen very clearly in Eq. 2.31. By modeling only one single saturated ringdown decay signal, both the

empty cavity and the gas absorption decay rates can be extracted simultaneously. In principle this should enhance the sensitivity of the measurements as the sources of fluctuations in the empty cavity decay rate, which often limit the ultimate sensitivity of CRDS, are eliminated. Note, however, that the underlying model is only applicable under certain assumptions. In particular, the cavity decay time constant must be longer than the population relaxation times (i.e., the excited state relaxes faster than the energy in the empty cavity gets lost). This is essential for treating the absorption as being in steady-state throughout the cavity decay as it was implicitly assumed in the elaborated derivation. This is called the *adiabatic approximation*. In addition, it is assumed that it is possible to average over the longitudinal field dependence of the light beam within the cavity (i.e., the $1/e^2$ change of the beam intensity radius within the cavity is negligible) and the standing wave effects of the light field are negligible (i.e., the node and antinode structure effects are not taken into account). Moreover, the displacement of the molecules within the beam diameter during time intervals shorter than the relaxation time must be negligible. This is called *local approximation*, which may fail at low pressure where the relaxation time may get longer. Finally, it is implicitly assumed that averaging over initial states with different values of the angular momentum projection quantum number (i.e., corresponding to different transition dipole moments, and hence different saturation) is possible.

The aforementioned theoretical treatment of the optical saturation of single species in optical cavities can be adopted for two-species detection. A more elaborated treatment of absorption saturation for the Two-species One-wavelength approach using direct laser absorption spectroscopy and Sat-CRDS will be introduced in Chapter 7.

2.3 Energy Transfer Dynamics

The vibrational energy transfer upon molecular collisions significantly affects the relaxation rate of the excited states and with it the degree of sample saturation. Other deactivation processes such as spontaneous emission and diffusional deactivation (including transient-time effects) control the population relaxation of the excited states as well, however, under the practical conditions of relatively high pressure, the collisional deactivation of the excited states is often predominant. It can be anticipated that the presence of two relaxing molecules with resonant rotational-vibrational transitions will show particularly efficient heteromolecular energy transfer. These collisions may significantly contribute to the overall quenching of the excited states even at low mixing ratio of the corresponding collider. This section briefly highlights the basic energy transfer theories that qualitatively explain the transfer efficiency as well as the relaxation times for mixtures of two molecules.

Molecules usually gain and lose vibrational and rotational energy in collisions. The nature of the collision process is of fundamental importance for energy transfer processes and the overall relaxation time. Detailed modeling of the collision process requires availability of an accurate intermolecular potential. A conventional representation of the intermolecular potential energy curve for the collision process is given by the Lennard-Jones 12-6 equation [30]

$$V(r) = 4 \epsilon \left[\left(\frac{\sigma}{r} \right)^{12} - \left(\frac{\sigma}{r} \right)^6 \right]. \quad (2.36)$$

Here, $V(r)$ is the potential energy at separation r . The parameter ϵ represents the potential depth, and σ is the separation at $V(r) = 0$. The first term of the Lennard-Jones equation represents the

short-term repulsive forces due to the overlap of electron orbitals and the second term represents the long-term attractive forces. Potentials other than Lennard-Jones often give a better fit for particular systems, however, inert and simple polyatomic gases are approximated to a fair level by the Lennard-Jones potential. Fig. 2.3 (red curve) shows simulations of the Lennard-Jones intermolecular potential of CH_4 showing the gentle attractive and the steep repulsive parts of the potential. The σ and ϵ values are taken from Ref.[30].

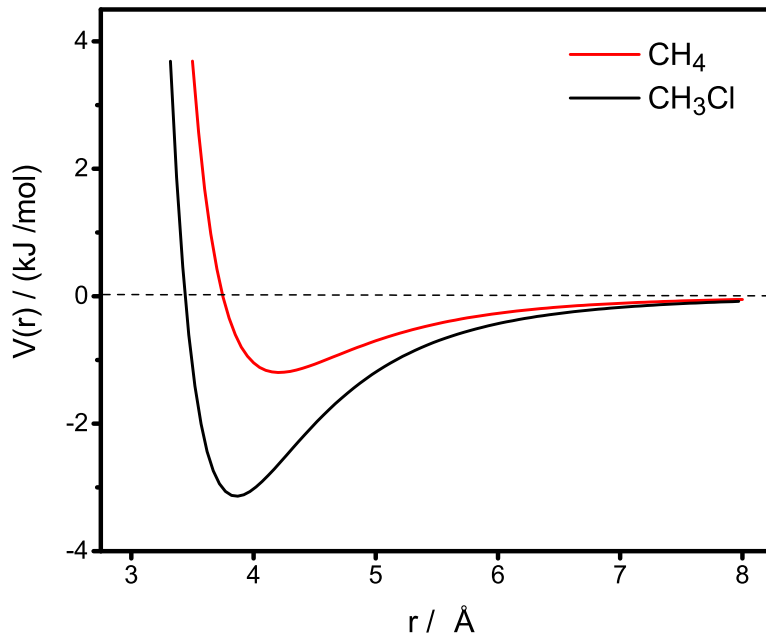


Figure 2.3: Lennard-Jones intermolecular potential of CH_4 (red curve), and Stockmayer intermolecular potential of CH_3Cl (black curve). The simulations are based on data taken from Ref. [30].

Another simple model to be considered for energy transfer is the collinear collision between a vibrating diatomic molecule AB , and a non-vibrating molecule CD . The difference between this model and that of Lennard-Jones is that the coordinate r will vary with time. In this case, the *Ehrenfest's adiabatic principle* [30] can introduce a physical interpretation of the energy transfer process. This principle states the following. If a changing force acts on a quantized periodic motion, the process will be *adiabatic* (i.e., no energy transfer) if the change of force is small during a period of motion, and *non-adiabatic* (i.e., energy transfer) if the change is large during this time. Therefore, the energy transfer is efficient when $\tau_c < t_v$, where τ_c and t_v are the collision and oscillation periods, respectively.

Based on this principle, Landau and Teller [31, 32, 33] developed an elementary theory for vibrational energy transfer. They neglected the attractive forces, assuming that the repulsive part is steep enough to dominate energy transfer. Modeling the interaction potential by an exponential function $V(r) = V_0 \exp(-\alpha r)$, they derived the temperature dependence of the average probability P_{10} for a collision induced $1 \rightarrow 0$ vibrational energy transfer.

$$P_{10} = \exp\left(-3\left(\frac{2\pi^4\mu\nu^2}{\alpha^2k_{\text{B}}T}\right)^{\frac{1}{3}}\right). \quad (2.37)$$

Thus, the energy transfer probability will be in general more favored for collisions between small-mass molecules (μ is the reduced mass of the colliding species), low vibration frequency (ν) and for molecules with steep potential (as accounted for by α).

Energy transfer between polar molecules will differ from the aforementioned two models because another term is needed to account for the angle-dependent dipole-dipole interactions. This is called the Stockmayer 12-6-3 intermolecular potential [30],

$$V(r) = 4 \epsilon \left[\left(\frac{\sigma}{r} \right)^{12} - \left(\frac{\sigma}{r} \right)^6 \right] - \frac{\mu_D^2}{r^3} g(\theta_1, \theta_2, \phi). \quad (2.38)$$

The last term represents the angle-dependent dipole-dipole (assuming identical dipoles) interaction with a dipole moment μ_D . θ_1 and θ_2 are the angles made by the dipoles vectors and the line joining their centers and ϕ is the angle between the planes which pass through their centers (i.e., dihedral-like angle). Fig. 2.3 (black curve) shows a simulated Stockmayer intermolecular potential of CH_3Cl considering an oriented dipole-dipole interaction (i.e., the last angle-dependent term is replaced by an effective value of $-2\frac{\mu_D^2}{r^3}$ for the maximum energy of interaction when the dipoles are in the end-to-end position) [30]. As shown in this figure, the gradients of both attractive and repulsive parts of the potential of CH_3Cl are steeper than that of CH_4 and the depth of the well increased as well. This results in a significant increase in the energy transfer efficiency in agreement with Landau and Teller predictions for potentials with larger α (see Eq. 2.37).

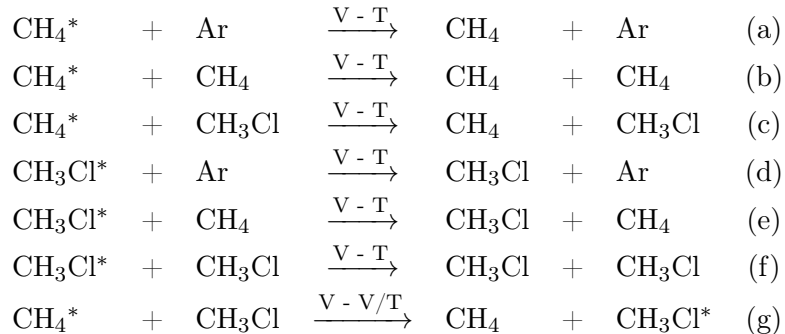
A semi-quantitative model capturing most of the principal features of vibrational energy transfer was introduced by the Schwartz-Slawsky-Herzfeld (SSH) [30]. The SSH theory is a quantum-mechanical treatment of the collision interactions as a stream of molecules falling on a molecule regarded as stationary. Similar to the Landau-Teller theory, an exponential potential is assumed

$$V(r) = V_0 \exp(-\alpha r) - \epsilon. \quad (2.39)$$

The SSH potential is essentially a repulsive potential, but with $-\epsilon$ representing the attractive part. $-\epsilon$ causes an increase in the velocity upon approach of the two colliders. In the SSH treatment, the probability $P_{k \rightarrow l}^{i \rightarrow j(a)}$ describes the simultaneous change of quantum states during binary collisions. Whereas vibrational mode (a) of one molecule will change its quantum state from i to j , simultaneously a second mode (b) in the other molecule will change its quantum state from k to l (i.e., vibrational-vibrational (V-V) energy transfer). The model also describes the simple vibrational-translational (V-T) transfer when only mode (a) changes state and the other mode does not (i.e., $k = l$). The SSH theory predicts that the vast majority of polyatomic molecules exhibit a single dominant vibration relaxation process that is responsible for the relaxation of the whole vibrational energy content of the molecule. This relaxation involves *complex* transfer of one quantum of vibrational energy from one mode plus the necessary increment of translational energy needed to excite a second mode (i.e., inter-mode V-V/T transfer). These rapid inter-mode V-V transfers will maintain a continuous equilibrium of vibrational energy between active vibrational modes. Eventually, as already outlined, the whole vibrational energy of the molecule will then relax via a single V-T transfer channel through the lowest mode.

For saturated absorption measurements as presented in Section 2.2, the degree of sample saturation and with it the saturation intensity heavily depends on the overall relaxation process. A mixture of the two relaxing gases CH_4 and CH_3Cl (as quantitatively measured in Chapter 7) may serve as an example. The overall relaxation scheme needs to consider V-T energy transfer from both excited CH_4^* and CH_3Cl^* in homomolecular (e.g., $\text{CH}_4^* + \text{CH}_4$) and heteromolecular (e.g., $\text{CH}_4^* + \text{CH}_3\text{Cl}$ and $\text{CH}_3\text{Cl}^* + \text{Ar}$, as buffer gas) collisions. In addition, a *near-resonant* V-V transfer processes between CH_4^* and

CH₃Cl is very likely, since the ν_4 vibrational mode of CH₄ and the ν_3 vibrational mode of CH₃Cl are very close in energy ($\Delta E = 20 \text{ cm}^{-1}$, which is a factor of ten lower than $k_B T$ at room temperature). A total of seven possible transfer processes needs to be considered:



As it is known that CH₃Cl relaxes much faster than CH₄ as predicted by SSH theory (since it has lower frequency modes) and confirmed experimentally [30], processes (d), (e), and (f) are generally faster than the processes (a), (b), and (c). On the one hand, if the rapid near-resonant V-V energy transfer (g) is faster than all the other processes, a vibrational equilibrium will be continuously maintained between CH₄ and CH₃Cl. Hence, the overall vibrational energy of the mixture will relax with a single relaxation time constant determined by the relaxation of the more rapidly relaxing molecule. Here, the fastest among processes (d), (e), and (f) will be observed for the relaxation of both CH₄ and CH₃Cl. On the other hand, if process (g) is slower than (d), (e), and (f), but faster than (a) (b), and (c), CH₄ will again relax mainly by route (g), followed by one of the (d), (e), and/or (f) routes. However, now route (g) will be the rate-determining step and rate of relaxation of CH₄ will be linearly dependent on CH₃Cl mole fraction. In contrast, CH₃Cl will relax independently and more rapidly via (d), (e), and/or (f). Hence, there will be two distinguishable relaxation processes with two relaxation times one describing CH₄ relaxation involving the vibrational energy transfer of CH₄ and the other describing CH₃Cl relaxation involving vibrational energy transfer of CH₃Cl.

2.4 Vibrational-Rotational Spectroscopy

High-resolution spectroscopy is the key to the quantum state-to-state analysis of molecular spectra and consequently for understanding the quantum dynamics of molecules. When the electric field of IR radiation interacts with molecular vibrations and rotations, the resulting spectra involve transitions between rotational levels in the two connected vibrational states. Thus, this type of high-resolution spectroscopy is referred to as vibrational-rotational spectroscopy. The importance of high-resolution spectroscopy arises for molecules that lack permanent dipole moments (e.g., highly symmetric fullerenes such as C₆₀, linear carbon chains), which leave only their rovibrational (rotational-vibrational) or rovibronic (UV-VIS-IR) signatures. In order to induce such transitions, the square of the transition dipole moment $\mu_{1,2}$ of the two connected states must be non-zero.

$$\mu_{1,2} = \int \Psi_2^* \mu \Psi_1 d\tau. \tag{2.40}$$

Here, Ψ_1 and Ψ_2 are the vibrational wavefunctions of the two-energy levels, and μ is the dipole moment operator along the τ direction of the electric field. The transition dipole moment can be further expanded in terms of the normal coordinates Q_i , where i refers the $3N$ coordinate system with N the number of atoms that rotate and translate with the molecule. Neglecting higher order contribution in the expansion, the transition dipole moment of Eq. 2.40 becomes the sum of two terms, one for the permanent dipole moment at equilibrium μ_e and another term for the derivative of the dipole moment as a function of the Q_i normal coordinate [34]

$$\mu_{1,2} = \mu_e \int \Psi_2^* \Psi_1 d\tau + \sum_i \left(\frac{\partial \mu}{\partial Q_i} \right) \int \Psi_2^* Q_i \Psi_1 d\tau \quad (2.41)$$

Knowing that the vibrational wavefunctions of the different states are orthogonal to each other, the first term vanishes. The second term is non-zero only when the dipole moment derivative (i.e., induced dipole moment) in front of the integral is non-zero. Since the absorption changes the vibrational and rotational quantum numbers simultaneously, the resulting IR absorption spectrum, at sufficient resolution, consists of a series of closely spaced absorption lines within each vibrational band, attributed to rotational excitation.

2.4.1 Rotational Assignment

The availability of the high-resolution spectra is essential for trace gas sensing of molecular species since it allows for a proper line selection with minimum interference with the gas matrix. The substantial development of laser technologies as well as the interferometric Fourier transform infrared (FTIR) spectroscopy extended the rovibrational measurements for more complex molecules, which were limited in the past to dispersive spectrometers, as extensively demonstrated by Herzberg [35].

The classification of the rotors and with it the complexity of the rotational features depends on the configuration of the nuclei and the associated moments of inertia. The moment of inertia I about any axis is given by [35]

$$I = \sum_i m_i r_i^2, \quad (2.42)$$

where m_i is the mass of atom i and r_i is the distance from the axis of the i^{th} nuclei. In the principle axis system, a molecule can be described by three principle moment of inertia. If two of these moments of inertia are equal, the molecule is classified as symmetric top, while molecules having three different principal moments of inertia are called asymmetric tops. Actually, asymmetric rotors include the majority of naturally occurring atmospheric molecules and they have the most complicated system of energy levels. Since the energy levels for asymmetric tops fall between those of the two limiting symmetric tops (i.e., the prolate and the oblate tops), the rotational properties of the asymmetric tops can be better approximated in relation to those of symmetric tops.

The analytical expression for the energy levels of a prolate top in the ground state, neglecting the

centrifugal distortion constants, is given by

$$E''(J'', K'') = B''J''(J'' + 1) + (A'' - B'')K''^2 \quad (2.43)$$

where B and A are the rotational constants, J is the angular momentum quantum number, and K is the projection of J along the A principal axis. For symmetric tops, there are $J + 1$ different values of energy for each value of J namely those with $K = 0, 1, 2, \dots, J$, of which all but one ($K = 0$) are doubly degenerate. For oblate tops, the energy equation takes the form of Eq. 2.43, but it has C in place of A . One fundamental difference between prolate and oblate tops is the change of energy of the levels for the same J with K . For the prolate top A is greater than B , so that the energy of levels with the same J increases for increasing $|K|$. For an oblate top B is greater than C , and E'' decreases for increasing $|K|$.

The energy levels of the asymmetric top cannot be expressed by closed formulae analogous to that for the symmetric tops of Eq. 2.43. However, there are still $2J + 1$ different energy levels for each J of the asymmetric top. For slight deviations from the case of the symmetric top, the splitting of the *originally* degenerate levels is weak. However, the splitting increases with increasing J , while it decreases with increasing K . For slight deviations from the symmetric top case, the quantum number K is still useful, while for large deviations both the quantum number K and the selection rule $\Delta K = 0$ cease to have any meaning [35]. In such cases, it is common practice to distinguish the sublevels by a subscript τ added to J with τ taking the values

$$\tau = -J, -J + 1, -J + 2, \dots, +J \quad (2.44)$$

with the lowest level being J_{-J} , the next lowest J_{-J+1} , and so on up to J_{+J} . To this end, it is still possible to compare qualitatively the energy levels of the asymmetric tops with the two limiting cases of prolate and oblate symmetric tops.

Fairly elaborated calculations [36, 37, 38] have been performed in order to obtain an approximated representation of the energy levels by quantitative formulae. Two of these expressions are frequently used. The first one according to Wang [36] is

$$E = \frac{1}{2}(B + C)J(J + 1) + \left[A - \frac{1}{2}(B + C) \right] W_\tau, \quad (2.45)$$

and the second according to Ray [37], as corrected by King et al. [38], is

$$E = \frac{1}{2}(B + C)J(J + 1) + \frac{1}{2}(A - C)E_\tau, \quad (2.46)$$

where A , B , and C are the rotational constants. W_τ and E_τ in Eq. 2.45 and 2.46 are closely related quantities that are a function of J and of the asymmetry parameter k , defined by Ray [37] as

$$k = \frac{2B - A - C}{A - C}. \quad (2.47)$$

For a prolate top $k = -1$ and for an oblate top $k = +1$. Algebraic equations for W_τ and E_τ can be found in the literature [35]. Simulations of the high-resolution absorption spectra of different rotors are readily achieved by freely available simulation and assignment software such as PGOPHER [39] (see also Section 3.4.3). The calculation of the asymmetric top energy levels in PGOPHER in fact uses the standard symmetric top functions, implying that a choice must be made as to which axis is chosen for K , the body-fixed projection of J .

2.4.2 Quantum-Chemically Assisted Spectrum Simulations

In this section, the use of quantum chemistry as a tool for understanding and assisting the simulation and the assignment of a complex high resolution spectra is introduced [40]. Computational chemistry has become crucial for the interpretation of complex experimental molecular spectroscopic data. Similarly, a high accuracy of the molecular spectroscopic measurements is important in order to provide a benchmark and for validating theoretical approaches. Chapter 5 of this thesis serves as a test of this approach—Is it possible to simulate the absorption spectrum with a resolution sufficient for atmospheric monitoring applications and without a need for experimental measurements? Which model chemistries (method, basis set) gives better simulation results?

A focus is set on strategies to account for anharmonicity and vibrational-rotational coupling terms. Among these approaches, the vibrational perturbation theory (VPT) [41, 42] is widely applied for computing rovibrational spectra. The perturbation theory is applied for the expansion of the Hamiltonian into a power series of products of vibrational and rotational operators (vide infra).

In quantum mechanics (QM), the stationary energy states of a specific molecular system, with a molecular wavefunction Ψ_{mol} , are the eigenvalues of the Hamiltonian \hat{H} . This can be described by the time-independent Schrödinger equation as

$$\hat{H}\Psi_{\text{mol}} = E\Psi_{\text{mol}}. \quad (2.48)$$

The eigenvalue E is the total energy of the molecule including contributions from electrons, nuclear vibrations, and overall rotation and translation of the molecule. In general, the accurate solutions of the stationary Schrödinger equation are not easily accessible except for *hydrogen-like* systems. However, the Born–Oppenheimer (BO) approximation makes it possible to compute the wave function in two less complicated consecutive steps. Within the BO assumption, the motion of the atomic nuclei and the electrons in a molecule are separated. The fundamental Schrödinger equation (Eq. 2.48) is split into

$$\hat{H}_e\Psi_e = [T_e + V(R, r)]\Psi_e(R, r) = E_e(R)\Psi_e(R, r), \quad (2.49)$$

$$\hat{H}_n\Psi_n = [T_n + E_e(R)]\Psi_n = E_{\text{mol}}\Psi_n. \quad (2.50)$$

Here, R and r stand for nuclear and electronic coordinates, respectively. Please note that the electronic eigenvalue E_e is a parametric function of the chosen nuclei position R . Varying the coordinate R in small steps and solving the electronic Schrödinger equation yields the potential energy surface (PES) $E_e(R)$. In the first step, the electronic Schrödinger equation is solved, producing the wave function

Ψ_e depending on electrons only. In this step, the nuclear kinetic energy is neglected and the corresponding kinetic energy operator is subtracted from the Hamiltonian (see Eq. 2.49). In a second step, the nuclear kinetic energy operator \hat{T}_n is reintroduced and the Schrödinger equation for the nuclear motion is solved (see Eq. 2.50). In that second step, the BO approximation involves separation of vibrational, translational, and rotational motions by applying the Eckart-Sayvertz conditions [43, 44]. The Eckart-Sayvertz conditions allow, to a large extent, the separation of rotation and translation (i.e., the external motions) from vibration (i.e., the internal motions). It also minimizes the coupling between rotational and vibrational wave functions.

To this end, the rovibrational QM Hamiltonian for the nuclei \hat{H}_n can be represented by a set of constituent operators \hat{H}_{fg} for all the terms with degree f in the vibrational operators and degree g in the rotational operators. So that, \hat{H}_{f0} collects purely vibrational terms and \hat{H}_{0g} collects purely rotational terms. The dependence of the rotational and centrifugal distortion constants on the vibrational quantum numbers is contained in the higher degree operators (e.g., \hat{H}_{22} , \hat{H}_{42} , ... etc.) [45].

$$\begin{aligned} H_n &= H_{20} + H_{30} + H_{40} + \dots \\ &H_{21} + H_{31} + H_{41} + \dots \\ &H_{02} + H_{12} + H_{22} + \dots \end{aligned} \quad (2.51)$$

In the frame work of this thesis, the ultimate objective of performing such quantum chemical calculation was to assist simulation of the high-resolution spectra. These calculations were used to provide the averaged state-dependent rotational constants of the vibrational states and to compute the vibrational-rotational coupling constant. Although the differences between the computed state-dependent rotational constants of the different vibrational states are very small, they turn out to drastically change the simulated spectrum.

The vibrational dependence of the rotational constants is typically described as a function of vibrational quantum numbers v

$$B_v = B_e - \sum_r [\alpha_r^B (v_r + 1/2)] + \sum_{r \geq s} [\gamma_{rs}^B (v_r + 1/2)(v_s + 1/2)] + \dots, \quad (2.52)$$

where α_r^B and γ_{rs}^B are the rotational-vibrational interaction constants and the summation is over all the normal modes. For asymmetric top molecules, the VPT approach derives α_r^B values from the diagonal matrix elements of \hat{H}_{22} , according to the formula [46]:

$$\begin{aligned} \alpha_r^B &= -\frac{2B_e^2}{\omega_r} \left[\sum_{\xi} \frac{3(a_r^{b\xi})^2}{4I_{\xi}} + \sum_{r \neq s} (\zeta_{rs}^b)^2 \frac{3\omega_r^2 + \omega_s^2}{\omega_r^2 - \omega_s^2} \right. \\ &\quad \left. + \pi \left(\frac{c}{h} \right)^{1/2} \sum_s \Phi_{rrs} a^{bb} \left(\frac{\omega_r}{\omega_s^{3/2}} \right) \right] \end{aligned} \quad (2.53)$$

where ω_r are the harmonic frequencies, I_{ξ} is the ξ -th principle moment of inertia at equilibrium geometry, $a_r^{b\xi}$ are the first derivatives of the $I_{b\xi}$ element of the inertia tensor of principal axis b with respect to the normal coordinate Q_r , ζ_{rs}^b are the Coriolis interaction constants coupling Q_r to Q_s through

rotation about the axis b , and Φ_{rrs} are the cubic force constants which appear in the expansion of the potential into a series of dimensionless normal coordinates. The first term of the rotational-vibrational perturbation formula accounts for the contribution from the moment of inertia correction related to the displacement along Q_r , the second term is due to the Coriolis interaction between ω_r and ω_s , and the third term is the anharmonic correction related to the change in Q_s resulting from the displacement of Q_r . Note that analytical second derivative are needed to perform such calculations. Therefore, the use of VPT2 is limited to selected *ab initio* methods. For example, the program suits GAUSSIAN09 makes available analytical second derivatives for the methods HF, DFT, CIS and MP2.

2.4.3 Spectral Line Intensities

The sensitivity of the measurements is directly related to the integrated absorption line intensities. Basically, the spectral line intensities and the quantitative absorption in general can be explained in terms of a simple two-state system. In case of mid-IR spectroscopy, these are a lower state vibrational-rotational level of energy E_1 and an upper state of energy E_2 . The absorption between the two connected states is induced by a photon with energy equal to the energy difference between the two states $\Delta E = h\nu$. The integrated spectral line intensity $S_{1,2}$ for an individual vibrational-rotational absorption transition can be expressed as the product of the vibrational band strength S_v , the rotational term $R_{1,2}$, and the Herman-Wallis vibrational-rotational interaction factor, F [47, 34]:

$$S_{1,2} = S_v R_{1,2} F. \quad (2.54)$$

The pure vibrational band strength is defined for a temperature T as

$$S_v(T) = \left(\frac{8\pi^3 \omega_0}{3hc} \right) \frac{\exp\left(\frac{-hcE''_v}{k_B T}\right)}{Q_v(T)} |\mu_v|^2. \quad (2.55)$$

Here, h is the Planck's constant, c is the speed of light, k_B is the Boltzmann constant, ω_0 is the band origin frequency, Q_v is the vibrational partition function at temperature T , μ_v is the transition dipole moment, and E''_v is the vibrational energy of the lower state. The rotational term $R_{1,2}$ of Eq. 2.54 can be expressed as

$$R_{1,2}(T) = (HL) \left(\frac{\nu_{1,2}}{\omega_0} \right) \exp\left(\frac{-hcE''_r}{k_B T}\right) \frac{\left[1 - \exp\left(\frac{-hc\nu_{1,2}}{k_B T}\right) \right]}{Q_r(T)} \quad (2.56)$$

where HL is the Hönl-London factor, which accounts for the intensity distribution of the transition over the rotational lines in the different rotational branches. It is a function of the vibrational and rotational quantum numbers in each rotational branch and vibrational band type; ω_0 and $\nu_{1,2}$ are the band origin and the vibrational-rotational frequencies, respectively; Q_r is the rotational partition function at temperature T , and E''_r is the rotational energy of the lower state. In addition to the Hönl-London factor, the rotational population, which is described by the first exponential term of Eq. 2.56, determines the intensity distribution of the rotational lines. These two factors explain why some observed rotational lines are stronger than the others. The Herman-Wallis factor F is calculated

from a power series expansion of rotational quantum numbers. It quantifies the vibrational-rotational interactions and corrects for error resulting from the separation of vibration from rotation. In some representations the Hönl-London factor and the Herman-Wallis factor are folded into the square of the transition dipole moment, μ^2 [34].

The spectral line intensity can be related to the absorption cross-section σ_c and the absorption coefficient at the line center $\alpha_c = \sigma_c[c] = \sigma_c(\frac{p}{k_B T})$, assuming a line shape function $g(\nu - \nu_0)$, by [48]

$$S_{1,2} = \frac{k_B T}{p} \int_{\nu_1}^{\nu_2} \alpha(\nu) d\nu = \frac{k_B T}{p} \int_{\nu_1}^{\nu_2} \alpha_c g(\nu - \nu_0) d\nu = \int_{\nu_1}^{\nu_2} \sigma(\nu) d\nu. \quad (2.57)$$

Here, the integration over the whole range of frequencies contributes to the line shape profile. From the above set of equations, it is clear that the intensity of an absorption line is directly proportional to the number density of the absorbing species, in contrast to the absorption cross-section which is concentration-independent. In addition, spectral line intensity is independent of the underlying line broadening mechanism, in contrast to the narrow-band absorption coefficient and cross-section.

References

- [1] D. Z. Anderson, J. C. Frisch, and C. S. Masser. Mirror reflectometer based on optical cavity decay time. *Appl. Opt.*, 23(8):1238, 1984.
- [2] J. M. Herbelin, J. A. McKay, M. A. Kwok, R. H. Ueunten, D. S. Urevig, D. J. Spencer, and D. J. Benard. Sensitive measurement of photon lifetime and true reflectances in an optical cavity by a phase-shift method. *Appl. Opt.*, 19(1):144–147, 1980.
- [3] T. M. Crawford. Error sources in the ring down optical cavity decay time mirror reflectometer. *Proc. SPIE*, 0540, 1985.
- [4] A. O’Keefe and D. A. G. Deacon. Cavity ring–down optical spectrometer for absorption measurements using pulsed laser sources. *Rev. Sci. Instrum.*, 59(12):2544–2551, 1988.
- [5] J. Martin, B. A. Paldus, P. Zalicki, E. H. Wahl, T. G. Owano, J. S. Harris, C. H. Kruger, and R. N. Zare. Cavity ring-down spectroscopy with Fourier-transform-limited light pulses. *Chem. Phys. Lett.*, 258(1-2):63–70, 1996.
- [6] J. T. Hodges, J. P. Looney, and R. D. van Zee. Response of a ring–down cavity to an arbitrary excitation. *J. Chem. Phys.*, 105(23):10278–10288, 1996.
- [7] K. K. Lehmann and D. Romanini. The superposition principle and cavity ring–down spectroscopy. *J. Chem. Phys.*, 105(23):10263–10277, 1996.
- [8] D. Romanini, A. A. Kachanov, N. Sadeghi, and F. Stoeckel. CW cavity ring down spectroscopy. *Chem. Phys. Lett.*, 264(3-4):316–322, 1997.
- [9] H. Huang and K. Lehmann. Noise in cavity ring-down spectroscopy caused by transverse mode coupling. *Opt. Express*, 15(14):8745, 2007.
- [10] H. Huang and K. K. Lehmann. Noise caused by a finite extinction ratio of the light modulator in cw cavity ring-down spectroscopy. *Appl. Phys. B*, 94(2):355–366, 2009.
- [11] H. Huang and K. K. Lehmann. Effects of linear birefringence and polarization-dependent loss of supermirrors in cavity ring-down spectroscopy. *Appl. Opt.*, 47(21):3817, 2008.
- [12] J. T. Hodges and D. Lisak. Frequency-stabilized cavity ring-down spectrometer for high-sensitivity measurements of water vapor concentration. *Appl. Phys. B*, 85(2-3):375–382, 2006.
- [13] B. A. Paldus, C. C. Harb, T. G. Spence, B. Wilke, J. Xie, J. S. Harris, and R. N. Zare. Cavity-locked ring-down spectroscopy. *J. Appl. Phys.*, 83(8):3991–3997, 1998.
- [14] M. D. Levenson, B. A. Paldus, T. G. Spence, C. C. Harb, J. S. Harris Jr, and R. N. Zare. Optical heterodyne detection in cavity ring-down spectroscopy. *Chem. Phys. Lett.*, 290(4-6):335–340, 1998.
- [15] J. W. Hahn, Y. S. Yoo, J. Y. Lee, J. W. Kim, and H.-W. Lee. Cavity ringdown spectroscopy with continuous-wave laser: Calculation of coupling efficiency and a new spectrometer design. *Appl. Opt.*, 38(9):1859–1866, 1999.

- [16] K. W. Busch and M. A. Busch, editors. *Cavity-ringdown spectroscopy: An ultratrace-absorption measurement technique*, volume 720 of *ACS symposium series*, 0097-6156. American Chemical Society, Washington, DC, 1999.
- [17] G. Berden and R. Engeln, editors. *Cavity ring-down spectroscopy: Techniques and applications*. Wiley-Blackwell, Oxford, 2009.
- [18] G. Gagliardi and H.-P. Loock, editors. *Cavity-enhanced spectroscopy and sensing*, volume 179 of *Springer series in optical sciences*, 0342-4111. Springer, Heidelberg, 2014.
- [19] K. K. Lehmann. Theoretical detection limit of saturated absorption cavity ring-down spectroscopy (SCAR) and two-photon absorption cavity ring-down spectroscopy. *Appl. Phys. B: Lasers Opt.*, 116:147–155, 2014.
- [20] I. Sadiq and G. Friedrichs. Saturation dynamics and working limits of saturated absorption cavity ringdown spectroscopy. *Phys. Chem. Chem. Phys.*, 18:22978–22989, 2016.
- [21] J. Y. Lee and J. W. Hahn. Theoretical analysis on the dynamic absorption saturation in pulsed cavity ringdown spectroscopy. *Appl. Phys. B*, 79(5):653–662, 2004.
- [22] S. S. Brown, H. Stark, and A. R. Ravishankara. Cavity ring-down spectroscopy for atmospheric trace gas detection: Application to the nitrate radical (NO_3). *Appl. Phys. B Lasers Opt.*, 75(2-3):173–182, 2002.
- [23] G. Giusfredi, S. Bartalini, S. Borri, P. Cancio, I. Galli, D. Mazzotti, and P. de Natale. Saturated-absorption cavity ring-down spectroscopy. *Phys. Rev. Lett.*, 104(11):110801/1–4, 2010.
- [24] I. Galli, S. Bartalini, S. Borri, P. Cancio, D. Mazzotti, P. de Natale, and G. Giusfredi. Molecular gas sensing below parts per trillion: Radiocarbon-dioxide optical detection. *Phys. Rev. Lett.*, 108(17):179902, 2012.
- [25] I. Galli, S. Bartalini, S. Borri, P. Cancio, D. Mazzotti, P. de Natale, and G. Giusfredi. Erratum: Molecular gas sensing below parts per trillion: Radiocarbon-dioxide optical detection. *Phys. Rev. Lett.*, 107:270801–270804, 2011.
- [26] G. Giusfredi, I. Galli, D. Mazzotti, P. Cancio, and P. de Natale. Theory of saturated-absorption cavity ring-down: Radiocarbon dioxide detection, a case study. *J. Opt. Soc. Am. B*, 32(10):2223, 2015.
- [27] A. E. Siegman. *Lasers*. University Science Books, Mill Valley, California, 1986.
- [28] W. Demtröder. *Laser Spectroscopy: Experimental Techniques*, volume 2. Springer, Berlin, Heidelberg, 2008.
- [29] A. Yariv. *Quantum Electronics*. John Wiley & Sons, New York, 3rd edition, 1989.
- [30] J. D. Lambert. *Vibrational and rotational relaxation in gases*, volume 1 of *International series of monographs on chemistry*. Clarendon Press, Oxford, 1977.
- [31] L. Landau and L. Teller. Theory of sound dispersion. *Phys. Z. Sowjetunion*, 10(34), 1936.

- [32] K. F. Herzfeld and T. A. Litovitz. *Absorption and dispersion of ultrasonic waves*, volume 7 of *Pure Appl. Phys.* Academic Press, New York, 1959.
- [33] E. E. Nikitin and J. Troe. 70 years of Landau-Teller theory for collisional energy transfer. Semi-classical three-dimensional generalizations of the classical collinear model. *Phys. Chem. Chem. Phys.*, 10(11):1483–1501, 2008.
- [34] A. Fried and D. Richter. *Infrared Absorption Spectroscopy. In Analytical Techniques for Atmospheric Measurement.* Blackwell Publishing, 2006.
- [35] G. Herzberg. *Molecular spectra and molecular structure: Infrared and Raman Spectra of Polyatomic Molecules*, volume 2. Van Nostrand Reinhold, New York, 1945.
- [36] S. C. Wang. On the asymmetrical top in quantum mechanics. *Phys. Rev.*, 34(2):243–252, 1929.
- [37] B. S. Ray. Über die eigenwerte des asymmetrischen kreisels. *Z. Phys.*, 78(1-2):74–91, 1932.
- [38] G. W. King, R. M. Hainer, and P. C. Cross. The asymmetric rotor I. Calculation and symmetry classification of energy levels. *J. Chem. Phys.*, 11(1):27–42, 1943.
- [39] C. M. Western. PGOPHER 8.0, a program for simulating rotational, vibrational and electronic spectra. University of Bristol, <http://pgopher.chm.bris.ac.uk>.
- [40] I. Sadiq and G. Friedrichs. Doppler-limited high-resolution spectrum and VPT2 assisted assignment of the C-H stretch of CH₂Br₂. *Spectrochim. Acta. A: Mol. Biomol. Spectrosc.*, 181:180–191, 2017.
- [41] V. Barone. Anharmonic vibrational properties by a fully automated second-order perturbative approach. *J. Chem. Phys.*, 122:014108/1–10, 2005.
- [42] V. Barone, J. Bloino, C. A. Guido, and F. Lipparini. A fully automated implementation of VPT2 infrared intensities. *Chem. Phys. Lett.*, 496:157–161, 2010.
- [43] C. Eckart. Some studies concerning rotating axes and polyatomic molecules. *Phys. Rev.*, 47:552–558, Apr 1935.
- [44] A. Sayvetz. The kinetic energy of polyatomic molecules. *J. Chem. Phys.*, 7(6):383–389, 1939.
- [45] M. Piccardo, J. Bloino, and V. Barone. Generalized vibrational perturbation theory for rovibrational energies of linear, symmetric and asymmetric tops: Theory, approximations, and automated approaches to deal with medium-to-large molecular systems. *Int. J. Quantum Chem.*, 115(15):948–982, 2015.
- [46] I. M. Mills. Vibration-rotation structure in asymmetric- and symmetric top molecules. In *Molecular Spectroscopy: Modern Research.* Academic Press, New York, 1972.
- [47] L. S. Rothman, R. L. Hawkins, R. B. Wattson, and R. R. Gamache. Energy levels, intensities, and linewidths of atmospheric carbon dioxide bands. *J. Quant. Spectrosc. Radiat. Transfer*, 48(5-6):537–566, 1992.

- [48] M. Quack, J. Stohner, H. L. Strauss, M. Takami, A. J. Thor, E. R. Cohen, T. Cvitas, J. G. Frey, B. Holström, and K. Kuchitsu *et al.* *Quantities, Units and Symbols in Physical Chemistry*. Royal Society of Chemistry, Cambridge, 2007.

Experimental

A new mid-IR-CRD spectrometer has been setup. Direct laser absorption spectroscopy (LAS) in the saturation regime has been used as a second spectroscopic scheme for proof-of-concept measurements of the “Two-species One-wavelength” approach. Several programming and computational tools have been used in this thesis. This includes self-written MATLAB [1] and LABVIEW [2] codes for numerical modeling of the Sat-CRDS signals and experiment automation, respectively. In addition, GAUSSIAN 09 program suite and PGOPHER 8.0 [3], a program for simulating rotational, vibrational and electronic spectra, have been used for quantum chemical calculations and high-resolution spectra simulations, respectively.

In addition to CRDS measurements, gas chromatography coupled with mass-spectrometry and electron capture detection (GC-MS/ECD) have been used for benchmarking with our mid-IR-CRDS system. GC-MS/ECD measurements have been performed in collaboration with Prof. Dr. D. Wallace (University of Dalhousie, Halifax, Canada) during a research visit to his laboratories. The details of the used GC-MS/ECD system and the designed tank-purge experiment for the comparative study are not outlined in this chapter, but are described in the corresponding publication [4] (see Chapter 4).

3.1 Sample Preparation and Chemicals

Analytical grade CH_3I ($> 99.5\%$, Sigma Aldrich) and CH_2Br_2 (99 %, Sigma Aldrich) have been degassed and further purified by several freeze-pump-thaw cycles before being introduced into the cavity for the high-resolution spectra measurements. Methane gas, CH_4 (99.5%, Air Liquide), and Methyl chloride, CH_3Cl (99.8%, Air Liquide), were used as test gases for absorption saturation measurements. N_2 (boil-off nitrogen) and Ar (99.999%, Air Liquide) were used as buffer gases. All gases were used as supplied without further purification. CH_4 was diluted with Ar using a gas mixing system.

Calibration of the GC-MS/ECD was performed using liquid CH_3I standards that have subsequently been checked against internal gas standards. Three stock standards (A) 5 μl of CH_3I ($M = 141.94$ g/mol, $\rho = 2.28$ g/ml) in 250 ml of hexane (Sigma Aldrich, $> 99\%$), (B) 500 μl from stock A in 250 ml of methanol (Sigma Aldrich, 99.9%), and (C) 100 μl of stock B in 200 ml of methanol were prepared by serial dilutions and stored at 4 °C. A system blank was analyzed before every standard measurement. A calibration curve was used for determining the concentrations of the extracted samples. The working standard was measured three times and the standard deviation of triplicate analyses was always around 12%.

3.2 cw Mid-IR Cavity Ringdown Spectrometer

3.2.1 Light Source

A continuous wave (cw) single resonant (SR) optical parametric oscillator (OPO), cw-SR-OPO (Lockheed Martin Aculight ARGOS 2400-SF-15) has been used as a light source in this study. It was capable of producing > 1000 mW of continuously tunable idler output between 2.2 and 4.6 μm . Such OPO systems have been applied in a broad range of applications that benefit from their high power output [5, 6, 7, 8], including high-resolution spectroscopy, Helium nanodroplet spectroscopy, laser cooling of atoms, trace gas sensing and photoacoustic spectroscopy. The Aculight Argos cw-SR-OPO can be used as a “turnkey” multi-watt system with an ultra-narrow linewidth ($< 1\text{MHz}$) of the idler beam. The all-in-fiber based design eliminates many of the problems associated with the through-space coupling of other high-power OPO lasers. The disadvantage of this system is the high threshold for laser oscillation, which made necessary a cw pump source capable of providing 10 W. In addition, the laser output could not be continuously tuned over a frequency range greater than 100 GHz without user involvement.

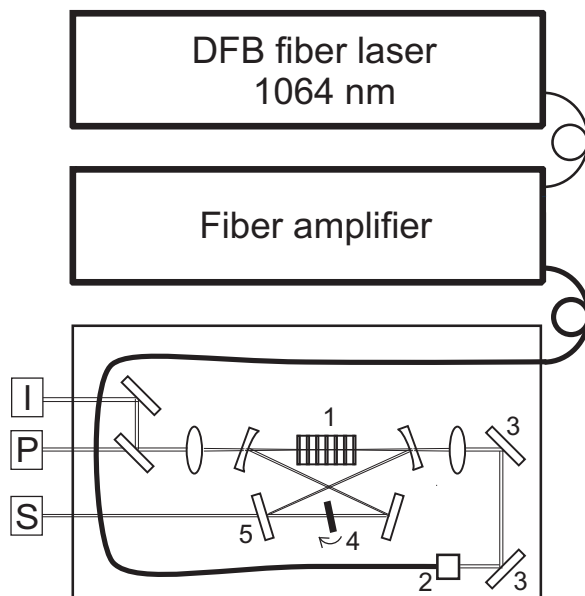


Figure 3.1: Schematic of the cw-SR-OPO pumped by an all-in-fiber laser. I/P/S: idler/pump/signal beams. The indicated numbers are as follow. 1: MgO-doped PPLN crystal, 2: collimator, 3: steering mirrors, 4: intracavity etalon (ICE), 5: output coupler.

Fig. 3.1 shows a schematic of the all-in-fiber cw-SR-OPO based laser system in a seed laser (master oscillator) power-amplifier configuration. The pump source is a continuous wave Yb-doped fiber laser (Koheras AdjustiK, NKT Photonics; 1064 nm, 15 mW, < 100 kHz) and the amplifier (IPG Photonics, YAR series fiber amplifier) produces 10 W at 1064 nm. The seed laser features a fine-tuning capability via piezo electric transducer (PZT) strain on the fiber. The pump source was directly coupled into the OPO cavity using an armored laser fiber and a collimator maintaining the light polarization. The 15 mW 1064 nm seed light, after being amplified, is reflected into a bow-tie cavity through two steering mirrors. Once the pump beam travels through the MgO-doped PPLN crystal (maintained at 58.5 $^{\circ}\text{C}$), optical parametric generation converts the pump beam (ω_{pump}) into two lower-energy beams known

as the *signal* (NIR, ω_{signal}) and *idler* (Mid-IR, ω_{idler}), where $\omega_{\text{pump}} = \omega_{\text{signal}} + \omega_{\text{idler}}$. A detailed description of the fabrication of the PPLN crystal has been introduced by Powers et al. [9]. The PPLN crystal is designed with a *fan-out* poling periodicity, producing a linearly varying poling period along the width of the crystal. Since the signal wave is the only resonant beam, and the pump and idler beams make a single pass through the PPLN crystal before exiting the cavity, much higher output powers, better stability, and ease of alignment and tuning have been provided in comparison to the doubly or triply resonant designs.

Three wavelength tuning mechanisms were implemented to access the full scan range of the OPO, including: (i) the translation of the *fan-out* PPLN crystal, (ii) changing the angle of the intracavity etalon (ICE), and (iii) fine and continuous tuning of the seed laser wavelength via piezoelectric strain. The ICE is mounted on a galvanometer, so that its angle can be varied by tuning the applied voltage. This allows the OPO output wavelength to be varied over a free spectral range (FSR) of the etalon. The ICE also acts as a filter for longitudinal cavity modes that are not coincident with the etalon transmission fringe, providing single mode operation of the OPO. Fig. 3.2 shows a schematic of the different elements used for wavelength scanning. In this figure, the phase matching (PM) gain curve (red curve), the transmission curve of the ICE (blue curve), and the cavity modes of the resonant signal wave (black vertical lines) are overlaid. In principle, the FSR of the ICE is designed to be broader than the PM gain curve, so that only one cavity mode lies underneath both the ICE transmission and PM gain curves. ICE rotation results in hopping of the signal wave to another longitudinal cavity mode. Similarly, translating the PPLN position results in discrete hops of the signal wavelength equal to one FSR of the etalon ($> 11 \text{ cm}^{-1}$).

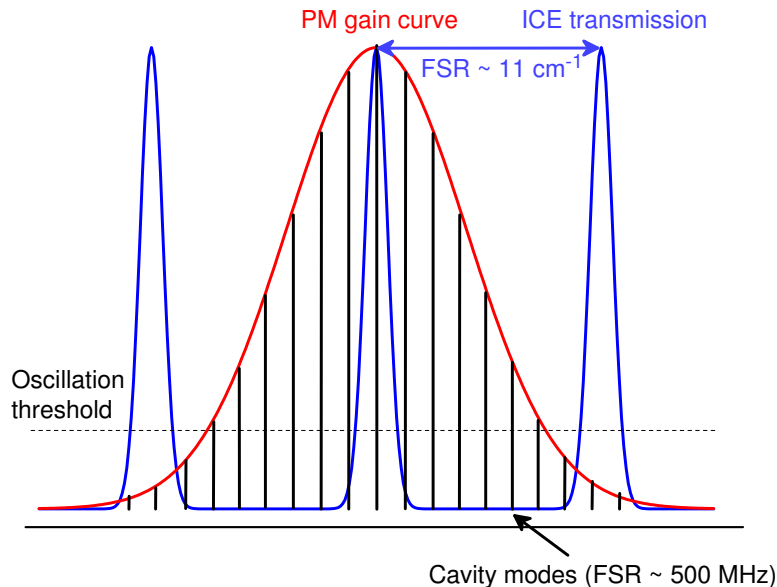


Figure 3.2: Schematic showing the different elements used for tuning the wavelength of the cw-SR-OPO. PPLN phase matching (PM) gain curve (red), intracavity etalon (ICE) transmission fringe curve (blue), and the longitudinal cavity modes of the signal wave (black).

3.2.2 CRD Spectrometer

Fig. 3.3 illustrates an overall schematic of the OPO coupled to the CRD spectrometer. Whereas the OPO signal and pump beams were dumped, the idler beam passed a ZnSe window acting as a beam splitter, allowing for a small fraction of light to be directed to the wavemeter. The wavemeter was a Michelson type interferometer (Bristol Instruments; Model 621A-IR) with a specified accuracy of $\pm 0.0006 \text{ cm}^{-1}$ at $3.3 \text{ }\mu\text{m}$ and a repeatability of $\pm 6 \text{ MHz}$ at a sampling frequency of 2.5 Hz .

The light beam passed an acousto-optical modulator (AOM, Gooch & Housego Model MM040-5C11B38-5) acting as a fast optical switch with a rise time of $\sim 20 \text{ ns}$ and a deflection efficiency of 60-70%. Since the first order diffracted beam $f = f_0 + \omega$ was shifted from the zero order beam f_0 by the AOM driver frequency ω , the laser frequency data were corrected for ω . The deflected first order beam was steered into a commercial quartz-coated stainless steel ringdown cell (CRD Optics). The CRD cell was equipped with multiple ports to establish a gas flow and monitor the pressure (MKS Baratron; Models 622B, 621B, 620B covering the ranges between 10^{-4} to 100 mbar) inside the cell. Mass flow controllers (FAP GmbH; Model FC-7700CU) and mass flow meters were used to monitor and control the gas flow.

The ringdown cell used in this study was a Fabry-Perot resonator of a focal configuration (1 m radius of curvature ringdown mirrors and 50 cm mirror separation). Later on, the focal configuration has been slightly changed by extending the cavity length to $\sim 51 \text{ cm}$ to suppress the beating of the predominantly excited TEM_{00} mode with the nearly degenerate higher transverse modes (see Chapter 6) [10]. The mirrors had an anti-reflection coating on their back surface and a specified reflectivity of 99.99% at $3.3 \text{ }\mu\text{m}$. Mirror adjustment was accomplished initially mechanically by the 100 TPI lead screws in the mirror mounts and then electronically with three piezo elements offering $15 \text{ }\mu\text{m}$ maximum travel. The frequency matching condition was achieved by modulating the cavity length by a triangle-wave voltage supplied to the three PZTs attached to the rear mirror using a three-channel piezo driver (MDT693B, Thorlabs). Alternatively, frequency matching could be achieved by modulating the seed laser wavelength over few cavity modes.

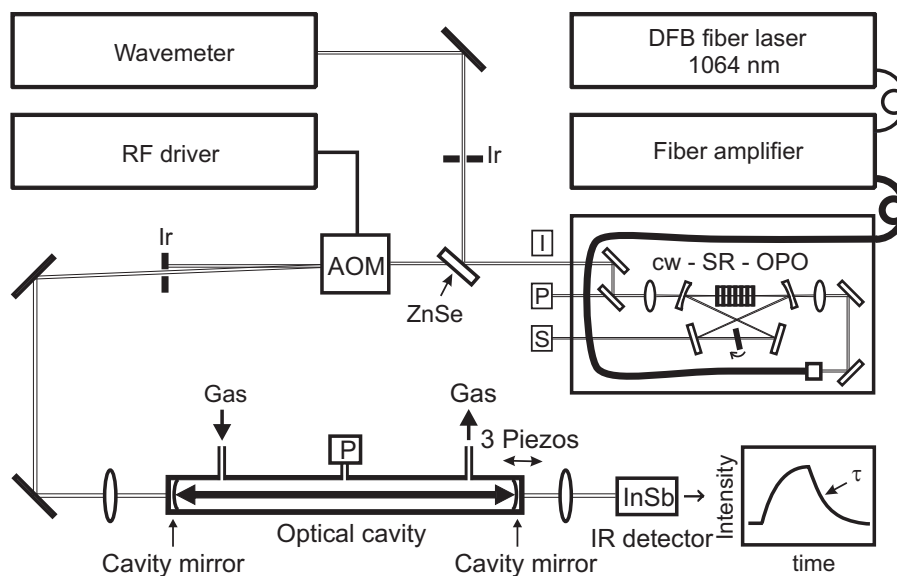


Figure 3.3: Schematic of the Mid-IR-cw-CRD spectrometer. I/P/S: idler/pump/signal beams, Ir: iris diaphragm, P: pressure transducer. Reproduced/Adapted from Ref.[10] with permission from the PCCP Owner Societies.

3.2.3 Signal Processing

The laser light leaking through the rear mirror of the cavity was detected by a high-linearity liquid nitrogen cooled 2 mm InSb photodiode/preamplifier combination (SVS-VISTEK, KISDP-2-A-6/KA-05-CI, DC-5 MHz bandwidth) corresponding to a rise time of 70 ns. The signal passed a comparator circuit which produced a TTL signal to switch off the AOM after a preset light level was reached. Sampling of the decay rates and continuous monitoring of the wavelength were achieved via National Instruments hardware and self-written LABVIEW software. The individual ringdown signals were digitized with a high-resolution flexible digitizer (National Instrument, NI 5922) at a sampling rate of 10 MHz and a vertical resolution of 18 bit. Each recorded ringdown transient consisted of > 1100 points extending over about ~ 10 decay times. For standard CRDS measurements, a single exponential function was fitted first to the transient by a Levenberg-Marquardt non-linear least-squares method, followed by the averaging process. For high-resolution spectra measurements, the decay times were recorded as a function of the laser frequency. Sat-CRDS data acquisition was accomplished by first collecting the saturated decay transients using LABVIEW, followed by parameter extraction numerically using MATLAB fitting routine (see Section 3.4.1).

3.3 Laser Absorption Spectroscopy

A direct LAS setup has been used to investigate the functionality of optical saturation for decoupling the absorption of two interfering gases (Fig. 3.4). All the LAS measurements have been performed at room temperature in a 15 cm long gas absorption cell made of glass. The cell was equipped with stopcocks for inlet and outlet flow and the windows were made of fused silica. The same cw-SR-OPO and wavemeter used for CRDS measurements were used in the direct LAS measurements. The incident 2.5 mm in diameter laser beam was passed through the measurement cell without any focusing, while the transmitted light was focused by a 10 cm focusing lens placed in front of the detector. The liquid nitrogen cooled 2 mm InSb photodiode (SVS-Vistek, model KISDP-2-A-6) combined with a preamplifier (SVS-Vistek, model KA-05-CI) was used as a main detector. A reference preamplifier/detector combination (Vigo System S.A.; Model FIP-1K-1G-F-M4-D/PVI-2TE-5-0) was used for continuous monitoring of the input laser intensity, I_0 . Also the same digitizer was used and the data were collected using a self-written LABVIEW code. The detection laser power was changed from 5 to 1200 mW. At each power level, the laser was scanned continuously with a scan rate of 10 mHz and the signals from the detectors were averaged and recorded as a function of the laser frequency.

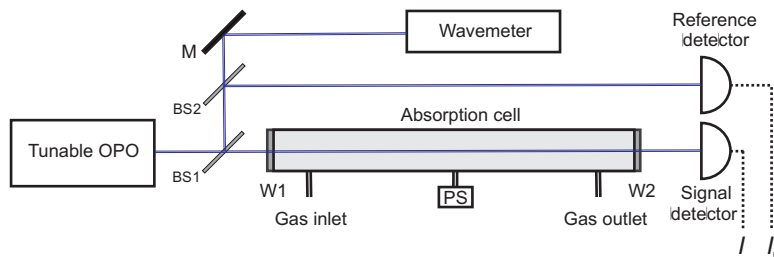


Figure 3.4: Schematic of the direct laser absorption spectroscopy (LAS) setup, with M: mirror, BS: beam splitter, W: optical window.

3.4 Computational Tools

3.4.1 Numerical Fitting

The Optimization Toolbox of MATLAB [1] was used for providing a numerical fitting routine of the Sat-CRDS decay signals. This toolbox provides functions for finding parameters that minimize or maximize objectives while satisfying constraints, if needed. In general, to set an optimization problem for solution, (i) an optimization solver has to be chosen; (ii) the objective function for minimization needs to be defined; (iii) constraints on parameters, if any, have to be specified; (iv) options, if needed have to be set; and (v) an appropriate solver has to be called.

In this study, the versatile non-linear programming solver *fmincon* implemented in MATLAB [1] has been used as a fitting routine to extract the parameter vector \mathbf{x} with γ_c , γ_g , Z^{1V} , S_0 , and the detector offset S_{Bg} as adjustable parameters. *fmincon* seeks the minimizer of a scalar function of multiple variables subject to linear (and non-linear) constraints and bounds. The solver is called by

$$\mathbf{x} = \text{fmincon}(\text{fun}, \mathbf{x}_0, \mathbf{A}, \mathbf{b}, \mathbf{A}_{\text{eq}}, \mathbf{b}_{\text{eq}}, \mathbf{lb}, \mathbf{ub}, \text{options}). \quad (3.1)$$

fun is the function handle (corresponding to the target function), where numerical integration of Eq. 2.32 and Eq. 2.33 as needed to calculate $S(t)$ and $f(t)$ (see Chapter 2) has been performed on-the-fly using the Runge-Kutta-Fehlberg method *RK45*. \mathbf{x}_0 defines the initial values for the optimizer, \mathbf{A} and \mathbf{b} define linear inequality constraints ($\mathbf{Ax} \leq \mathbf{b}$), \mathbf{A}_{eq} and \mathbf{b}_{eq} linear equality constraints ($\mathbf{A}_{\text{eq}}\mathbf{x} = \mathbf{b}_{\text{eq}}$), and \mathbf{lb} and \mathbf{ub} the lower and upper bounds ($\mathbf{lb} \leq \mathbf{x} \leq \mathbf{ub}$). Actually, no linear constraints needed to be implemented in this work, however, the lower bound of the solution has been set to 0, except for the detector offset. The *options* keyword specifies some additional optimization options such as the type of algorithm. The '*interior-point*' algorithm has been used in this work. A documentation of the MATLAB fitting routines including the main code, the objective and the cost functions are listed in Table 3.1.

Table 3.1: MATLAB main code as well as objective and cost functions used as a fitting routine for modeling Sat-CRDS signals.

```

% Main codea
% @ Ibrahim Sadiak (e-mail: sadiak@phc.uni-kiel.de, sadiak@yahoo.com)
% This model can be used for simulating Sat-CRDS signals for analysis and learning purposes. To do so, the values
% of the gas absorption decay rates and the empty cavity decay rates need to be defined as follow:
c = 3.e+10; % speed of light (cm/s).
R = 0.99985; % mirror reflectivity (user defined).
l = 50; % mirror separation, cm (user defined).
gamma_c = c * (1.0 - R) / l; % Empty cavity decay rate (1/s).
alpha_0 = 1.e-4; % absorption coefficient (1/cm).
gamma_g = c * alpha_0 % gas absorption decay rate (1/s).
tspan = [0 : 0.0000001 : 1400 * 0.0000001]; % set time interval(e.g., microsecond).
% For using this code as a fitting routine for Sat-CRDS signal, the experimental decay signal has to be set as a target
% for the minimization/optimization solver, as follow:
Sat_CRDS = importdata('Sat_Ring_signal_000.txt'); % import the saturated decay signal [tspan:S_target].
S_target = Sat_CRDS(:,2); % define the target.
tspan = Sat_CRDS(:,1)*1.e-6; % define the time span from the experimental data (optional).
u_target = [gamma_c; gamma_g; Baseline; S_0];
% compute target solution: for learning purposes.
[T,F_target] = ode45(@(t, f) Ffun(t, f, u_target(1:4)), tspan, u_target(4)); % see Ffun.
S_target = (exp(-u_target(1)*tspan)).*F_target + u_target(3);
% Start the optimization
u0 = [1; 1; 1; 1]; % Initial values.
% compute initial solution.
[T,F_initial] = ode45(@(t, f) Ffun(t, f, u0(1:4)), tspan, 1);
S_initial = (u0(4) * exp(-u0(1)*tspan)).*F_initial + u0(3);
A = [-1,1,0,0]; b = 0; % matrix and rhd side for linear inequality constraint (optional).
lb = [0;0;0;0]; ub = [0;0;0;0]; % lower and upper bounds for parameters, user defined (optional).
options = optimset('display','iter','Algorithm','interior-point'); % set options for optimizer.
[u_opt, costval] = fmincon(@(u)cost_f(u,tspan, S_target),u0,A,b,[],[],lb,[],[],options); % see cost_f.
% compute optimized solution.
[T,F_opt] = ode45(@(t, f) Ffun(t, f, u_opt(1:4)), tspan, 1);
S_opt = (u_opt(4) * exp(-u_opt(1) * tspan)).*F_opt + u_opt(3);
semilogy(T,S_target, 'r*',T,S_opt, 'b') % plot target & optimization.

% Ffun (objective function)
function dfdt = Ffun(t, f, u)
gamma_c = u(1);
gamma_g = u(2);
Z_1v =u(3);
B = u(4);
S_0 =u(5);
dfdt = -gamma_g * 2 * f / (1.0 + sqrt(1.0 + S_0 * Z_1v *exp(-gamma_c * t) * f));
S = u(4) * exp(-u(1) * t).*f + u(3);
end

% cost_f (cost function)
function costval_1 = cost_f(u, t, S_target)
[T,Fval] = ode45(@(t, f) Ffun(t, f, u(1:4)), t, 1);
Sval = u(4).*exp(-u(1) * t).*Fval + u(3);
costval_1 = (Sval-S_target)ᵀ *(Sval-S_target);
end

```

^a The actual *main code* starts from the command “Sat_CRDS = importdata ...” downwards, where the optimization target is the experimental decay transients. The first commands are intended for analysis and learning purposes, where the target has to be defined.

3.4.2 Quantum Chemical Calculations

Quantum chemical calculations of the molecular structures and the anharmonic frequencies of the different isotopologues of CH₂Br₂ were performed using GAUSSIAN 09 [11]. The DFT calculations have been carried out using different functionals including the three-parameter hybrid density functional (B3LYP)[12], the CAM-B3LYP long-range corrected three-parameter hybrid density functional by Handy and coworkers [13], and the M06 hybrid meta exchange correlation functionals of Truhlar and Zhao [14]. In addition, second-order Møller-Plesset perturbation calculations (MP2) [15] have been carried out. A split-valence basis set (e.g., 6-311+G(d,p)) type has been used and the effect of basis set upgrading on the computed molecular structures has been investigated for the different density functionals. The second order vibrational perturbative (VPT2) [16, 17, 18, 19] routine was only available for *ab initio* methods with analytic second derivatives (e.g., HF, DFT, CIS and MP2) [11]. The VPT2 made available the anharmonic rotational constants as well as the vibration-rotation coupling constants (see Chapter 2). These constants have been used as an initial fitting parameters estimate for the spectra simulations.

3.4.3 PGOPHER Simulations

PGOPHER [3] is a spectrum simulation and assignment software that allows for assigning transitions and fitting effective Hamiltonians to yield molecular parameters for the target molecule. This section describes the use of PGOPHER as it has been used for simulating and analyzing a high-resolution vibrational-rotational spectrum. Here, the ν_1 and ν_6 vibrational bands of CH₂Br₂ are chosen as an example, which is further outlined in the recent paper published in Chapter 5 [20]. For more detailed description of the program, it is referred to the online documentation [3].

PGOPHER currently allows the simulation of the rotational structure of three types of rotors (i.e., linear molecules, symmetric tops, and asymmetric tops). The first step in spectrum simulation in PGOPHER is the selection of the molecule type by using the option “File » New » Asymmetric Top”, as it is appropriate for CH₂Br₂. This creates the transition manifolds including vibrational ground state, excited state, and a transition moment matrix element ($\langle \text{excited} | \mu | \text{ground} \rangle$) in a separate constant window. In this window, under “Sample » Species » Asymmetric Top”, the following must be set correctly: **PointGroup**, **Representation**, **SReduction**, the position of the symmetry elements within the molecule (i.e., **C2zAxis** and **C2xAxis**), and the statistical weights (i.e., **eeWt**, **eoWT**, **oeWT**, and **ooWT**). The **PointGroup** option defines the point group symmetry of the molecule. The **Representation** option selects which axis is chosen for K , the body-fixed projection of J . The choice dictates the symmetric top basis functions used in the asymmetric top energy level calculation. For the asymmetric CH₂Br₂ top, C_{2V} symmetry and the I^r representation have been adopted. The **SReduction** setting can be flagged either true or false; if false the A-reduction of the asymmetric top Hamiltonian will be used, and if true then the program will use the S-reduction of the asymmetric top Hamiltonian. S- and A-reduction of the asymmetric top Hamiltonian are the proposed reduced forms of Hamiltonian by Watson [21]. Actually, the choice of the reduction is mostly based on what form of the reduced Hamiltonian was used for fitting microwave data to extract the vibrational ground state constants. The **C2zAxis** and **C2Aaxis** parameters assign two of the principal axes (i.e., a , b , and c) to the axis system of the molecular point group (i.e., x , y , and z). The setting of these axes is very critical. Failure to do so properly will result in no simulation, or an incorrect simulation of the vibrational band. For

CH_2Br_2 , the principle b -axis corresponds to `C2zAxis` and the c -axis to `C2xAxis`. Furthermore, the nuclear spin values for H ($I = 1/2$), and ^{79}Br and ^{81}Br ($I = 5/2$) have been used for the calculation of the spin statistical weights for the symmetric isotopologues ($\text{CH}_2^{79}\text{Br}_2$ and $\text{CH}_2^{81}\text{Br}_2$), while the lower symmetry $\text{CH}_2^{79}\text{Br}^{81}\text{Br}$ lacks spin statistics.

Under “Sample»Species»Asymmetric Top»Ground»v=0” and “ ... »Excited»v=1”, the ground and excited state constants have to be provided, respectively. In this work, the ground state vibrational constants were adopted from microwave data, which exist for most of the atmospherically important molecules [22, 23]. If the ground state rotational constants are not available from microwave measurements, sophisticated high-level quantum chemical calculation should be used to provide a reliable estimate for the ground state rotational constants. In contrast, the excited vibrational state constants need an *educated* guess. One trivial approach is to start with the same set of constants from the ground vibrational state. In chapter 5, a more sophisticated approach for providing an initial estimate for the rotational constants of the excited vibrational states has been tested. In this quantum-chemically assisted approach, the difference between the calculated anharmonic rotational constants of the excited vibrational state and the ground vibrational state is simply added to the already known ground state constants from the microwave data. Another critical setting for the simulations is the transition dipole matrix element, specifically, the principal axis along which the transition dipole moment change during the vibration. This can be set under “ Sample»Species»Asymmetric Top» <Excited| μ |Ground> ”. PGOPHER allows for adding more than one principal axes for the projection of the transition dipole moment, which might be the case for hybrid bands. Additionally, the simulation temperature in Kelvin can be specified in the main window together with the Gaussian “Gau” and the Lorentzian “Lor” contributions to the linewidth. To this end, the spectra can be simulated and the experimental spectra can be compared for assignment and fitting purposes.

By using the quantum-chemically assisted assignment approach, an initial good match between the experimental and the simulated spectrum could be obtained both for the ν_6 and ν_1 bands of CH_2Br_2 [20] (see Chapter 5). From that point, first reliable assignments of prominent transitions in the spectrum become feasible, in particular near the band origin as the molecular perturbation effects (e.g., Coriolis coupling) are minimum. To fit the assigned transitions, the spectroscopic parameters to be floated must be flagged “yes”. As a rule of thumb, it is often a good strategy to float the most important parameters first (i.e., the band center followed by the rotational constants). Once the fitting started, PGOPHER will diagonalize the asymmetric top Hamiltonian matrix. This involves the diagonalization of a $2J+1 \times 2J+1$ matrix for each value of J , using a symmetric top basis ($|J,K,M\rangle$). The unknown molecular parameters appear in the resulting expressions for the eigenenergies of the rotational levels as polynomial functions in terms of the quantum numbers J and K . To provide the best spectral fit, in an iterative process, transitions with large obs-calc values were unassigned and others were added to the fitting pool.

The overall standard deviation σ for the assigned transition is given by[3],

$$\sigma = \sqrt{\frac{\sum_i^{n_{\text{obs}}} (\text{obs}_i - \text{calc}_i)^2}{n_{\text{obs}} - n_{\text{para}}}}, \quad (3.2)$$

where, n_{obs} is the total number of assigned transitions, obs_i is the observed frequency position of

the i^{th} assigned transition, calc_i is the calculated frequency position for the i^{th} transition, and n_{para} is the number of parameters floated in the least squares fitting procedure.

References

- [1] *MATLAB Optimization Toolbox, Version 8.5 (R2015a)*. The MathWorks Inc., Natick, Massachusetts, 2015.
- [2] C. Elliott, V. Vijayakumar, W Zink, and R Hansen. National Instruments LabVIEW: A programming environment for laboratory automation and measurement. *JALA*, 12(1):17–24, 2007.
- [3] C. M. Western. PGOPHER 8.0, a program for simulating rotational, vibrational and electronic spectra. University of Bristol, <http://pgopher.chm.bris.ac.uk>.
- [4] I. Sadiék, Q. Shi, D. Wallace, and G. Friedrichs. Quantitative mid-infrared cavity ringdown detection of methyl iodide for monitoring applications. *Anal. Chem.*, 2017, Article ASAP, DOI: 10.1021/acs.analchem.7b01970.
- [5] B. L. Yoder, R. Bisson, and R. D. Beck. Steric effects in the chemisorption of vibrationally excited methane on Ni(100). *Science*, 329(5991):553–556, 2010.
- [6] K. N. Crabtree, J. N. Hodges, B. M. Siller, A. J. Perry, J. E. Kelly, P. A. Jenkins, and B. J. McCall. Sub-doppler mid-infrared spectroscopy of molecular ions. *Chem. Phys. Lett.*, 551:1–6, 2012.
- [7] O. Asvany, J. Krieg, and S. Schlemmer. Frequency comb assisted mid-infrared spectroscopy of cold molecular ions. *Rev. Sci. Instrum.*, 83(9):093110/1–5, 2012.
- [8] Y. N. Martinez de Escobar, P. G. Mickelson, P. Pellegrini, S. B. Nagel, A. Traverso, M. Yan, R. Côté, and T. C. Killian. Two-photon photoassociative spectroscopy of ultracold Sr88. *Phys. Rev. A*, 78(6), 2008.
- [9] P. E. Powers, Thomas J. Kulp, and S. E. Bisson. Continuous tuning of a continuous-wave periodically poled lithium niobate optical parametric oscillator by use of a fan-out grating design. *Opt. Lett.*, 23(3):159, 1998.
- [10] I. Sadiék and G. Friedrichs. Saturation dynamics and working limits of saturated absorption cavity ringdown spectroscopy. *Phys. Chem. Chem. Phys.*, 18:22978–22989, 2016.
- [11] M. J. Frisch, G. W. Trucks, H. B. Schlegel, G. E. Scuseria, M. A. Robb, J. R. Cheeseman, G. Scalmani, V. Barone, B. Mennucci, and G. A. Petersson *et al.* *Gaussian 09 Revision A.02*. Gaussian Inc, Wallingford, CT, USA, 2009.
- [12] A. D. Becke. Density–functional thermochemistry. I. The effect of the exchange–only gradient correction. *J. Chem. Phys.*, 96(3):2155–2160, 1992.
- [13] T. Yanai, D. Tew, and N. Handy. A new hybrid exchange–correlation functional using the Coulomb–attenuating method (CAM-B3LYP). *Chem. Phys. Lett.*, 393:51–57, 2004.
- [14] Y. Zhao and D. G. Truhlar. The M06 suite of density functionals for main group thermochemistry, thermochemical kinetics, noncovalent interactions, excited states, and transition elements: Two new functionals and systematic testing of four M06-class functionals and 12 other functionals. *Theor. Chem. Account*, 120:215–241, 2008.

- [15] Chr. Møller and M. S. Plesset. Note on an approximation treatment for many-electron systems. *Phys. Rev.*, 46(7):618–622, 1934.
- [16] V. Barone. Vibrational zero-point energies and thermodynamic functions beyond the harmonic approximation. *J. Chem. Phys.*, 120:3059–3065, 2004.
- [17] V. Barone. Anharmonic vibrational properties by a fully automated second-order perturbative approach. *J. Chem. Phys.*, 122:014108/1–10, 2005.
- [18] V. Barone, J. Bloino, C. A. Guido, and F. Lipparini. A fully automated implementation of VPT2 infrared intensities. *Chem. Phys. Lett.*, 496:157–161, 2010.
- [19] J. Bloino and V. Barone. A second-order perturbation theory route to vibrational averages and transition properties of molecules: General formulation and application to infrared and vibrational circular dichroism spectroscopies. *J. Chem. Phys.*, 136:124108/1–15, 2012.
- [20] I. Sadiq and G. Friedrichs. Doppler-limited high-resolution spectrum and VPT2 assisted assignment of the C-H stretch of CH₂Br₂. *Spectrochim. Acta. A: Mol. Biomol. Spectrosc.*, 181:180–191, 2017.
- [21] J. K. G. Watson. Vibrational spectra and structure: Aspects of quartic and sextic centrifugal effects on rotational energy levels. In *Vibrational Spectra and Structure*, volume 6. Elsevier, Amsterdam, 1977.
- [22] T. Shimanouchi. Tables of molecular vibrational frequencies. Nat. Stand. Ref. Data Ser., Nat. Bur. Stand., 1972.
- [23] M. E. Jacox. *Vibrational and Electronic Energy Levels of Polyatomic Transient Molecules*. National Institute of Standards and Technology, Gaithersburg MD, 20899, <http://webbook.nist.gov> (visited July 30, 2017).

Quantitative Mid-Infrared Cavity Ringdown Detection of Methyl Iodide for Monitoring Applications

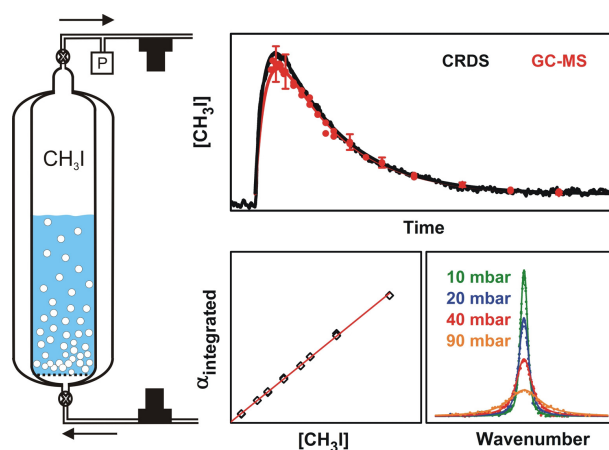
Ibrahim Sadiek,^a Qiang Shi,^b Douglas W. R. Wallace,^b and Gernot Friedrichs^{*ac}

^aInstitut für Physikalische Chemie, Christian-Albrechts-Universität zu Kiel, Max-Eyth-Str. 1, D-24118 Kiel, Germany. ^b Department of Oceanography, Dalhousie University, 15000 Halifax, NS, Canada ^cKMS Kiel Marine Science - Centre for Interdisciplinary Marine Sciences, Olshausenstr. 40, D-24098 Kiel, Germany.

Anal. Chem., 2017, DOI: 10.1021/acs.analchem.7b01970

Received 24th May 2016, Accepted 24th July 2017, First published on the web 24th July 2016

Copyright 2017 American Chemical Society



Own contributions:

- Experimental setup of the cw Mid-IR cavity ringdown spectrometer.
- Implementation of a complete instrument automation in LABVIEW.
- Experimental work on CRDS in Kiel and GC-MS/ECD in Halifax.
- Analysis of experimental and spectroscopic data and of the kinetic model.
- Writing of paper draft.

ABSTRACT: Methyl iodide is a toxic halocarbon with diverse industrial and agricultural applications and is an important ocean-derived trace gas that contributes to the iodine burden of the atmosphere. Quantitative analysis of CH₃I is mostly based on gas chromatography coupled with mass spectrometry or electron capture detection (GC-MS/ECD) as yet, which limits the ability to conduct in situ high-frequency monitoring at workplaces, in the environment as well as in laboratory process studies. This work developed and assessed the potential of mid-infrared continuous wave cavity ring-down spectroscopy (mid-IR cw-CRDS). CH₃I was detected at the ^RR₂(15) rovibrational absorption transition at $\tilde{\nu}=3090.4289\text{ cm}^{-1}$, part of the corresponding ν_4 vibration band has been measured with Doppler limited resolution for the first time. A line strength of $S(T = 295\text{ K}) = (545 \pm 20)\text{ cm/mol}$, corresponding to a line center absorption cross-section $\sigma_c(p = 0\text{ bar}) = (1.60 \pm 0.06) \times 10^5\text{ cm}^2/\text{mol}$, and pressure broadening coefficients $\gamma_p(\text{Ar}) = (0.094 \pm 0.002)\text{ cm}^{-1}/\text{bar}$ and $\gamma_p(\text{N}_2) = (0.112 \pm 0.003)\text{ cm}^{-1}/\text{bar}$ have been determined. The performance of the detection system has been demonstrated with a tank-purging experiment and has been directly compared with a conventional GC-MS/ECD detection system. Quantitative detection with high reproducibility and continuous sampling is possible with a current noise-equivalent limit of detection of 15 ppb at 20 mbar absorption cell pressure and 70 s averaging time. This limit of detection is suitable for practical applications in the ppm mixing ratio level range such as workplace monitoring, leak detection, and process studies. Natural environmental abundances are much lower, therefore possibilities for future improvement of the detection limit are discussed.

METHYL iodide (CH₃I) is a naturally occurring volatile halocarbon (boiling point 42.4 °C), a synthetic agent used in organic synthesis, and a fumigant in buildings and soils. Its use as an agricultural pesticide was promoted following control of methyl bromide for such purposes under the Montreal Protocol. In contrast to methyl bromide, methyl iodide is referred to as a very short-lived substance (VSLs) with an atmospheric lifetime of only a few days [1]. This is much shorter than tropospheric transport time scales and hence CH₃I is not generally considered a major contributor to stratospheric ozone depletion.

With its high acute toxicity and associated risk of exposure to workers and residents, the use of methyl iodide in agricultural applications has been controversial, leading to it being banned as a soil fumigant in California in 2012. It remains registered for use in other countries including Japan, Mexico, Morocco, New Zealand, Turkey, and Uruguay [2]. Current occupational safety guidelines set the personal exposure limit to 0.3 – 5 ppm, depending on the regulatory authority. Nevertheless, due to significant advantages over other substances, it is still used for other dispersive applications. For example, as a response to criminal contaminations of buildings with resilient *Bacillus anthracis* spores (anthrax), methyl iodide is proposed as a replacement for decontaminants such as chlorine dioxide, vaporous hydrogen peroxide and paraformaldehyde that are often incompatible with materials [3]. Moreover, it is still used as fire extinguisher as a replacement of methyl bromide [4]. In the industrial scale, 75% of the acetic acid production is currently based on the conversion of methanol to methyl iodide as a key step of the Monsanto and Cativa processes (i.e., the catalytic carbonylation of methanol)[5, 6]. Even in nuclear power plants, the possible emission of radioactive iodine in the form of methyl iodide during a core melt accident is of major concern [7]. Relevant to all these applications is the capability to monitor personal exposure limits as well as to install suitable leak detectors.

Despite the fact that naturally-produced CH₃I yields a very low atmospheric mixing ratio of 0.1 – 2 ppt

[8], it is an important carrier of iodine from the ocean to the atmosphere and plays a significant role in atmospheric chemistry. It is photodissociated by UV light and can contribute to aerosol formation in the troposphere [9]. Source and sink mechanisms and rates affecting CH₃I production within the ocean are uncertain [10]. For example, incubation experiments conducted in a coastal fjord [11, 12] revealed seasonal variations in net production consistent with the annual cycle of measured dissolved organic matter abundance, but observed night-time degradation rates could not be explained. The difficulty and, especially, the limited rate of analysis of methyl iodide with current methods represents a barrier to experimental studies of processes underlying these observations.

To date, analysis is based on water and/or air sampling followed by extraction and gas chromatography coupled with mass spectrometry or electron capture detection (GC-MS/ECD). These approaches allow for only discrete measurements and require considerable calibration efforts. The time consuming analysis (i.e., several tens of minutes per sample) limits workspace monitoring, leak detection, or process studies that examine rapid changes associated with production and loss processes.

A way forward would be the implementation of a cavity ringdown spectroscopy (CRDS)-based detection scheme. This ultrasensitive optical detection method benefits from very long (up to tens of km) effective absorption path length through the sample gas, which is realized by trapping laser light inside a 0.1 – 1 m long optical resonator (ringdown cell). CRDS as well as CEAS (cavity enhanced absorption spectroscopy) are increasingly used for fundamental work on high-resolution spectroscopy, trace gas detection and chemical kinetics [13, 14, 15]. Thanks to the availability of commercial turn-key CRDS/CEAS analyzers for trace gases such as CO₂, CH₄, N₂O, CO, NH₃, HCl, H₂S, many environmental and industrial applications have been realized. Advantages over gas chromatography include the possibility of near-continuous, high-frequency measurement (i.e., on the order of seconds) as well as field measurements. The robust instrumentation even allows operation aboard ships and aircrafts [16, 17].

To the best of our knowledge, there have been no near-IR or mid-IR based CRDS detection schemes reported for CH₃I or other similar halogenated volatile organic compounds (HVOCs). A Challenge for such measurements include scarcity and, in many cases, non-availability of the high-resolution spectrum and related spectroscopic parameters such as line intensities, line shape parameters. Another challenge exists in the comparatively low absorption cross-sections, which are about 50 times lower than those of CH₄ in the mid-IR range.

In this study, we investigate the potential of mid-IR continuous-wave (cw)-CRDS for HVOCs detection, with CH₃I as specific case study. As a pre-requisite, part of the high-resolution spectrum of the ν_4 vibrational band of CH₃I at wavelengths around 3.235 μm (3091 cm^{-1}) has been measured. Accurate measurements of the absorption cross-section and of the pressure broadening coefficient are presented. Moreover, the performance of CRDS for experimental studies is demonstrated with the help of a straightforward tank-purging experiment and a comparison with corresponding GC-MS/ECD measurements. Finally, the potential of advanced mid-IR cw-CRDS detection schemes for in-situ detection of CH₃I in practical applications is evaluated.

4.1 Experimental Section

The CRDS measurements were performed in Kiel, Germany and the GC-MS/ECD measurements were conducted in Halifax, Canada. The same purge-tank and associated experimental conditions were used

with both measurement systems so that the analytical performance of the geographically separated systems could be directly compared. Stock solutions were prepared from two freshly opened bottles of CH₃I (Sigma Aldrich, > 99.5%, main impurity CH₂I₂). For the spectroscopic measurements, pure CH₃I was degassed and further purified by several freeze-pump-thaw cycles. Deionized water was taken from the in-house supply systems. N₂ (99.999%) and Ar (99.999%) were used as buffer gases, hexane (Sigma Aldrich, > 99%) and methanol (Sigma Aldrich, 99.9%) were used as solvents.

4.1.1 CRD Spectrometer

CRDS is an absorption method that measures the decrease of the decay rate of light trapped in a ringdown resonator. The frequency dependent absorption coefficient $\alpha(\nu)$ and absorption cross-section $\sigma(\nu)$ are directly linked to the change of the ringdown time,

$$\alpha(\nu) = \sigma(\nu)[C] = \frac{1}{c} \left(\frac{1}{\tau} - \frac{1}{\tau_0} \right). \quad (4.1)$$

Here, c is the speed of light, $[C]$ the absorber concentration (i.e., number of molecules per unit volume), and τ and τ_0 are the cavity-decay times with and without absorber, which are determined separately by fitting the observed mono-exponential ringdown transients or by measuring on and off resonance. Note that due to the narrow linewidth of the detection laser ($\Delta\nu < 60$ kHz on a 500 μ s and ≈ 1 MHz on a 80 ms timescale), and the high finesse of the resonator (intrinsic cavity mode linewidth $\delta\nu = 12.5$ kHz), the spectral resolution is well below the absorption linewidth (Doppler broadening ≈ 95 MHz), and hence, $\sigma(\nu)$ corresponds to the narrow-bandwidth absorption cross-section σ_c .

The real forte of CRDS for gas analysis lies with the very long effective absorption path lengths made possible by the use of supermirrors with high reflectivities $R > 99.97\%$. In contrast to GC-MS/ECD, CRDS can also be a calibration-free detection technique with the absorption cross-section being a molecule-specific quantity that needs to be measured only once.

The schematic of the recently set up cw-IR-CRD spectrometer, which has been described in detail in Ref. [18, 19], is shown in Figure 4.1. Briefly, the light source was an all-in-fiber continuous wave, single resonant, optical parametric oscillator, cw-SR-OPO (Argos Model 2400 SF - Module C, Lockheed Martin Aculight), capable of generating continuously tunable idler output, $3.2 \mu\text{m} < \lambda < 3.9 \mu\text{m}$, and signal output, $1.46 \mu\text{m} < \lambda < 1.60 \mu\text{m}$, with light powers > 900 mW. A Michelson interferometer-type wavemeter (Bristol Instruments; 621A-IR) was used to measure the wavelength with a specified accuracy of $\pm 0.0006 \text{ cm}^{-1}$ at $3.3 \mu\text{m}$ and a repeatability of $\pm 0.0002 \text{ cm}^{-1}$. The wavelength was checked independently by measuring the line positions of methane absorption features, which were within 0.0008 cm^{-1} with their HITRAN reference database values [20]. The light beam passed an acousto-optic modulator (AOM) acting as a fast optical switch. The first-order diffracted beam was sent to the ringdown cell made of quartz-coated stainless steel and equipped with multiple ports to establish a gas flow as well as to monitor the gas pressure (MKS Baratron; Models 620B, 622B, covering the range from 10^{-4} to 100 mbar). A focal, 50 cm in length Fabry-Perot resonator configuration with two 1 m radius of curvature mirrors with a specified reflectivity of 99.99% at $3.3 \mu\text{m}$ was used. Mirror adjustment was accomplished mechanically with mirror mounts and electromechanically with three piezo electric transducers (PZTs). The length of the cavity was modulated with a scanning speed of the

cavity resonance frequency of about 15 GHz s^{-1} in order to achieve the frequency matching condition. Alternatively, a laser wavelength modulation scheme could be applied by fine tuning the seed laser with a scan frequency of 10 Hz and a scan interval of about 1 GHz. The laser light leaking through the rear mirror of the cavity was detected with a liquid nitrogen cooled InSb photodiode/preamplifier combination with a bandwidth of DC - 5 MHz. A comparator circuit was implemented to trigger the AOM at a preset light level. The sampling of the ringdown signal, the determination of decay constants, and the continuous measurement of the wavelength were achieved via National Instruments hardware (PCI-5022, 10 MHz, 18 bit) and a self-written LABVIEW [21] program. The collected ringdown decay curves were individually fitted to a single-exponential function by a nonlinear least-squares method, averaged and stored as a function of the laser frequency. The measured ringdown time of the empty cavity was $12.5 \mu\text{s}$ corresponding to a mirror reflectivity of 99.985% and an effective path length of 3.75 km.

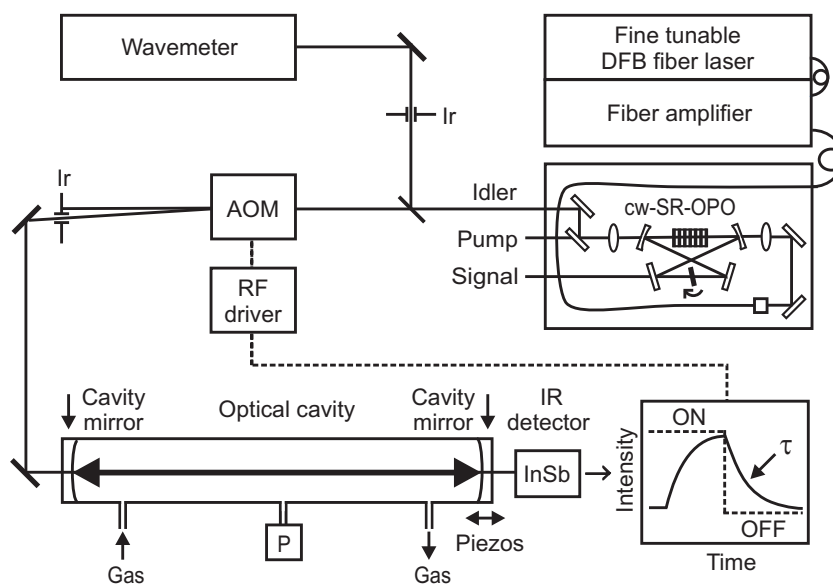


Figure 4.1: Schematic setup of the cw-IR-CRD spectrometer using a cw-SR-OPO as a tunable high resolution light source. AOM: acousto-optic modulator, Ir: iris diaphragm, P: pressure sensor.

4.1.2 GC-MS/ECD Analysis

The measurements in Halifax used an Agilent 7890B gas chromatograph equipped with both a mass spectrometer (Agilent 5977A) and an electron capture detector (Agilent, Ni-63 foil). The GC-column was a wall-coated open tubular (WCOT) type with a RTX-VGC coating (60 m; $1.4 \mu\text{m}$ coating; 0.25 mm inside diameter; 2 ml/min flow rate). The GC was temperature-programmed (initial temperature 50°C for 8 minutes; ramp to 150°C at $10^\circ\text{C}/\text{min}$; 150°C for 1 min; ramp to 200°C at $10^\circ\text{C}/\text{min}$).

An automated purge-and-trap system (“Versatile Sample Preparator” VSP4000; Innovative Messtechnik GmbH) was used to extract CH_3I from water samples (10 ml) as well as gas samples that were contained in 20 ml vials sealed with a septum, followed by preconcentration on a micropacked cryotrap. Rapid heating of the trap led to desorption of all analytes and transfer by a heated transfer line to the GC column. The combined system was capable of automated extraction/analysis at a rate of 1 sample/hour (including time for reference measurements and calibration). The in-vial purging approach allowed for detection limits in the lower ppt mixing ratio range.

Calibration of the GC-MS/ECD was performed using liquid CH_3I standards that have subsequently

been checked against internal gas standards. Three stock standards (A) 5 μl of CH_3I ($M = 141.94$ g/mol, $\rho = 2.28$ g/ml) in 250 ml of hexane, (B) 500 μl from stock A in 250 ml of methanol, and (C) 100 μl of stock B in 200 ml of methanol were prepared by serial dilutions and stored at 4 $^\circ\text{C}$. A system blank was analyzed before every standard measurement. A calibration curve was used for determining the concentrations of the extracted samples. The working standard was measured three times and the standard deviation of triplicate analyses was always around 12%.

4.1.3 Purge Tank Experiments

A simple tank-purging experiment was designed to allow direct comparison of mid-IR cw-CRDS performance with that of the GC-MS/ECD system. The experiment mimics close-to-real experimental conditions as they may apply in process studies addressing the environmental fate of contaminated surface water. Figure 4.2 shows a schematic of the 2 liter purge tank with removable cap which was used with both GC-MS/ECD and CRDS measurements. For each purge experiment, one liter of water was introduced into the tank and a known volume (0.09 – 5.6 ml) from the stock standard solution (A) was injected into the water; this was followed by purging with N_2 gas at a flow rate of 120 mL/min at a pressure of 1 atm at room temperature (22 $^\circ\text{C}$) for up to 4 hours. The gas outflow from the purge tank was directed to the ringdown cell in the case of CRDS, whereas for GC-MS/ECD analysis it was subsampled with a microsyringe of 100 μl and introduced into sample vials through a septum. Samples for GC-MS/ECD were collected every minute for the initial 10 minutes, every 10 minutes over the next hour and every 30 minutes subsequently. CRDS measurements were performed continuously with a repetition frequency of about 5 – 10 Hz.

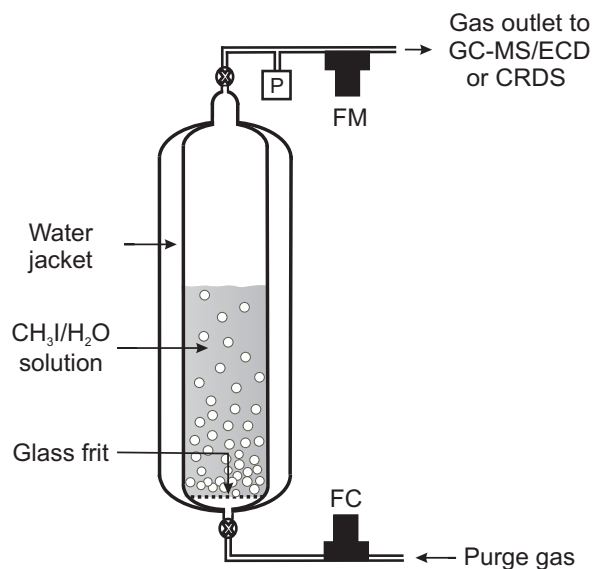


Figure 4.2: Schematic of the purge vessel. FC: flow controller, FM: flow meter, P: pressure sensor.

4.2 Results and Discussion

4.2.1 CRDS Measurement Performance

Figure 4.3 illustrates an analysis of the performance of the CRD spectrometer in terms of the Allan standard deviation of the empty cavity decay constant $k_0 = 1/\tau_0$. Allan plots are used to estimate the limit of detection (LOD) based on the noise level and the temporal stability of the collected

ringdown times. The two alternative cavity excitation schemes, cavity length modulation (red symbols) and laser wavelength modulation (black symbols), were used to analyze the performance of the CRD spectrometer. Figure 4.3 reveals that the wavelength modulation scheme exhibits about a factor of two lower noise, which is partly due to a two times higher repetition frequency (factor of $\sqrt{2}$ enhancement) and to the lower sensitivity of this method to acoustic and mode coupling noise components. As can be seen from the comparison with the theoretical white noise prediction (blue lines with a slope of -0.5), up to about 100 s averaging the Allan standard deviation sd decreases statistically, hence revealing a very good stability of the spectrometer. The optimum averaging times of about 70 s and 200 s yield minimum standard deviations of $sd(k_0) = 1.7 \times 10^{-5} \mu\text{s}^{-1}$ and $2.1 \times 10^{-5} \mu\text{s}^{-1}$ for wavelength and cavity-length modulation, respectively. Using Eq. 4.1, this corresponds a minimum detectable absorption coefficient $\alpha_{\min} = 7.0 \times 10^{-10} \text{ cm}^{-1}$ for the cavity modulation scheme and based on the absorption cross-section $\sigma_c = 5.8 \times 10^4 \text{ cm}^2/\text{mol}$ reported below, they correspond to a noise-equivalent concentration of $1.2 \times 10^{-14} \text{ mol}/\text{cm}^3$ (15 ppb mixing ratio at 20 mbar N_2 buffer and $T = 295 \text{ K}$). The single-shot standard deviation of the extracted absorption coefficient, $sd(\alpha, 1 \text{ shot}) = 1.5 \times 10^{-8} \text{ cm}^{-1}$, compares very well with previously reported values of $0.2 - 1.5 \times 10^{-7} \text{ cm}^{-1}$, achieved for quantum cascade-laser-based cw-IR-CRDS implementations [22].

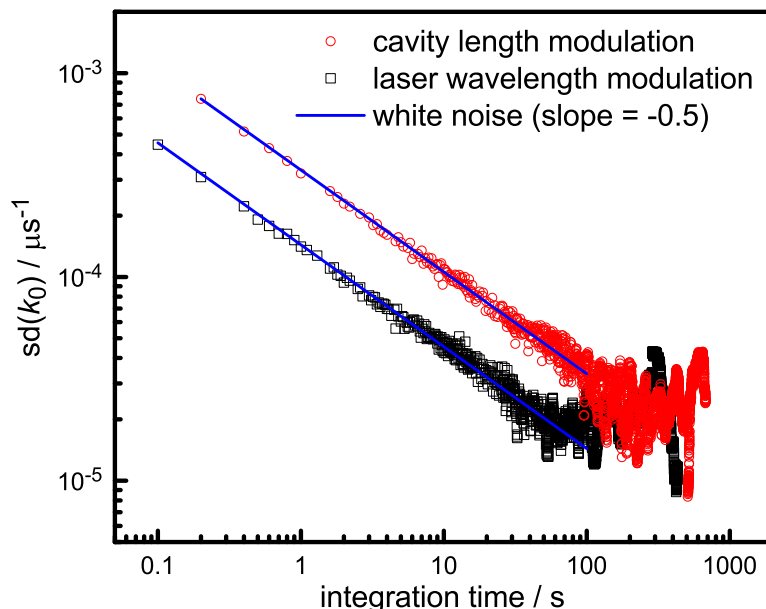


Figure 4.3: Allan plots of the collected empty cavity decay constants (symbols) in comparison white-noise-limited ideal behavior (lines).

4.2.2 The High-Resolution Spectrum of CH_3I

Figure 4.4a presents absorption spectrum of CH_3I together with spectra of the main interfering molecules in the atmosphere. High-resolution spectra of the latter four trace gases are available from HITRAN[20], whereas the low-resolution (0.112 cm^{-1}) spectrum of methyl iodide has been adopted from the PNNL database[23]. All spectra refer to a total pressure of 1 atm and room temperature. In the accessible spectral window from 2565 to 3125 cm^{-1} , absorption cross-sections of methyl iodide are about a factor of 20 lower than that of CH_4 , but a factor of 10 – 1000 higher than that of H_2O , N_2O , and CO_2 , respectively.

CH_3I exhibits a complex rovibrational spectrum with three main vibrational structures. The observed

weakest vibrational feature extending from 2750 to 2900 cm^{-1} was assigned by Lattanzi [24] to several overlapping parallel vibrational bands including the $2\nu_5$, $\nu_3 + \nu_5 + \nu_6$, and $2\nu_3 + 2\nu_6$ transitions. The stronger, heavily congested ν_1 band centered at 2971 cm^{-1} was measured by Paso et al.[25] with medium spectral resolution of 0.04 cm^{-1} and corresponds to the CH_3 symmetric stretch motion. Finally, the ν_4 band around 3060 cm^{-1} with well separated Q branches in the range from 3000 to 3175 cm^{-1} corresponds to the CH_3 asymmetric stretch.

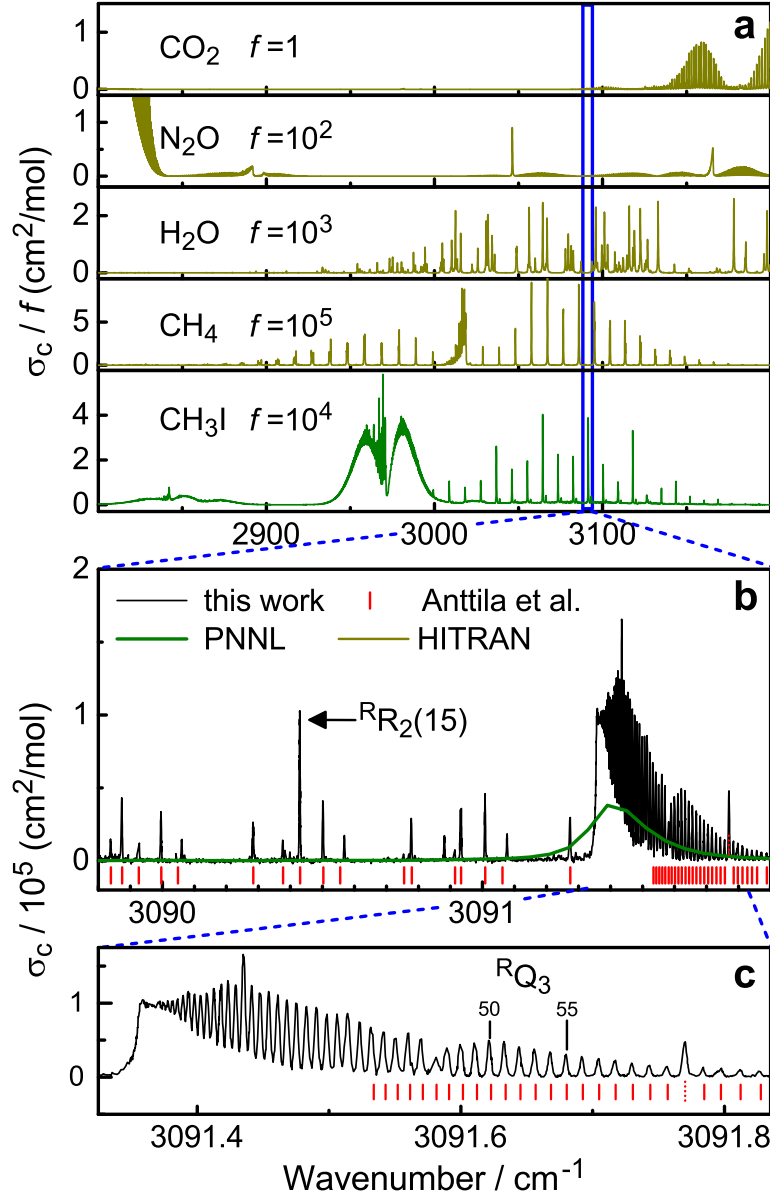


Figure 4.4: (a) Comparison of absorption spectra of CO_2 , H_2O , CH_4 , and CH_3I at $p = 1$ atm based on HITRAN [20] and PNNL[23] data. The blue box highlights a spectral window for CH_3I detection with low interference of the main interfering atmospheric trace gases. (b) Part of the Doppler limited high-resolution spectrum of CH_3I measured in this work. (c) J-resolved ${}^R Q_3$ band transitions.

This band has been measured and assigned with a fairly high resolution of 0.0054 cm^{-1} by Anttila et al.[26] No information about line intensities or pressure broadening coefficients are available from previous spectroscopic studies for single absorption lines. Due to its well resolved structure and its low interference with the atmospheric absorbers, the spectral range around the ${}^R Q_3$ band (marked by the blue box in Figure 4.4a) has been chosen in this work as a suitable spectroscopic window for CH_3I detection. Figure 4.4b presents part of the measured high-resolution spectrum of CH_3I (black curve)

in comparison with the low-resolution PNNL data (green curve) and line positions and assignments adopted from the work of Anttila et al.[26] (red markers). The complete experimental spectrum ranging from 3088.7 to 3093.3 cm^{-1} is provided in the Supporting Information. The spectrum has been recorded for 1% mixture of CH_3I in Ar at a total pressure of 1 mbar. At this pressure, a Doppler-limited rotational-vibrational spectrum with nicely J -resolved ${}^{\text{R}}\text{Q}_3$ band transition down to $J \approx 15$ could be observed (Figure 4.4c).

4.2.3 Quantitative Analysis of ν_4 - ${}^{\text{R}}\text{R}_2(15)$ Absorption Line

For further quantitative measurements we selected the strong, well-separated ${}^{\text{R}}\text{R}_2(15)$ line at 3090.4289 cm^{-1} . Note that this line is not observed in the low resolution FTIR spectrum at all (Figure 4.4b), again highlighting the need for accurate high-resolution spectral measurements prior to line selection. Figure 4.5a illustrates the very good linearity of the integrated absorption coefficient of the ${}^{\text{R}}\text{R}_2(15)$ line as a function of CH_3I partial pressure. The slope of the line corresponds to a line strength (i.e., the integrated absorption cross-section) of $S = (553 \pm 23)$ cm/mol . Here, as well as for all other spectroscopic quantities given in this section, the error accounts for the combined 2σ standard error of the fit and the 2% uncertainty of the total pressure measurements. As it was known from our previous study on CH_2Br_2 that the high light intensities attainable within the ringdown cavity can easily saturate the optical transition, [19] care was taken to limit the laser intensity and to measure at sufficiently high pressure to ensure linear absorption. For the experiment shown in Figure 4.5, the concentration of CH_3I was varied by successive dilution of the gas sample and the pressure was kept constant at 20.0 mbar using argon as buffer gas.

Figure 4.5b presents a Voigt line shape analysis of absorption profiles measured at different total pressures, which were used to determine the pressure line-broadening coefficient $\Delta\tilde{\nu}_p = 2\gamma_p \cdot p$ and the pressure-dependent narrow-bandwidth absorption cross-section σ_c . From measurements in N_2 and Ar with the partial pressure of CH_3I kept constant at 320 nbar, the data points shown in Figure 4.5c have been extracted. The slope of the solid lines of the plot of $\Delta\tilde{\nu}_p$ versus p_{total} yield $\gamma_p(\text{Ar}) = (0.094 \pm 0.002)$ $\text{cm}^{-1}/\text{bar}$ and, as expected for a diatomic molecule, a somewhat larger value $\gamma_p(\text{N}_2) = (0.112 \pm 0.003)$ $\text{cm}^{-1}/\text{bar}$. The obtained values are within the typical range of $0.086 \text{ cm}^{-1}/\text{bar} < \gamma_p(\text{air}) < 0.119 \text{ cm}^{-1}/\text{bar}$ known for other halocarbons [20]. Finally, the dashed curves in Figure 4.5c represent Voigt fits of the cross-section σ_c data for Ar and N_2 yielding a consistent Doppler limited value of $\sigma_c(T = 295 \text{ K}, p = 0 \text{ bar}) = (1.57 \pm 0.06) \times 10^5 \text{ cm}^2/\text{mol}$. This corresponds to $S = (534 \pm 19)$ cm/mol , hence in excellent agreement with the line strength value reported above. A weighted average value of $S = (545 \pm 20)$ cm/mol and $\sigma_c(T = 295 \text{ K}, p = 0 \text{ bar}) = (1.60 \pm 0.06) \times 10^5 \text{ cm}^2/\text{mol}$ is recommended for future use.

A proper selection of the absorption cell pressure used for trace gas detection is always a trade-off between required limit of detection and selectivity. Whereas for a given mixing ratio of the analyte, the signal increases with increasing cell pressure and increasing line broadening effects lower the selectivity due to possible absorption-line overlap with nearby peaks of interfering species. Typically, a cell pressure is chosen where significant pressure broadening effects start to prevail ($\Delta\tilde{\nu}_p > \Delta\tilde{\nu}_D$), about 14 mbar in the case of CH_3I (see Figure 4.5c)

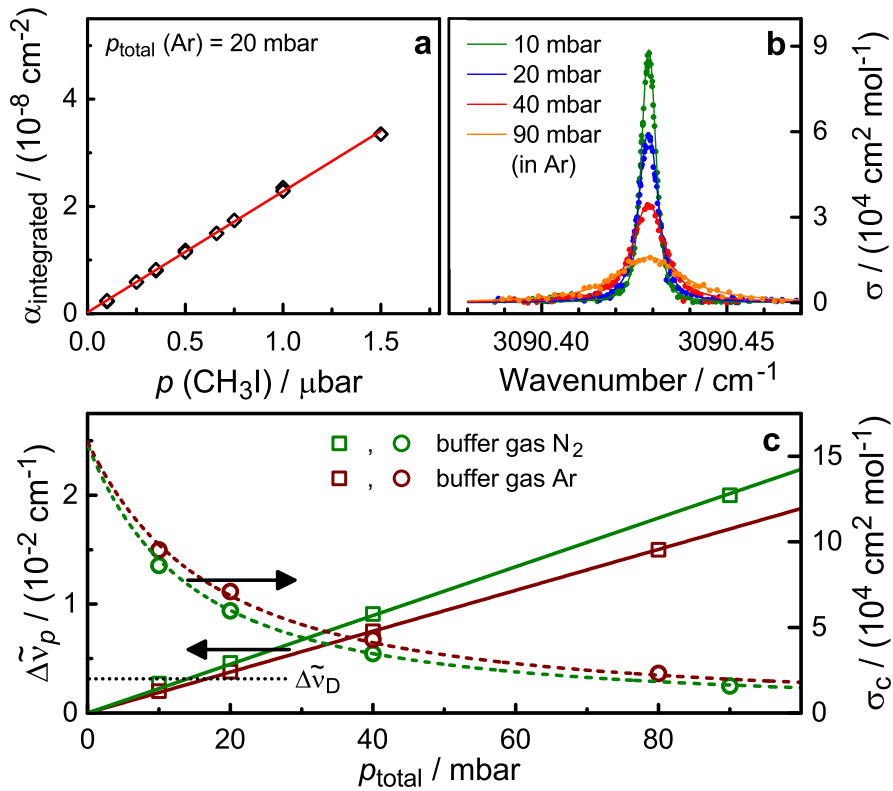
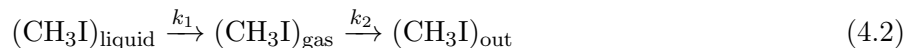


Figure 4.5: Determination of quantitative spectroscopic data for the $R R_2(15)$ transition at $3090.4289 \text{ cm}^{-1}$. a) Linearity and determination of the absorption line strength. b) Typical pressure dependent line profiles. (c) Voigt analysis yielding the pressure broadening coefficients and the Doppler limited narrow-bandwidth absorption cross-section (see text). $\Delta\tilde{\nu}_p$ and $\Delta\tilde{\nu}_D$ are the pressure and Doppler broadening (FWHM) of the absorption line, respectively.

4.2.4 Purge-Tank Experiment

Figure 4.6 shows concentration-time profiles of CH_3I in the gas outflow from the purge-tank for two comparable experiments using either GC-MS (red symbols with error bars) or CRDS analysis. The continuous CRDS measurements are averaged for 6 s (grey) and 60 s (black curve), whereas the GC-MS analyses are for discrete samples. Following injection of CH_3I , the headspace concentration reaches a maximum within less than 10 min and then decreases exponentially due to the slow removal of CH_3I from the system. Overall, very good agreement has been found between the two measurement approaches for both the temporal behavior as well as the absolute CH_3I concentration. Clearly, the in situ CRDS detection holds an advantage in terms of reduced noise and increased data density. The overall temporal behavior can be described by two consecutive first-order processes with time constants $\tau_1 = 1/k_1$ and $\tau_2 = 1/k_2$,



Here, k_1 reflects the rate of exchange of the gas-phase volume $V_{\text{gas}} \approx 1 \text{ L}$ by the equilibrated purge gas flow $\dot{V} = 7.39 \text{ L/h}$ (including a 2.6% correction to account for the partial pressure of water, 26.3 mbar at $22 \text{ }^\circ\text{C}$), which can be approximated by the initial gradient to be on the order of $k_1 \approx 7.4 \text{ h}^{-1}$:

$$k_1 = \frac{1}{V_{\text{gas}}} \left(\frac{dV}{dt} \right)_{t=0} = \frac{\dot{V}}{V_{\text{gas}}} \quad (4.3)$$

k_2 describes the loss of CH_3I due to the continuous equilibration and removal of CH_3I by the purge gas flow,

$$k_2 = \frac{1}{n_{\text{liquid}}^0} \left(\frac{dn_{\text{liquid}}}{dt} \right)_{t=0} = \frac{1}{c_{\text{liquid}}^0 V_{\text{liquid}}} \left(\frac{dn_{\text{liquid}}}{dt} \right)_{t=0} \quad (4.4)$$

n_{liquid}^0 and c_{liquid}^0 correspond to the initial amount and concentration of CH_3I in the liquid phase volume $V_{\text{liquid}} = 1$ L. The loss of substance in the liquid phase is equal to the amount of substance transported by the purge gas flow, $dn_{\text{liquid}}/dt = c_{\text{gas}}^0 \dot{V}$, yielding

$$k_2 = \frac{c_{\text{gas}}^0}{c_{\text{liquid}}^0} \frac{\dot{V}}{V_{\text{liquid}}} = H_{cc} \frac{\dot{V}}{V_{\text{liquid}}}. \quad (4.5)$$

Here, H_{cc} is the dimensionless air-to-water concentration ratio (Henry constant), which is known from literature to be $H_{cc}(\text{CH}_3\text{I}, 295 \text{ K}) = 0.183$ [27]. Hence, a value of $k_2 \approx 1.35 \text{ h}^{-1}$ can be estimated for the conducted purge-tank experiments.

Experiments as shown in Figure 4.6, with a number of small variations, were repeated 6 times in Halifax (in parallel GC-MS and GC-ECD) and 11 times in Kiel (CRDS). According to Eq. 4.2, the overall concentration-time profiles measured in the headspace can be described by the following integrated rate law:

$$[\text{CH}_3\text{I}] = [\text{CH}_3\text{I}]_0 \frac{k_1}{k_2 - k_1} \left(e^{-k_1 t} - e^{-k_2 t} \right). \quad (4.6)$$

The key results of simulations of the experiments using Eq. 4.6 with $[\text{CH}_3\text{I}]_0$, k_1 , and k_2 as adjustable parameters (solid red and green curves in Figure 4.6) are summarized in Table 4.1. Note that for the GC data, due to insufficient data coverage, k_1 was kept at the value deduced from the CRDS data to properly describe the fast initial increase of the signal. Moreover, allowance was made for small baseline offsets to properly describe the signal for long purging times. In case of CRDS, this offset was needed to account for minor changes of the empty cavity time constant (measured before the experiment with an evacuated cavity) after introducing the water vapor loaded gas flow into the cavity. In case of GC, the offsets were minor and reflect the uncertainties regarding calibration and false signal detection. The stated errors in Table 4.1, which are smaller for the CRDS measurements, reflect the scatter of the extracted data on a 1σ uncertainty level. Within error limits, all k_1 , and k_2 values are consistent and, moreover, agree very well with the values estimated from Eqs. 4.3 and 4.5. Obviously, the proposed model adequately describes the observed temporal behavior. Also the fitted $[\text{CH}_3\text{I}]_0$ values are in accordance with the expected values using Henry's law. Finally, the area below the concentration-time profile multiplied with the gas flow rate yields the amount of extracted CH_3I , hence the extraction ratio can be calculated according to

$$\frac{n_{\text{extracted}}^0}{n_{\text{injected}}^0} = \frac{\int_0^\infty [\text{CH}_3\text{I}] dt \dot{V}}{n_{\text{injected}}^0} = \frac{[\text{CH}_3\text{I}]_0 k_1 (k_1^{-1} - k_2^{-1}) \dot{V}}{(k_2 - k_1) n_{\text{injected}}^0}. \quad (4.7)$$

As can be seen from Table 4.1, with a value of $(97 \pm 8)\%$ for CRDS and $(88 \pm 13)\%$ for GC-MS or $(88 \pm 22)\%$ for GC-ECD, the extraction ratio was close to 100% in all cases. This reveals that both CRDS and GC methodology allow for reliable and quantitative detection of CH_3I . The somewhat lower value obtained from GC experiments may be attributed to a limited stability of the CH_3I samples, which had to be stored up to 20 h prior to the long GC analysis time. Stability experiments with

Table 4.1: Model parameters extracted from CH₃I concentration-time profiles measured during the purge-tank experiments using CRDS and GC-MS/ECD detection.

Exp.	Location	No. of Exp.	k_1/h^{-1}	k_2/h^{-1}	$[\text{CH}_3\text{I}]/(H_{cc} c_{\text{liq}}^0)$	Offset/mol L ⁻¹	$n_{\text{ext.}}^0/n_{\text{inj.}}^0$
CRDS	Kiel	11	8.8 ± 1.8	1.28 ± 0.20	(91 ± 13) %	$(8.1 \pm 2.2) \times 10^{-9}$	(97 ± 8)
GC-MS	Halifax	6	8.8 ^a	1.36 ± 0.33	(94 ± 22) %	$(8.1 \pm 0.7) \times 10^{-9}$	(88 ± 13)
GC-ECD	Halifax	6	8.8 ^a	1.33 ± 0.28	(90 ± 26) %	$(1.2 \pm 1.5) \times 10^{-9}$	(88 ± 22)
		model	7.4	1.35	100 %		

^a k_1 for the GC-MS/ECD measurements was fixed at the averaged value obtained from the CRDS measurements.

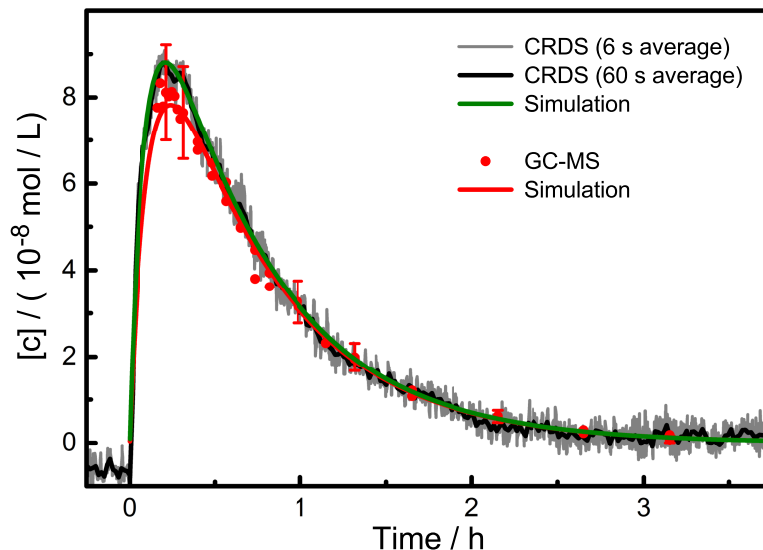


Figure 4.6: Typical CH₃I concentration-time profiles of two purge-tank experiment using either CRDS or GC-MS detection. Solid curves correspond to simulations based on the model outlined in the text. The error bars represent a typical 12% relative uncertainty of a GC measurement.

samples of CH₃I in Milli-Q water, which were kept in the dark over 15 h, showed that the measured concentration of CH₃I decreased by a few percent. In summary, the simple purge-tank experiment highlights the possibility to perform quantitative CH₃I measurements and underlines advantages of CRDS over the GC based detection systems, including its in-situ and fast analysis capability and a better reproducibility.

4.2.5 Potential of CRDS Analyzers for CH₃I Monitoring

Two main limitations control the applicability of CRDS analyzers for practical applications: (i) the limit of detection of the spectrometer, and (ii) potential interference with other absorbing molecules (i.e., the so-called cross sensitivity issue).

Limit of detection. The achieved LOD of CH₃I using a standard IR-CRDS implementation has been shown in this paper to be on the order of 15 ppb mixing ratio (vide supra). With current allowable exposure limits being about two orders of magnitude higher, this LOD is sufficient to be useful for leak detection or for monitoring personal exposure limits at industrial or agricultural workplaces. The capacity for high frequency analyses on pumped air streams would allow for near-continuous monitoring of exposure risk within different rooms and/or different field locations, using a single analyzer. Further, the speed of analysis makes CRDS useful for environmental process studies where higher than ambient concentrations are often used.

Typical atmospheric mixing ratios of CH₃I are 0.1 to 2 ppt, [8] but environmental background levels

are often higher. For example, surface seawater is typically supersaturated by a factor of 2 – 10 [28]. However, the resulting mixing ratio levels are still three to four orders of magnitude too low for direct detection with the current CRDS system. An often used approach to achieve acceptable limits of detection for volatile organic compounds in such cases is to pre-concentrate the atmospheric sample [29]. Common techniques used for pre-concentration include sorbent or cryogenic trapping. In deed, sorbent tubes can sample efficiently at wide range of flow rates in the range 10 – 1000 ml/min, collecting sample volumes of 0.1 – 150 liters [30]. On-line sorbent trap and membrane extraction techniques allow for on-site or real-time analysis, which is ideal for spectroscopic techniques because of their short analysis time. In principle, analyzing a pre-concentrated sample from 1000 mL gas at atmospheric pressure instead of flowing the gas directly through the 0.5 L cavity at 20 mbar would increase the sensitivity by a factor of 100 in our case. Moreover, by using smaller mirrors and a corresponding cell diameter, the ringdown cavity volume could be easily reduced by a factor 8. Combining both measures, i.e., 2 minutes sampling, trapping, and analysis of 2 L atmospheric gas would in the ideal case result in a detection limit of 9 ppt.

From a technical point of view, a further sensitivity enhancement is possible by increasing the frequency of ringdown acquisition. Repetition frequencies of several kHz (instead of 5 – 10 Hz used in this work) have been reported, hence an additional sensitivity enhancement of up to a factor of 10 to 20 should be possible. All in all, a LOD of < 1 ppt is feasible, however, pre-concentration approaches and fast ringdown acquisition that often relies on cavity-locking schemes would compromise some of the key advantages of CRDS, namely its continuous measurement capability and its ease of operation under tough conditions in the field.

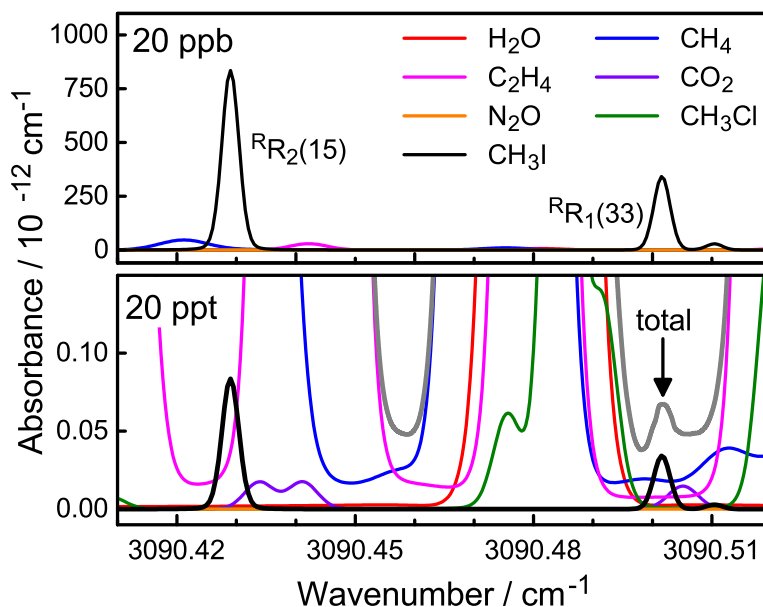


Figure 4.7: Simulation of the absorption spectrum of a mixture containing several trace gases at their typical atmospheric mixing ratios ($p_{\text{total}} = 1$ mbar, $T = 295$ K, see text).

Selectivity. The cross-sensitivity issue resulting from the strong overlap of the absorption spectra of more abundant molecules is another challenging problem for the direct detection of minor trace gas species such as CH_3I . Nevertheless, the high spectral resolution of continuous wave laser systems combined with careful selection of the spectroscopic window may still allow for the direct analysis of CH_3I without the need for an upstream separation step. Figure 4.7 illustrates a simulated absorption

spectrum of an atmospheric sample using spectroscopic data from the HITRAN database [20]. Here, the sample is composed of CO₂ (400 ppm), CH₄ (17 ppm), N₂O (320 ppb), C₂H₄ (2 ppb), and CH₃Cl (550 ppt), as they may be faced in the practical applications. We also included H₂O, however, assumed a pre-dried sample with a water mixing ratio of 300 ppm. Reducing the water vapor content by a factor of 100 is easily achievable with desiccants, cryo-condensation, adsorbents, or permeation [31]. The upper plot of Figure 4.7 reveals that selective CH₃I is possible on a 20 ppb mixing ratio level. However, for the mixing ratio of 20 ppt assumed for the lower plot, the ^RR₂(15) absorption line of CH₃I would be hidden behind the absorption contribution from a very weak absorption line of CH₄, which is present in 5.5×10^6 excess over CH₃I. Still it is possible to find detection wavelengths with clear spectral signatures arising from CH₃I (e.g., the ^RR₁(33) line in Figure 4.7). However, in such situations many other trace gases at low mixing level may interfere as well. Therefore, any detection scheme should be carefully tested for cross-sensitivities under realistic field conditions.

4.3 Conclusions

A sensitive mid-IR cw-CRDS detection scheme for quantitative measurement of CH₃I has been developed. The reported limit of detection, 15 ppb (at 70 s averaging time) at 23 mbar absorption cell pressure (corresponding to 8.5×10^9 molecules/cm³), is much better than current CH₃I exposure limit of 0.3 – 5 ppm and hence is suitable for workplace monitoring and leak detection applications. Future development of a field-going CRDS spectrometer for CH₃I detection should be straightforward and can be based on already available commercial spectrometer platforms. To do so, the expensive cw-SR-OPO, which has been used in this work as a versatile light source for trace gas sensor development, can be replaced by a DFB based IR laser diode matching the selected absorption transition. Further, the fast and in situ detection capability makes CRDS a method of choice for process studies, where enriched samples are often used. However, the method is, in contrast to GC based systems, not sensitive enough to directly detect the < 20 ppt mixing ratio level found in natural environmental samples. Here, further technical development is necessary (and possible) and/or pre-concentration strategies need to be employed in combination with careful line selection in order to escape from cross-sensitivity issues. Part of the high-resolution spectrum of the ν_4 band has been measured with Doppler-limited resolution for the first time. The line strength, $S = (545 \pm 20)$ cm/mol, and line center absorption cross-section, $\sigma_c(T = 295 \text{ K}, p = 0 \text{ bar}) = (1.60 \pm 0.06) \times 10^5$ cm²/mol, as well as the pressure broadening coefficient, $\gamma_p(\text{Ar}) = (0.094 \pm 0.002)$ cm⁻¹/bar and $\gamma_p(\text{N}_2) = (0.112 \pm 0.003)$ cm⁻¹/bar, have been determined for the ^RR₂(15) absorption line at 3090.4289 cm⁻¹. Finally, a simple tank-purging experiment has been performed in order to highlight the advantages of CRDS in comparison with the well-established GC-MS/ECD system. The experiments reveal that calibration-free quantitative detection of CH₃I is possible with a time-resolution of several seconds and with high reproducibility.

ASSOCIATED CONTENT

Supporting Information

The Supporting Information is available free of charge on the ACS Publication website at DOI: 10.1021/acs.analchem.7b01970.

High-resolution experimental spectrum of the ν_4 band of CH₃I (1 % CH₃I in argon at a total pressure of 1 mbar, from 3088.715 to 3093.378 cm⁻¹).

AUTHOR INFORMATION

Corresponding Author

* Gernot Friedrichs; Phone: +49 0431 880 7742; Fax: +49 0431 880 7743;

Email: friedrichs@phc.uni-kiel.de

Notes

Authors declare no competing financial interests

ACKNOWLEDGMENT

We would like to thank the Helmholtz Research School Ocean Science and Technology (HOSST) at the Helmholtz Centre of Ocean Research Kiel (GEOMAR) and the Cluster of Excellence FUTURE OCEAN at Kiel University for funding. Q.S. and D.W.R.W were supported by the Canada Excellence Research Chair in Ocean Science and Technology.

References

- [1] S. A. Montzka, S. Reimann, S. O'Doherty, A. Engel, A. K. Kruger, W. T. Sturges, D. Blake, M. Dorf, P. Fraser, and L. Froidevaux *et al.* *Scientific assessment of ozone depletion:2010*. Global Ozone Research and Monitoring Project report: No. 52. World Meteorological Organization, Geneva Switzerland, 2011.
- [2] D. J. Ashworth, S. R. Yates, L. Luo, S. R. Lee, and R. Xuan. Coupling of soil solarization and reduced rate fumigation: Effects on methyl iodide emissions from raised beds under field conditions. *J. Agric. Food Chem.*, 61(51):12510–12515, 2013.
- [3] M. Sutton, S. R. Kane, and J. R. Wollard. Methyl iodide fumigation of bacillus anthracis spores. *LLNL-Technical Report-562673*, 2012.
- [4] G. D. Clayton, F. E. Clayton, R. E. Allan, and F. A. Patty, editors. *Patty's industrial hygiene and toxicology*. Wiley, New York and Chichester, 4th edition, 1994.
- [5] J. F. Roth. The production of acetic acid. *Platinum Met. Rev.*, 19(1):12–14, 1975.
- [6] J. H. Jones. The cativa™ process for the manufacture of acetic acid. *Platinum Met. Rev.*, 44(3):94–105, 2000.
- [7] A. Karhu. *Methods to prevent the source term of methyl iodide during a core melt accident*. NKS, Roskilde, 2000.
- [8] M. J. Kurylo, J.M. Rodríguez, M. O. Andreae, E. L. Atlas, D. R. Blake, J. H. Butler, S. Lal, D. J. Lary, P. M. Midgley, and S. A. Montzka *et al.* *Scientific assessment of Ozone depletion: 1998: Shortlived ozone-related compounds*. Global Ozone Research and Monitoring Project report: No. 44. World Meteorological Organization, Geneva Switzerland, 1999.
- [9] W. L. Chameides and D. D. Davis. Iodine: Its possible role in tropospheric photochemistry. *J. Geophys. Res.*, 85(C12):7383–7398, 1980.
- [10] J. D. Happell and D. W. R. Wallace. Methyl iodide in the Greenland/Norwegian seas and the tropical Atlantic ocean: Evidence for photochemical production. *Geophys. Res. Lett.*, 23(16):2105–2108, 1996.
- [11] Q. Shi, G. Petrick, B. Quack, C. Marandino, and D. Wallace. Seasonal variability of methyl iodide in the kiel fjord. *J. Geophys. Res. Oceans*, 119(3):1609–1620, 2014.
- [12] Q. Shi, C. Marandino, B. Petrick, G. Quack, and D. Wallace. A time series of incubation experiments to examine the production and loss of CH₃I in surface seawater. *J. Geophys. Res. Oceans*, 119(12):8242–8254, 2014.
- [13] G. Gagliardi and H.-P. Loock, editors. *Cavity-enhanced spectroscopy and sensing*, volume 179 of *Springer series in optical sciences*, 0342-4111. Springer, Heidelberg, 2014.
- [14] G. Friedrichs, M. Colberg, M. Fikri, Z. Huang, J. Neumann, and F. Temps. Validation of the extended simultaneous kinetics and ringdown model by measurements of the reaction NH₂ + NO. *JPCA*, 109(21):4785–4795, 2005.

- [15] G. Friedrichs. Sensitive absorption methods for quantitative gas phase kinetic measurements. Part 2: Cavity ringdown spectroscopy. *Z. Phys. Chem.*, 222(1):31–61, 2008.
- [16] H. Chen, J. Winderlich, C. Gerbig, A. Hofer, C. W. Rella, E. R. Crosson, A. D. van Pelt, J. Steinbach, O. Kolle, and V. Beck *et al.* High-accuracy continuous airborne measurements of greenhouse gases (CO₂ and CH₄) using the cavity ring-down spectroscopy (CRDS) technique. *Atmos. Meas. Tech.*, 3(2):375–386, 2010.
- [17] M. Becker, N. Andersen, B. Fiedler, P. Fietzek, A. Körtzinger, T. Steinhoff, and G. Friedrichs. Using cavity ringdown spectroscopy for continuous monitoring of $\delta^{13}\text{C}(\text{CO}_2)$ and $f\text{CO}_2$ in the surface ocean. *Limnol. Oceanogr.: Methods*, 10(10):752–766, 2012.
- [18] I. Sadiq and G. Friedrichs. Saturation dynamics and working limits of saturated absorption cavity ringdown spectroscopy. *Phys. Chem. Chem. Phys.*, 18:22978–22989, 2016.
- [19] I. Sadiq and G. Friedrichs. Doppler-limited high-resolution spectrum and VPT2 assisted assignment of the C-H stretch of CH₂Br₂. *Spectrochim. Acta. A: Mol. Biomol. Spectrosc.*, 181:180–191, 2017.
- [20] L. S. Rothman, I. E. Gordon, Y. Babikov, A. Barbe, D. Chris Benner, P. F. Bernath, M. Birk, L. Bizzocchi, V. Boudon, and L. R. Brown *et al.* The HITRAN2012 molecular spectroscopic database. *J. Quant. Spectrosc. Radiat. Transfer*, 130:4–50, 2013.
- [21] C. Elliott, V. Vijayakumar, W Zink, and R Hansen. National Instruments LabVIEW: A programming environment for laboratory automation and measurement. *JALA*, 12(1):17–24, 2007.
- [22] B. E. Brumfield, J. T. Stewart, S. L. Widicus Weaver, M. D. Escarra, S. S. Howard, C. F. Gmachl, and B. J. McCall. A quantum cascade laser cw cavity ringdown spectrometer coupled to a supersonic expansion source. *Rev. Sci. Instrum.*, 81(6):063102, 2010.
- [23] W. S. Steven, J. J. Timothy, L. S. Robert, M. C. Pamela, C. R. George, and A. J. Patricia. Gas-phase databases for quantitative infrared spectroscopy. *Appl. Spectrosc.*, 58(12):1452–1461, 2004.
- [24] F. Lattanzi. Parallel vibrational states of CH₃I in the high resolution infrared spectrum from 2770 to 2900 cm⁻¹. *J. Chem. Phys.*, 92(7):4380, 1990.
- [25] R. Paso, V.-M. Horneman, and R. Anttila. Analysis of the ν_1 band of CH₃I. *J. Mol. Spectrosc.*, 101(1):193–198, 1983.
- [26] R. Anttila, R. Paso, and G. Guelachvili. A high-resolution infrared study of the ν_4 band of CH₃I. *J. Mol. Spectrosc.*, 119(1):190–200, 1986.
- [27] J. Staudinger and P. V. Roberts. A critical compilation of henry’s law constant temperature dependence relations for organic compounds in dilute aqueous solutions. *Chemosphere*, 44(4):561–576, 2001.
- [28] L. Wang, R. M. Moore, and J. J. Cullen. Methyl iodide in the NW Atlantic: Spatial and seasonal variation. *J. Geophys. Res.*, 114(C07):007/1–13, 2009.

- [29] M. R. Ras, F. Borrull, and R. M. Marcé. Sampling and preconcentration techniques for determination of volatile organic compounds in air samples. *TrAC, Trends Anal. Chem.*, 28(3):347–361, 2009.
- [30] A. Kumar and I. Viden. Volatile organic compounds: Sampling methods and their worldwide profile in ambient air. *Environ. Monit. Assess.*, 131(1-3):301–321, 2007.
- [31] D. K. W. Wang and C. C. Austin. Determination of complex mixtures of volatile organic compounds in ambient air: Canister methodology. *Anal. Bioanal. Chem.*, 386(4):1099–1120, 2006.

Doppler-Limited High-Resolution Spectrum and VPT2 Assisted Assignment of the C-H Stretch of CH₂Br₂

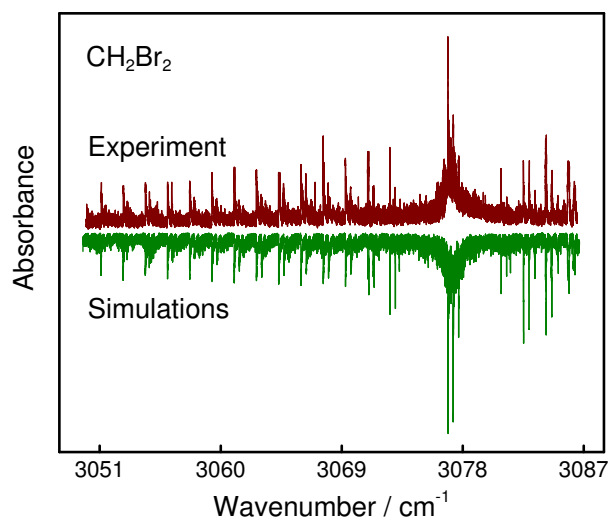
Ibrahim Sadiek,^a and Gernot Friedrichs^{*ab}

^aInstitut für Physikalische Chemie, Christian-Albrechts-Universität zu Kiel, Max-Eyth-Str. 1, D-24118 Kiel, Germany. ^bKMS Kiel Marine Science - Centre for Interdisciplinary Marine Sciences, Olshausenstr. 40, D-24098 Kiel, Germany.

Spectrochim. Acta. A: Mol. Biomol. Spectrosc., 181: 180–191, 2017, DOI: 10.1016/j.saa.2017.03.027

Received 10th November 2016, Accepted 13th March 2017, First published on the web 16th March 2016

Elsevier B.V. All rights reserved, 2017.



Own contributions:

- High-resolution spectra measurements of the ν_6 band of CH₂Br₂ .
- All quantum-chemical calculations presented in the publication.
- Spectra simulation and assignment using PGOPHER.
- Analysis and discussion of the experimental and theoretical data.
- Writing of paper draft.

ABSTRACT: The Doppler limited non-saturated rotationally resolved infrared spectra of the symmetric and asymmetric CH-stretch bands of CH₂Br₂ have been measured. A continuous wave cavity ringdown setup with a widely tunable Mid-IR-OPO laser light source yielded a single-shot minimum absorption of $4.9 \times 10^{-8} \text{ cm}^{-1}$. In contrast to the heavily congested ν_1 band, the ν_6 band showed partially resolved rotational features that may serve as suitable absorption targets in future environmental detection schemes for CH₂Br₂. A straightforward, VPT2 (second-order vibrational perturbation theory) assisted quantum-chemical approach for assigning the rotational structure has been tested using different model chemistries. The molecular structures, anharmonic frequencies and the structural changes upon vibrational excitation of CH₂Br₂ have been investigated. The predicted changes of the anharmonic rotational constants have been used together with available spectroscopic ground state constants to simulate the rovibrational structures of the ν_1 and ν_6 bands of CH₂Br₂. A refined analysis of the ν_6 band is presented yielding accurate values for the band origin and the rotational constants. A fit of the line positions of 312 prominent transitions of the three isotopologues revealed a low standard error of 0.00056 cm^{-1} , hence within the absolute 0.0009 cm^{-1} wavelength accuracy of the used spectrometer setup. A combined analysis of the predicted line strengths and positions of the strong Q sub-branches of the ν_6 band has been performed to test the ability of the different density functionals for VPT2 prediction of anharmonic molecular constants. The M06/6-311++G(d,p) model chemistry turned out to yield reliable state-dependent rotational constants that are accurate enough to reproduce the overall rotational structure even without fitting.

Keywords: High resolution infrared spectrum, Dibromomethane, VPT2, Spectral assignment

5.1 Introduction

Photochemically active brominated compounds exhibit high ozone destruction potential and affect the oxidation capacity of the atmosphere. Methylene bromide (CH₂Br₂) is one of the brominated compounds that is mainly emitted from the ocean [1, 2, 3]. With a tropospheric lifetime of about 120 days, CH₂Br₂ is classified by the World Meteorological Organization as a very short-lived substance (VSLS), i.e., a trace gas with a local lifetime comparable to or shorter than the tropospheric transport time scale [4]. Despite their short lifetimes, VSLS contribute to the stratospheric bromine burden due to fast vertical transportation mediated by tropical deep convection. With a tropospheric mixing ratio of about 1 ppt [1, 4], with up to 3.5 ppt levels observed in marine upwelling areas [5], CH₂Br₂ may significantly contribute to the so far unidentified source of bromine to the stratosphere [4] as well. So far, the quantitative environmental detection of brominated hydrocarbons is mainly based on gas chromatography/mass spectrometry (GC/MS) techniques that require considerable calibration effort and offer only low sampling frequencies [6, 7, 8].

Fast and sensitive optical detection schemes based on cavity ringdown spectroscopy (CRDS), which has become a very well-established technique with widespread applications in trace gas detection, spectroscopy, and reaction kinetics [9, 10, 11], are expected to overcome these limitations. CRDS has been widely used for the measurements of the high-resolution spectra, however, mid-IR applications are still demanding due to the limited availability of highly reflective mirror coatings and suitable narrow-linewidth light sources. The formerly quite commonly used lead salt diode lasers are difficult to operate and offer a limited tuning range [12, 13]. They have been replaced by the more versatile quantum

cascade lasers (QCLs) and, more recently, interband cascade lasers (ICLs) entered the market [14]. External cavity setups and arrays of QCLs have been introduced in order to extend their frequency coverage [15, 16, 17]. Alternatively, optical parametric oscillators (OPO) and difference frequency generation (DFG) systems based on periodically poled lithium niobate (PPLN) crystals are capable of generating light in the range between 2 - 5 microns. The large tunability, narrow linewidth, and high output power of the modern cw-OPO systems make them ideal for a broad range of applications, including laser cooling of atoms and high-resolution spectroscopy of molecules and ions [18, 19, 20].

Spectroscopic Detection of CH₂Br₂

The implementation of laser based detection schemes for environmental sensing applications of dibromomethane faces several challenges including (*i*) the comparably small mid-IR absorption cross-sections (about three orders of magnitude lower than that of methane), (*ii*) the low atmospheric mixing ratio of CH₂Br₂ (making it difficult to perform interference-free spectral measurements in natural samples), and (*iii*) the complexity of the spectrum (partly due to the near equal isotopic abundance of the two bromine isotopes ⁷⁹Br and ⁸¹Br and the distinct anharmonicities expected for halogenated compounds). As a prerequisite for the selection of a suitable detection frequency (i.e., a preferably strong, spectrally separated, and interference-free absorption line), the high-resolution mid-IR spectrum of CH₂Br₂ needs to be measured and assigned. Surprisingly, high resolution spectroscopic data are only available for the strong ν_8 vibrational band (CH₂ wagging) at wavelengths around 1197 cm⁻¹ as yet. In their work, Brumfield et al. [21, 22] used a quantum cascade laser based continuous wave-(*cw*)-CRDS spectrometer, which was coupled to a supersonic expansion source. Additionally, several earlier microwave and electron diffraction studies of the accurate molecular structure are available. The reported spectroscopic and structural investigations on CH₂Br₂ include highly precise microwave measurements of the internuclear distances corresponding to the hypothetical vibrationless r_e structure, the average nuclear positions at the vibrational ground state (r_z structure), and the electron diffraction data of the so-called r_g structure, which is corresponding to the averaged value of the internuclear distance for a particular temperature [23, 24, 25, 26, 27, 28]. More recently, CH₂Br₂ has been the a subject of several other spectroscopic investigations, in particular UV-VUV spectroscopy [29] and ultrafast photochemical reaction dynamics [30].

Quantum-Chemically Assisted Assignment of Rovibrational Spectra

Spectral assignment and determination of the relevant spectroscopic quantities can often be accomplished in combination with computational tools [31, 32]. On the one hand, a fully quantum mechanical approach such as the second-order vibrational perturbative (VPT2) implementation [33, 34] can yield the required molecular equilibrium geometries together with a set of second, third and semi-diagonal fourth energy derivatives with respect to the normal modes. On the other hand, the relevant spectroscopic quantities can be obtained by fitting the experimentally measured high resolution spectrum based on an effective Hamiltonian, which yields the respective energy levels. For the latter approach, a set of spectroscopic constants for both the ground and excited vibrational states are needed as input parameters for the simulation. Whereas the ground state rotational constants are usually available from microwave measurements [35], in particular the excited state properties often require an initial educated guess or need to be estimated by theoretical means.

Beyond the harmonic-oscillator rigid-rotor approximation, cubic and quartic force constants can be

derived in the context of second-order perturbation theory yielding anharmonicity corrections, Coriolis couplings, and other spectroscopic constants of interest [36]. Although such an approach is in principle straightforward, criteria for a reasonable choice of a suitable electronic structure method and their availability for anharmonic calculations is less clear. Systematic assessments of different electronic structure methods and basis sets with respect to their ability to predict reliable spectroscopic constants are rather scarce. For example, Pawlowski et al. [37] evaluated the accuracy of molecular equilibrium geometries obtained from least squares fits involving experimental rotational constants and calculated vibration-rotation interaction constants. They used HF, MP2, CCSD, and CCSD(T) levels of theory with successively larger correlation-consistent basis sets. Not unexpected, in comparison with experimental values, the uncertainty was smallest for the most sophisticated CCSD(T)/cc-pVQZ calculation. In another example, Krasnoshchekov and Stepanov [38] concluded that corrections for rotational-vibrational interactions are sufficiently accurate on the computationally less demanding B3LYP/cc-pVTZ density functional level of theory to predict a reliable equilibrium geometry of formaldehyde. However, equilibrium structure determinations that require only an accurate sum of the vibration-rotation interaction constants, $\sum_r \alpha_r^B$, may benefit from error compensation. Recently, the sensitivity of vibronic calculations to different density functionals has been studied using the $S_1 \leftarrow S_0$ electronic transition of phenylacetylene as a test case [39]. Compared to the widely-used B3LYP, the long-range-corrected density functionals CAM-B3LYP and LC-B3LYP produced better values for the equilibrium geometry transition moments, but overemphasized the vibronic coupling of some normal modes. B3LYP provided better-balanced vibronic coupling, but poor equilibrium transition moments.

Scope of This Work

This work is aiming at the first measurement of the high-resolution spectrum of the ν_1 (symmetric C-H stretch, around 3013 cm^{-1}) and ν_6 (asymmetric C-H stretch, around 3077 cm^{-1}) vibrational bands as well as the spectral assignment of the better resolved ν_6 band of CH_2Br_2 . A *cw*-CRDS setup with a single resonant optical parametric oscillator, SR-OPO, as a light source has been used for recording the Doppler-limited spectrum. Quantum chemical calculations using different DFT methods (B3LYP, CAM-B3LYP, and M06) and the post-Hartree-Fock MP2 method have been performed in order to predict the state-dependent rotational constants of the vibrationally excited electronic ground state. The second order vibrational perturbative (VPT2) quantum chemistry assisted approach [34] implemented in GAUSSIAN 09 software [40] has been used to obtain initial fitting parameters for the anharmonic rotational constants. In a pragmatic approach, which will be outlined in more detail below, the capability of VPT2 to assist with the quantitative prediction of the rovibrational spectra was tested. For this purpose, the theoretically calculated *change* of the rotational constants upon vibrational excitation was used to derive reliable values for the rotational constants of the vibrationally excited state. To this end, the ability of the different density functionals for the prediction of the excited state rotational constants has been investigated.

5.2 Experimental

5.2.1 Cavity Ringdown Spectrometer

Absorption measurements have been accomplished with a *cw*-CRDS setup equipped with a versatile single-resonant optical parametric oscillator (SR-OPO, Argos Model 2400, Module C, Lockheed Mar-

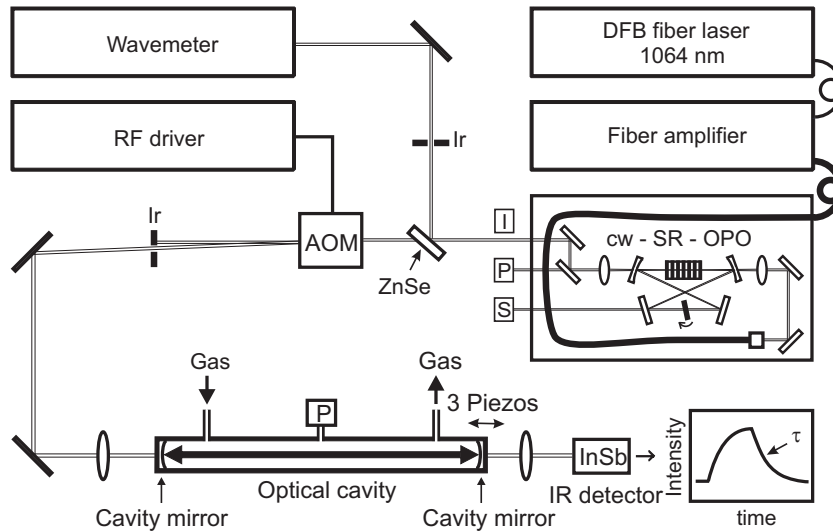


Figure 5.1: Schematic of the Mid-IR-cw-CRD spectrometer. I/P/S: idler/pump/signal beam, Ir: iris diaphragm, P: pressure transducer. Reproduced/Adapted from Ref.[41] with permission from the PCCP Owner Societies.

tin Aculight). The schematic experimental setup, which has been described in detail elsewhere [41], is shown in Fig. 5.1. Briefly, the SR-OPO was capable of generating > 600 mW continuously tunable idler output between 2550 cm^{-1} and 3125 cm^{-1} with an effective linewidth of $< 60\text{ kHz}$ ($< 0.000002\text{ cm}^{-1}$) on a $500\text{ }\mu\text{s}$ timescale and $\sim 1\text{ MHz}$ ($< 0.000033\text{ cm}^{-1}$) on a longer timescale of 80 ms . Three independent wavelength tuning mechanisms have been implemented to scan the frequency of the idler beam: (i) A coarse tuning mechanism in steps of $10 - 20\text{ cm}^{-1}$ by changing the PPLN crystal position; (ii) an intermediate tuning mechanism, resulting from the angle tuning of the intracavity etalon (1 cm^{-1} steps), and (iii) a mode-hop free fine tuning mechanism of the seed laser frequency over $\sim 3\text{ cm}^{-1}$ achieved by using a piezoelectric transducer (PZT) implying a strain on the seed laser fiber. The wavelength was determined with Michelson interferometer type wavemeter (Bristol Instruments; Model 621A-IR) with a specified accuracy of $\pm 0.2\text{ ppm}$ ($\pm 0.0006\text{ cm}^{-1}$, $\pm 18\text{ MHz}$ at $3.3\text{ }\mu\text{m}$) and a repeatability of $\pm 6\text{ MHz}$ at a sampling frequency of 2.5 Hz . The wavelength was calibrated independently by measuring strong absorption features of methane. An agreement with HITRAN database line positions [42] within 0.0009 cm^{-1} was achieved, which is considered as the actual accuracy of the measurements.

The main laser beam passed an acoustic optical modulator (AOM, 20 ns rise time, Gooch & Housego Model MM040-5C11B38-5) acting as a fast optical switch. The deflected first order beam was guided into a commercial quartz-coated stainless steel ringdown cell (CRD Optics) through a collimating lens of 50 cm focal length for approximate mode matching to the TEM_{00} cavity mode. A focal 50 cm in length Fabry-Perot resonator configuration with two 1 m radius of curvature mirrors (CRD Optics) with a reflectivity of 99.99% at $3.3\text{ }\mu\text{m}$ has been used. The cavity resonance condition was achieved by modulating the length of the cavity using piezo elements, resulting in a CRDS repetition frequency of about 30 Hz . The actually measured ringdown time of the empty cavity was about $12.5\text{ }\mu\text{s}$ corresponding to an effective mirror reflectivity of 99.985% and an effective absorption path length of 3.90 km . Finally, the laser light leaking through the rear mirror of the cavity was detected with a liquid nitrogen cooled InSb photodiode/preamplifier combination (SVS-VISTEK, KISDP-2-A-6/KA-05-CI) with a bandwidth of DC- 5 MHz . A comparator circuit was used to trigger the AOM at a preset light level. A home-written LabVIEW code was used to control a high-resolution flexible digitizer (National

Instrument, NI5022) used for recording the individual ringdown signals at a sampling rate of 10 MHz with a vertical resolution of 18 bit. Each recorded ringdown transient consisting of 1100 data points was fitted to a single exponential function by using a nonlinear least-squares fitting algorithm, followed by an averaging of typically 50 ringdown time constants. Simultaneous to the ringdown measurements, the wavelengths of the detection laser was readout from the wavemeter. The detection laser was slowly scanned resulting in a measurement of ~ 10 data points per absorption feature with spectral increments of $\sim 6.4 \times 10^{-4} \text{ cm}^{-1}$.

Analytical grade CH_2Br_2 (99 %, Sigma Aldrich), which has been degassed by several freeze-pump-thaw cycles, was introduced into the cavity equipped with multiple ports to establish a gas flow as well as to monitor the cell pressure (MKS Baratron; Model 622B, 10^{-4} –1 mbar). Typically, a partial pressure of $11.0 \pm 0.5 \text{ } \mu\text{bar}$ CH_2Br_2 has been used at a total pressure of 830 μbar using Argon as the buffer gas. All measurements have been performed at room temperature $T = 295 \pm 1 \text{ K}$.

5.2.2 Computations

The molecular structures and the anharmonic frequency calculations of CH_2Br_2 have been conducted using the GAUSSIAN 09 package [40]. The DFT calculations have been performed with different functionals including the three-parameter hybrid density functional (B3LYP), the CAM-B3LYP long-range corrected three-parameter hybrid density functional by Handy and coworkers [43], and the M06 hybrid meta exchange correlation functionals of Truhlar and Zhao [44]. In addition, second-order Møller-Plesset perturbation calculations, MP2, have been carried out. The 6-311++G(*d,p*) basis set has been used and the effect of using different basis sets on the computed molecular structures has been investigated. The second order vibrational perturbative (VPT2) quantum chemistry assisted approach [33, 34, 45, 46] has been applied to obtain initial fitting parameters for the anharmonic rotational constants and the corresponding vibration-rotation interaction constants. The vibrational dependence of the rotational constants has the general form

$$B_v = B_e - \sum_r [\alpha_r^B (v_r + 1/2)] + \sum_{r \geq s} [\gamma_{rs}^B (v_r + 1/2)(v_s + 1/2)] + \dots, \quad (5.1)$$

where α_r^B and γ_{rs}^B are the rotational-vibrational interaction constants and the summation is over all the normal modes. For asymmetric top molecules, the VPT approach derives α_r^B values according to the formula [47]:

$$\alpha_r^B = -\frac{2B_e^2}{\omega_r} \left[\sum_{\xi} \frac{3(a_r^{b\xi})^2}{4I_{\xi}} + \sum_{r \neq s} (\zeta_{rs}^b)^2 \frac{3\omega_r^2 + \omega_s^2}{\omega_r^2 - \omega_s^2} + \pi \left(\frac{c}{h} \right)^{1/2} \sum_s \Phi_{rrs} a^{bb} \left(\frac{\omega_r}{\omega_s^{3/2}} \right) \right] \quad (5.2)$$

where ω_r are the harmonic frequencies, I_{ξ} are the ξ -th principle moment of inertia at equilibrium geometry, $a_r^{b\xi}$ are the first derivatives of the $I_{b\xi}$ element of the inertia tensor with respect to the normal coordinate Q_r , ζ_{rs}^b are the Coriolis interaction constants coupling Q_r to Q_s through rotation about the axis b , and Φ_{rrs} are the cubic force constants which appear in the expansion of the potential into a series of dimensionless normal coordinates. The first term of the rotational-vibrational perturbation formula accounts for the contribution from the moment of inertia correction related to the displacement

along Q_r , the second term is due to the Coriolis interaction between ω_r and ω_s , and the third term is the anharmonic correction related to the change in Q_s resulting from the displacement of Q_r .

The VPT2 GAUSSIAN routine was available for *ab initio* methods with analytic second derivatives (HF, DFT, CIS and MP2) only. Spectral simulation and of the rovibrational structures of the ν_1 and ν_6 vibration bands of the asymmetric top CH_2Br_2 molecule have been performed using the spectral simulation and assignment software PGOPHER from C. M. Western [48]. The PGOPHER input file is available as a Supporting Information.

5.3 Results and Discussion

5.3.1 Absorption Saturation

While the principles of CRDS for recording absorption spectra are straightforward, care has to be taken to measure in the linear absorption regime. As the light intensity enhancement in optical resonators may easily cause optical saturation of the sample [49, 50], the experimental conditions need to be properly chosen to minimize saturation effects in the recorded spectra. In a standard linear CRD absorption experiment, the absorption of the sample is deduced from the differences of the ringdown time constants k or the corresponding ringdown times $\tau = 1/k$ measured without (empty cavity ringdown time τ_0) and with absorbing species present in the cavity (τ). The corresponding τ -values are directly determined from the single-exponential ringdown signals observed after switching-off the exciting laser beam by the optical switch. The non-saturated absorption coefficient $\alpha_0(\tilde{\nu})$ in units of cm^{-1} is determined according to

$$\alpha_0(\tilde{\nu}) = \frac{1}{c} \left(\frac{1}{\tau(\tilde{\nu})} - \frac{1}{\tau_0(\tilde{\nu})} \right) \quad (5.3)$$

with $\tau_0 = L/(c(1 - R))$. c is the speed of light, L the ringdown mirror separation, and R the effective mirror reflectivity. The CRD spectrum is typically obtained by scanning the detection laser frequency over the absorption feature and $\tau_0(\tilde{\nu})$ is deduced from a baseline fitting procedure. In cases with strongly overlapping absorption features, as it is the case for CH_2Br_2 , baseline fitting is often not accurate and the empty cavity background signal needs be recorded in a separate experiment.

Saturation underestimates the measured gas absorption decay rate and, first of all, causes non-exponential ringdown curves. This is due to the subtle interplay of decaying light intensity (going along with a decreasing pumping rate of the ground state) and the excited state relaxation mediated by molecular collisions. We have recently thoroughly studied the related saturation dynamics which control the general shape of the decay transients [41]. In principle, within the so-called Sat-CRDS approach, saturation effects can be accounted for and procedures have been developed to extract reliable absorption coefficients from saturated ringdown signals [50, 41]. However, from a practical point of view, the statement that saturation should be avoided for the measurement of comprehensive overview spectra still holds.

Fig. 5.2 presents the measured absorption coefficient at the top of a strong absorption line of CH_2Br_2 ($\tilde{\nu} = 3003.74 \text{ cm}^{-1}$) as a function of the overall cell pressure, which was controlled by adding Argon. The initial intracavity light intensity was kept low (about 39 mW initial light power within the cavity), but high enough to ensure a good signal-to-noise ratio. As shown in Fig. 5.2, the measured absorption coefficient α increases with adding buffer gas until it levels off at cell pressures $\geq 300 \mu\text{bar}$ reaching a

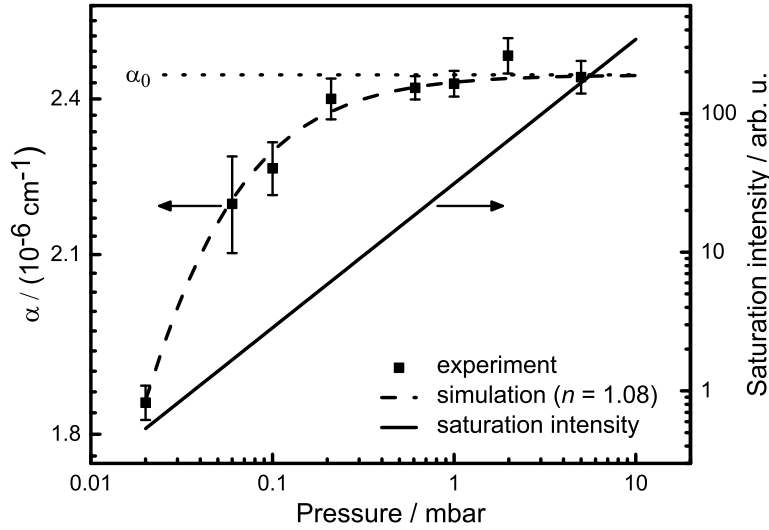


Figure 5.2: Experimental absorption coefficients (symbols) as a function of the total cell pressure (10 μ bar CH_2Br_2 in Argon). Fitted absorption coefficient (dashed curve) and corresponding trend of the saturation intensity (solid line) according to Eq. 5.4.

value corresponding to the non-saturated absorption coefficient α_0 . The dropping α value at too low pressures clearly indicates the onset of saturation, whereas at higher pressures the collisional relaxation is fast enough to avoid any saturation effect. For an inhomogeneously broadened absorption line, the saturation of α can be expressed as

$$\alpha(\tilde{\nu}) = \frac{\alpha_0(\tilde{\nu})}{\sqrt{1 + I_0/I_S}}. \quad (5.4)$$

I_S is the saturation intensity that is proportional to the pressure according to $I_S = a \times p^n$. Here, the constant a is a parameter, which is proportional to the absorption probability of the transition. By fitting the experimental data (dashed curve in Fig. 5.2), a pressure exponent of $n = 1.04$ was obtained, hence very close to the value of $n = 1.08$ obtained for a CH_4 line analyzed in our previous work [41]. Note that $I_S \propto p^2$ is expected for a collision dominated relaxation process, however, at too low pressures diffusion and transit-time become effective causing n to drop to lower values [41].

More important for the sake of this study is that non-saturated measurements are possible at total pressures where collisional broadening effects are still negligible. All absorption spectra presented in this work have been measured at $p = 830 \mu\text{bar}$ where typical pressure broadening coefficients are about $1.8 \times 10^{-4} \text{ cm}^{-1} (2\gamma)$ [42]. The FWHM Doppler broadening of $2.79 \times 10^{-3} \text{ cm}^{-1}$ is much larger, hence nearly Doppler-limited resolved spectra with expected Voigt line widths only 3.5% broader than the Doppler limit are measured. Note that the additional distortion due to the slow scanning of the detection laser during spectrum acquisition is negligible as well. Overall, the convoluted line profile including pressure broadening and a $6.4 \times 10^{-4} \text{ cm}^{-1}$ boxcar convolution that accounts for the low scanning results in 4.6% line broadening with an effective line width of $2.91 \times 10^{-3} \text{ cm}^{-1}$.

5.3.2 High-Resolution Spectrum

The ν_1 and ν_6 bands of methylene bromide have been recorded from 2955 to 3086 cm^{-1} . The high-resolution spectrum in Fig. 5.3 (black curve) is reported in terms of the narrow bandwidth absorption cross-section $\sigma = \alpha/[c]$. It is composed of 85 individual spectral scans with 2.0 - 4.0 cm^{-1} width. These

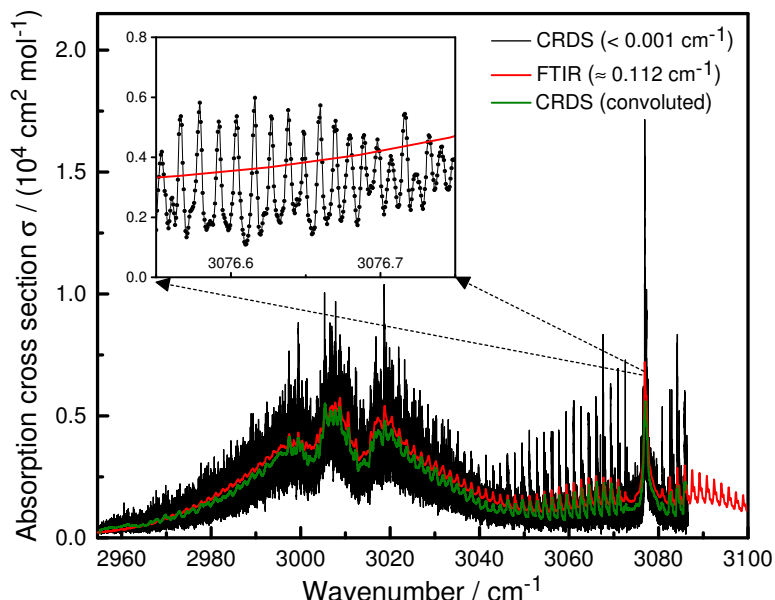


Figure 5.3: High-resolution absorption spectrum of the ν_1 and ν_6 vibrational band of CH_2Br_2 (black) in comparison with the boxcar (0.48 cm^{-1}) convoluted (green) and low resolution FTIR spectrum adopted from PNNL database (red, 0.112 cm^{-1} instrumental resolution) [51]. The inset highlights a small part of the spectrum to visualize the Doppler-limited resolution of the line-rich spectrum.

scans were independently collected and corrected for the empty cavity signal. Within noise level, a perfect overlap of the peak positions and intensities of the individual spectral scans has been obtained. The original spectrum as well as a processed version with an evenly spaced wavenumber increment is available as a Supporting Information.

The noise level of the spectrum can be estimated based on the corresponding empty cavity measurements. For a single-shot decay constant measurement, a standard deviation of $\sigma(k) = \pm 1.5 \times 10^{-3} \mu\text{s}^{-1}$ has been observed, which corresponds to a minimum detectable absorption coefficient of $\alpha_{\min} = 4.9 \times 10^{-8} \text{ cm}^{-1}$. With a typical repetition frequency of $f_{\text{rep}} = 25 \text{ Hz}$, the noise equivalent absorption becomes $\text{NEA} = \alpha_{\min} / \sqrt{f_{\text{rep}}} = 9.8 \times 10^{-9} \text{ cm}^{-1} \text{ Hz}^{-1/2}$. Each point in the spectrum shown in Fig. 5.3 corresponds to an average of about 50 ringdown events. Therefore, with a 2σ noise floor of about $3.8 \times 10^{-9} \text{ cm}^{-1}$, the highest peak in the spectrum at 3076.898 cm^{-1} exhibits a signal-to-noise ratio of $S/N = 2060$, hence demonstrating the wide dynamic range of the spectral measurement.

For direct comparison with a low resolution FTIR spectrum adopted from the PNNL database [51] (red colored spectrum in Fig. 5.3; 0.112 cm^{-1} instrumental resolution), the high-resolution spectrum has been convoluted (green colored spectrum) using an appropriate boxcar width. Both the overall band contours and the absolute values of the absorption cross-sections are in a very good agreement with the PNNL data. We attribute the slight remaining systematic deviations to residual baseline uncertainties in the FTIR data set.

The inset in Fig. 5.3 illustrates a small part of the spectrum to visualize the line-rich spectrum with near Doppler-limited resolution. The standard FTIR spectrum cannot resolve the underlying rotational structure at all. However, due to the complexity of the spectrum with many overlapping lines and contributions from the three different CH_2Br_2 isotopologues, the identification of single absorption lines remains difficult. Even in better resolved parts of the CRD spectrum such as the one shown in the inset of Fig. 5.3, the observed distinct peaks may exhibit contributions from a number of underlying absorption lines. This can be deduced from a multi-peak fitting analysis of the spectrum yielding peak widths

of about $3.2 \times 10^{-3} \text{ cm}^{-1}$ (FWHM), which is significantly broader than the expected $2.9 \times 10^{-3} \text{ cm}^{-1}$ effective line width of a well-separated absorption peak (vide supra). Consequently, a rigorous assignment of the spectra has to be based on a full spectral simulation as presented below. Note that the spectral assignment and line shape analysis may be further complicated by significant hyperfine splittings due to the presence of the nuclear quadrupole moments of the two bromine atoms. For $J'' > 1$ transitions, the 16 hyperfine components resemble a triplet pattern with the center peak appearing close to the underlying main transition with a wavenumber spread of up to $1.5 \times 10^{-3} \text{ cm}^{-1}$ [52, 28, 22]. Consequently, hyperfine splitting is not expected to be fully resolved in the room temperature spectrum measured in this work, but should become noticeable as an (asymmetric) line broadening effect. As we have not found convincing evidence for this effect, we did not take into account hyperfine splitting for further spectral analysis.

5.3.3 Computational Results

The main objective of performing the anharmonic frequency calculations was to provide a good prediction for the state-dependent rotational constants of the vibrationally excited states. In this section, the predicted molecular structure and anharmonic (fundamental) frequencies are compared with literature data. In addition, the calculated anharmonic rotational constants that serve as input for the spectral simulations are presented. It can be anticipated that the electronic structure method and basis set that predict more accurately the molecular structure, in particular the C-H bond length and the $\angle(\text{HCH})$ bond angle, will give a good prediction for the rotational structure of the symmetric ν_1 and asymmetric ν_6 C-H vibrational band.

Molecular Structures

The optimized bond lengths, bond angles, and resulting dipole moments of $\text{CH}_2^{79}\text{Br}^{81}\text{Br}$ together with experimental microwave and electron diffraction data [23, 24, 25, 26, 27] are listed in Table 5.1. The computational data refer to the r_e equilibrium structure and hence are best compared with the corresponding microwave structure of Davis and Gerry [27].

The B3LYP and CAM-B3LYP model chemistries slightly underestimate the C-H bond length by (0.0017-0.0023) Å, while the C-Br bond length is significantly overestimated by 0.0187 Å using B3LYP, but not CAM-B3LYP. Good agreement was also found for the experimental $\angle(\text{HCBBr})$ and $\angle(\text{HCH})$ bond angles, while the $\angle(\text{BrCBr})$ bond angle is overestimated by more than 1° in both cases. A comparison of B3LYP with CAM-B3LYP reveals that the long-range correction does not produce significantly better molecular parameters. The density functional M06 predicts well the C-H and the C-Br bond lengths as well as the $\angle(\text{HCBBr})$ bond angle, however, it slightly underestimates the important $\angle(\text{HCH})$ bond angle by 1.14° . Nevertheless, the very similar M06 and MP2 data yield an overall better agreement with the microwave data than the B3LYP and CAM-B3LYP functionals. The same holds for the predicted dipole moment of about 1.5 D, which is in good agreement with the experimental value of 1.489 D.

The molecular structure data can be further compared with the previous results of systematic DFT, MP2, and CCSD(T) calculations on the molecular structures of bromomethanes performed by Venkatraman et al. [53]. They used a larger basis set regarding polarization functions, 6-311G(2d,2p), but did not add diffuse functions. For dibromomethane, other than the data listed in Table 5.1, they have

Table 5.1: Molecular structures of ground state $\text{CH}_2^{79}\text{Br}^{81}\text{Br}$, calculated at different levels of theory using the 6-311++G(d,p) basis set, in comparison with experimental data.

	B3LYP	CAM-B3LYP	M06	MP2	Experimental			
	this work				MW ^a , r_e	MW ^b , r_z	MW ^c	ED ^d , r_g
$r(\text{CH}) / \text{\AA}$	1.0828	1.0822	1.0867	1.0860	1.0845	1.0872(38)	1.097(5)	1.08(4)
$r(\text{CBr}) / \text{\AA}$	1.9512	1.9323	1.9302	1.9298	1.9325	1.9291(8)	1.929(2)	1.921(2)
$\angle(\text{HCH}) / ^\circ$	112.45	111.78	111.29	111.54	112.43	112.64(7)	110.9(8)	108
$\angle(\text{HCB}) / ^\circ$	107.52	107.76	107.95	107.83	109(2)	107.84		
$\angle(\text{BrCB}) / ^\circ$	114.42	114.10	113.79	114.03	112.64	112.43(55)	112.9(2)	113.2(4)
μ / D	1.608	1.628	1.434	1.543	1.489			

^a Equilibrium structure based on microwave measurements [27].

^b Ground state average structure based on microwave measurements [27].

^c Preferred microwave structure based on $r(\text{CH}) = 1.097(5)\text{\AA}$ [25, 26].

^d Based on electron diffraction measurements [24].

performed calculations on the $\text{CH}_2^{79}\text{Br}_2$ isotopologue. However, the molecular structural changes are almost negligible between the three isotopologues of CH_2Br_2 (see supplemental Table 5.S2). Interestingly, all their calculation yielded too short CH bond lengths of (1.0765-1.0789) \AA , with deviations of (0.0055-0.0080) \AA from the literature values. This deviation is significantly larger than that obtained in our calculations. However, we also performed calculations using 6-311G(d,p) and 6-311++G(d,p) as well as 6-311G(2d,2p) and 6-311++G(2d,2p) revealing that the addition of diffuse functions does not significantly change the CH bond length. In both cases, the DFT(B3LYP) calculations with and without diffuse functions yielded coinciding CH bond lengths within 0.0001 \AA . Hence, the too short CH bond lengths resulting from the addition of the (2d,2p) polarization functions has to be attributed to a subtle basis set effect. Actually, Venkatraman et al. also investigated the effect of the inclusion of additional f polarization function and found moderate improvement of the predicted molecular structure; but in all cases their calculated CH bond lengths remained too low. We conclude, for the purpose of this study, that the M06/6-311++G(d,p) model chemistry turns out to be the best choice in terms of molecular structure prediction and computational cost.

Anharmonic Vibrational Constants

Instead of relying on the widely used scaling factors for harmonic vibrational frequencies [54], anharmonic calculations make possible a direct prediction of the experimentally observed vibration frequency including combination and overtone bands. However, even with very sophisticated theoretical treatments, the accuracy of anharmonic vibrational constants is often limited to a few cm^{-1} [55]. Table 5.2 lists the calculated (M06/6-311++G(d,p) level of theory) harmonic, anharmonic, scaled-harmonic (scaling factor of 0.979 [56]), and experimental values for the ν_1 and ν_6 vibration of the $\text{CH}_2^{79}\text{Br}^{81}\text{Br}$ isotopologue. A complete list of vibrational frequencies can be found in the Supporting Information Table 5.S1. Although the calculated anharmonic vibrational frequencies show the closest agreement with the experiment, their absolute values are still off by a few cm^{-1} . Therefore, the vibrational constants were treated as adjustable parameters in the spectral fitting of the high-resolution rovibrational spectra. An intuitive starting value could be quickly obtained by simply shifting the band origin of the simulated spectrum to give a good match with the band contours of the experimental spectrum. It should be noted that the calculations for the different isotopologues captured the trend of the isotopic shift of the vibration frequencies (i.e., $\tilde{\nu}(\text{CH}_2^{79}\text{Br}_2) > \tilde{\nu}(\text{CH}_2^{79}\text{Br}^{81}\text{Br}) > \tilde{\nu}(\text{CH}_2^{81}\text{Br}_2)$), but the absolute values of the isotopic shifts were much smaller than deduced from the fitted values.

Table 5.2: Calculated harmonic, scaled-harmonic, and anharmonic vibrational frequencies (in cm^{-1}) at M06/6-311++G(d,p) level of theory together with the experimental values for the ν_1 and ν_6 vibrational bands of $\text{CH}_2^{79}\text{Br}^{81}\text{Br}$.

	Harmonic	Scaled-harmonic	Anharmonic	Experimental	
		this work ^a		this work ^b	Ref. [57]
ν_1	3105.407	3040.193	3001.024	3013.026	3009 ± 6
ν_6	3190.912	3123.903	3074.866	3077.126	3073 ± 3

^a A scaling factor of 0.979 has been adopted from the M06-2x/6-311++G(d,p) study in Ref. [56].

^b Experimental fit.

For example, the calculated isotopic shift for $\tilde{\nu}_6(\text{CH}_2^{81}\text{Br}_2)$ was only about 0.007 cm^{-1} , whereas a value of 0.395 cm^{-1} was deduced from the experiment. However, for other vibrations that involve bromine atom motion, a larger isotopic shift up to 2.0 cm^{-1} was predicted.

State-Dependent Rotational Constants

Although the differences in the rotational constants between vibrational ground and excited states are small, they have a pronounced effect on the spectrum simulations. Table 5.3 lists the values of the computed rotational constants of the vibrational ground state, $\nu(v=0)$, and excited state, $\nu(v=1)$, for the ν_1 and ν_6 vibrations of $\text{CH}_2^{81}\text{Br}_2$ calculated at different levels of theory. The corresponding values for the $\text{CH}_2^{79}\text{Br}^{81}\text{Br}$ and $\text{CH}_2^{79}\text{Br}_2$ isotopologues are reported in Tables 5.S3 and 5.S4 of the supporting material. The differences in the rotational constants $\Delta_i(X) = X(\nu_i(v=1)) - X(\nu_i(v=0))$ ($X = A, B, C$) represent the structural changes upon vibrational excitation. For the sake of clarity, Fig. 5.4 illustrates the displacement vectors (black arrows), and the direction of the dipole moment vectors (yellow vectors) corresponding to the symmetric (a symmetry) and asymmetric (b symmetry) C-H stretch motions. Here, the principal inertial axes a , b , and c correspond to the rotational constants A , B , and C and the y -, z -, and x -axes. The y -axis lies in the plane of the molecule that contains the two bromine atoms, the z -axis goes through the C atom and intersects the $\angle(\text{HCH})$ angle, and the x -axis lies in the perpendicular molecular plane containing the two hydrogen atoms.

As it can be seen from the data in Table 5.3, the most significant effect of vibrational excitation is the predicted decrease of the rotational constant A . It goes along with a slight increase of the rotational constants B and C . For ν_1 , the relative change of A is about four times the relative change of B and C , whereas for ν_6 the relative changes are about the same for all three rotational constants. Taking the B3LYP calculation as an example, $\Delta_1(A) = -2.41 \times 10^{-3} \text{ cm}^{-1}$ indicates an elongation of the molecule along the z -axis, consistent with the vibrational excitation of the symmetric C-H stretch. For the asymmetric C-H vibration, the contribution resulting from the moment of inertia correction term is expected to be small due to symmetry reasons, however, the effect of vibrational excitation on A is still pronounced. Hence, the Coriolis interaction and the anharmonic correction terms in Eq. 5.2 play important roles as well.

Finally, the calculated ground state rotational constants are compared with the most recent vibrational ground state microwave data from Davis and Gerry [27] who reported $A = 0.86675642 \text{ cm}^{-1}$, $B = 0.040297341 \text{ cm}^{-1}$, and $C = 0.038782329 \text{ cm}^{-1}$ for $\text{CH}_2^{81}\text{Br}_2$ isotopologue. For all model chemistries, the predicted A value is slightly too high by $(6.5 \times 10^{-3} - 1.4 \times 10^{-2}) \text{ cm}^{-1}$ and B and C values are slightly too low by $(7.6 \times 10^{-4} - 1.9 \times 10^{-3}) \text{ cm}^{-1}$. Again, the M06 density functional yields the overall best agreement. Although the remaining discrepancies are small, they still result in distinct deviations

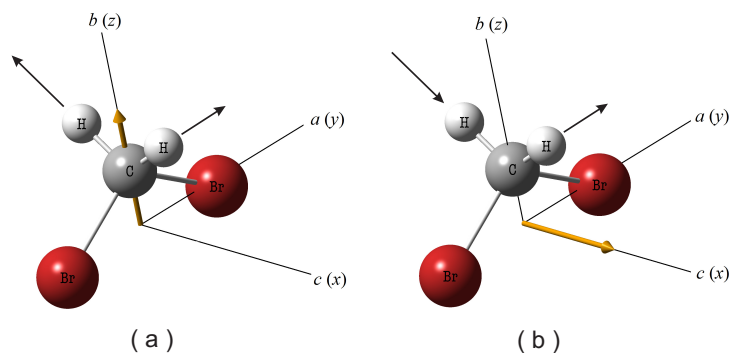


Figure 5.4: Molecular structure of CH_2Br_2 . The black and yellow arrows represent the displacement vectors and the direction of the transition dipole moment, respectively, as a result of the symmetric (a) and asymmetric (b) C-H vibration.

Table 5.3: Anharmonic rotational constants of $\text{CH}_2^{81}\text{Br}_2$ in its vibrational ground $\nu(v=0)$ and first excited state $\nu(v=1)$ of ν_1 and ν_6 . All values are given in units of cm^{-1} as calculated at different levels of theory using the 6-311++G(d,p) basis set.

	$\nu_i(v=0)$	$\nu_i(v=1)$	$\Delta_i/10^{-5}{}^a$	$\nu_1^{\text{exp}}(v=0){}^b$	$\bar{\nu}_1(v=1){}^c$	$\nu_6(v=1)$	$\Delta_6/10^{-5}{}^a$	$\bar{\nu}_6(v=1)$
B3LYP								
A	0.873289	0.870878	-241.1	0.86675642(56)	0.8643454	0.872351	-94.0	0.8658184
B	0.038364	0.038391	2.7	0.040297341(27)	0.0403243	0.038406	4.2	0.0403393
C	0.037001	0.037026	2.5	0.038782329(30)	0.0388073	0.037039	3.8	0.0388203
CAM-B3LYP								
A	0.880943	0.878589	-235.4	0.86675642(56)	0.8644024	0.880019	-92.8	0.8658324
B	0.039277	0.039298	2.1	0.040297341(27)	0.0403183	0.039307	3.0	0.0403273
C	0.037861	0.037881	2.0	0.038782329(30)	0.0388023	0.037889	2.8	0.0388103
M06								
A	0.874976	0.872692	-228.4	0.86675642(56)	0.8644724	0.874221	-75.5	0.8660014
B	0.039532	0.039549	1.7	0.040297341(27)	0.0403143	0.039556	2.4	0.0403213
C	0.038088	0.038103	1.5	0.038782329(87)	0.0392687	0.038110	2.2	0.0388043
MP2								
A	0.880562	0.878321	-224.1	0.86675642(56)	0.8645154	0.879511	-105.1	0.8657054
B	0.039427	0.039438	1.1	0.040297341(27)	0.0403083	0.039448	2.1	0.0403183
C	0.038002	0.038012	1.0	0.038782329(30)	0.0387923	0.038021	1.9	0.0388013

^a $\Delta_i = X(\nu_i(v=1)) - X(\nu_i(v=0))$ (with $X = A, B, C$).

^b Vibrational ground state data of Davis and Gerry [27].

^c $X(\bar{\nu}_i(v=1)) = X^{\text{exp}}(\nu_i(v=0)) + \Delta_i$ (with $X = A, B, C$).

of the calculated rovibrational spectra (vide infra). As it can be expected that the calculated *change* in the rotational constants going from ($v=0$) to ($v=1$) is less susceptible to subtle structural differences, it can be used as a more reliable estimate to predict the rotational constants of the vibrationally excited molecule based on the experimental ($v=0$) data. Corresponding values, for instance $X(\bar{\nu}_i(v=1)) = X^{\text{exp}}(\nu_i(v=0)) + \Delta_i$ (with $X = A, B, C$), are listed in Table 5.3 as well.

5.3.4 Spectrum Simulation

The spectrum simulations and assignments were carried out using the reduced form (I^r representation) of the asymmetric top Hamiltonian as proposed by Watson [58] and as implemented in PGOPHER. Although the microwave analysis of Davis and Gerry [27] showed that the correlations between the corresponding A - and S -reduction parameters were nearly identical, the choice of the reduction for each isotopologue was in fact governed by the availability of the corresponding ground state constants provided by the microwave studies. The ground state rotational constants and centrifugal distortion constants of $\text{CH}_2^{79}\text{Br}_2$ and $\text{CH}_2^{81}\text{Br}_2$ isotopologues have been adopted from the microwave measure-

ments of Davis and Gerry [27] (*A*-reduction), while for $\text{CH}_2^{79}\text{Br}^{81}\text{Br}$ isotopologue they were taken from the microwave measurement of Niide et al [28] (*S*-reduction).

Fig. 5.5 illustrates the sensitivity of the simulated spectra to both the rotational constants and the centrifugal distortion constants by comparing the general shape and the rotational fine structures of the simulated spectra with that of the experiment. Trace (a) is the experimental spectrum, while (b), (c), and (d) resemble the simulated spectra using different sets of the rotational and centrifugal distortion constants. Simulation (b) has been performed with the ground state rotational and centrifugal distortion constants from the microwave data, whereas the excited state rotational constants were derived from the *change* of the quantum-chemically predicted rotational constants as outline in the preceding Section (M06 model chemistry, $X(\bar{\nu}_i(v=1))$ in Table 5.3). The centrifugal distortion constants were initialized by their ground state values from microwave measurements. Simulation (c) uses the same set of rotational constants but the centrifugal distortion constants were adopted from the results of the quantum chemical calculations. Simulation (d) is based on the set of *absolute* values for both the rotational and centrifugal constants directly taken from the calculation. In all three simulations the band origins have been set to our final fitting results to allow for direct comparison with the experiment. Obviously, both cases (b) and (c) yield a good approximation of the overall rotational band structure whereas simulation (d) fails to reproduce the experiment. This highlights the fact that, on the one hand, a direct prediction of the rotational structure based on spectroscopic constants derived from conventional VPT2 calculations alone is not yet sufficiently accurate. On the other hand, the estimation of the spectroscopic constants of the excited state based on the *change* of the rotational constants predicted by VPT2 yields remarkably good results. Of course, when expanding parts of the spectrum, residual discrepancies arising from the uncertainties of the assumed anharmonic rotational constants and of the not yet tuned centrifugal distortion constants of the excited state become apparent. Nevertheless, taking up the motivation of this work to assess the potential of quantum-chemical assisted development of environmental sensors for halocarbon detection, the achieved agreement with the high-resolution spectrum is already very satisfying. In particular this holds true for the well resolved rotational features of the ν_6 band. Provided that the respective band origins are known with sufficient precision from lower resolution spectra, the rotationally resolved prediction is good enough to guide a first selection of a suitable spectral window for selective halocarbon detection.

5.3.5 Spectrum Assignment

In this section, a more detailed analysis of the asymmetric C-H stretch band is presented. CH_2Br_2 exhibits C_{2v} symmetry and it is a near-prolate top molecule with an asymmetry parameter of -0.996 . From its nine fundamental vibrational modes four modes have A_1 , one A_2 , two B_1 , and two B_2 symmetry. The asymmetric C-H stretch motion, ν_6 , exhibits B_1 symmetry resulting in a change in the dipole moment along the molecular *c*-axis, while the symmetric C-H stretch motion, ν_1 , has A_1 symmetry with a change in the dipole moment along the molecular *b*-axis. Considering the symmetry of the two motions, a Coriolis coupling between them is allowed and expected to be rather strong since the band origins are separated by only about 64 cm^{-1} .

The asymmetric C-H vibration gives rise to a perpendicular *c*-type transition with a band shape dominated by a series of strong and sharp features corresponding to Q sub-branch transitions. Panel (a) of Fig. 5.6 illustrates simulated spectra of the ν_6 band for the three isotopologues ($\text{CH}_2^{81}\text{Br}_2$ (magenta), $\text{CH}_2^{81}\text{Br}^{79}\text{Br}$ (blue), and $\text{CH}_2^{79}\text{Br}_2$ (green)) and the sum of those (red) together with the measured spec-

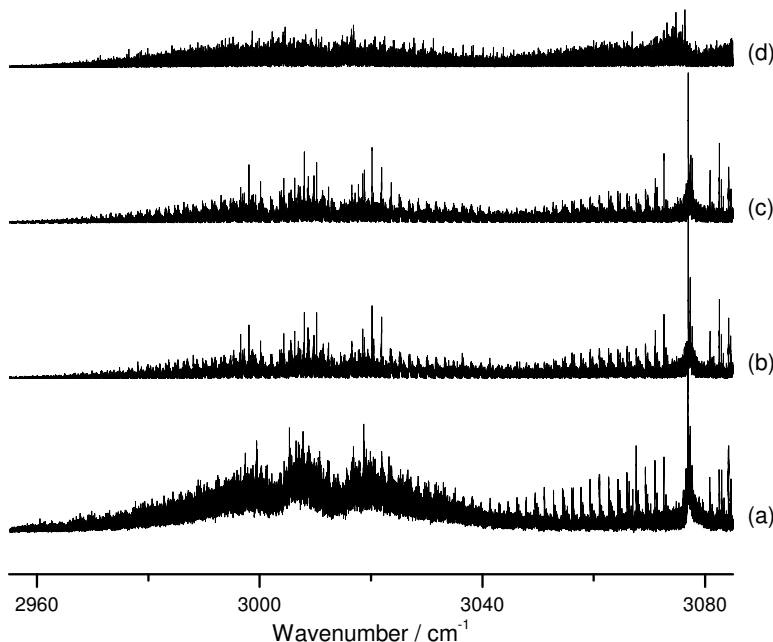


Figure 5.5: Measured spectrum (a) in comparison with simulated spectra without spectroscopic parameter adjustment. (b) Simulation using excited state rotational constants $X(\bar{\nu}_i(v=1))$ (see text and Table 5.3) and microwave ground state centrifugal distortion constants; (c) simulation using $X(\bar{\nu}_i(v=1))$ rotational constants and calculated VPT2 centrifugal distortion constants; (d) simulation using absolute values of the VPT2 rotational and centrifugal distortion constants.

trum (black). A relative transition dipole moment ratio $\text{CH}_2^{81}\text{Br}_2$: $\text{CH}_2^{81}\text{Br}^{79}\text{Br}$: $\text{CH}_2^{79}\text{Br}_2$ of 1.45:1:1 was chosen in order to reproduce the experimentally observed progression intensities of the Q sub-branches. In accordance with the typical trend observed for isotopic substitution, the middle progression was assigned to the mixed $\text{CH}_2^{81}\text{Br}^{79}\text{Br}$ isotopologue, while $\text{CH}_2^{81}\text{Br}_2$ and $\text{CH}_2^{79}\text{Br}_2$ were assigned to the red and blue shifted progressions, respectively. As the abundances of the three isotopologues (1:2:1) have been separately taken into account and as the overall structural changes between the three isotopologues are small, the expected transition dipole moment ratio is about 1:1:1 instead of the 1.45:1:1 ratio reported here. Note that simply turning over the assignments for $\text{CH}_2^{81}\text{Br}_2$ and $\text{CH}_2^{81}\text{Br}^{79}\text{Br}$, yielding a ratio of 1.05:0.707:1, would not resolve this issue. Actually, different transition dipole moments for the same vibrational band of different isotopologues have been reported for molecules with pronounced anharmonicities in several cases. For example, Milloud et al.[59] observed a ratio of 1.03:1.0:1.29:1.26 for the $6\nu_3$ overtone band of the $^{14}\text{N}^{14}\text{N}^{16}\text{O}$: $^{15}\text{N}^{15}\text{N}^{16}\text{O}$: $^{14}\text{N}^{15}\text{N}^{16}\text{O}$: $^{15}\text{N}^{14}\text{N}^{16}\text{O}$ isotopologues. An even stronger effect with transition dipole moment ratios of 1.02 – 2.28 has been found for several stretching vibration transitions of $^{35}\text{ClH}^{35}\text{Cl}^-$ and $^{35}\text{ClD}^{35}\text{Cl}^-$ [60]. Further spectroscopic investigation is needed to work out an exclusive explanation for this interesting finding, which may be due to subtle anharmonic, Coriolis coupling, or other effects.

Each progression in Fig. 5.6 consists of clusters of ${}^{p/r}Q_{K_a}(J)$ transitions. These clusters are evenly spaced and separated by approximately $2(A - \bar{B}) = 1.65 \text{ cm}^{-1}$, where $\bar{B} = (B + C)/2$. The strong feature around 3077 cm^{-1} evolves from the strong overlap of several transitions with $K_a = 0, 1, 2$. Panels b and c in Fig. 5.6 show two enlarged spectral windows around 3077 cm^{-1} and 3054 cm^{-1} . Each single, blue-shaded sub-branch feature is composed of a series of tightly packed partially resolved transitions resulting from increasing J with $\Delta K_c = 0, \pm 2$.

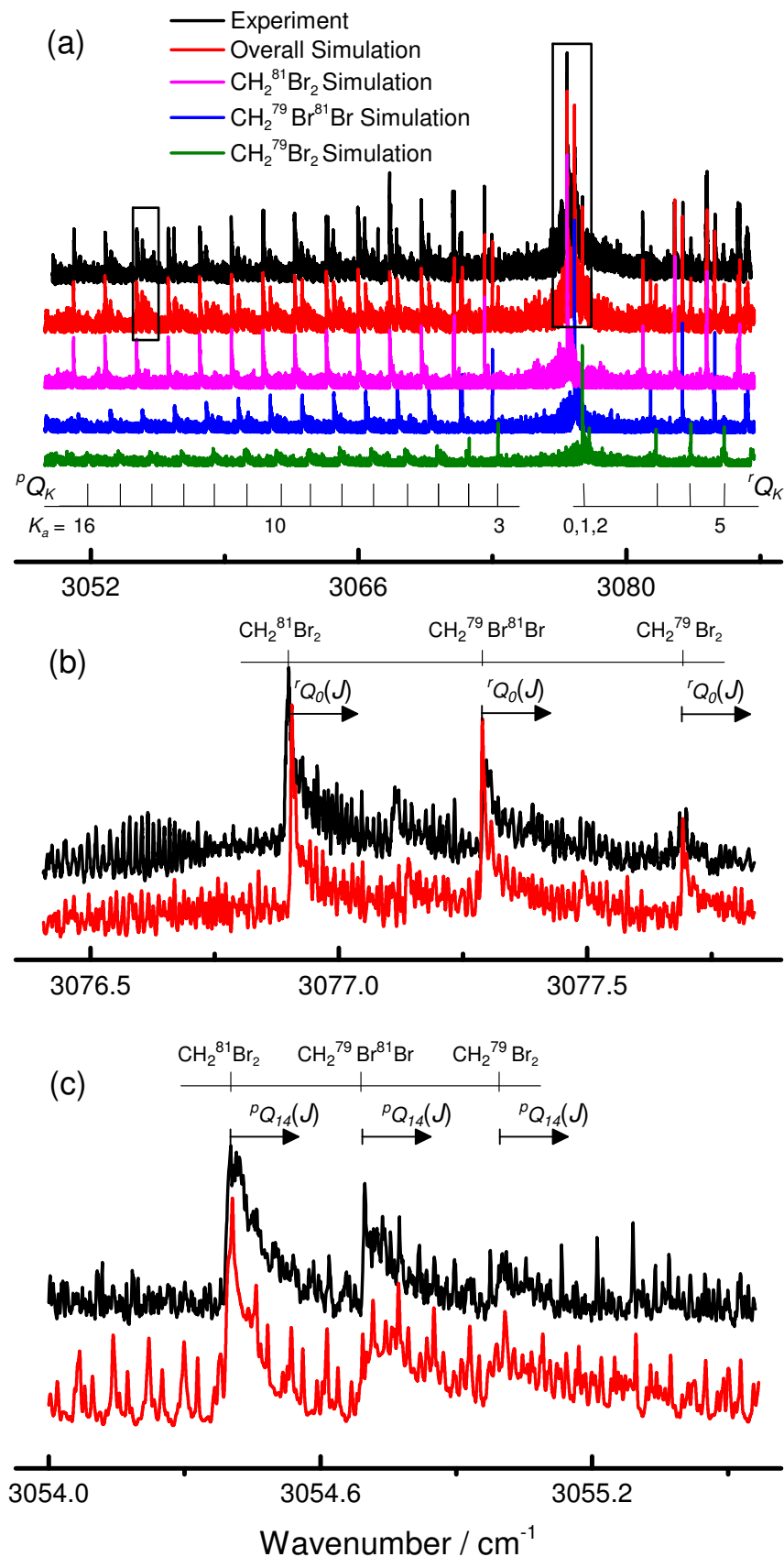


Figure 5.6: Comparison of the measured (black spectrum) and simulated (red) asymmetric C-H band of CH_2Br_2 using the final fitted rotational constants presented in Tables 5.4 and 5.5. The overall simulated spectrum is the sum of the individual spectra of the three isotopologues ($\text{CH}_2^{81}\text{Br}_2$ (magenta), $\text{CH}_2^{81}\text{Br}^{79}\text{Br}$ (blue), and $\text{CH}_2^{79}\text{Br}_2$ (green)). The middle and the lower panels show the enlargements of the outlined spectral sections indicated in the upper panel. For a better visualization, the individual spectra were offset.

Table 5.4: Band origin and rotational constants of the ν_6 band of $\text{CH}_2^{79}\text{Br}^{81}\text{Br}$. Values in parantheses denote the fit parameter uncertainties on a 1σ confidence level. All values are given in units of cm^{-1} .

$\text{CH}_2^{79}\text{Br}^{81}\text{Br}$		
	$v = 0$	$v = 1$
	Niide et al. [28]	this work
ν_0		3077.125726(94)
A	0.86751916(86)	0.86649338(340)
B	0.040804716(73)	0.04082770(5)
C	0.039253679(87)	0.03927221(5)
$D_K \times 10^5$	1.3694 ^a	
$D_{KJ} \times 10^7$	-3.81(16)	
$D_J \times 10^9$	7.75(25)	
$d_1 \times 10^{10}$	-6.44(90)	
$d_2 \times 10^9$	-1.03(1.03)	

^a D_K has been adopted from our M06/6-311++G(d,p) calculations.

 Table 5.5: Band origin and rotational constants of the ν_6 band of $\text{CH}_2^{81}\text{Br}_2$ and $\text{CH}_2^{79}\text{Br}_2$. Values in parantheses denote the fit parameter uncertainties on a 1σ confidence level. All values are given in units of cm^{-1} .

	$\text{CH}_2^{81}\text{Br}_2$		$\text{CH}_2^{79}\text{Br}_2$	
	$v = 0$	$v = 1$	$v = 0$	$v = 1$
	Davis and Gerry [27]	this work	Davis and Gerry [27]	this work
ν_0		3076.730548(83)		3077.405453(480)
A	0.86675642(56)	0.86594956(160)	0.8683441(13)	0.8675719(110)
B	0.040297341(27)	0.04031873(4)	0.041313137(47)	0.0413626(4)
C	0.038782329(30)	0.03880163(5)	0.039725549(53)	0.0397692(3)
$\Delta_K \times 10^5$	1.2879(15)		2.2922	
$\Delta_{KJ} \times 10^7$	-3.7483(56)		-3.8403(70)	
$\Delta_J \times 10^9$	7.5662(40)		7.9321	
$\delta_k \times 10^8$	3.7482(50)		3.93	
$\delta_j \times 10^{10}$	4.8773(70)		5.2279(63)	

The strong $Q_{K_a}(J)$ transitions offer the possibility to extract accurate spectroscopic parameters. Based on the initial assignments of the $^{p/r}Q_{K_a}(J)$ sub-branches outlined above, the experimental spectrum was fit. In the fitting procedure the predicted rotational constants as well as the band origin were allowed to float. As their influence turned out to be minor, the centrifugal distortion constants were fixed to their ground state values. Again, all ground state parameters were taken from the microwave measurements [28, 27]. As there was no reported value of D_K for the $\text{CH}_2^{79}\text{Br}^{81}\text{Br}$ isotopologue, its value has been adopted from our DFT calculations. Among more than 90000 transitions with intensities higher than 10^{-6} relative to the strongest peaks of each isotopologue, 312 prominent lines were selected as a target set for fitting the rotational constants. These lines were representative for the whole vibrational band and all three isotopologues. The fitting results of the $\text{CH}_2^{79}\text{Br}^{81}\text{Br}$ isotopologue (S reduced Hamiltonian), including the band origin and the rotational constants together with the corresponding ground state constants, are shown in Table 5.4 and those of $\text{CH}_2^{81}\text{Br}_2$ and $\text{CH}_2^{79}\text{Br}_2$ (A reduced Hamiltonian) in Table 5.5.

There are no literature values of the spectroscopic parameters of the excited ν_6 band available as yet. Previous IR measurements of CH_2Br_2 spectrum showed only the main band contours of the

P , Q , and R branches [61, 51]. The band origin has been reported from FTIR measurements to be 3073 cm^{-1} with very large uncertainty [57]. The line positions of the selected transitions were reproduced with an average standard deviation of 0.00056 cm^{-1} , which is less than the experimental wavelength accuracy. Overall, as it can be deduced from the direct comparison of the spectra outlined in Fig. 5.6, the agreement between the final simulated and experimental spectrum is very good. It should be mentioned, however, that there were many peaks that were not reproduced by the spectral simulations. These may indicate additional perturbations of the rotational structure by the nearby ν_1 vibrational band.

5.3.6 Choice of Density Functional

The quantum-chemical assisted prediction of the spectra outlined above is sufficient to guide a first selection of a suitable spectral window for selective halocarbon detection. It also provides a good prediction for the initial values of the rotational constants for fitting the experimental spectrum. However, the question arises which density functional or which model chemistry to use for such applications to ensure accurate results. Although a final answer to this question should be based on a more systematic analysis of many halocarbon spectra, which would have been beyond the scope of this paper, a first conclusion can be drawn by a comparison of the model chemistries used in this work.

In principle, when two vibrational bands are spectrally close, the Coriolis interaction becomes large (see second term in Eq. 5.2). This together with inertia and anharmonicity effects results in a perturbation of the line positions and intensities of the experimental spectra. Therefore, a direct comparison of the predicted spectra based on the computed rotational constants should allow for testing the capability of the different methods to accurately capture rotational-vibrational coupling. In order to quantitatively compare the different density functionals, line positions and intensities of 18 intense $^{p/r}Q_{K_a}$ transitions covering the whole vibrational band up to $K_a = 16$ have been selected as a simulation target.

For the strong $^{p/r}Q_{K_a}$ transitions, the computed and experimental intensities are compared based on the weighted error percentages $\overline{\text{Err}}\%$ according to

$$\overline{\text{Err}}\% = 100 \times \sum_i (W_i \cdot \text{Err}_i) = 100 \times \sum_i \left(\frac{\text{EI}_i}{\sum_i \text{EI}_i} \cdot \frac{\text{CI}_i - \text{EI}_i}{\text{EI}_i} \right). \quad (5.5)$$

Here, W_i are the fractional experimental line intensities, Err_i the relative intensity errors, and CI_i and EI_i the calculated and experimental peak intensities, respectively. Both peak intensities as well as the integrated areas of the $^{p/r}Q_{K_a}(J)$ clusters were used in the evaluation. Table 5.6 presents the average $\overline{\text{Err}}\%$ values obtained for the different model chemistries. Overall, the same trends were obtained for both peak intensities and integrated areas showing that the analysis is robust. All methods yield comparable errors with the M06 value being smallest among all the density functionals and slightly larger than for the MP2 prediction.

The peak positions of the same set of distinct and strong $^{p/r}Q_{K_a}$ transitions used as a second test criterion for the quality of the predicted spectra. Fig. 5.7 shows the remaining difference in the peak position (observed - calculated). Again, the ground state rotational and centrifugal distortion constants are taken from the microwave measurements, the excited state rotational constants are taken from the calculations ($X(\bar{\nu}_i(\nu = 1))$), as outlined in Section 5.3.3), and the centrifugal distortion constants were fixed to their ground state values. With differences $< 0.10 \text{ cm}^{-1}$, all density functionals reproduce

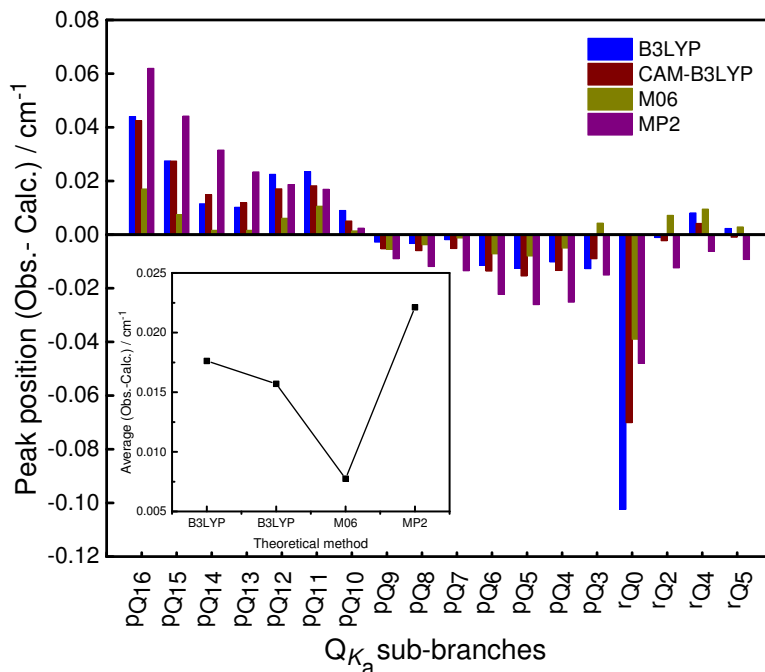


Figure 5.7: Difference in peak positions (observation - simulation) for selected transitions of the strong Q sub-branch features. Comparison of results based on rotational constants calculated by different theoretical models.

very well the experimental spectrum. The inset in Fig. 5.7 shows the average error in peak position for the different model chemistries. With an averaged error of merely 0.0075 cm^{-1} , the best agreement with the experiment is obtained for the M06 density functional. For all four model chemistries, a clear trend towards larger differences with higher K_a values is visible in Fig. 5.7. As both M06 and MP2 predicted well the experimentally observed molecular structure (c.f. Section 5.3.3), the two and a half times larger average error in case of MP2 indicates that MP2 overestimates the change in the rotational constants upon vibrational excitation. Since the spacing between the Q_{K_a} clusters is about $2(A - \bar{B})$ (with $A \gg \bar{B}$), it can be anticipated that it is the uncertainty in the value of the rotational constant A that is mainly responsible for this effect. Indeed, the trends of the Δ_6 values A , B , and C listed in Table 5.3 and the trend of the average errors outlined in Fig. 5.7 is most consistent with an effect resulting from the used value of the rotational constant $A(v = 1)$. A close inspection of the computed vibration-rotational coupling constant and its components along the different axes (Supplemental Table 5.S5) reveals that the observed differences in Δ_6 are mainly due to the calculated anharmonicity correction terms. Whereas the inertia correction is negligible along the y -axis (a -axis), the Coriolis and anharmonicity terms contribute about the same to Δ_6 . But only the anharmonicity terms are significantly different for the four model chemistries. Hence, we conclude that it is the treatment of anharmonicity that is most critical for an accurate prediction of the rotational structure of the ν_6 band.

Table 5.6: Weighted mean average error $\overline{\text{Err}}\%$ of the simulated intensity of the selected $^{p/r}Q_{K_a}(J)$ clusters.

	B3LYP	CAM-B3LYP	M06	MP2
Peak	2.3	1.9	1.8	1.4
Area	1.8	1.7	1.3	1.2

5.4 Conclusions

The Doppler limited high-resolution spectrum of the symmetric (ν_1) and asymmetric (ν_6) C-H stretch bands of CH_2Br_2 have been measured for the first time. Using a widely tunable Mid-IR-OPO laser light source and a cavity ringdown setup, a single-shot minimum absorption of $4.9 \times 10^{-8} \text{ cm}^{-1}$ has been achieved. In contrast to the heavily congested ν_1 band, the ν_6 band showed partially resolved rotational features. These could serve as suitable absorption targets in future environmental detection schemes. Different model chemistries have been used for geometry optimization and anharmonic VPT2 frequency calculations to assist the spectrum simulations and assignment. Using the predicted changes of the anharmonic rotational constants upon vibrational excitation together with available spectroscopic vibrational ground state constants from microwave measurements, a very good prediction of the rovibrational structures has been obtained without the need for spectral fitting. Hence, the presented spectrum modeling approach may prove very useful to reliably predict the rovibrational spectra of halogenated hydrocarbons in cases where high resolution IR data are not readily available.

A more detailed analysis of the ν_6 band has been presented yielding accurate values for the band origins and the rotational constants for all three CH_2Br_2 isotopologues. An unusual transition dipole moment ratio with more intense $\text{CH}_2^{81}\text{Br}_2$ transitions has been observed for the three isotopologues. The simulation were not sensitive to changes in the centrifugal distortion constants, hence the respective ground state values have been used throughout. The spectral line position of 312 representative transitions could be reproduced with a standard error of 0.00056 cm^{-1} , which is below the actual 0.0009 cm^{-1} resolution of the measurement scheme. A comparison of the results obtained with different model chemistries revealed that for CH_2Br_2 the M06/6-311++G(d,p) approach yielded the best results. Future studies on an extended set of atmospheric molecules shall be performed to substantiate both the choice of the theoretical method and to critically test the reliability of the presented spectrum prediction approach.

Acknowledgements

We would like to thank the Helmholtz Research School Ocean Science and Technology (HOSST) at the Helmholtz Centre of Ocean Research Kiel (GEOMAR) and the Cluster of Excellence "Future Ocean" (DFG - EC80) at Kiel University for funding. We would like to cordially thank Christian Smets for laboratory assistance during his practical course. Stimulating discussions with C. M. Western (University of Bristol, UK) and G. Rauhut (University of Stuttgart, Germany) are gratefully acknowledged.

References

- [1] J. H. Butler, D. B. King, J. M. Lobert, S. A. Montzka, S. A. Yvon-Lewis, B. D. Hall, N. J. Warwick, D. J. Mondeel, M. Aydin, and J. W. Elkins. Oceanic distributions and emissions of short-lived halocarbons. *Global Biogeochem. Cycles*, 21(1), 2007.
- [2] L. J. Carpenter, C. E. Jones, R. M. Dunk, K. E. Hornsby, and J. Woeltjen. Air-sea fluxes of biogenic bromine from the tropical and north Atlantic ocean. *Atmos. Chem. Phys.*, 9:1805–1816, 2009.
- [3] H. Hepach, B. Quack, F. Ziska, S. Fuhlbrügge, E. L. Atlas, K. Krüger, I. Peeken, and D. W. R. Wallace. Drivers of diel and regional variations of halocarbon emissions from the tropical north east Atlantic. *Atmos. Chem. Phys.*, 14:1255–1275, 2014.
- [4] S. A. Montzka, S. Reimann, S. O’Doherty, A. Engel, A. K. Kruger, W. T. Sturges, D. Blake, M. Dorf, P. Fraser, and L. Froidevaux *et al.* *Scientific assessment of ozone depletion:2010*. Global Ozone Research and Monitoring Project report: No. 52. World Meteorological Organization, Geneva Switzerland, 2011.
- [5] B. Quack, E. Atlas, G. Petrick, and D. W. R. Wallace. Bromoform and dibromomethane above the Mauritanian upwelling: Atmospheric distributions and oceanic emissions. *J. Geophys. Res.*, 112:D09312/1–9, 2007.
- [6] G. J. Sharp, Y. Yokouchi, and H. Akimoto. Trace analysis of organobromine compounds in air by adsorbent trapping and capillary gas chromatography/mass spectroscopy. *Environ. Sci. Technol.*, 26:815–816, 1992.
- [7] J. W. Munch. Measurement of purgeable organic compounds in water by capillary column gas chromatography/mass spectrometry. Technical report, U.S. Environmental Protection Agency, Cincinnati, Ohio, 1992.
- [8] D. J. Wevill and L. J. Carpenter. Automated measurement and calibration of reactive volatile halogenated organic compounds in the atmosphere. *Analyst*, 129:634–638, 2004.
- [9] M. Mazurenka, A. J. Orr-Ewing, R. Peverall, and G. A. D. Ritchie. Cavity ring-down and cavity enhanced spectroscopy using diode lasers. *Annu. Rep. Prog. Chem., Sect. C*, 101:100–142, 2005.
- [10] G. Friedrichs. Sensitive absorption methods for quantitative gas phase kinetic measurements. Part 2: Cavity ringdown spectroscopy. *Z. Phys. Chem.*, 222(1):31–61, 2008.
- [11] G. Berden and R. Engeln, editors. *Cavity ring-down spectroscopy: Techniques and applications*. Wiley-Blackwell, Oxford, 2009.
- [12] P. R. Brown, P. B. Davies, G. M. Hansford, and N. A. Martin. Diode laser jet spectroscopy of 1,4-dioxane. *J. Mol. Spectrosc.*, 158(2):468–478, 1993.
- [13] P. B. Davies, G. M. Hansford, and T. C. Killian. Diode laser jet spectroscopy of hexafluorobenzene in the 10- μm region. *J. Mol. Spectrosc.*, 163(1):138–158, 1994.

- [14] S. Welzel, R. Engeln, and J. Röpcke. *Quantum Cascade Laser Based Chemical Sensing Using Optically Resonant Cavities*, volume 179. Springer Series in Optical Sciences: Cavity-Enhanced Spectroscopy and Sensing, 2014.
- [15] B. G. Lee, M. A. Belkin, R. Audet, J. MacArthur, L. Diehl, C. Pflügl, F. Capasso, D. C. Oakley, D. Chapman, and A. Napoleone *et al.* Widely tunable single-mode quantum cascade laser source for mid-infrared spectroscopy. *Appl. Phys. Lett.*, 91(23):231101, 2007.
- [16] G. Wysocki, R. Lewicki, R. F. Curl, F. K. Tittel, L. Diehl, F. Capasso, M. Troccoli, G. Hofler, D. Bour, and S. Corzine *et al.* Widely tunable mode-hop free external cavity quantum cascade lasers for high resolution spectroscopy and chemical sensing. *Appl. Phys. B*, 92(3):305–311, 2008.
- [17] B. G. Lee, H. A. Zhang, C. Pflugl, L. Diehl, M. A. Belkin, M. Fischer, A. Wittmann, J. Faist, and F. Capasso. Broadband distributed-feedback quantum cascade laser array operating from 8.0 to 9.8 μm . *IEEE Photonics Technol. Lett.*, 21(13):914–916, 2009.
- [18] D. Zhao and H. Linnartz. The high-resolution infrared spectrum of the $\nu_3+\nu_8$ combination band of jet-cooled propyne. *Chem. Phys. Lett.*, 595-596:256–259, 2014.
- [19] M. Zeppenfeld, B. G. U. Englert, R. Glöckner, A. Prehn, M. Mielenz, C. Sommer, L. D. van Buuren, M. Motsch, and G. Rempe. Sisyphus cooling of electrically trapped polyatomic molecules. *Nature*, 491(7425):570–573, 2012.
- [20] K. N. Crabtree, J. N. Hodges, B. M. Siller, A. J. Perry, J. E. Kelly, P. A. Jenkins, and B. J. McCall. Sub-doppler mid-infrared spectroscopy of molecular ions. *Chem. Phys. Lett.*, 551:1–6, 2012.
- [21] B. E. Brumfield, J. T. Stewart, S. L. Widicus Weaver, M. D. Escarra, S. S. Howard, C. F. Gmachl, and B. J. McCall. A quantum cascade laser cw cavity ringdown spectrometer coupled to a supersonic expansion source. *Rev. Sci. Instrum.*, 81(6):063102, 2010.
- [22] B. E. Brumfield, J. T. Stewart, and B. J. McCall. High-resolution spectroscopy of the ν_8 band of methylene bromide using a quantum cascade laser. *J. Mol. Spectrosc.*, 266(1):57–62, 2011.
- [23] Krishnaaji, S. L. Srivastava, and A. S. Rajput. Microwave spectrum of methylene bromide. *Phys. Lett. A*, 31(7):411–412, 1970.
- [24] B. Beagley, D. P. Brown, and S. M. Freeman. The molecular structure of methylene bromide by gas-phase electron diffraction. *J. Mol. Struct.*, 20(2):315–316, 1974.
- [25] D. Chadwick and D. J. Millen. Microwave spectrum of dibromomethane. Part 1. – Molecular structure. *Trans. Faraday Soc.*, 67:1539–1550, 1971.
- [26] D. Chadwick and D. J. Millen. Molecular structure of methylene bromide: Comparison of structures of halogenomethanes. *J. Mol. Struct.*, 25(1):216–218, 1975.
- [27] R. W. Davis and M. C. L. Gerry. The microwave spectrum, centrifugal distortion constants, harmonic force field, and structure of dibromomethane. *J. Mol. Spectrosc.*, 109(2):269–282, 1985.

- [28] Y. Niide, H. Tanaka, and I. Ohkoshi. Microwave spectrum of dibromomethane in the ground and excited bending vibrational states: Hyperfine structure by coupling of ^{79}Br and ^{81}Br nuclei. *J. Mol. Spectrosc.*, 139(1):11–29, 1990.
- [29] A. Mandal, P. J. Singh, A. Shastri, V. Kumar, B. R. Sekhar, and B. N. Jagatap. Rydberg and valence excited states of dibromomethane in 35,000–95,000 cm^{-1} region studied using synchrotron radiation. *J. Quant. Spectrosc. Radiat. Transfer*, 144:164–173, 2014.
- [30] P. Z. El-Khoury, Suman K. Pal, A. S. Mereshchenko, and A. N. Tarnovsky. The formation and back isomerization of iso- $\text{H}_2\text{C}-\text{Br}-\text{Br}$ on a 100-ps time scale following 255-nm excitation of CH_2Br_2 in acetonitrile. *Chem. Phys. Lett.*, 493(1-3):61–66, 2010.
- [31] C. Puzzarini, J. F. Stanton, and J. Gauss. Quantum-chemical calculation of spectroscopic parameters for rotational spectroscopy. *Int. Rev. Phys. Chem.*, 29(2):273–367, 2010.
- [32] J. Breidung and W. Thiel. *Prediction of vibrational spectra from ab initio theory*. Wiley: Handbook of High-resolution Spectroscopy, 2011.
- [33] V. Barone. Vibrational zero-point energies and thermodynamic functions beyond the harmonic approximation. *J. Chem. Phys.*, 120:3059–3065, 2004.
- [34] V. Barone. Anharmonic vibrational properties by a fully automated second-order perturbative approach. *J. Chem. Phys.*, 122:014108/1–10, 2005.
- [35] J. Vogt, E. Popov, R. Rudert, R. Kramer, and N. Vogt. 3D visualization of molecular structures in the MOGADOC database. *J. Mol. Struct.*, 978:201–204, 2010.
- [36] M. R. Aliev and J. K. G. Watson. Molecular spectroscopy: Modern research. In *Higher-order Effects in the Vibration-Rotation Spectra of Semirigid Molecules*. Academic Press, 1985.
- [37] F. Pawlowski, P. Jorgensen, J. Olsen, F. Hegelund, T. Helgaker, J. Gauss, K. L. Bak, and J. F. Stanton. Molecular equilibrium structures from experimental rotational constants and calculated vibration-rotation interaction constants. *J. Chem. Phys.*, 116:6482–6496, 2002.
- [38] S. V. Krasnoshchekov and N. F. Stepanov. The determination of the equilibrium geometry of a molecule with the use of microwave data and theoretical rotational-vibrational interaction constants. *Russ. J. Phys. Chem.*, 80:1636–1644, 2006.
- [39] G. V. Lopez, C.-H. Chang, P. M. Johnson, G. E. Hall, T. J. Sears, B. Markiewicz, M. Milan, and A. Teslja. What is the best DFT functional for vibronic calculations? A comparison of the calculated vibronic structure of the S_1-S_0 transition of phenylacetylene with cavity ringdown band intensities. *J. Phys. Chem. A*, 116(25):6750–6758, 2012.
- [40] M. J. Frisch, G. W. Trucks, H. B. Schlegel, G. E. Scuseria, M. A. Robb, J. R. Cheeseman, G. Scalmani, V. Barone, B. Mennucci, and G. A. Petersson *et al.* *Gaussian 09 Revision A.02*. Gaussian Inc, Wallingford, CT, USA, 2009.
- [41] I. Sadiq and G. Friedrichs. Saturation dynamics and working limits of saturated absorption cavity ringdown spectroscopy. *Phys. Chem. Chem. Phys.*, 18:22978–22989, 2016.

- [42] L. S. Rothman, I. E. Gordon, Y. Babikov, A. Barbe, D. Chris Benner, P. F. Bernath, M. Birk, L. Bizzocchi, V. Boudon, and L. R. Brown *et al.* The HITRAN2012 molecular spectroscopic database. *J. Quant. Spectrosc. Radiat. Transfer*, 130:4–50, 2013.
- [43] T. Yanai, D. Tew, and N. Handy. A new hybrid exchange-correlation functional using the coulomb-attenuating method (CAM-B3LYP). *Chem. Phys. Lett.*, 393:51–57, 2004.
- [44] Y. Zhao and D. G. Truhlar. The M06 suite of density functionals for main group thermochemistry, thermochemical kinetics, noncovalent interactions, excited states, and transition elements: two new functionals and systematic testing of four M06-class functionals and 12 other functionals. *Theor. Chem. Acc.*, 120:215–241, 2008.
- [45] V. Barone, J. Bloino, C. A. Guido, and F. Lipparini. A fully automated implementation of VPT2 infrared intensities. *Chem. Phys. Lett.*, 496:157–161, 2010.
- [46] J. Bloino and V. Barone. A second-order perturbation theory route to vibrational averages and transition properties of molecules: General formulation and application to infrared and vibrational circular dichroism spectroscopies. *J. Chem. Phys.*, 136:124108/1–15, 2012.
- [47] I. M. Mills. Vibration-rotation structure in asymmetric- and symmetric top molecules. In *Molecular Spectroscopy: Modern Research*. Academic Press, New York, 1972.
- [48] C. M. Western. PGOPHER 8.0, a program for simulating rotational, vibrational and electronic spectra. University of Bristol, <http://pgopher.chm.bris.ac.uk>.
- [49] J. Y. Lee and J. W. Hahn. Theoretical analysis on the dynamic absorption saturation in pulsed cavity ringdown spectroscopy. *Appl. Phys. B*, 79(5):653–662, 2004.
- [50] G. Giusfredi, I. Galli, D. Mazzotti, P. Cancio, and P. de Natale. Theory of saturated-absorption cavity ring-down: Radiocarbon dioxide detection, a case study. *J. Opt. Soc. Am. B*, 32(10):2223, 2015.
- [51] W. S. Steven, J. J. Timothy, L. S. Robert, M. C. Pamela, C. R. George, and A. J. Patricia. Gas-phase databases for quantitative infrared spectroscopy. *Appl. Spectrosc.*, 58(12):1452–1461, 2004.
- [52] D. Chadwick and D. J. Millen. Microwave spectrum of dibromomethane. Part 2 – Nuclear quadrupole coupling. *Trans. Faraday Soc.*, 67:1551–1568, 1971.
- [53] R. Venkatraman, J. S. Kwiatkowski, Bakalarski. G., and J. Leszczynski. Molecular structure and IR spectra of bromomethanes by DFT and post-Hartree-Fock MP2 and CCSD(T) calculations. *Mol. Phys.*, 98(6):371–386, 2000.
- [54] A. P. Scott and L. Radom. Harmonic Vibrational Frequencies: An Evaluation of Hartree-Fock, Møller-Plesset, Quadratic Configuration Interaction, Density Functional Theory, and Semiempirical Scale Factors. *J. Phys. Chem.*, 100:16502–16513, 1996.
- [55] F. Pfeiffer, G. Rauhut, D. Feller, and K. A. Peterson. Anharmonic zero point vibrational energies: Tipping the scales in accurate thermochemistry calculations? *J. Chem. Phys.*, 138(4):044311/1–10, 2013.

- [56] I. M. Alecu, J. Zheng, Y. Zhao, and D. G. Truhlar. Computational thermochemistry: Scale factor databases and scale factors for vibrational frequencies obtained from electronic model chemistries. *J. Chem. Theory Comput.*, 6(9):2872–2887, 2010.
- [57] T. Shimanouchi. Tables of molecular vibrational frequencies. Nat. Stand. Ref. Data Ser., Nat. Bur. Stand., 1972.
- [58] J. K. G. Watson. Vibrational spectra and structure: Aspects of quartic and sextic centrifugal effects on rotational energy levels. In *Vibrational Spectra and Structure*, volume 6. Elsevier, Amsterdam, 1977.
- [59] R. Milloud, V. I. Perevalov, S. A. Tashkun, and A. Campargue. Rotational analysis of $6\nu_3$ and $6\nu_3 + \nu_2 - \nu_2$ bands of $^{14}\text{N}_2^{16}\text{O}$ from ICLAS spectra between 12,760 and 12,900 cm^{-1} . *J. Quant. Spectrosc. Radiat. Transfer*, 112(3):553–557, 2011.
- [60] P. Sebald, R. Oswald, P. Botschwina, and K. Kawaguchi. Rovibrational states of ClHCl^- isotopologues up to high J : A joint theoretical and spectroscopic investigation. *Phy. Chem. Chem. Phys.*, 15(18):6737–6748, 2013.
- [61] D. Bârc-Gleanu. Das ultrarote Absorptionsspektrum des Methylenbromiddampfes. *Z. Phys.*, 117(9-10):589–595, 1941.

5.5 Supplementary Material

Doppler-Limited High-Resolution Spectrum and VPT2 Assisted Assignment of the C-H Stretch of CH₂Br₂

Ibrahim Sadiek,^a and Gernot Friedrichs^{*ab}

^aInstitut für Physikalische Chemie, Christian-Albrechts-Universität zu Kiel, Max-Eyth-Str. 1, D-24118 Kiel, Germany. ^bKMS Kiel Marine Science - Centre for Interdisciplinary Marine Sciences, Olshausenstr. 40, D-24098 Kiel, Germany.

Spectrochim. Acta. A: Mol. Biomol. Spectrosc. **181: 180–191, 2017, DOI: 10.1016/j.saa.2017.03.027**

Received 10th November 2016, Accepted 13th March 2017, First published on the web 16th March 2016

Elsevier B.V. All rights reserved, 2017.

This Supplementary Material includes:

- PGOPHER input file, see file “ CH₂Br₂_v1_v6.pgo ” (available online).
- Experimental data of the measured spectrum, see files “Spectrum_Original.dat ” (available online) and “Spectrum_EvenlySpaced.dat ” (available online).
- Table 5.S1 Harmonic and anharmonic frequencies of the fundamental bands, overtones, and combination bands of CH₂⁷⁹Br⁸¹Br (this file).
- Table 5.S2 Comparison of structural parameters of the three isotopologues, calculated at M06/6-311++G(d,p) level of theory (this file).
- Table 5.S3 Anharmonic rotational constants of CH₂⁷⁹Br⁸¹Br in its vibrational ground state ($v = 0$) and first excited vibrational state ($v = 1$) of ν_1 and ν_6 (this file).
- Table 5.S4 Anharmonic rotational constants of CH₂⁷⁹Br₂ in its vibrational ground state ($v = 0$) and first excited vibrational state ($v = 1$) of ν_1 and ν_6 (this file).
- Table 5.S5 Inertia, Coriolis, and anharmonicity correction terms of the rotational-vibrational coupling constant (α_6) of CH₂⁷⁹Br⁸¹Br (this file).

Table 5.S1: Harmonic and anharmonic frequencies (in cm^{-1}) of fundamental bands, overtones, and combination bands of $\text{CH}_2^{79}\text{Br}^{81}\text{Br}$, calculated at M06/6-311++G(d,p) level of theory.

Fundamental bands			Overtones		
	Harmonic	Anharmonic		Harmonic	Anharmonic
ν_1	3105.41	3001.02	$2\nu_1$	6210.813	5924.26
ν_2	1400.22	1404.71	$2\nu_2$	2800.448	2802.04
ν_3	587.063	582.880	$2\nu_3$	1174.126	1164.60
ν_4	170.140	168.098	$2\nu_4$	340.281	335.961
ν_5	1104.62	1099.35	$2\nu_5$	2209.231	2187.32
ν_6	3190.91	3074.87	$2\nu_6$	6381.824	6068.49
ν_7	795.871	826.283	$2\nu_7$	1591.741	1646.51
ν_8	1206.29	1202.06	$2\nu_8$	2412.577	2388.85
ν_9	662.056	646.778	$2\nu_9$	1324.112	1285.67
Combination bands			Combination bands		
	Harmonic	Anharmonic		Harmonic	Anharmonic
$\nu_2+\nu_1$	4505.63	4425.30	$\nu_7+\nu_4$	966.011	993.782
$\nu_3+\nu_1$	3692.47	3583.58	$\nu_7+\nu_5$	1900.49	1933.68
$\nu_3+\nu_2$	1987.29	1986.14	$\nu_7+\nu_6$	3986.78	3935.21
$\nu_4+\nu_1$	3275.55	3169.14	$\nu_8+\nu_1$	4311.69	4229.97
$\nu_4+\nu_2$	1570.36	1572.60	$\nu_8+\nu_2$	2606.51	2610.29
$\nu_4+\nu_3$	757.203	750.082	$\nu_8+\nu_3$	1793.35	1784.99
$\nu_5+\nu_1$	4210.02	4118.23	$\nu_8+\nu_4$	1376.43	1369.91
$\nu_5+\nu_2$	2504.84	2507.00	$\nu_8+\nu_5$	2310.90	2273.94
$\nu_5+\nu_3$	1691.68	1682.02	$\nu_8+\nu_6$	4397.20	4293.32
$\nu_5+\nu_4$	1274.76	1267.36	$\nu_8+\nu_7$	2002.16	2036.90
$\nu_6+\nu_1$	6296.32	5924.74	$\nu_9+\nu_1$	3767.46	3649.25
$\nu_6+\nu_2$	4591.14	4487.70	$\nu_9+\nu_2$	2062.28	2050.17
$\nu_6+\nu_3$	3777.97	3658.04	$\nu_9+\nu_3$	1249.12	1228.02
$\nu_6+\nu_4$	3361.05	3243.15	$\nu_9+\nu_4$	832.196	813.099
$\nu_6+\nu_5$	4295.53	4193.84	$\nu_9+\nu_5$	1766.67	1737.66
$\nu_7+\nu_1$	3901.28	3859.82	$\nu_9+\nu_6$	3852.97	3724.50
$\nu_7+\nu_2$	2196.09	2223.56	$\nu_9+\nu_7$	1457.93	1472.72
$\nu_7+\nu_3$	1382.93	1407.29	$\nu_9+\nu_8$	1868.34	1843.30

Table 5.S2: Comparison of structural parameters of the three isotopologues, calculated at M06/6-311++G(d,p) level of theory.

	$\text{CH}_2^{81}\text{Br}_2$	$\text{CH}_2^{79}\text{Br}^{81}\text{Br}$	$\text{CH}_2^{79}\text{Br}_2$
$r(\text{CH}) / \text{\AA}$	1.0867	1.0867	1.0867
$r(\text{CBr}) / \text{\AA}$	1.9302	1.9302	1.9302
$\angle(\text{HCH})$	111.2919	111.2919	111.2920
$\angle(\text{HCBBr})$	107.9508	107.9508	107.9508
$\angle(\text{BrCBr})$	113.7922	113.7924	113.7923
μ	1.4343	1.4344	1.4343

Table 5.S3: Anharmonic rotational constants of $\text{CH}_2^{79}\text{Br}^{81}\text{Br}$ in its vibrational ground $\nu(v=0)$ and first excited state $\nu(v=1)$ of ν_1 and ν_6 . All values are given in units of cm^{-1} as calculated at different levels of theory using the 6-311++G(d,p) basis set. Values in parentheses denote the fit parameter uncertainties on a 1σ confidence level.

	$\nu_i(v=0)$	$\nu_i(v=1)$	$\Delta_1/10^{-5}{}^a$	$\nu_1^{\text{exp}}(v=0){}^b$	$\bar{\nu}_1(v=1){}^c$	$\nu_6(v=1)$	$\Delta_6/10^{-5}{}^a$	$\bar{\nu}_6(v=1)$
B3LYP								
A	0.874851	0.872433	-241.8	0.86751916(86)	0.865926	0.873910	-94.1	0.867403
B	0.039331	0.039359	2.8	0.040804716(73)	0.041341	0.039374	4.3	0.041356
C	0.037903	0.037928	2.5	0.039253679(87)	0.039751	0.037942	3.9	0.039765
CAM-B3LYP								
A	0.882497	0.880137	-236	0.86751916(86)	0.865984	0.881569	-92.8	0.867416
B	0.040267	0.040289	2.2	0.040804716(73)	0.041335	0.040299	3.2	0.041345
C	0.038784	0.038804	2.0	0.039253679(87)	0.039746	0.038813	2.9	0.039755
M06								
A	0.876546	0.874255	-229.1	0.86751916(86)	0.866053	0.875787	-75.9	0.867585
B	0.040528	0.040546	1.8	0.040804716(73)	0.041331	0.040553	2.5	0.041338
C	0.039015	0.039031	1.6	0.039253679(87))	0.039742	0.038813	2.3	0.039749
MP2								
A	0.882132	0.879885	-224.7	0.86751916(86)	0.866097	0.881078	-105.4	0.867290
B	0.040421	0.040432	1.1	0.040804716(73)	0.041324	0.040443	2.2	0.041335
C	0.038928	0.038938	1.0	0.039253679(87)	0.039736	0.038947	1.9	0.039745

^a $\Delta_i = X(\nu_i(v=1)) - X(\nu_i(v=0))$ (with $X = A, B, C$).

^b Vibrational ground state data of Niide et al.[1].

^c $X(\bar{\nu}_i(v=1)) = X^{\text{exp}}(\nu_i(v=0)) + \Delta_i$ (with $X = A, B, C$).

Table 5.S4: Anharmonic rotational constants of $\text{CH}_2^{79}\text{Br}_2$ in its vibrational ground $\nu(v=0)$ and first excited state $\nu(v=1)$ of ν_1 and ν_6 . All values are given in units of cm^{-1} as calculated at different levels of theory using the 6-311++G(d,p) basis set. Values in parentheses denote the fit parameter uncertainties on a 1σ confidence level.

	$\nu_i(v=0)$	$\nu_i(v=1)$	$\Delta_1/10^{-5}{}^a$	$\nu_1^{\text{exp}}(v=0){}^b$	$\bar{\nu}_1(v=1){}^c$	$\nu_6(v=1)$	$\Delta_6/10^{-5}{}^a$	$\bar{\nu}_6(v=1)$
B3LYP								
A	0.874851	0.872433	-241.8	0.8683441(13)	0.865926	0.873909	-94.2	0.867402
B	0.039331	0.039359	2.8	0.041313137(47)	0.041341	0.039374	4.3	0.041356
C	0.037903	0.037928	2.5	0.039725549(53)	0.039751	0.037942	3.9	0.039765
CAM-B3LYP								
A	0.882517	0.880157	-236	0.8683441(13)	0.865984	0.881589	-92.8	0.867416
B	0.040267	0.040289	2.2	0.041313137(47)	0.041335	0.040298	3.1	0.041344
C	0.038784	0.038803	1.9	0.039725549(53)	0.039746	0.038812	2.8	0.039754
M06								
A	0.876542	0.874252	-229.0	0.8683441(13)	0.866054	0.875784	-75.8	0.867586
B	0.040528	0.040546	1.8	0.041313137(47)	0.041331	0.040553	2.5	0.041338
C	0.039015	0.039031	1.6	0.039725549(53)	0.039742	0.038813	2.3	0.039749
MP2								
A	0.882133	0.879886	-224.7	0.8683441(13)	0.8645154	0.881079	-105.4	0.867290
B	0.040421	0.040432	1.1	0.041313137(47)	0.0403083	0.040443	2.2	0.041335
C	0.038928	0.038938	1.0	0.039725549(53)	0.039736	0.038947	1.9	0.039745

^a $\Delta_i = X(\nu_i(v=1)) - X(\nu_i(v=0))$ (with $X = A, B, C$).

^b Vibrational ground state data of Davis and Gerry [2].

^c $X(\bar{\nu}_i(v=1)) = X^{\text{exp}}(\nu_i(v=0)) + \Delta_i$ (with $X = A, B, C$).

Table 5.S5: Inertia, Coriolis, and anharmonicity correction terms (in cm^{-1}) of the rotational-vibrational coupling constant (α_6) of $\text{CH}_2^{79}\text{Br}^{81}\text{Br}$ calculated at M06/6-311++G(d,p) level of theory.

	Inertia	Coriolis	Anharmonicity	Total (α_6)
B3LYP				
x(c)	-2.77×10^{-9}	-8.51×10^{-7}	-3.83×10^{-5}	-3.91×10^{-5}
y(a)	-1.03×10^{-21}	-2.01×10^{-3}	$+2.95 \times 10^{-3}$	$+9.42 \times 10^{-4}$
z(b)	-2.87×10^{-9}	-2.61×10^{-6}	-4.02×10^{-5}	-4.28×10^{-5}
CAM-B3LYP				
x(c)	-2.98×10^{-9}	-9.00×10^{-7}	-2.77×10^{-5}	-2.86×10^{-5}
y(a)	-1.93×10^{-20}	-2.05×10^{-3}	$+2.98 \times 10^{-3}$	$+9.28 \times 10^{-4}$
z(b)	-3.09×10^{-9}	-2.71×10^{-6}	-2.89×10^{-5}	-3.16×10^{-5}
M06				
x(c)	-3.16×10^{-9}	-9.50×10^{-7}	-2.18×10^{-5}	-2.27×10^{-5}
y(a)	-5.98×10^{-21}	-2.01×10^{-3}	$+2.77 \times 10^{-3}$	$+7.59 \times 10^{-4}$
z(b)	-3.17×10^{-9}	-2.72×10^{-6}	1.86×10^{-5}	-2.14×10^{-5}
MP2				
x(c)	-3.28×10^{-9}	-2.07×10^{-6}	-2.07×10^{-5}	-2.50×10^{-5}
y(a)	-3.90×10^{-26}	-2.03×10^{-3}	$+3.08 \times 10^{-3}$	$+3.08 \times 10^{-4}$
z(b)	-3.05×10^{-9}	-9.23×10^{-7}	-9.23×10^{-5}	-1.90×10^{-5}

References

- [1] Y. Niide, H. Tanaka, and I. Ohkoshi. Microwave spectrum of dibromomethane in the ground and excited bending vibrational states: Hyperfine structure by coupling of ^{79}Br and ^{81}Br nuclei. *J. Mol. Spectrosc.*, 139(1):11–29, 1990.
- [2] R. W. Davis and M. C. L. Gerry. The microwave spectrum, centrifugal distortion constants, harmonic force field, and structure of dibromomethane. *J. Mol. Spectrosc.*, 109(2):269–282, 1985.

Saturation Dynamics and Working Limits of Saturated Absorption Cavity Ringdown Spectroscopy

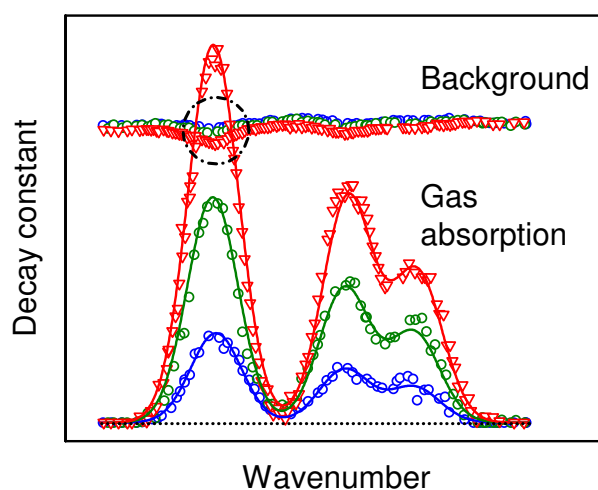
Ibrahim Sadiek,^a and Gernot Friedrichs^{*ab}

^aInstitut für Physikalische Chemie, Christian-Albrechts-Universität zu Kiel, Max-Eyth-Str. 1, D-24118 Kiel, Germany. ^bKMS Kiel Marine Science - Centre for Interdisciplinary Marine Sciences, Olshausenstr. 40, D-24098 Kiel, Germany.

Phys. Chem. Chem Phys., 18: 22978–22989, 2016, DOI: 10.1039/C6CP01966H

Received 24th March 2016, Accepted 28th July 2016, First published on the web 28th July 2016

Published by the PCCP Owner Societies.



Own contributions:

- All saturated absorption cavity ringdown spectroscopy measurements.
- Writing a MATLAB fitting routine for modeling the Sat-CRDS signal.
- Analysis and discussion of the experimental data.
- Writing of paper draft.

ABSTRACT: Cavity ringdown spectroscopy (CRDS) in the linear absorption regime is a well-established method for sensitive trace gas detection, but only a few studies have addressed quantitative measurements in the presence of a saturated sample. In fact, saturation is usually avoided in order to escape from the required complex modeling of the saturation process that depends on the characteristics of the absorbing species, its interaction with the surrounding gas as well as on the temporal and spectral characteristics of the cavity excitation. Conversely, the novel saturated-absorption cavity ringdown spectroscopy approach (SCAR/Sat-CRDS) takes advantage of sample saturation in order to allow one to extract both the gas absorption and the empty cavity loss rates from a single ringdown event. Using a new continuous-wave infrared CRD spectrometer equipped with a tunable narrow-bandwidth high-power OPO laser system and a 18 bit digitizer, the transient dynamics of absorption saturation and the working limits of the Sat-CRDS approach in terms of its ability to extract reliable trace gas concentrations have been experimentally studied in this work. Using a strong methane transition as a test case, the excitation power P_0 and saturation power P_S have been systematically varied to explore a wide range of saturation regimes. At pressures $5 \mu\text{bar} < p < 2 \text{ mbar}$, the saturation intensity revealed a nearly linear pressure dependence showing that non-collisional processes contribute to the overall relaxation. A ratio of $P_0/P_S \approx 15$ turned out to be optimal with working limits of $5 < P_0/P_S < 300$. Moreover, the ratio of the absorption and empty cavity loss rates, γ_g/γ_c , has been varied to test the dynamic range of the method. At $\gamma_g > \gamma_c$, a pronounced coupling between the two parameters has been observed. Finally, a standard error analysis was performed revealing that the Sat-CRDS approach holds its advantages over conventional CRDS implementations in particular when the attainable ultimate detection sensitivity is limited by uncertainties in the empty cavity ringdown constant.

6.1 Introduction

Sensitive light absorption measurements by means of cavity ringdown spectroscopy (CRDS) have become a very well-established technique with widespread applications in trace gas detection, spectroscopy, and reaction kinetics [1, 2, 3]. Almost all CRDS implementations are performed in the linear absorption regime where the difference between the measured ringdown time with absorber present in the cavity, τ , and the empty cavity ringdown time, τ_0 , is a direct measure of the concentration $[c]$ of the detected species.

$$[c] = \frac{1}{c\sigma} \times \left(\frac{1}{\tau} - \frac{1}{\tau_0} \right) \quad (6.1)$$

Here, c is the speed of light and σ the absorption cross-section. The ringdown times are extracted from measured single-exponential decays of light coupled into a high-finesse optical resonator forming the ringdown cavity. For reaching the ultimate sensitivity limit of CRDS, care has to be taken to avoid non- or multi-exponential ringdown events. Such ringdown signals may result from transversal and longitudinal multi-mode excitation of the cavity, especially when pulsed lasers with spectral bandwidths wider than the mode spacing of the cavity are used (so-called laser bandwidth effect) [4]. Consequently, most modern CRDS implementations for quantitative concentration measurements are based on narrow-bandwidth laser light sources. With the use of such lasers, however, the coupling efficiency of the light into the single excited cavity mode increases and high intracavity light levels are easily observed. This may cause significant optical saturation, again resulting in deviations from the

perfectly exponential ringdown behavior [5, 6]. Next to avoiding ringdown anomalies, another limitation of CRDS is the need for measuring τ and τ_0 independently. Typically, this is achieved by scanning the detection laser over the absorption feature of interest and then extracting τ_0 from the off-resonance baseline of the measured spectrum. In practice, etaloning effects causing baseline undulations, spectral interferences, and drift components of the ringdown times often limit the attainable sensitivity of the detection system. Therefore, the possibility to measure both τ and τ_0 during one single ringdown event would be advantageous.

To this end, in an idealized experiment, the absorption of the sample would have to be switched on or off during the ringdown. This condition can be approximately met for transient species that are formed or depleted on the timescale of the ringdown event. Provided that the rate law for the formation or the decay of the detected species is known, the empty cavity ringdown time constant can still be determined by fitting the observed ringdown based on the so-called Simultaneous Kinetics and Ringdown (SKaR) model [7] or its extended version eSKaR, which also takes laser bandwidth effects into account [8]. Due to the limitation to transient species, the use of SKaR for improving the detection sensitivity is very limited and, in fact, has not been exploited so far. In contrast, an alternative way of switching the effective net absorption by taking advantage of the optical saturation effect, the so-called saturated absorption cavity ringdown spectroscopy (Sat-CRDS), has been first implemented by Giusfredi et al. [9] and will be further outlined below. Sat-CRDS has been demonstrated to result in impressive sensitivities with a $^{14}\text{CO}_2$ detection limit down to a few parts per quadrillion, hence comparable to the one obtained with accelerator mass spectrometric approaches [10, 11, 12, 13]. Although the method has been termed SCAR in the original papers, here we prefer the acronym Sat-CRDS to avoid confusion with the above-mentioned SKaR method.

Saturation effects in CRDS such as deviations from single-exponential ringdown behavior, spectral Lamb dips, and power broadened line profiles have long been observed and analyzed in some detail [14, 15, 16, 17, 18, 19]. For example, Labazan et al.[16] have reported non-linear ringdown effects in pulsed CRDS of lithium vapor. Depending on the time-window and the length of the portion of the ringdown transient used for extracting the decay rate, the apparent absorption as well as the line shape profile changed. This was due to the fact that during the ringdown event the intracavity light intensity decays and with it the saturation and the net absorption of the sample. The resulting ambiguity in extracting reliable decay constants has often been considered disadvantageous with regard to quantitative concentration measurements [2, 20]. Otherwise, the advantageous possibility to perform high-resolution Doppler-free spectroscopy is inherent to the counter-propagating wave configuration of CRD cavities. For example, Bucher et al.[17] have studied optical saturation effects in the ethylene spectrum using continuous-wave (cw-) CRDS. Interestingly, despite of the detection of Lamb dips, single exponential ringdown decays have been observed in that work. This surprising result has been attributed to a relaxation time of the excited state being long compared to the ringdown decay. This limiting case is called the *non-relaxing* condition in contrast to the *adiabatic* case. The latter assumes a relaxation rate that is fast compared to the empty cavity decay rate such that the relative steady-state population in the lower and upper absorption state responds instantaneously to the intracavity light intensity.

In Sat-CRDS the issue of non-exponential ringdown curves is overcome by properly modeling the whole ringdown curve taking into account an appropriate saturation model. In the simplest case, the sample is completely saturated and shows almost no net absorption at the beginning of the ringdown event

and, with diminishing intracavity light intensity, is not saturated at all at its end. Then it is possible to directly measure the empty cavity decay constant τ_0^{-1} at short ringdown times, whereas at long ringdown times the intensity decay is described by $\tau_0^{-1} + c\sigma[c]$. On the one hand, this approach makes the scanning of the laser frequency over the absorption line dispensable. In principle, this enhances the measurement speed by a factor of n and with it reduces the statistical noise by \sqrt{n} . Here, n is equal to the number of data points that would be needed to scan over the whole absorption line to determine a reliable spectrum baseline. Moreover, performing a single measurement at a fixed detection wavelength should significantly reduce the uncertainties related to baseline undulation and drift. On the other hand, the need for extracting at least two more or less correlated parameters from a single ringdown curve may cause additional uncertainty in parameter estimation, hence partly outweighing the outlined sensitivity enhancement. Recently, Lehmann [21] introduced a theoretical error analysis trying to predict the ultimate sensitivity limits of Sat-CRDS. In his simulations, due to the strong parameter correlation, the standard error of the absorption extracted from the saturated ringdown curve turned out to be even one order of magnitude worse than that of a standard CRDS experiment. Moreover, it was pointed out that the standard error is a strong function of the initial degree of saturation and therefore a sensitive Sat-CRDS detection scheme would rely on a proper choice of the experimental conditions.

In the context of the current status of development and theoretical understanding of the Sat-CRDS approach, the aim of this study was to provide a systematic experimental assessment of the limiting factors that have to be taken into consideration for sensitive Sat-CRDS detection. First, a new IR-cw-CRDS experiment based on a high power OPO laser system has been setup that allowed us to easily vary the saturation conditions over a wide range. The saturation dynamics, which is controlled by the interplay of optical pumping and relaxation rate, has been investigated. The transition from the highly saturated absorption regime to a lower degree of saturation has been studied by varying both the intracavity intensity as well as the saturation intensity. The latter was tuned independently by setting the detection cell pressure. An experimental standard error analysis has been performed and compared to the theoretical predictions of Lehmann in order to determine the optimum working conditions. Finally, the ability of the model to retrieve the gas absorption decay rate for absorption lines with different line strengths has been examined.

6.2 Sat-CRDS Model

6.2.1 Saturation and Relaxation Dynamics

Lee and Hahn [6] have introduced an extensive theoretical analysis on the dynamic absorption saturation in pulsed CRDS. In their study, a broad dynamic range of saturation conditions covering the adiabatic and the non-relaxing regime has been simulated considering homogeneous and inhomogeneous broadening of the absorption line. Somewhat earlier, Brown et al.[5] presented the equations governing the saturated ringdown decay for the adiabatic case assuming a homogeneous line broadening regime and, very recently, Giusfredi et al. [22] depicted fitting strategies to retrieve quantitative absorption data from Sat-CRDS experiments at pressures resulting in absorption line profiles in the Voigt broadening regime.

The saturation changes the population of the energy levels involved in the transition from the thermal Boltzmann equilibrium situation. For probing vibrational-rotational transitions, a detailed treatment

of this effect should be based on an open two-energy-level or multilevel relaxation scheme [23, 24]. However, the overall effect can be illustrated in a simple two-state model with ground state (g) and excited state (e). The population dynamics during a ringdown event can then be described by the population densities $N_g(t)$ and $N_e(t)$ and the decay of the intracavity spectral energy density $\rho_\nu(t)$. For the non-degenerate case with statistical weights $g_g = g_e = 1$, the populations are changed by the excitation and deexcitation rates $B_{ge}\rho_\nu N_g = \mathcal{P}N_g$ and $\mathcal{P}N_e$ as well as the overall relaxation rate $\mathcal{R}_i N_e$. Here, B_{ge} is the Einstein- B coefficient of the respective transition and \mathcal{P} the absorption and stimulated emission probability. The relaxation probability R_i accounts for all other deexcitation processes such as spontaneous emission, $A = 1/\tau_{\text{natural}}$, collisional excitation and deexcitation, $k = 1/\tau_{\text{collision}}$ as well as net population changes caused by diffusional or ballistic motion of ground state molecules into and excited state molecules out of the observation volume, $k = 1/\tau_{\text{diffusion}}$ (including effects from transit-time broadening and wall quenching). In the adiabatic case, the saturation parameter $\mathcal{S} = \mathcal{P}/\mathcal{R}_i$ is related to the steady-state population difference $\Delta N = \Delta N_0/(1+\mathcal{S})$ (for an homogeneously broadened absorption line) or $\Delta N = \Delta N_0/\sqrt{1+\mathcal{S}}$ (for an inhomogeneously broadened absorption line; at line center) between the excited and the ground state. ΔN_0 corresponds to the population difference without the light field ($\mathcal{S} = 0$). Instead of using the saturation parameter \mathcal{S} , it is common to express the saturation in terms of the saturation light intensity I_S , where $\mathcal{S} = I/I_S$. Hence, in a closed two-level system, for $\mathcal{S} \rightarrow \infty$ (i.e., $I \gg I_S$) both states become equally populated ($\Delta N = 0$) and an absorbing sample becomes optical transparent at these high saturation levels.

For a specific transition, the saturation intensity is determined by the relaxation rates of the involved energy states and, as many relaxation processes involve molecular collisions, it is a pressure dependent and collider specific quantity. Theoretically, $I_S \propto \tau^{-1}g(\nu)^{-1}$ (homogeneous broadening) or $I_S \propto \tau^{-1}g(\nu_0)^{-1}$ (inhomogeneous broadening, ν_0 is the line center frequency) [23]. Here, τ corresponds to the pressure dependent inversion lifetime (typically the lifetime of the upper level) with $\tau^{-1} = A + Q(p)$. $Q(p)$ is the overall pressure-dependent quenching rate. Typically $Q(p) \propto p$ and with it $\tau^{-1} \propto p$ holds for a quenching rate that is dominated by collisional processes. $g(\nu)$ corresponds to the normalized Lorentzian line shape function of the underlying *homogeneous* line profile with line width $\Delta\nu_L$. Considering a pressure broadened homogeneous line width with $\Delta\nu_L \propto p$ and using $\Delta\nu_L \times g(\nu_0) = \text{const.}$, it follows that $g(\nu_0)^{-1} \propto p$. Therefore, at not too low pressures, the line center saturation intensity is expected to scale quadratically with pressure, $I_S \propto p^2$. Note that for an inhomogeneously broadened line this holds for all ν . Towards lower pressures, however, $g(\nu_0)$ eventually becomes pressure independent and, more important, diffusion, wall deexcitation and transit-time effects start to prevail the overall quenching. This results in a distinct deviation of I_S from the anticipated p^2 dependence. For example, gain saturation measurements of CO₂ lasers at pressures from 133-267 mbar clearly showed [25] that $I_S \propto p^2$, whereas at pressures below 100 mbar the pressure exponent declined to values well below one [26]. Similarly, for a Doppler-broadened transition of NH₂D, the observed pressure dependence decreased from $p^{1.4}$ at 150 μbar to $p^{0.4}$ at 15 μbar [27]. Hence, in order to elucidate the best working conditions for the Sat-CRDS method, the pressure dependence of the saturation intensity needs to be considered as well.

6.2.2 Ringdown Equation

Under saturation conditions, the effective absorption coefficient of an inhomogeneous broadened line at steady-state condition becomes $\alpha(I, \nu, r, t) = \alpha_0(\nu)/\sqrt{(1 + (I(r, t)/I_S))}$. $\alpha_0(\nu)$ is the non-saturated

absorption coefficient at frequency ν and $I(r, t)$ is the time dependent intensity of the cavity light field, which varies both radially, $r = \sqrt{(x^2 + y^2)}$, and longitudinally along the propagation direction z . Considering that (i) the overall relaxation rate is faster than the empty cavity decay rate (adiabatic case, steady-state condition is fulfilled for all t), (ii) the displacement of a molecule with respect to the beam size is small during a time interval similar to the relaxation time (local approximation, allowing for spatial integration over the transverse Gaussian beam profile [9, 22]), (iii) standing wave effects of the light field can be neglected, and (iv) averaging over the longitudinal field dependence of the light beam within the cavity is possible (i.e, the beam diameter remains nearly constant within the cavity), the power attenuation within the cavity for an inhomogeneously broadened absorption line can be written as [9]

$$\frac{dP(t)}{dt} = -\gamma_c P(t) - \frac{2\gamma_g P(t)}{1 + \sqrt{1 + P(t)/P_S}}. \quad (6.2)$$

$\gamma_c = 1/\tau_c = 2(1 - R)/t_r$ accounts for the intracavity power decay of the empty cavity with a mirror reflectivity R and a round-trip time $t_r = 2L/c$ (i.e., $P(t) = P_0 \times \exp(-\gamma_c t)$). $\gamma_g = c\alpha_0$ is the gas absorption decay rate, which accounts for the non-saturated absorption of the sample, and P_S is the saturation power, $P_S = I_S \times (\pi\omega^2/2)$, with ω the beam waist radius. Note that for $(P(t)/P_S) \rightarrow 0$ the standard ringdown equation is recovered, whereas for $(P(t)/P_S) \rightarrow \infty$ the sample becomes transparent. The intracavity power $P(t)$ is related to the detector signal $S(t)$ (measured in Volt) by a calibration parameter C , $S(t) = C \times P(t)$. In accordance with the literature [22], we define the fitting parameter $Z^{1V} = 1/(CP_S) = 1/S_S$. Z^{1V} is independent of the initial signal amplitude and corresponds to the value of P/P_S for a measured signal amplitude of 1 V. Eq. 6.2 can be rewritten as

$$\frac{dS(t)}{dt} = -\gamma_c S(t) - \frac{2\gamma_g S(t)}{1 + \sqrt{1 + S(t)Z^{1V}}}. \quad (6.3)$$

Eq. 6.3 resembles the Sat-CRDS model that can be fitted to the experimentally observed signal with the adjustable parameters γ_c , γ_g , and Z^{1V} . We also accounted for the detector background signal S_{Bg} , so that the observed signal was fitted to $S(t) + S_{Bg}$. Alternatively, as a numerically more stable variant, the evolution of the signal relative to the empty cavity decay can be described by defining the ratio function $f(t)$ according to

$$f(t, \gamma_c, \gamma_g, Z^{1V}) = S(t)/[S_0 \times \exp(-\gamma_c t)]. \quad (6.4)$$

with its first derivative given by

$$\frac{df(t)}{dt} = -\frac{2\gamma_g f(t)}{1 + \sqrt{1 + S_0 Z^{1V} \exp(-\gamma_c t) f(t)}}. \quad (6.5)$$

Numerical integration is needed to simulate the observed ringdown transient $S(t)$ using Eqs. 6.4 and 6.5.

6.3 Experimental

IR-cw-CRDS Setup

A continuous-wave single resonant optical parametric oscillator (cw-SR-OPO, Lockheed-Martin Aculight Argos 2400-SF Module C) pumped by 10 W of a fiber-amplified (IPG Photonics; YAR series) Yb-doped DFB fiber laser (NKT Photonics; Koheras Adjustik) operated at 1064 nm has been used as

the light source. It was capable of producing > 700 mW of continuously tunable idler output between 3.2 and 3.9 μm with a specified narrow linewidth of < 60 kHz. Fig. 6.1 illustrates a schematic of the OPO coupled to the CRD spectrometer. Whereas the OPO signal and pump beams were dumped, the idler beam passed a ZnSe window acting as a beam splitter to measure the wavelength employing a Michelson type wavemeter (Bristol Instruments; Model 621A-IR) with a specified accuracy of ± 0.2 ppm (i.e., ± 0.0006 cm^{-1} or ± 18 MHz at 3.3 μm) and a repeatability of ± 6 MHz at a sampling frequency of 2.5 Hz. The main beam passed an acoustic optical modulator (AOM, Gooch & Housego Model MM040-5C11B38-5) acting as a fast optical switch with a rise time of 20 ns and a deflection efficiency of 60-70%. The deflected first order beam was guided into a commercial quartz-coated stainless steel ringdown cell (CRD Optics) equipped with multiple ports to establish a gas flow as well as to monitor the gas pressure (MKS Baratron; Model 622B 1 to 10^{-4} mbar) inside the cell. The test gas methane (99.5%) as well as the buffer gas argon (99.999%) were used as supplied.

A focal 50 cm in length Fabry-Perot resonator configuration with two 1 m radius of curvature ring-down mirrors (CRD Optics) with a specified reflectivity of 99.99% at 3.3 μm and a corresponding anti-reflection coating on the back surface has been used. A single 50 cm focusing lens was placed before the input CRD mirror to match both the beam waist position of the cavity as well as the TEM_{00} mode diameter on the mirror surfaces. Based on the resulting Gaussian beam transformation, neglecting the phase mismatch and the wavefront curvature, the theoretical mode matching coupling efficiency can be estimated to be around $\epsilon_{\text{mode}} = 0.58$. Mirror adjustment was accomplished mechanically with mirror mounts equipped with 100 TPI lead screws providing 4 mm of coarse travel and electronically with three piezo elements offering 15 μm maximum travel. The frequency matching condition was achieved by modulating the length of the cavity by a triangle-wave voltage supplied to the three PZTs attached to the rear mirror using a three-channel piezo driver (MDT693B, Thorlabs) and a function generator (33210A, Agilent). Typically, a scanning speed of the cavity resonance frequency of 15 GHz/s has been used.

The geometry of the cavity corresponds to a round trip time of 3.33 ns, a Free Spectral Range $\text{FSR} = c/2L$ of 300 MHz, and a transverse mode spacing of 100 MHz. At 3.3 μm , the TEM_{00} mode of the cavity has a $1/e$ beam waist radius of 0.674 mm and a beam diameter of 0.778 mm on the mirror surfaces, hence the variation of the beam cross-section was merely 33% over the entire cavity (i.e., the Rayleigh range represents 86% of the cavity length). The Fresnel number $F = a^2/(\lambda L) = 78$, with $2a = 22.7$ mm corresponding to the clear aperture of the mirrors, implies that diffraction losses were negligible. The actually measured ringdown time of the empty cavity was about 13.0 μs corresponding to a mirror reflectivity of 99.987% (including losses from scattering, coating absorption, etc.), an effective path length of 3.90 km, a Finesse $\mathcal{F} = 2.4 \times 10^4$, and a cavity mode line width of 12.5 kHz. Finally, the laser light leaking through the rear mirror of the cavity was detected with a high-linearity liquid nitrogen cooled 2 mm InSb photodiode/preamplifier combination (SVS-VISTEK, KISDP-2-A-6/KA-05-CI) with a bandwidth of DC-5 MHz, corresponding to a rise time of 70 ns. The linearity of the detector has been checked by measuring single exponential transients of the empty cavity at different light levels impinging on the detector; for the experiment light levels were kept well below the saturation level of the used amplifier. A comparator circuit was used to trigger the AOM at a preset light level.

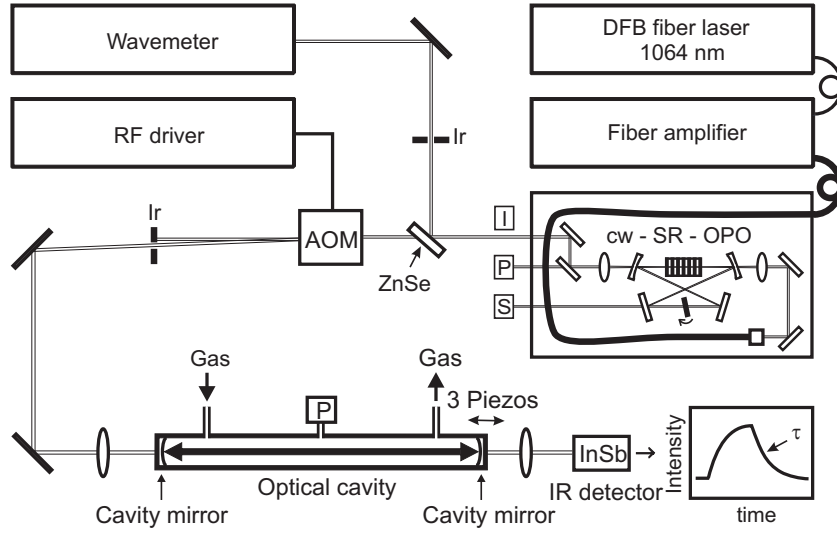


Figure 6.1: Schematic of experimental setup. I, P, S: idler, pump, and signal light beams; Ir: iris diaphragm; P: pressure transducer.

Data Acquisition and Numerical Modeling

Sampling of the decay rates and continuous monitoring of the wavelength were achieved via National Instruments hardware and home-written LabVIEW software. A high-resolution flexible digitizer (National Instrument, NI 5922) was used for digitizing the individual ringdown signals at a sampling rate of 10 MHz and a vertical resolution of 18 bit. High vertical resolution is crucial for Sat-CRDS experiment to prevent the digitized signal to fall below noise level before reaching the transition between the high saturation and the linear absorption regime. Each recorded ringdown transient consisted of 1300 points extending over about 10 decay times. For standard CRDS measurements, a single exponential function was fitted to the transient by a Levenberg-Marquardt nonlinear least-squares method, followed by averaging of typically 100 decay transients. For scanning the spectral line, the decay times were recorded as a function of the laser frequency. Sat-CRDS data acquisition was accomplished by first collecting a total of 400 decay transients, followed by sorting all measured ringdown transients as a function of the initial intensity I_0 and then averaging the set of 100 signals with the highest and the set of 100 signals with the lowest I_0 values. Despite the preset comparator level, due to a $0.7 \mu\text{s}$ delayed response of the AOM switch, this sorting procedure was necessary to confine the 7% variation of I_0 levels to $< 1\%$.

The versatile nonlinear programming solver *fmincon* implemented in MATLAB [28] has been used as a fitting routine to extract the parameter vector \mathbf{x} with γ_c , γ_g , Z^{1V} , I_0 , and the detector offset S_{Bg} as adjustable parameters. *fmincon* seeks the minimizer of a scalar function of multiple variables subject to linear (and non-linear) constraints and bounds. The solver is called by

$$\mathbf{x} = \text{fmincon}(\text{fun}, \mathbf{x}_0, \mathbf{A}, \mathbf{b}, \mathbf{A}_{\text{eq}}, \mathbf{b}_{\text{eq}}, \mathbf{lb}, \mathbf{ub}, \text{options}). \quad (6.6)$$

fun is the function handle (corresponding to the target function, given by the sum of squares of the vertical deviations of $S(t)$ or $f(t)$ from the data points), where numerical integration of Eqs. 6.4 and 6.5 as needed to calculate $S(t)$ and $f(t)$ has been performed on-the-fly using the Runge-Kutta-Fehlberg method *RK45*. \mathbf{x}_0 defines the initial values for the optimizer, \mathbf{A} and \mathbf{b} define linear inequality constraints ($\mathbf{Ax} \leq \mathbf{b}$), \mathbf{A}_{eq} and \mathbf{b}_{eq} linear equality constraints ($\mathbf{A}_{\text{eq}}\mathbf{x} = \mathbf{b}_{\text{eq}}$), and \mathbf{lb} and \mathbf{ub} the lower

and upper bounds ($\mathbf{lb} \leq \mathbf{x} \leq \mathbf{ub}$). Actually, no linear constraints needed to be implemented in this work, however, the lower bound of the solution has been set to 0, except for the detector offset. The *options* keyword specifies some additional optimization options such as the type of algorithm. The *'interior-point'* algorithm has been used in this work.

6.4 Results and Discussion

In the following sections, (i) the ringdown characteristics under different degrees of initial saturation, (ii) the effective working limits of Sat-CRDS with respect to a variable relaxation rate, pumping rate as well as γ_g/γ_c ratio, and (iii) a standard error analysis are presented.

6.4.1 Ringdown Characteristics

As a rule of thumb, optical saturation takes place when the rate of stimulated emission dominates the overall relaxation processes that refill the ground state. Consequently, the extent of optical saturation critically depends on the characteristics of the selected optical transition and on the interaction of the absorbing molecule with the surrounding buffer gas matrix. Moreover, the dynamics of sample saturation is determined by the ratio of relaxation rate and empty cavity decay rate. For fast relaxation the population dynamics can be assumed to be adiabatic all along the ringdown event, but the resulting high I_S values require high intracavity intensities in order to clearly observe non-exponential ringdown curves.

Non-linear Ringdown Curves

The very pronounced effect of a variation of the relaxation rate by changing the sample cell pressure is illustrated in Fig. 6.2. The empty cavity ringdown curve (green) is compared with ringdown curves (red) using argon as a buffer gas at total cell pressures of 200 μbar (Fig. 6.2a) and 5.0 μbar (Fig. 6.2b), respectively, while keeping the initial intracavity power P_0 constant for both experiments. 5.0 nanobar of methane has been added as the saturable absorber. CH_4 has been detected on its strong ($0010 \ ^1F_2 \leftarrow 0000 \ ^1A_1$) transition at $\tilde{\nu} = 3014.711728 \text{ cm}^{-1}$ with a line intensity of $8.217 \times 10^{-20} \text{ cm}$ [29]. As can be seen from the dashed black lines, the saturated ringdown signals are similar to the empty cavity signal at short ringdown times but start to deviate towards lower values at long ringdown times. At $t > 100 \mu\text{s}$ the signals fall below noise level. Obviously, as the ringdown decay is dominated by the empty cavity decay constant at short times, the sample is nearly transparent showing that CH_4 is highly saturated. The overall behavior can be seen even more clearly from the ratio of the Sat-CRD signal and the empty cavity signal (blue curves). In case (a), due to the higher pressure and hence higher relaxation rate, sample absorption starts to recover at $t > 40 \mu\text{s}$ whereas in case (b) the pressure and with it the relaxation rate are so low that the whole saturated ringdown keeps similar to the empty cavity curve. A simulation with the Sat-CRD model (dotted curves) reveals that the ratio $Z_b^{1V}/Z_a^{1V} = 104$ and with it the ratio of the saturation intensities is $I_{S,a}/I_{S,b} = 104$.

A reliable extraction of γ_c and γ_g relies on the measurements of non-exponential ringdown curves. Hence case (b) depicts an unfavorable scenario with too high intracavity light intensity and/or too low saturation intensity. The overall trend of non-exponential behavior upon variation of the cell pressure can be visualized in a comprehensible way by plotting the residuals of single-exponential fits to the Sat-CRDS transients [30]. Fig. 6.3a illustrates such an analysis for typical data of this work

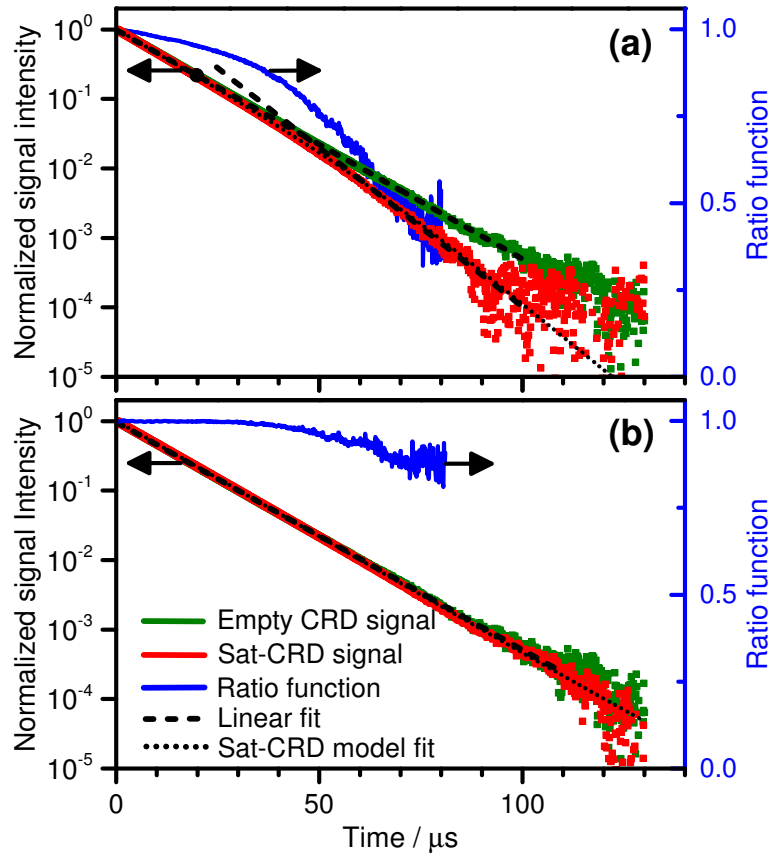


Figure 6.2: Characteristics of Sat-CRD signals. Ringdowns have been measured without (green, empty cavity) and with 5.0 nanobar CH_4 (red) in argon buffer gas at (a) $p = 200 \mu\text{bar}$ and (b) $p = 5.0 \mu\text{bar}$. The left axis refers to the normalized signal intensities for all ringdowns whereas the right axis belongs to the ratio curves (blue). Each signal is an average of 100 transients.

measured at variable cell pressures from $5 \mu\text{bar}$ to 2 mbar. The corresponding reduced χ^2 values and single-exponential decay constants are shown in Fig. 6.3b. The resulting residuals are smallest for the experiment at $5 \mu\text{bar}$ showing that the signal behaves more or less like an empty cavity signal. Obviously, this is due to the achieved high degree of saturation, where at this low pressure the collision deactivation of the excited state is almost negligible. Addition of buffer gas results in an increase of molecular collisions that deactivate the excited state. Thus, the degree of saturation decreases and the transition to the linear absorption regime happens at earlier times during the decay transient. In Fig. 6.3a the increasing non-linearity shows up as a pronounced systematic deviation in the residuals and in Fig. 6.3b as an increase of the reduced χ^2 values. Towards higher pressures χ^2 passes through a maximum with the largest deviation obtained at a pressure about $300 \mu\text{bar}$. Actually, at this pressure the transition from saturated to non-saturated behavior takes place in about the middle of the analyzed ringdown time window. At even higher pressures the saturation intensity continues to increase until it becomes comparable to the initial intensity within the cavity. Consequently, the ringdown curves approach a situation with an overall decay constant representing the single-exponential, non-saturated linear absorption regime.

To summarize, whereas at too low pressures the transition from saturated to non-saturated conditions takes place too late to be resolved within the dynamic range of the digitizer, at too high pressures the saturation effect is shifted to very short times and overall diminishes. Clearly, placing the transition between the two regimes on about the middle of the ringdown event is best for a reliable extraction of

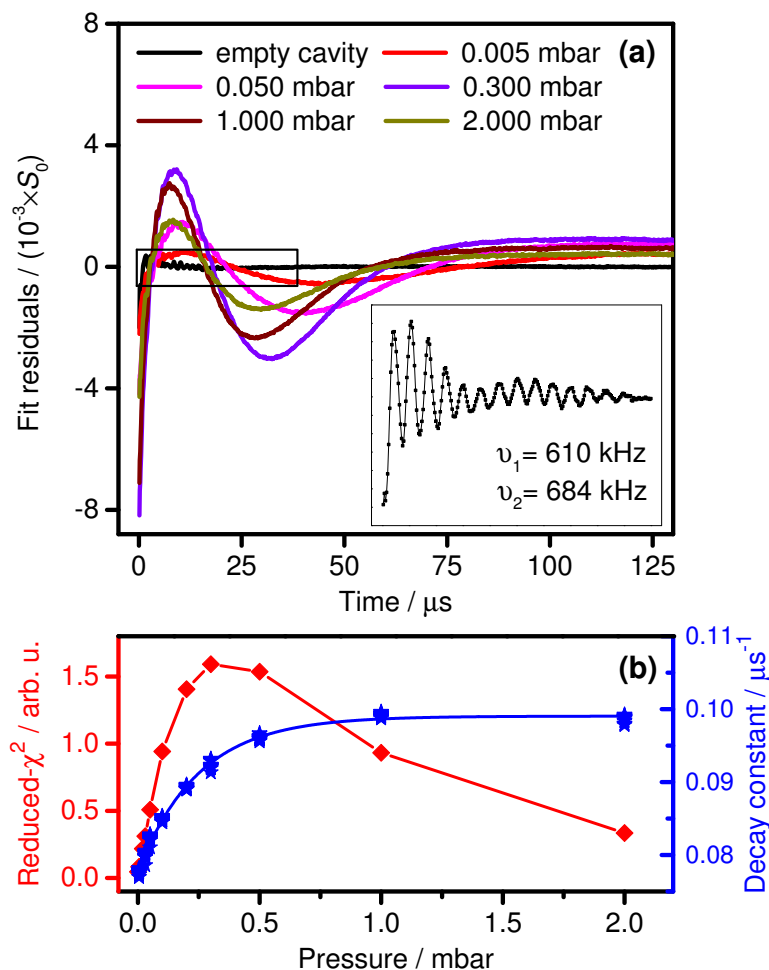


Figure 6.3: (a) Single-exponential fit residuals of Sat-CRDS signals at different cell pressures. $p(\text{CH}_4) = 5.0$ nanobar and $P_0 \approx 3.0$ W for all experiments. The inset illustrates a minor residual oscillation of the ringdown signal containing two distinct frequency components. (b) Corresponding reduced- χ^2 values (left axis) and decay constants obtained from the single-exponential fit of the Sat-CRDS signals (right axis).

γ_c and γ_g . Moreover, in order to clearly separate both regimes it is of utmost importance to digitize the ringdown signals with high vertical resolution. 8 bit digitizers as used in many conventional CRD implementations are not suitable for Sat-CRDS measurements.

It is worth to mention here that nicely resolved oscillations have been observed in the residuals of the fits (inset of Fig. 6.3a). Overall, due to the low amplitude ($< 4 \times 10^{-4}$ relative amplitudes with respect to the initial S_0 signal level), these oscillations were clearly a minor effect that did not critically interfere with the ringdown fitting procedure. The frequency of the oscillations did not change with varied initial intensity I_0 or cell pressure indicating that it is neither a molecular absorption nor a related acoustic effect resulting from thermal heating of the sample. The oscillation frequencies were found to be independent of the scanning speed of the cavity. Typically, the Fourier transform of the residual revealed two dominant frequency components of about 610 kHz and 684 kHz, hence noise components resulting from the operation of the AOM (50 MHz) and ringing effects of the detector/amplifier combination (5 MHz bandwidth) can be ruled out as well. Most likely, the oscillations are a result of a mode-beating of the predominantly excited TEM₀₀ mode with a nearly degenerate higher transverse mode, which can be slightly excited during the fast scan of the cavity

resonance as well. For a perfect focal cavity, degenerate transverse modes with $n + m = 3, 6, 9, \dots$ (n and m are the mode indices) are present, however, already minor deviations from the focal condition removes this degeneracy. In addition, the two distinct frequency components could be explained by an astigmatism of the mirrors. For a cavity with two identical mirrors but small variations of the mirror curvature along the different transverse directions x and y , the astigmatic eigenfrequencies of the cavity are given by [31]:

$$\nu_{q, nm}^{\text{astigmatic}} = \frac{c}{2L} \left[q + \left(\frac{1}{2} + n \right) \frac{\theta_x}{2\pi} + \left(\frac{1}{2} + m \right) \frac{\theta_y}{2\pi} \right]. \quad (6.7)$$

Here, $\theta_{x,y} = 2\arccos(1 - L/R_{x,y})$ are round-trip Gouy phase shifts with a cavity length L and a mirror radius of curvature along the transverse dimension $R_{x,y}$. A deviation in the radius of curvature of $|R_y - R_x|/R = 0.27\%$ would be consistent with the observed frequency separation of 74 kHz.

Saturation Intensity

I_S values were obtained by fitting the saturated ringdown signals collected at the maximum of the absorption line using γ_c , γ_g , Z^{1V} , S_0 , and the detector offset S_{Bg} as free parameters. Z^{1V} is related to the intracavity saturation intensity by the equation

$$I_S = \frac{2}{\pi\omega^2 C Z^{1V}}. \quad (6.8)$$

with the calibration factor

$$C = R_D \times \frac{T(1-L)}{2} \approx R_D \times \frac{(1-R)(1-L)}{2}. \quad (6.9)$$

$R_D = S/P_{\text{out}}$ is the detector responsivity with P_{out} equal to the laser power impinging on the detector. $R_D = 1.29 \times 10^5$ V/W was determined experimentally using a thermal power meter (Thorlabs S302C/PM100D) and was found to be in very good agreement with a value of $R_D = r \times G = 1.25 \times 10^5$ V/W estimated from the specifications of the photodetector responsivity $r = 2.5$ A/W and transimpedance amplifier gain $G = 5.0 \times 10^4$ V/A.

Eq. 6.9 also accounts for the conversion of P_{out} into the intracavity power P . Here, the transmission T of the rear mirror of the ringdown cavity has been set to $(1 - R)$. In principle, the transmission of the mirrors could have been somewhat smaller in case absorption of the coating significantly contributed to the measured overall reflection loss. Allowance was made for an additional loss term $(1 - L)$ and the factor of 2 accounts for intracavity light power in both propagation directions [6]. For example, for an initial power of P_0 of 0.20 W impinging on the cavity front mirror, a transmitted power of 32 μ W was measured, corresponding to a 4.0 V detector signal level and an intracavity power of 0.50 W (only losses L resulting from surface reflections of the focusing lens in front of the detector with $L = 0.06$ have been considered). Hence, the overall experimental coupling efficiency with $\epsilon_{\text{total}} = 1.6 \times 10^{-4}$ was much lower than expected for a perfectly impedance matched cavity with $\epsilon_{\text{total}} = 1$. A quick estimate of the expected injection efficiency for our experimental setup can be based on the consideration that (i) the laser linewidth was five times the cavity mode linewidth (60 kHz versus 12.5 kHz), (ii) the passage time over the cavity resonance was short compared to the ringdown time (15 GHz/s cavity scan speed), and (iii) the mode coupling efficiency was about $\epsilon_{\text{mode}} = 0.58$ as outlined in Section 6.3. Relying on the well elaborated effective injection efficiencies for a scanned cavity reported by Romanini

et al. [32], an ideal coupling efficiency of about $\epsilon_{\text{total}} = 4 \times 10^{-2}$ should have been possible in our case. Clearly, the experimental value was much lower. Possible reasons are a strongly overestimated mirror transmission T (e.g., by not accounting for significant scattering or absorption of the mirror coating), an underestimated loss term $(1 - L)$ (e.g., by additional unidentified transmission/absorption losses of the CRD mirrors) or, probably more important, a larger than expected effective linewidth of the light source. The latter may have resulted from spectral noise components of the OPO seed laser, where noise of the piezo drive voltage directly translates to spectral noise. Note that a better coupling of light radiation into the cavity would allow for Sat-CRDS measurements at higher pressures, therefore future work is necessary to pin down the actual reason. Nevertheless, the achieved intracavity light levels with intensity ratios up to $I_0/I_S = 1000$ (see below) were high enough to investigate the full dynamic range of the Sat-CRDS model.

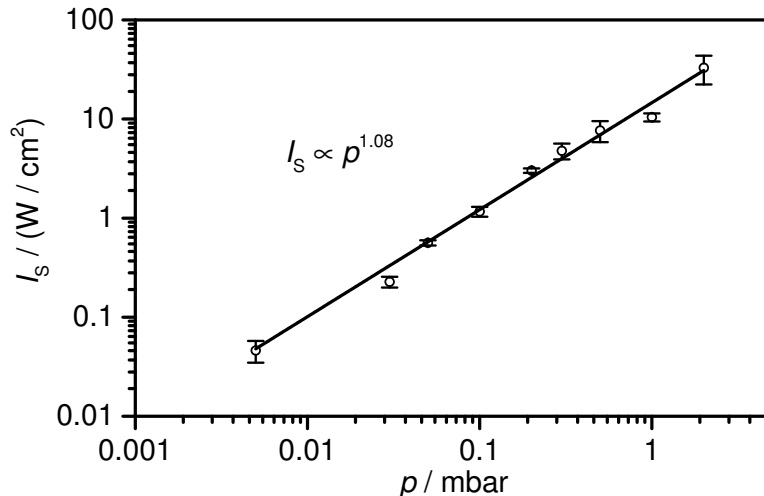


Figure 6.4: Saturation intensity as a function of argon buffer gas pressure. 10 nanobar CH_4 in argon, $\tilde{\nu} = 3014.712 \text{ cm}^{-1}$ ($0010 \ ^1F_2 \leftarrow 0000 \ ^1A_1$). Reported I_S values are based on a minimum loss term of $L = 0.06$ and a mirror transmission set to $T = 1 - R$ (see text); assuming higher losses or lower transmission would result in higher I_S values (see Eqs. 6.8 and 6.9).

Fig. 6.4 shows the determined values of I_S as a function of the cell pressure. The slope of the line in Fig. 6.4 reveals a $p^{1.08}$ pressure dependence of the saturation intensity. As it has been pointed out in Section 6.2.1, the often assumed p^2 dependence is not found at low pressures due to the fact that the overall relaxation becomes dominated by non-collision processes. From simple collision theory, assuming a collision cross-section $\sigma_{\text{Ar-CH}_4} = 0.409 \text{ nm}^2$, a cell temperature $T = 295 \text{ K}$, and a rotational-translational energy transfer probability of $1/12$ [33], each methane molecule suffers a gas phase relaxation collision each $324 \mu\text{s}$ at $p = 5 \mu\text{bar}$ and 809 ns at $p = 2.0 \text{ mbar}$. These numbers can be compared with the collision-free transit time $T_t = 2\omega/v_x = 4.3 \mu\text{s}$ of a molecule with 1D velocity v_x passing through the Gaussian beam within the cavity. Hence, even at a cell pressure of 2 mbar, the relaxation process can be assumed to be significantly influenced by transit-time effects, which is consistent with the low pressure exponent. The estimated values with T_t being close to the observed ringdown decay times also reveal that the assumed adiabatic as well as the local approximation may not be fully satisfied under all experimental conditions. Relaxation rates slow compared to the ringdown decay have the effect that the ringdown transient stays longer saturated than in the adiabatic case. Consequently, fitting such ringdown curves with an adiabatic model yields too low I_S values. This effect may have obscured an even weaker pressure dependence towards lower pressures that can

be expected for a transit-time dominated relaxation scenario.

6.4.2 Working Limits

Since the initial degree of sample saturation P_0/P_S depends on both the relaxation and the pumping rates, the working regime of the Sat-CRDS has been investigated by changing both parameters independently. In addition, at very low pressures, inaccuracies of the Sat-CRDS model may become prominent due to the limiting adiabatic and local approximations. Finally, the ability of the Sat-CRDS model to retrieve the gas absorption decay rate at different absorber concentrations has been investigated.

Relaxation and Pumping Rate

Fig. 6.5 depicts the retrieved values for γ_g and γ_c as a function of the initial degree of saturation P_0/P_S . All data points are based on 20 experiments (each an average of 100 ringdowns) with the detection laser tuned to the maximum of the absorption line. In the experiments shown in Fig. 6.5a, P_0/P_S has been varied by changing the saturation power P_S while keeping the intracavity power constant. P_S was adjusted by changing the cell pressure by adding buffer gas from 5 μbar to 2 mbar. For $P_0/P_S \geq 5$, the extracted values of γ_g and γ_c are consistent and fully agree with the corresponding values obtained from a linear CRD experiments performed at very low intracavity power. However, at $P_0/P_S < 5$ (corresponding to $p > 500 \mu\text{bar}$) the model considerably underestimates the extracted value of γ_g . Obviously, the saturation and the related non-exponential ringdown effects become too small for a reliable parameter extraction.

In the experiments shown in Fig. 6.5b, the P_0/P_S ratio has been controlled by changing the intracavity power P_0 by adjusting the output power of the light source and/or the trigger level of the signal. These measurements were performed at pressures as low as 5 μbar in order to be able to achieve high P_0/P_S ratios. The aim was to explore the upper limit of P_0/P_S at which the Sat-CRDS model fails to extract γ_g due to the fact that throughout the dynamic range of the digitizer the sample essentially stays saturated. At $P_0/P_S \approx 970$ already two signals out of 20 gave outliers for γ_g and at $P_0/P_S \approx 1360$ three outliers have been observed. Including these outliers in the average, the mean value of γ_g yielded too low values with large error bars (dashed line with dashed error bars in Fig. 6.5b). By omitting the outliers, however, the model still predicted consistent γ_g values (solid line with solid error bars). Note that also at $P_0/P_S \approx 390$ the uncertainty of the extracted γ_g was substantial showing that already at this ratio the model started to reach its working limit. Also in Fig. 6.5a the data point at $P_0/P_S \approx 1000$ exhibits a comparably large uncertainty.

Interestingly, no obvious sign was found for the potential failure of the Sat-CRDS model towards the lowest experimental pressures caused by the possible breakdown of the adiabatic and local approximations. The weak trend of lower γ_g and higher γ_c values towards higher P_0/P_S is close to the error limits of the experiments and the effects related to parameter correlation seem to prevail.

Overall, to guarantee reliable parameter extraction, reasonable lower and upper working limits of $5 < P_0/P_S < 300$ can be specified. Actually, the requirement of $P_0/P_S > 5$ can be a limiting factor for practical trace gas measurements at a given mixing ratio level of the absorbing species. As a trade-off between too low signal-to-noise ratio and a too broad absorption line (causing cross-sensitivity issues resulting from nearby absorption lines from interfering species), such measurements are often

performed at cell pressures of several mbar. However, constantly evolving laser technology provides both narrow bandwidth (resulting in a better coupling efficiency to the high-finesse ringdown cavity) and high power lasers (such as modern quantum or interband cascade lasers or the cw-OPO used in this work), hence enabling high P_0/P_S ratios even at mbar pressure levels. Moreover, the problem is relaxed somewhat due to the fact that with higher pressures the absorption feature will no longer be in the inhomogeneously but homogeneously broadened line shape regime. Homogeneously broadened absorption lines, due to the $(1 + \mathcal{S})^{-1}$ instead of $(1 + \mathcal{S})^{-\frac{1}{2}}$ dependence of the absorption coefficient, are easier to saturate. For example, the $^{14}\text{CO}_2$ Sat-CRDS measurements reported by Galli et al.[10] were performed at a pressure of 11.6 mbar with an initial degree of saturation of about 30.

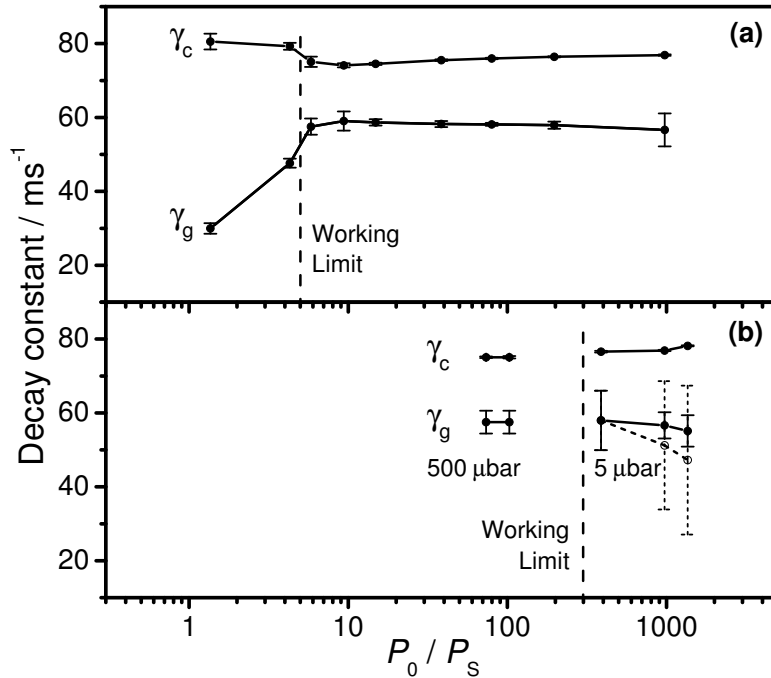


Figure 6.5: Working limits of Sat-CRDS model. (a) Variation of the relaxation rate by changing the cell pressure; the pumping rate is kept constant at $P_0 \approx 0.19$ W. (b) Variation of the pumping rate at fixed cell pressures. For γ_g , the dashed lines are based on all data whereas the solid lines allow for an outlier correction (see text). The error bars correspond to the 1σ standard deviation.

γ_g/γ_c Ratio

Fig. 6.6a illustrates Doppler-limited absorption lines of three rovibrational transitions of methane recorded with Sat-CRDS at different concentrations. The laser frequency was slowly scanned continuously over the absorption transitions by applying a voltage on the seed laser PZT. The seed laser can provide a continuous fine tuning of the idler beam frequency over 100 GHz. γ_g , γ_c , S_0 , and the detector offset were treated as free parameters. As all transition exhibit similar Einstein-A coefficients (24.57 ± 0.11) [29], P_S can be safely assumed to be constant, and hence Z^{1V} was kept fixed. The experimental intensity ratios of the three absorption peaks agree very well with the relative intensities adopted from the HITRAN database [29] and the assigned peak positions are within ~ 0.0009 cm^{-1} of the literature data as well, which is close to the wavemeter resolution. Note that Lamb dips have not been observed due to the relatively fast scan speed of the laser frequency and the ringdown averaging procedure. As presented in Fig. 6.6a, it is possible to simultaneously retrieve reliable γ_g and γ_c values for different peak intensities. However, for the higher concentration experiments and/or

stronger absorption lines with ratios $\gamma_g / \gamma_c \gtrsim 1$, the model starts to show a coupling between the gas absorption and the cavity loss decay rates. This is visible as negative peaks in the extracted empty cavity decay constants. As Sat-CRDS is typically used for measuring very weak absorption features with gas absorption decay constants up to 5 orders of magnitudes lower than the empty cavity decay constant [10], this working limit is of less concern in practical applications. More important is a linear response of the extracted γ_g values with respect to the absorber concentration. The outcome of a corresponding experiment is shown in Fig. 6.6b. Up to a partial pressure of 10 nanobar methane, the linearity of the γ_g values is conserved whereas the γ_c data point at the highest pressure is already lower than expected.

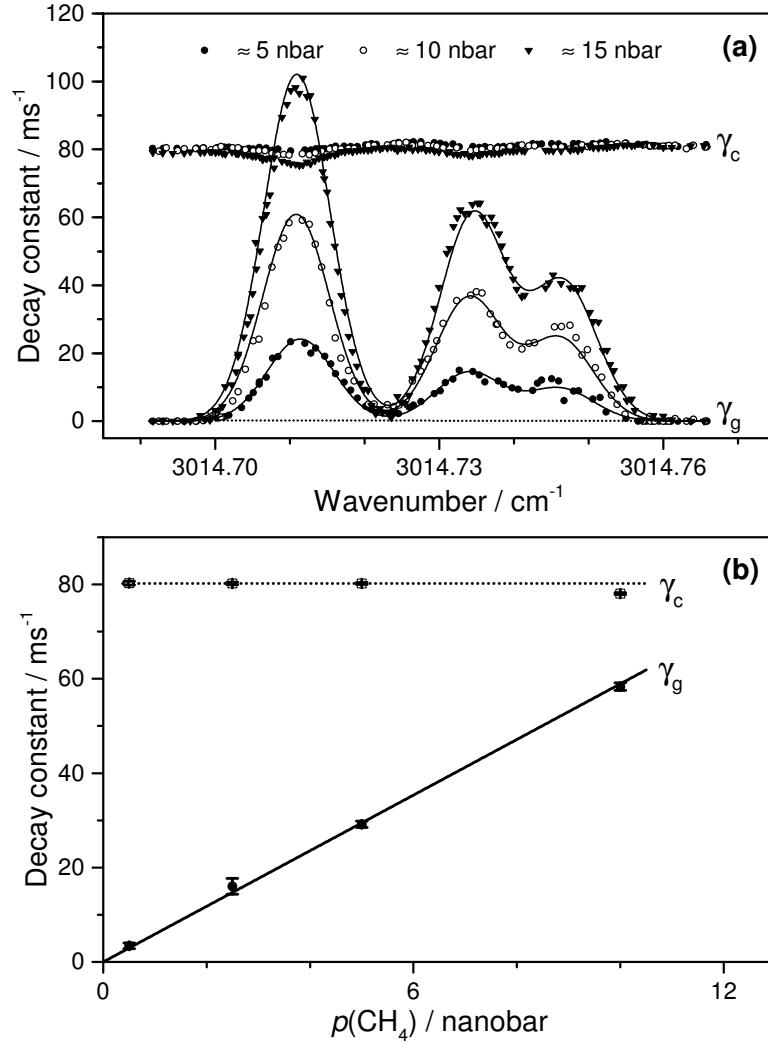


Figure 6.6: (a) CH_4 absorption feature measured by Sat-CRDS method. $p_{\text{total}} = 200 \mu\text{bar}$, $P_0/P_S \approx 67$. The solid curve is based on relative line intensities adopted from the HITRAN database [29]. (b) Linear response of Sat-CRDS. The solid curve represents a line fit of the γ_g data through the origin with $R^2 = 0.9991$.

6.4.3 Standard Error Analysis

A standard error analysis approach has been used to address the optimal Sat-CRDS detection conditions (i.e., the value of the initial degree of saturation that is corresponding to the smallest standard error σ_g for the extracted gas absorption decay rate γ_g). Recent simulations by K. Lehmann [21]

showed that the smallest standard error for γ_g extracted from the saturated signals is about one order of magnitude worse than that of a standard CRDS measurement. This interesting result, which was attributed to strong parameter correlation of γ_g and γ_c , eventually means that the ultimate sensitivity of Sat-CRDS is not expected to be better than for a standard CRDS approach. It is important to note, however, that in his simulations “ideal” noise conditions were assumed, not accounting for additional technical noise sources such as thermal drift, baseline undulations, acoustic interferences, etc. For a detector-noise-dominated situation, which is appropriate for the experimental setup used here, Huang and Lehmann [34] showed that an “ideal” standard error of $\sigma_{\text{total}} = \sqrt{8}\gamma_{\text{total}}^{3/2}P_N/P_0$ can be assumed. Based on this expression, they previously presented a very detailed analysis of the resulting sensitivity limits of non-saturated standard cw-CRDS for variable conditions (trigger level, detection system bandwidth, maximum repetition rate, fit interval, etc.). They also compared the theoretical “ideal” predictions with experimental ringdown data, which were recorded with their very well-characterized CRDS setup. Experimental sensitivities were reported to be about several times lower than the theoretical estimate.

For practical purposes, the experimental standard error of γ_c is often assumed as a more reasonable, straightforward estimate of the detection limit of a standard CRDS experiment. Therefore, in the following discussion we normalize the standard error σ_g of the γ_g values extracted from the Sat-CRDS experiments with respect to the experimental standard error σ_c obtained for γ_c . In this way, the ratio σ_g/σ_c is a rough measure for the precision of the extracted γ_g value relative to the precision of the standard CRDS experiment. A corresponding standard error analysis is presented in Fig. 6.7. The experimental data are given as symbols (left axis) and are compared to the theoretically predicted trend curves reported by Lehmann [34] for a $\gamma_g/\gamma_c = 1.0$ scenario, which is close to the experimental ratio of about 0.75 used in this work (right axis).

For the experimental data, σ_c was determined from empty cavity ringdown signals using the same number of ringdown events as for the determination of σ_g from the Sat-CRDS signals (20 experiments, each an average of 100 transients). In contrast, the theoretical values were referenced with respect to the “ideal” σ_c calculated by setting $\gamma_{\text{total}} = \gamma_c$ in the expression for γ_{total} outlined above. The theoretical prediction have been included in Fig. 6.7 as dashed curves (right axis) for a three-parameter fitting scenario (i.e., γ_g, γ_c, P_0 ; marked with “3” in the Figure) as well as a four-parameter fitting scenario (i.e., $\gamma_g, \gamma_g, P_0, P_s$; marked with “4” in the Figure). Yet another five-parameter fitting scenario with the baseline as an additional parameter was presented by Lehmann as well, but was found to yield essentially the same results as the four-parameter scenario. For our experimental data, a corresponding three-parameter fit (filled symbols) and a fit using the baseline as an additional parameter (open symbols) has been performed. In agreement with Lehmann we find that baseline fitting is not an important issue for the overall analysis.

Experimental values obtained by systematically changing the saturation power (variable cell pressure, P_0 kept constant) are included in Fig. 6.7a whereas Fig. 6.7b illustrates data obtained by changing both the intracavity and saturation power. The connected points in Fig. 6.7b are measured at the same saturation intensity but different intracavity power. The systematically lower σ_g/σ_c ratios for the experiments with higher P_0 can be understood by the higher signal-to-noise ratio of the corresponding ringdown transients. The thick solid lines in Fig. 6.7 reflect the overall trends of the experimental data. The trends are similar to the theoretically predicted ones with a somewhat more pronounced increase towards higher P_0/P_S values with respect to the theoretical 3-parameter fit. Moreover, comparable

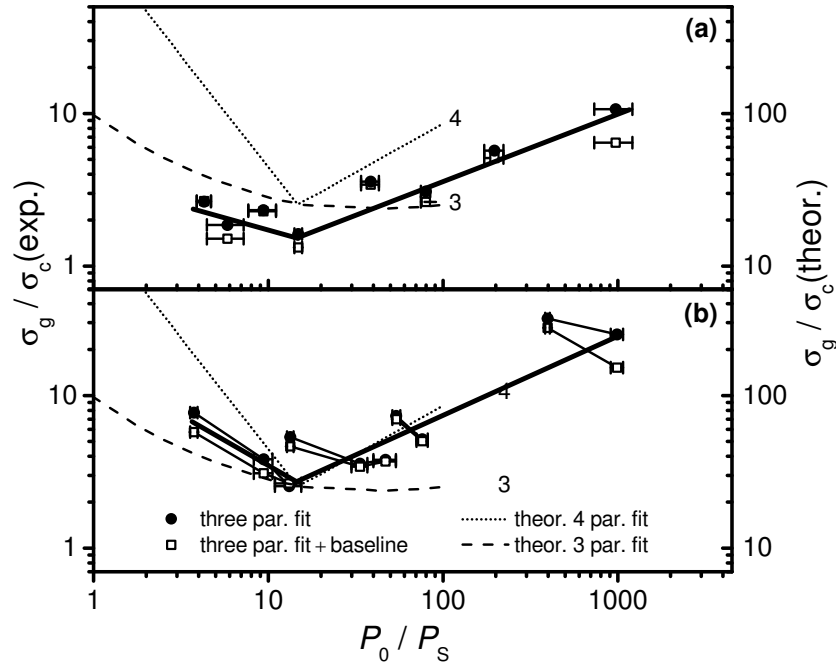


Figure 6.7: Plot of standard error σ_g of γ_g relative to the standard error σ_c of γ_c for (a) a variable P_S and (b) variable P_S and P_0 . Symbols with error bars (1σ standard deviation) refer to experimental values (left axis, referenced to the experimental σ_c). The thick solid lines depict the overall trend of the data. The dashed curves (right axis) are theoretical predictions for a detector noise limited scenario adopted from Lehmann [21]. This prediction is referenced to the “ideal” σ_c value. For details see text.

minima at about $P_0/P_S \approx 15$ are obtained. The good agreement of experiment and theory suggests that this level of initial saturation can serve as a reliable guideline to the experimentalist when designing a sensitive Sat-CRDS detection scheme.

The absolute values of the experimental σ_g/σ_c ratios are about one order of magnitude lower than the theoretical prediction. As already outlined above this difference can be traced back to the different σ_c values used for the normalization. Hence the lower experimental ratios reflect the importance of technical noise contributions in a typical cw-CRDS implementation as used in this work. The experimental minimum value of about 2 further reveals that the precision of the σ_g extraction from the Sat-CRDS approach and with it the ultimate detection sensitivity is comparable to a standard CRDS approach.

However, as our experiments were performed at a fixed frequency, a fair comparison should also consider uncertainties in the empty cavity decay constant and the attainable repetition rate. On the one hand, due to the requirement of using high trigger levels in the Sat-CRDS approach to ensure high saturation levels, the latter tends to be lower. On the other hand, reliable empty cavity decay constant determination in a standard CRDS experiments typically requires scanning over the entire absorption line while the detection frequency can be kept fixed in the Sat-CRDS approach. For example, assuming that 25 spectral data points needs to be measured, the Sat-CRDS approach gains a sensitivity factor of up to $\sqrt{25}$ compared to the standard CRDS approach. Moreover, especially for spectrum acquisition over a wider wavelength range where baseline undulations resulting from etaloning effects become a more serious issue, the Sat-CRDS approach is advantageous. The same holds true when detecting species with dense spectra where, due to line overlapping issues, the precise determination of the empty cavity decay constant often is hardly possible. Altogether, the Sat-CRDS approach holds the potential

to be more sensitive than a standard CRDS approach, especially in cases where the determination of the spectrum baseline is difficult. In other cases, as Lehmann [21] pointed out, “the ‘price’ that parameter correlation will make the standard error in γ_g larger than that of γ_{total} , which is what is determined in a traditional CRDS experiment” may be too high and a well-designed standard CRDS measurement will prevail.

6.5 Conclusion

A new cw-IR-CRDS experimental setup based on a versatile OPO laser system has been established in order to investigate the saturation dynamics and working limits of the Sat-CRDS approach.

The transient dynamics of absorption saturation depends on the interaction of the absorbing molecule with the buffer gas, the overall relaxation as well as the empty cavity decay rate. This behavior is well reflected in the experimentally observed saturated ringdown curves, which have been explored under different saturation conditions ranging from high to low initial degree of saturation and from the *adiabatic* close to the *non-relaxing* limit. An analysis of the residuals resulting from single-exponential fits of the non-exponential Sat-CRDS signals can be used as a quick estimate to determine a reasonable cell pressure for sensitive Sat-CRDS measurements.

For the selected absorption line of methane and with argon as the buffer gas, the pressure dependence of the saturation intensity has been determined at pressures of $5 \mu\text{bar} < p < 2 \text{ mbar}$. It turned out to be about $p^{1.08}$ instead of the typically assumed p^2 dependence showing that the relaxation is significantly influenced by non-collision induced processes such as the transit time.

The working limits of the Sat-CRDS approach, where the model fails to extract reliable gas absorption decay rates γ_g , have been investigated by changing the pumping rate (P_0 , laser power, trigger level), the saturation power (P_S , variable cell pressure) and the γ_g/γ_c ratio. The working limits for the initial saturation are about $5 < P_0/P_S < 300$ for our experimental setup, which is characterized by an empty cavity decay time of about $13 \mu\text{s}$ and 10 MHz/18 bit digitization of the ringdown signals. The Sat-CRDS approach was able to retrieve the absorption spectrum of several absorption lines with different intensities and exhibits linear response with respect to sample concentrations. Moreover, even at low pressures where the underlying adiabatic and local approximation starts to fail, reliable γ_g values were obtained showing that the Sat-CRDS model assumptions are robust. However, for $\gamma_g/\gamma_c \gtrsim 1$ a pronounced coupling of the fitting parameters was observed, hence limiting the dynamic range of Sat-CRDS.

Finally, a standard error analysis has been performed to elucidate an optimized value of the initial degree of saturation. A value of $P_0/P_S \approx 15$ turns out to be optimal, in good agreement with theoretical predictions of Lehmann [21]. The obtained best experimental value for the ratio $\sigma_g/\sigma_c \approx 2$ reveals that the Sat-CRDS approach is not necessarily more sensitive than a standard CRDS detection scheme, however, with careful cavity and mode matching design as well as cavity stabilization measures a smaller relative standard error may be achieved for the Sat-CRDS method. The extra uncertainty resulting from the correlation of the fitting parameters γ_g and γ_c , however, is worth the extra “price” especially in cases where the determination of the empty cavity decay constant is difficult due to baseline instabilities and/or broad absorption features.

Acknowledgements

We would like to thank the Helmholtz Research School Ocean System Science and Technology (HOSST) at the Helmholtz Centre for Ocean Research Kiel - GEOMAR and the Cluster of Excellence “The Future Ocean” (DFG - EC80) at Kiel University for funding. Stimulating discussions with Doug Wallace (Transatlantic Ocean System Science and Technology (TOSST) research school, Dalhousie University, Canada), Arne Körtzinger (GEOMAR, Germany) and the entire HOSST-TOSST team were very helpful to sharpen the practical aspects of the project. Technical support and advice by Lockheed Martin Aculight, the supplier of the cw-OPO laser system, are gratefully acknowledged. We thank the anonymous referees for carefully reading the manuscript and their competent and constructive comments and suggestions for future work.

References

- [1] M. Mazurenka, A. J. Orr-Ewing, R. Peeverall, and G. A. D. Ritchie. Cavity ring-down and cavity enhanced spectroscopy using diode lasers. *Annu. Rep. Prog. Chem., Sect. C*, 101:100–142, 2005.
- [2] G. Friedrichs. Sensitive absorption methods for quantitative gas phase kinetic measurements. Part 2: Cavity ringdown spectroscopy. *Z. Phys. Chem.*, 222(1):31–61, 2008.
- [3] G. Berden and R. Engeln, editors. *Cavity ring-down spectroscopy: Techniques and applications*. Wiley-Blackwell, Oxford, 2009.
- [4] A. P. Yalin and R. N. Zare. Effect of laser lineshape on the quantitative analysis of cavity-ringdown signals. *Laser Phys.*, 12:1065–1072, 2002.
- [5] S. S. Brown, H. Stark, and A. R. Ravishankara. Cavity ring-down spectroscopy for atmospheric trace gas detection: Application to the nitrate radical (NO_3). *Appl. Phys. B Lasers Opt.*, 75(2-3):173–182, 2002.
- [6] J. Y. Lee and J. W. Hahn. Theoretical analysis on the dynamic absorption saturation in pulsed cavity ringdown spectroscopy. *Appl. Phys. B*, 79(5):653–662, 2004.
- [7] S. S. Brown, A. R. Ravishankara, and H. Stark. Simultaneous kinetics and Ring-down: Rate coefficients from single cavity loss temporal profiles. *JPCA*, 104:7044–7052, 2000.
- [8] G. Friedrichs, M. Colberg, M. Fikri, Z. Huang, J. Neumann, and F. Temps. Validation of the extended simultaneous kinetics and ringdown model by measurements of the reaction $\text{NH}_2 + \text{NO}$. *JPCA*, 109(21):4785–4795, 2005.
- [9] G. Giusfredi, S. Bartalini, S. Borri, P. Cancio, I. Galli, D. Mazzotti, and P. de Natale. Saturated-absorption cavity ring-down spectroscopy. *Phys. Rev. Lett.*, 104(11):110801/1–4, 2010.
- [10] I. Galli, S. Bartalini, S. Borri, P. Cancio, D. Mazzotti, P. de Natale, and G. Giusfredi. Molecular gas sensing below parts per trillion: Radiocarbon-dioxide optical detection. *Phys. Rev. Lett.*, 108(17):179902, 2012.
- [11] I. Galli, S. Bartalini, S. Borri, P. Cancio, D. Mazzotti, P. de Natale, and G. Giusfredi. Erratum: Molecular gas sensing below parts per trillion: Radiocarbon-dioxide optical detection. *Phys. Rev. Lett.*, 107:270801–270804, 2011.
- [12] I. Galli, S. Bartalini, P. Cancio, P. De Natale, D. Mazzotti, G. Giusfredi, M. E. Fedi, and P. A. Mando. Optical detection of radiocarbon dioxide: First results and AMS intercomparison. *Radio-carbon*, 55:213–223, 2013.
- [13] I. Galli, S. Bartalini, R. Ballerini, M. Barucci, P. Cancio, M. de Pas, G. Giusfredi, D. Mazzotti, N. Akikusa, and P. de Natale. Spectroscopic detection of radiocarbon dioxide at parts-per-quadrillion sensitivity. *Optica*, 3(4):385, 2016.
- [14] L. Lehr and P. Hering. Quantitative nonlinear spectroscopy: A direct comparison of degenerate four-wave mixing with cavity ring-down spectroscopy applied to NaH. *IEEE J. Quantum Elec.*, 33(9):1465–1473, 1997.

- [15] D. Romanini, P. Dupré, and R. Jost. Non-linear effects by continuous wave cavity ringdown spectroscopy in jet-cooled no_2 . *Vib. Spectrosc.*, 19(1):93–106, 1999.
- [16] I. Labazan, S. Rudić, and S. Milošević. Nonlinear effects in pulsed cavity ringdown spectroscopy of lithium vapour. *Chem. Phys. Lett.*, 320:613–622, 2000.
- [17] C. R. Bucher, K. K. Lehmann, D. F. Plusquellic, and G. T. Fraser. Doppler-free nonlinear absorption in ethylene by use of continuous-wave cavity ringdown spectroscopy. *Appl. Opt.*, 39(18):3154–3164, 2000.
- [18] D. Lisak and J. T. Hodges. High-resolution cavity ring-down spectroscopy measurements of blended H_2O transitions. *Appl. Phys. B Lasers Opt.*, 88:317–325, 2007.
- [19] A. A. Mills, B. M. Siller, and B. J. McCall. Precision cavity enhanced velocity modulation spectroscopy. *Chem. Phys. Lett.*, 501:1–5, 2010.
- [20] A. McIlroy and J. B. Jeffries. *Cavity Ringdown Spectroscopy for Concentration Measurements*. Taylor and Francis, New York, 2002.
- [21] K. K. Lehmann. Theoretical detection limit of saturated absorption cavity ring-down spectroscopy (SCAR) and two-photon absorption cavity ring-down spectroscopy. *Appl. Phys. B: Lasers Opt.*, 116:147–155, 2014.
- [22] G. Giusfredi, I. Galli, D. Mazzotti, P. Cancio, and P. de Natale. Theory of saturated-absorption cavity ring-down: Radiocarbon dioxide detection, a case study. *J. Opt. Soc. Am. B*, 32(10):2223, 2015.
- [23] A. Yariv. *Quantum Electronics*. John Wiley & Sons, New York, 3rd edition, 1989.
- [24] W. Demtröder. *Laser Spectroscopy: Experimental Techniques*, volume 2. Springer, Berlin, Heidelberg, 2008.
- [25] R. L. Abrams and W. B. Bridges. Characteristics of sealed-off waveguide CO_2 , lasers. *IEEE J. Quant. Electr.*, 9:940–946, 1973.
- [26] K. Matsumoto, H. Shirahata, and T. Fujioka. The effect of wall deexcitation on saturation intensity in a CO_2 waveguide laser. *IEEE J. Quant. Electr.*, 14:781–782, 1978.
- [27] L. Thielman and L. W. Davis. Determination of saturation intensity in NH_2D . *Appl. Phys. Lett.*, 25:461–463, 1974.
- [28] *MATLAB Optimization Toolbox, Version 8.5 (R2015a)*. The MathWorks Inc., Natick, Massachusetts, 2015.
- [29] L. S. Rothman, I. E. Gordon, Y. Babikov, A. Barbe, D. Chris Benner, P. F. Bernath, M. Birk, L. Bizzocchi, V. Boudon, and L. R. Brown *et al.* The HITRAN2012 molecular spectroscopic database. *J. Quant. Spectrosc. Radiat. Transfer*, 130:4–50, 2013.
- [30] P. Cancio, I. Galli, S. Bartalini, G. Giusfredi, D. Mazzotti, and P. De Natale. *Saturated-Absorption Cavity Ring-Down (SCAR) for High-Sensitivity and High-Resolution Molecular Spectroscopy in the Mid IR*. Springer, Heidelberg, 2014.

- [31] J. Courtois, A. Mohamed, and D. Romanini. Degenerate astigmatic cavities. *Phys. Rev. A*, 88:043844, Oct 2013.
- [32] G. Gagliardi and H.-P. Loock, editors. *Cavity-enhanced spectroscopy and sensing*, volume 179 of *Springer series in optical sciences*, 0342-4111. Springer, Heidelberg, 2014.
- [33] P. G. Kistemaker, M. M. Hanna, A. Tom, and A. E. De Vries. Rotational relaxation in mixtures of methane with helium, argon and xenon. *Physica*, 60:459–471, 1972.
- [34] H. Huang and K. K. Lehmann. Sensitivity limits of continuous wave cavity ringdown spectroscopy. *J. Phys. Chem. A*, 117:13399–13411, 2013.

Two-Species One-Wavelength Detection Based on Selective Optical Saturation

Ibrahim Sadiek,^a and Gernot Friedrichs^{*ab}

^aInstitut für Physikalische Chemie, Christian-Albrechts-Universität zu Kiel, Max-Eyth-Str. 1, D-24118 Kiel, Germany. ^bKMS Kiel Marine Science - Centre for Interdisciplinary Marine Sciences, Olshausenstr. 40, D-24098 Kiel, Germany.

To be submitted.

Own contributions:

- Realization of the “Two-species One-wavelength” detection approach.
- Performing all CRDS and direct LAS measurements.
- Analysis and discussion of the experimental data.
- Writing of paper draft.

ABSTRACT: Cross-sensitivity represents a barrier for quantitative measurements in all sensor technologies. In optical absorption based sensors, the acquired spectrum will be a superposition of all the interfering molecules at the same wavelength. Herein, we report a new approach for two species detection at the same wavelength utilizing the different optical saturation behavior of interfering transitions. In the Two-species One-wavelength detection approach, the absorption-saturation is introduced as a second dimension to the standard absorption-frequency (absorption spectrum) to differentiate between the absorption of overlapping transitions. The functionality of the approach relies on the fact that different molecules have different degrees of saturation that is determined by the transition probabilities of the overlapping transitions and the energy transfer probabilities of the different molecular systems. Therefore, tuning the degree of saturation by controlling the pumping power and/or the deactivation rates of the populated excited states results in discrimination of the individual absorption in the mixture. As a proof-of-concept, direct laser absorption spectroscopy (LAS) and cavity ringdown spectroscopy (CRDS) have been implemented to retrieve the individual absorption of several overlapping transitions of CH_4 and CH_3Cl . A double-banded absorbance-power behavior for LAS measurements is essential for efficient extraction of the individual absorption. The CRDS scheme provides large optical pathlength and low limit of detection which enhance the saturation power difference between the overlapping transitions. In addition, the concentration of both interfering species can be extracted from a single ringdown event, hence a typical measurements time of few tens of μs . A very good linearity with respect to the determined mixing ratios of both species has been accomplished for pressures up to 10 mbar. Two-species One-wavelength detection, next to enhancing the capability of laser absorption spectroscopy for multi-species sensing applications, can be used to investigate the energy transfer pathways upon molecular collisions as well.

Laser based absorption spectroscopy involves the measurements of the attenuation of a light beam transmitted through a sample as function of photon energy, resulting in the absorption spectrum [1, 2, 3, 4]. In linear absorption regime, Beer-Lambert's law can be directly used to determine the sample concentration, assuming that the absorption cross section is known. Very often the spectral overlap (i.e., so-called absorption cross-sensitivity) is the critical limiting factor for implementing laser based absorption spectroscopy for molecular sensing applications. Even for a carefully selected spectral window, the overlap of a very weak absorption features often limits the accuracy for quantitative sensing applications. Next to careful spectral line selection, there exist some precautions that may reduce the cross-sensitivity issue including (i) the use of narrow bandwidth light sources that enable absorption features of different molecular species to be better separated, in particular at low sample pressure and temperature; or (ii) the measurement of the absorption spectra over a wide spectral range and use of fitting routines to retrieve the mixture composition more reliably (e.g., by FTIR [5] or optical frequency comb based spectrometers [6]). In many cases this is not sufficient and upstream separation of the sample mixture based on their physicochemical properties is necessary [7, 8, 9], often accomplished by gas chromatography based techniques. Such separation approaches usually add extra complexity, and in most cases, require regular instrument calibration.

Herein, we explore the use of optical saturation to efficiently discriminate between a target absorber (which is usually the easier saturable species) and an interfering absorber (typically the non-saturated species). In addition, by using a cavity ringdown scheme as outlined below, quantitative detection of

both species can be accomplished simultaneously at single frequency (Two-species One-wavelength) within few tens of μs . Two-species One-wavelength detection based on saturated absorption spectroscopy can be considered as a type of two-dimensional (2D) spectroscopy, where the sample absorption saturation is a second dimension next to the frequency axis of the absorption spectrum. As this type of spectroscopy allows one to separately measure the concentration of two species absorbing exactly at the same wavelength, it overcomes, or at least significantly reduces, the limitations arising from spectral band overlap and, at the same time, enhances the versatility of absorption spectrometers for multi-species detection.

Saturation of optical transitions is a well-known effect in laser spectroscopy and has been mainly used as an extremely powerful tool to push the frequency precision far below the Doppler limit. On the one hand, the term ‘‘saturation spectroscopy’’ typically alludes to spectroscopic detection schemes that try to achieve higher spectral resolution (e.g., Lamb-dip spectroscopy [10]) and not for the intentional use to perform quantitative single or multi-species detection. On the other hand, the concept of using partial saturation intentionally has been demonstrated to simplify the spectrum assignment in nuclear magnetic resonance experiments (e.g., broadband decoupling, nuclear overhauser effect spectroscopy) or to allow for performing conformer specific spectroscopy in many double-resonance experiments [11]. Yet another example is saturation transfer difference nuclear magnetic resonance (STD-NMR) that is frequently used for the study of protein-ligand interactions [12].

For two overlapping absorption transitions under saturation conditions, the effectively measured absorption coefficient (assuming homogeneously broadened absorption profiles ¹) becomes a function of the light power P and the saturation power P_s .

$$\alpha(\nu, P) = \frac{\alpha_0^{\text{gas1}}(\nu)}{1 + P/P_s^{\text{gas1}}} + \frac{\alpha_0^{\text{gas2}}(\nu)}{1 + P/P_s^{\text{gas2}}}, \quad (7.1)$$

Here, α_0^{gas1} and α_0^{gas2} are the non-saturated (i.e., linear) absorption coefficients of the interfering gases, with P_s^{gas1} and P_s^{gas2} representing the corresponding saturation powers. The input light power P controls the depletion efficiency of the ground state population, while the saturation power P_s , a molecule and collider specific property, is proportional to the overall relaxation rate of the excited state as well as the absorption transition probability that is related to the Einstein-A coefficient of spontaneous emission. In an ideal Two-species One-wavelength experiment, P_s^{gas1} and P_s^{gas2} are largely different. Therefore, by gradually increasing/or decreasing the laser power, the measured effective absorption coefficient for two overlapping transitions of sufficiently different saturation powers will show a ‘‘double-bended’’ behavior as a function of the laser power. At low laser power the absorption coefficient $\alpha(\nu)$ corresponds to the sum of α_0^{gas1} and α_0^{gas2} . With increasing power, a first bend in $\alpha(\nu)$ is observed corresponding to the saturation of the strong saturable absorber. A second bend is observed at even more higher input laser power corresponding to saturation of the second saturable absorber. The observation of the double-bended behavior is controlled by the difference in saturation powers of the overlapping transitions. For molecules with comparable transition probabilities as well as energy transfer probabilities, the onset of the saturation of the two species will be hardly separable. Therefore, for intentional use of optical saturation for two-species detection, the overlapping transitions should be selected properly to support a large difference in saturation power.

¹For inhomogeneous absorption profiles the denominator of Eq. 7.1 needs to be replaced by $\sqrt{1 + P/P_s^{\text{gas1}}}$.

Here, we demonstrate the functionality of optical saturation for two-species measurements both in a direct laser absorption spectroscopy (LAS) and in a cavity ringdown spectroscopy (CRDS) schemes. As proof-of-concept, a set of blended rotational-vibrational transitions of the $3\nu_6$, ν_4 , and ν_1 bands of CH_3Cl (gas1: weak saturable absorber) with that of the ν_3 band of CH_4 (gas2: strong saturable absorber) has been targeted. For the direct LAS scheme (see Fig. 7.S1, in the Supplement), we used Eq. 7.1 to directly model the measured saturated absorption as a function of the input laser power.

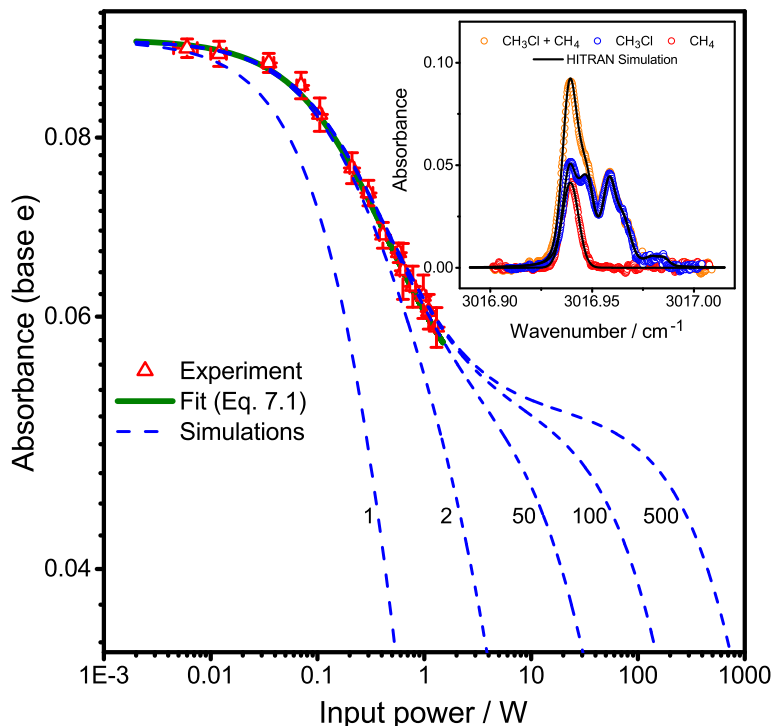


Figure 7.1: Absorbance (red points) measured as a function of the laser input power at the top of overlapping transitions for a mixture of $20 \pm 0.5 \mu\text{bar}$ CH_4 and $1.85 \pm 0.05 \text{ mbar}$ CH_3Cl in 10 mbar of Ar using a direct LAS setup. The green curve represents the fitting of Eq. 7.1 to the experimental data. The different blue dashed curves represent simulations using Eq. 7.1 for different $P_s^{\text{CH}_3\text{Cl}}$ (the numbers on the curves depict the ratios of $P_s^{\text{CH}_3\text{Cl}} / P_s^{\text{CH}_4}$ (see text)). The inset presents linear spectra measured for the gas mixture and the individual species with the same concentration and total cell pressure, at very low input power of $< 4 \text{ mW}$.

Figure 7.1 presents the measured outcome of such a direct LAS experiment. In this figure, the absorbance measured at the top of overlapping rovibrational transitions of CH_3Cl and CH_4 around 3016.94 cm^{-1} (see inset of Fig. 7.1) is presented as a function of the detection laser power in logarithmic scale. Complete spectral scans at different input power are shown in the supplementary Fig. 7.S2. The measurements were performed for a mixture of $20.0 \pm 0.5 \mu\text{bar}$ CH_4 and $1.85 \pm 0.05 \text{ mbar}$ CH_3Cl in 10 mbar of Ar. Individual spectra of CH_3Cl and CH_4 in 10.0 mbar Ar were also measured independently at linear absorption conditions of very low power, yielding a $\text{CH}_4/\text{CH}_3\text{Cl}$ absorbance ratio of 0.82 ± 0.02 . As shown in Fig. 7.1, a first bend in the absorbance appears at relatively low input power of about 50 mWatt, attributed to the saturation of the CH_4 transition. In principle, a second transition, which is not fully captured with the experimentally available input powers, should indicate the saturation of CH_3Cl . The data were fit using the “double-bended” absorbance-power relationship Eq. 7.1 with $\alpha_0^{\text{CH}_4}$, $\alpha_0^{\text{CH}_3\text{Cl}}$, $P_s^{\text{CH}_4}$ and $P_s^{\text{CH}_3\text{Cl}}$ as adjustable parameters. The extracted $\alpha_0^{\text{CH}_4}$ and $\alpha_0^{\text{CH}_3\text{Cl}}$ yielded a $\text{CH}_4/\text{CH}_3\text{Cl}$ absorbance ratio of 0.84 ± 0.04 , hence in very good agreement with the independent result obtained from the independent linear measurements of the individual species. Actually, the

model was not able to give a reliable fit value for $P_s^{\text{CH}_3\text{Cl}}$ since the saturation of CH_3Cl was not fully captured. In addition, simulations of double-banded profiles using Eq. 7.1 for $P_s^{\text{CH}_3\text{Cl}} = nP_s^{\text{CH}_4}$, with $n = 1, 2, 50, 100,$ and 500 are presented in Fig. 7.1. In this simulations $\alpha_0^{\text{CH}_4}$ and $\alpha_0^{\text{CH}_3\text{Cl}}$ were fixed to their values obtained from the linear measurements and $P_s^{\text{CH}_4}$ was fixed to the value obtained from the fitting results. The aim of this exercise was to estimate the saturation power ratio required for reproducing a double-banded profile for efficient parameters extraction. As shown in this figure, for simulations with $P_s^{\text{CH}_3\text{Cl}}/P_s^{\text{CH}_4} = 1$, not surprisingly, the whole absorbance profile is similar to an absorption saturation profile of single species. An obvious double-banded profile is revealed for saturation power ratio n of more than 20. The presented experimental data (red points) are best reproduced by a double-banded profile corresponding to a saturation power ratio of ≈ 50 . This difference in case of CH_3Cl and CH_4 is favored by about one order of magnitude lower transition probability (based on the values of the Einstein- A coefficient tabulated in HITRAN database [13]) of CH_3Cl and more than one order of magnitude faster relaxation rate of CH_3Cl relative to that of CH_4 [14].

Saturated-absorption cavity ringdown spectroscopy (Sat-CRDS) has been used as a second optical detection scheme to demonstrate the functionality of the Two-species One-wavelength detection approach. Using a CRD scheme holds the advantage of a simple setup together with the strong immunity against both laser intensity fluctuations and laser frequency noise [15]. Moreover, (i) the high-finesse optical cavity effectively multiplies the intracavity power (hence enabling the use of relatively low power light sources); (ii) the measurement is intrinsically fast as the intracavity power decays within a few tens of μs (hence allowing quick and continuous change from strong saturated to non-saturated conditions); (iii) the attainable limit of detection (LOD) is very low and allows for measurements of trace amounts of target species. Low absorber densities in the buffer gas matrix also simplifies the energy transfer dynamics by ensuring almost independent relaxation dynamics of each of the interfering molecules (see Supplementary text); Finally, (iv) the measurement of the decay rates rather than the absolute laser intensity allows for a better constrained data fit with low uncertainties by using well-developed models for the analysis of the saturated ringdown transients [16, 17, 18, 19, 20]. Giusfredi et al. [18, 19] have demonstrated in their Sat-CRDS experiments that the gas absorption of a single species can be “switched-off” during the beginning of the ringdown event. This enabled the measurement of both empty cavity decay rate (i.e., the decay rate without an absorber in the cavity) and the absorption of the species (i.e., the gas absorption decay rate) within only one single decay transient. The analysis relies on the *adiabatic* saturation assumption: At sufficiently high cavity pressure, the overall relaxation rate is fast compared to the empty cavity decay rate, hence keeping the saturation level in a quasi-steady state during the ringdown event. Recently, by using CH_4 as a saturable absorber, we have investigated the dynamic evolution of the optical saturation and the working limits of Sat-CRDS. Error analysis revealed that the standard error of Sat-CRDS is comparable to that of standard CRDS [20, 21].

When two absorbing molecules with different degree of saturation are present inside optical resonator, the intracavity power decay still reflects the saturation evolution of the absorbing molecules relative to the empty cavity decay rate. Let us assume that, at the beginning of the decay transient, the transition with the lower saturation power will saturate (i.e., “switched-off”). Then the initial ringdown decay will be determined by the empty cavity losses plus the absorption losses from non-saturated transitions. Later on, the decay becomes faster due to the absorption contribution of the initially saturated species since it restores the linear absorption with power attenuation. Consequently, in the *adiabatic* limit,

the absorption of the two transitions can be decoupled by proper modeling of the observed ringdown transient.

For the analysis of the resulting ringdown transients, we strongly rely on the saturation model [22] put forward by Giusfredi et al. [18, 19] and as used by us in our recent paper [20]. The saturation model represents the intracavity power $P(t)$ in the general form,

$$P(t) = P_0 \times \exp(-\gamma_{\text{empty}}t) \times [f_1(t, \gamma_{\text{empty}}, \gamma_{\text{gas1}}, P_s^{\text{gas1}}) + f_2(t, \gamma_{\text{empty}}, \gamma_{\text{gas2}}, P_s^{\text{gas2}})], \quad (7.2)$$

with functions f_1 and f_2 describing the saturation evolution of gas1 (i.e., with gas absorption decay rate γ_{gas1}) and gas2 (i.e., with gas absorption decay rate γ_{gas2}) relative to the empty cavity decay rate γ_{empty} , respectively. Details of the mathematical model are outlined in the Supplement. Here, we assume that gas2 has significantly lower saturation power than gas1, $P_s^{\text{gas1}} \gg P_s^{\text{gas2}}$. This reduces the general equation Eq. 7.2 to the standard Sat-CRDS equation

$$P(t) = P_0 \times \exp(-\gamma_1 t) \times f(t, \gamma_1, \gamma_2, P_s) \quad (7.3)$$

with $\gamma_1 = \gamma_{\text{empty}} + \gamma_{\text{gas1}}$ (as an overall “non-saturated channel”) and $\gamma_2 = \gamma_{\text{gas2}}$ (as an overall “saturated channel”). Without this assumption, the measured Sat-CRDS transients would need to be fitted by floating three beating decay rates ($\gamma_{\text{empty}}, \gamma_{\text{gas1}}, \gamma_{\text{gas2}}$), which turned out to be unstable. In order to be able to determine these three decay rates, the saturation powers P_s^{gas1} and P_s^{gas2} need to be sufficiently different such that the decay rates can be temporally separated. The assumptions of Eq. 7.3 can be more easily satisfied by tuning the intracavity power as well as the relaxation rate of the absorbing species (i.e., by adjusting the cell pressure).

Figure 7.2 illustrates the outcome of a Sat-CRDS experiment with a mixture of 30 μbar CH_3Cl and 8.0 nbar CH_4 in 2.50 mbar of argon at intracavity light power of about 1.6 W. The laser was scanned continuously over the overlapping transitions and the ringdown decay transients were analyzed by the saturation model. The extracted $\gamma_1 = \gamma_{\text{empty}} + \gamma_{\text{CH}_3\text{Cl}}$ and $\gamma_2 = \gamma_{\text{CH}_4}$ decay rates are depicted in Fig. 7.2A and B, respectively. For reference, the linear spectra of CH_4 and CH_3Cl , as measured with the same CRDS setup at very low intracavity power, are included in the same panels. CH_3Cl absorption shows up as distinct absorption peaks over the empty cavity losses, while that of CH_4 is captured by the absorption related decay constant relative to γ_1 . The spectra extracted from Sat-CRDS measurements are in agreement with the linear spectra showing that both the $\gamma_{\text{CH}_3\text{Cl}}$ and γ_{CH_4} parameters are nicely decoupled. This is further underlined by the saturated decay transients and their fit residuals to the single exponential function shown in Fig. 7.S3, which reflect the expected saturation evolution within the decay transients. The experiment of Fig. 7.2 is highlighting a key advantage of Two-species One-wavelength approach, which is the possibility to extract a target absorption in the presence of congested background absorption.

It can also be seen in Fig. 7.2A and B that the noise level in the extracted γ_{CH_4} absorption is somewhat higher than that of $\gamma_{\text{empty}+\text{CH}_3\text{Cl}}$, although the empty cavity background may even add some noise. This is due to the fact that the intrinsic noise level in the later part of the ringdown event, which is used for γ_{CH_4} extraction, is higher. Another example of decoupled individual absorption spectra for a less congested spectra over a wide spectral window is presented in Fig. 7.S4. Again, the extracted $\gamma_{\text{empty}+\text{CH}_3\text{Cl}}$ and γ_{CH_4} decay parameters for the strong absorption features were in very good agree-

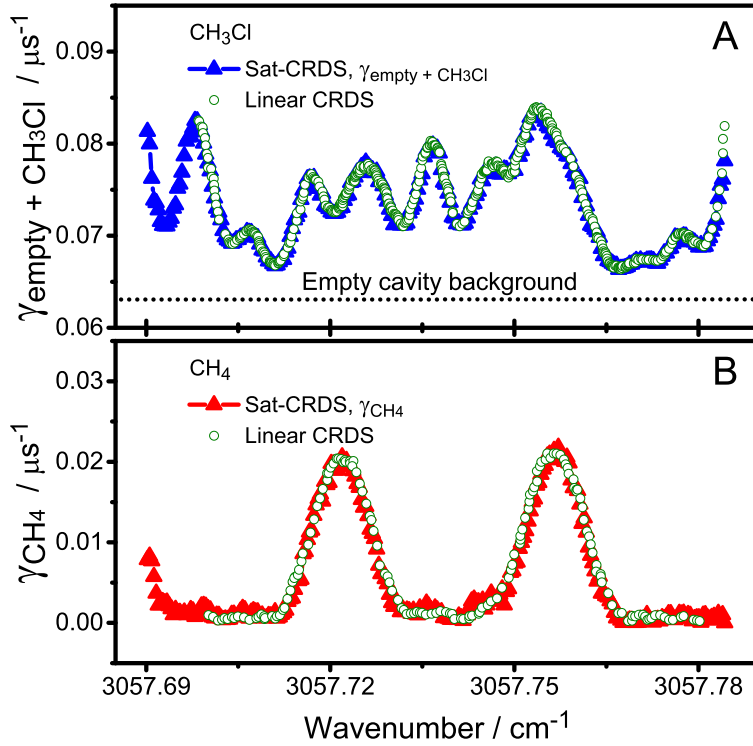


Figure 7.2: Rovibrational absorption spectra of CH_3Cl (blue) and CH_4 (red) recorded for a mixture of $30 \mu\text{bar}$ CH_3Cl and 8 nbar CH_4 in 2.50 mbar of Ar. The laser frequency was scanned and the saturated decay transients were recorded and analyzed separately (5 Hz repetition, 10 s averaged spectra are shown). The collected decay transients were fit with $\gamma_{\text{empty}+\text{CH}_3\text{Cl}}$, γ_{CH_4} , P_0 , and detector offset as adjustable parameters. The linear absorption spectra for individual species (green) have been recorded with the same setup in separate experiment.

ment with the simulated spectra (see Supplement). Actually, a small residuals in the extracted γ_{CH_4} (highlighted by dotted circles in Fig. 7.S4) indicated imperfect decoupling of $\gamma_{\text{CH}_3\text{Cl}}$ and γ_{CH_4} . This is probably due to residual saturation of the strong CH_3Cl absorption lines. As perfectly linear absorption has been assumed for CH_3Cl in the saturation model according to Eq. 7.3, residual saturation are expected to show up in the “saturated channel” attributed to γ_{CH_4} . Also note that this imperfect decoupling causes the CH_3Cl absorption to be slightly underestimated and the CH_4 absorption to be slightly overestimated in the overlapping region.

A more detailed analysis of the performance of the CRD spectrometer in terms of the Allan standard deviation of the extracted γ_{CH_4} and $\gamma_{\text{empty}+\text{CH}_3\text{Cl}}$ decay rates (Fig. 7.S5), reveals that $\gamma_{\text{empty}+\text{CH}_3\text{Cl}}$ exhibits about a factor of 1.5 lower noise compared to γ_{CH_4} . The optimum averaging time of $\sim 200 \text{ s}$ yields a standard deviation of $7 \times 10^{-5} \mu\text{s}^{-1}$ and $1 \times 10^{-4} \mu\text{s}^{-1}$ for $\gamma_{\text{empty}+\text{CH}_3\text{Cl}}$ and γ_{CH_4} , respectively. This corresponds to a single-shot standard deviations of absorption coefficient of $\sigma(\alpha_{\text{CH}_3\text{Cl}}, 1 \text{ shot}) \sim 6.7 \times 10^{-8} \text{ cm}^{-1}$ and $\sigma(\alpha_{\text{CH}_4}, 1 \text{ shot}) \sim 2.0 \times 10^{-7} \text{ cm}^{-1}$, respectively. This limit of detection compares very well with previously reported values of $0.2 - 1.5 \times 10^{-7} \text{ cm}^{-1}$ achieved for a quantum cascade laser based cw-IR-CRDS implementation for single species detection in the linear regime [23].

Figure 7.3 depicts the linearity of the extracted γ values for different CH_4 and CH_3Cl mixtures, measured at the top of overlapping transition at $3057.7565 \text{ cm}^{-1}$. Two series of experiments are presented both were performed at a total cell pressure of 2.50 mbar and an intracavity power of about 1.7 W . For the experiments in panel A, CH_3Cl partial pressure was kept constant at $30 \mu\text{bar}$ and

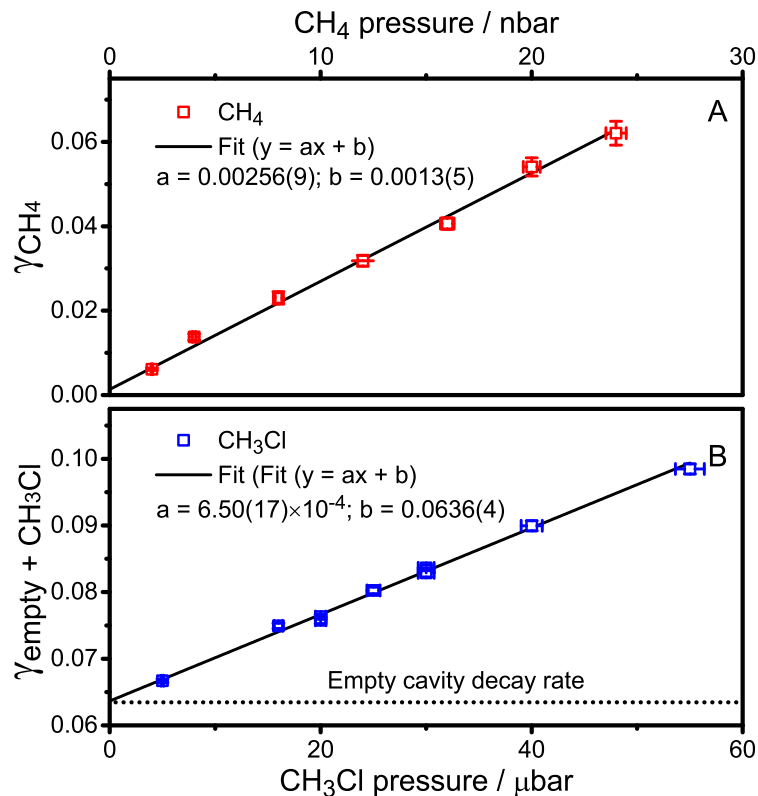


Figure 7.3: Extracted decay rates from ringdown transients as a function of the partial pressure of CH₄, while keeping CH₃Cl constant at 30 μbar (panel A), and CH₃Cl, while keeping CH₄ constant at 8 nbar (panel B). The measurements were performed at the top of the overlapping transitions around 3057.7565 cm^{-1} at a total cell pressure of 2.50 mbar and intracavity power of ~ 1.7 W. The horizontal error bars represent an estimated 2 % uncertainty in the pressure sensors, while the vertical error bars are the standard deviation of 10 - 20 points extracted from the decay transients, each was an average of 10 shots.

the CH₄ pressure was varied from 2 – 24 nbar. For panel B, CH₄ was kept constant at 8 nbar and CH₃Cl was varied from 5 – 55 μbar . As shown in Fig. 7.3, the extracted decay rates show a very good linearity both with respect to CH₃Cl and CH₄ partial pressures. The error bars represent the standard deviation of 10 – 20 repeated measurements each an average of 10 saturated CRD transients. Representative complete spectral scans for the two experiments are presented in Fig. 7.S6.

In order to check the validity and the working limits of the saturation model for Two-species One-wavelength detection, the analysis of saturated CRD transients were extended over a wider dynamic range of cell pressures. Figure 7.4 shows the extracted decay rates for overlapping CH₄ and CH₃Cl transitions as a function of the total cell pressure (changed by adding Ar as a buffer gas), while keeping the intracavity power constant at about 1.6 W. The complete spectra for this experiment are shown in Fig. 7.S7 of the supplement. For a comparison of the data points at different cell pressure, the extracted γ_{CH_4} and $\gamma_{\text{CH}_3\text{Cl}}$ were normalized with respect to the non-saturated spectra obtained from linear CRDS measurements and have been corrected for pressure broadening effects based on a Voigt line shape model. For pressures ranging from 2.0 mbar to 10 mbar, the saturation model extracts reliable values for the absorptions of CH₄ and CH₃Cl. However, at pressures higher than 15 mbar, due to increasingly fast relaxation, the saturation of CH₄ decreases and the model starts to underestimate the corresponding decay rates of the saturated channel. At the same time, a pronounced overestimation of the $\gamma_{\text{empty} + \text{CH}_3\text{Cl}}$ value is observed in the non-saturated channel. In contrast, at pressures lower than

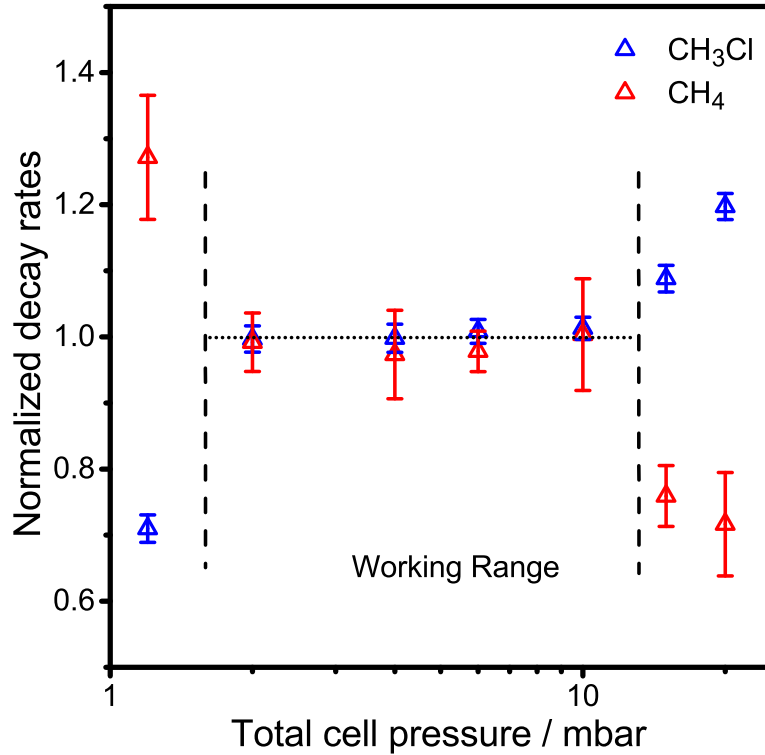


Figure 7.4: Extracted γ_{CH_4} (red) and $\gamma_{\text{empty}+\text{CH}_3\text{Cl}}$ (blue) from the ringdown transient as a function of the total cell pressure. The presented decay rates were normalized to the linear measured individual spectra and Voigt line shape model simulations. The measurements were performed at the top of the overlapping transitions around $3057.7565 \text{ cm}^{-1}$ for a mixture of $30 \mu\text{bar}$ CH_3Cl and 8 nbar CH_4 , the total cell pressure was changed by adding Ar as a buffer gas.

2.0 mbar, $\gamma_{\text{empty}+\text{CH}_3\text{Cl}}$ is underestimated because saturation of CH_3Cl takes effect. Please note that both the deviations at high and low pressures that define the working range of the method, are simply a deviation from the assumed saturation model with two channels (i.e., overall saturated and overall non-saturated). This working range presented in Fig. 7.4 will be shifted towards lower or higher pressures depending on the saturation powers of the overlapping transitions as well as the intracavity power. For example, increasing the intracavity power will shift the working range towards higher pressures.

It should also be noted that, the saturation power as estimated from the fits revealed a pressure dependence of $P_s(\text{CH}_4)$ according to $p^{0.68 \pm 0.12}$. This is slightly different from the previously reported $p^{1.08}$ dependence obtained for pure CH_4 in Ar [20]. This suggests that a fast *near-resonant* energy relaxation of CH_4 via collision with CH_3Cl may significantly contribute to the overall relaxation process (see Supplementary Text). Since CH_3Cl mole fraction decreases with increasing overall pressure, its relative contribution for quenching excited CH_4 decreases with increasing pressure. Hence, the exponent of the pressure dependence should decrease, in agreement with the experimental findings.

In summary, Two-species One-wavelength detection can be performed by utilizing the different optical saturation behavior of the interfering absorbers. Measuring two species at the same wavelength in terms of a 2D absorption spectroscopy, with the frequency axis as the first dimension and the sample saturation as the second dimension, enhances the capability of laser absorption spectroscopy for trace gas sensing applications. First of all, it holds the potential to reduce limitations of absorption cross-sensitivity issues that often limit the accuracy of trace gas sensors for practical applications. This new optical saturation based approach can be implemented in all variants of laser absorption spectroscopy

schemes, however, as demonstrated in this study, Sat-CRDS scheme is superior to a direct LAS scheme in terms of fast and reliable parameter extraction. We have demonstrated the use of optical saturation for extracting the individual absorption spectra of variable mixtures for CH₄ and CH₃Cl at different saturation levels as a test case. The extracted gas absorptions revealed a very good linearity for both species.

A systematic extension of the method by measuring absorption spectra of mixtures of gases over a wider range of wavelengths at once will exploit the full potential of the presented multi-species detection approach. For example, this could be demonstrated in conjunction with the new advances in comb-locked Lamb-dip spectrometers [24]. They have been demonstrated to offer a broad range of 130 nm coverage with intracavity field enhancements up to 1.5 kW/cm², which is more than one order of magnitude higher than the reported saturation intensities of ¹⁴CO₂ [19] and CH₄ [20] at the same pressure.

References

- [1] A. Fried and D. Richter. Infrared absorption spectroscopy. In *Analytical Techniques for Atmospheric Measurement*. Blackwell Publishing, 2007.
- [2] G. C. Bjorklund, M. D. Levenson, W. Lenth, and C. Ortiz. Frequency modulation (FM) spectroscopy. *Appl. Phys. B: Photophys. Laser Chem.*, 32(3):145–152, 1983.
- [3] D. T. Cassidy and J. Reid. Atmospheric pressure monitoring of trace gases using tunable diode lasers. *Appl. Opt.*, 21(7):1185–1190, 1982.
- [4] B. A. Paldus and A. A. Kachanov. A historical overview of cavity-enhanced methods. *Can. J. Phys.*, 83(10):975–999, 2005.
- [5] K. Fritz, G. Christoph, and H. Ronald. Time-domain mid-infrared frequency-comb spectrometer. *Opt. Lett.*, 29(13):1542–1544, 2004.
- [6] M. J. Thorpe, K. D. Moll, R. J. Jones, B. Safdi, and Jun Ye. Broadband cavity ringdown spectroscopy for sensitive and rapid molecular detection. *Science*, 311(5767):1595–1599, 2006.
- [7] K. Demeestere, B. Dewulf, J. and de Witte, and H. van Langenhove. Sample preparation for the analysis of volatile organic compounds in air and water matrices. *J. Chromatogr. A*, 1153(1-2):130–144, 2007.
- [8] M. R. Ras, F. Borrull, and R. M. Marcé. Sampling and preconcentration techniques for determination of volatile organic compounds in air samples. *TrAC, Trends Anal. Chem.*, 28(3):347–361, 2009.
- [9] W. M. A. Niessen, editor. *Current practice of gas chromatography-mass spectrometry*, volume 86 of *Chromatographic science series*. Marcel Dekker, New York, 2001.
- [10] R. A. McFarlane, W. R. Bennett, and W. E. Lamb. Single mode tuning dip in the power output of an He–Ne optical Maser. *Appl. Phys. Lett.*, 2(10):189–190, 1963.
- [11] J. C. Dean, E. G. Buchanan, and T. S. Zwier. Mixed 14/16 helices in the gas phase: Conformation-specific spectroscopy of Z-(Gly)_n, $n = 1, 3, 5$. *J. Am. Chem. Soc.*, 134(41):17186–17201, 2012.
- [12] M. Mayer and B. Meyer. Characterization of ligand binding by saturation transfer difference NMR spectroscopy. *Angew. Chem., Int. Ed.*, 38(12):1784–1788, 1999.
- [13] L. S. Rothman, I. E. Gordon, Y. Babikov, A. Barbe, D. Chris Benner, P. F. Bernath, M. Birk, L. Bizzocchi, V. Boudon, and L. R. Brown *et al.* The HITRAN2012 molecular spectroscopic database. *J. Quant. Spectrosc. Radiat. Transfer*, 130:4–50, 2013.
- [14] J. D. Lambert. *Vibrational and rotational relaxation in gases*, volume 1 of *International series of monographs on chemistry*. Clarendon Press, Oxford, 1977.
- [15] D. Romanini, A. A. Kachanov, N. Sadeghi, and F. Stoeckel. CW cavity ring down spectroscopy. *Chem. Phys. Lett.*, 264(3-4):316–322, 1997.
- [16] J. Y. Lee and J. W. Hahn. Theoretical analysis on the dynamic absorption saturation in pulsed cavity ringdown spectroscopy. *Appl. Phys. B*, 79(5):653–662, 2004.

- [17] S. S. Brown, H. Stark, and A. R. Ravishankara. Cavity ring-down spectroscopy for atmospheric trace gas detection: Application to the nitrate radical (NO_3). *Appl. Phys. B Lasers Opt.*, 75(2-3):173–182, 2002.
- [18] G. Giusfredi, S. Bartalini, S. Borri, P. Cancio, I. Galli, D. Mazzotti, and P. de Natale. Saturated-absorption cavity ring-down spectroscopy. *Phys. Rev. Lett.*, 104(11):110801/1–4, 2010.
- [19] G. Giusfredi, I. Galli, D. Mazzotti, P. Cancio, and P. de Natale. Theory of saturated-absorption cavity ring-down: Radiocarbon dioxide detection, a case study. *J. Opt. Soc. Am. B*, 32(10):2223, 2015.
- [20] I. Sadiek and G. Friedrichs. Saturation dynamics and working limits of saturated absorption cavity ringdown spectroscopy. *Phys. Chem. Chem. Phys.*, 18:22978–22989, 2016.
- [21] K. K. Lehmann. Theoretical detection limit of saturated absorption cavity ring-down spectroscopy (SCAR) and two-photon absorption cavity ring-down spectroscopy. *Appl. Phys. B: Lasers Opt.*, 116:147–155, 2014.
- [22] Materials and methods are available as Supplementary Materials.
- [23] B. E. Brumfield, J. T. Stewart, S. L. Widicus Weaver, M. D. Escarra, S. S. Howard, C. F. Gmachl, and B. J. McCall. A quantum cascade laser cw cavity ringdown spectrometer coupled to a supersonic expansion source. *Rev. Sci. Instrum.*, 81(6):063102, 2010.
- [24] D. Gatti, R. Gotti, A. Gambetta, M. Belmonte, G. Galzerano, P. Laporta, and M. Marangoni. Comb-locked lamb-dip spectrometer. *Sci. Rep.*, 6:27183, 2016.

7.1 Supplementary Material

Two-Species One-Wavelength Detection Based on Selective Optical Saturation

Ibrahim Sadiek,^a and Gernot Friedrichs^{*ab}

^aInstitut für Physikalische Chemie, Christian-Albrechts-Universität zu Kiel, Max-Eyth-Str. 1, D-24118 Kiel, Germany. ^bKMS Kiel Marine Science - Centre for Interdisciplinary Marine Sciences, Olshausenstr. 40, D-24098 Kiel, Germany.

To be submitted.

This supplementary material includes:

- Materials and Methods.
- Supplementary Figures (Figs. 7.S1 to 7.S7).
- Supplementary Tables (Table 7.S1).
- Supplementary Text.

Materials and Methods

Methane gas, CH₄ (99.5%) and Methyl chloride, CH₃Cl (99.8%) were used as test gases and argon (99.999 %) was used as a buffer gas. All gases were used as supplied without further purification. Several overlapping rovibrational transitions of the ν_3 fundamental band of CH₄ and that of ν_4 , $2\nu_6$, and ν_1 bands of CH₃Cl were investigated in the wavelength range 3016 - 3058 cm⁻¹.

Laser Absorption Spectroscopy (LAS)

The direct laser absorption spectroscopy LAS (Fig. 7.S1-A) setup has been used to demonstrate the functionality of optical saturation for decoupling the absorption of two interfering species. All the LAS measurements have been performed at room temperature in a 15 cm long gas absorption cell made of glass. The cell was equipped with stopcocks for inlet and outlet flow and the optical windows were made of fused silica. A turn-key, commercial continuous-wave, single resonant, optical parametric oscillator (cw-SR-OPO, Lockheed-Martin Aculight Argos 2400-SF Module C) pumped by 10W of a fiber-amplified (IPG Photonics; YAR series) Yb-doped DFB fiber laser (NKT Photonics; Koheras Adjustik) operated at 1064 nm has been used as the light source. The cw-SR-OPO light source was capable of producing > 1200 mW of continuously tunable idler output between 3.2 and 3.9 μm , with an out-beam diameter of ~ 2.5 mm. Michelson interferometer based wavemeter (Bristol Instruments; Model 621A-IR) with an accuracy of ± 0.0006 cm⁻¹ at 3.3 μm was used for wavelength measurements. The incident 2.5 mm in diameter laser beam was passed through the measurement cell without any focusing, while the transmitted light was focused by a 10 cm focusing lens placed in front of the detector. A liquid nitrogen cooled 2 mm InSb photodiode (SVS-Vistek, model KISDP-2-A-6) combined with a preamplifier (SVS-Vistek, model KA-05-CI, DC-5 MHz bandwidth) was used as the main detector. A reference preamplifier/detector combination (Vigo System S.A.; Model FIP-1K-1G-F-M4-D/PVI-2TE-5-0) was used for continuous monitoring of the input laser intensity, I_0 . As an example of the measured spectra, Fig. 7.S2 presents the rovibrational absorption spectra for mixture of CH₃Cl and CH₄, at variable input laser power P_0 from 6 to 1300 mW. The saturation of left peak, attributed an overlapped transitions of CH₃Cl and CH₄, is more pronounced than for the right peak where CH₃Cl is the main absorber.

Mid-IR cavity ringdown spectrometer (mid-IR CRDS)

A schematic for the mid-IR CRDS setup used in this study is presented in Fig. 7.S1-B. The detailed description has been given elsewhere [1, 2, 3]. The measurement were carried out at room temperature in a quartz-coated stainless steel ringdown cell equipped with ports for gas inlet, outlet and for pressure monitoring. All the measurements were conducted in a closed cavity with no gas flow. The same cw-SR-OPO and wavemeter as described for the direct LAS setup were used in the CRD spectrometer. An acoustic optical modulator (AOM, Gooch & Housego Model MM040-5C11B38-5) served as a fast optical switch to cut the excitation light level after intracavity light level had reached a pre-set trigger level. Frequency matching of the cavity was achieved by modulating the cavity length using triangle-wave voltage supplied to three piezo electric transducers attached to the rear mirror using three channel piezo driver (MDT693B, Thorlabs) resulting in a scanning speed of the cavity resonance frequency of 15 GHz/s. An 2 mm InSb photodiode (SVS-Vistek, model KISDP-2-A-6) combined with a preamplifier (SVS-Vistek, model KA-05-CI, , DC-5 MHz bandwidth) was used for detecting transmitted light from the rear CRD mirror. The actual measured ringdown time of the empty cavity was

about $16 \mu\text{s}$, with a repetition frequency of about 5 to 10 Hz.

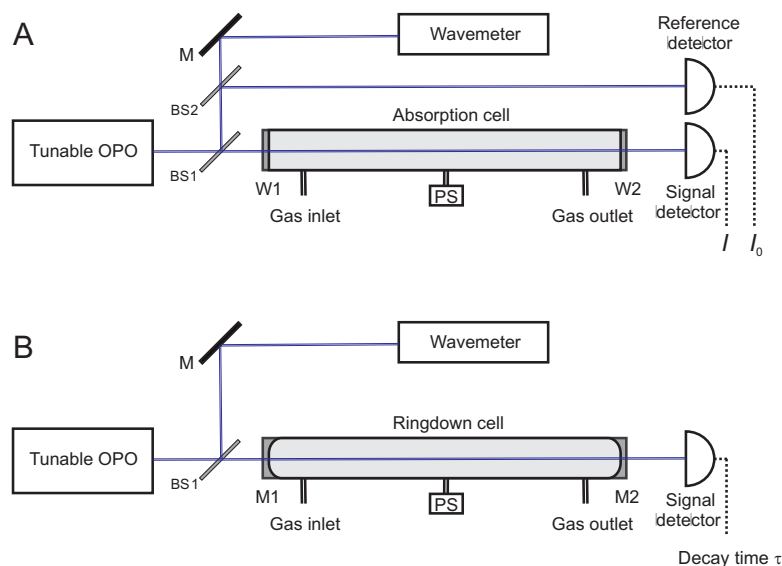


Figure 7.S1: Schematic of the direct laser absorption spectroscopy (LAS) setup (A) and the cavity ringdown spectroscopy (CRDS) setup (B). M: mirror, BS: beam splitter, W: optical window.

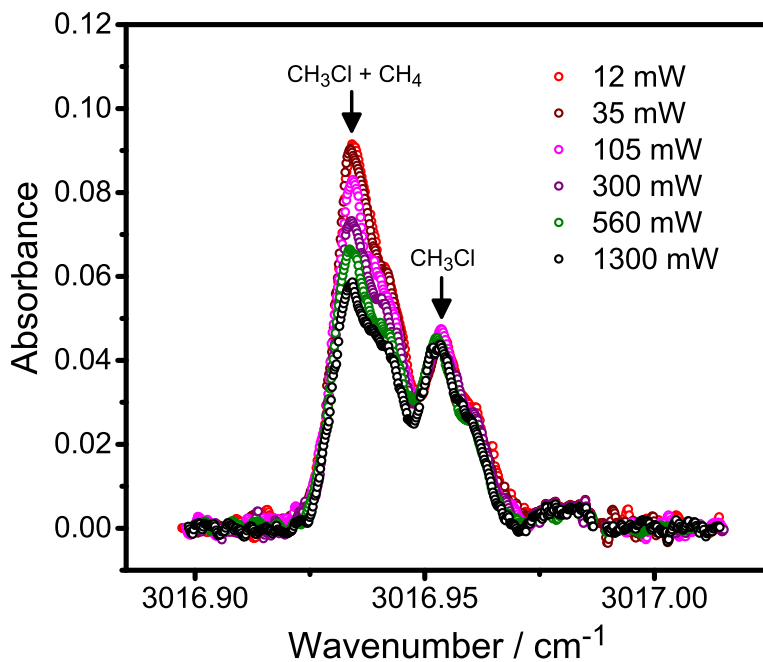


Figure 7.S2: Measured absorbance of overlapping absorption profiles for a mixture of $20 \pm 0.5 \mu\text{bar}$ CH_4 and $1.85 \pm 0.05 \text{ mbar}$ CH_3Cl in 10 mbar of Ar at variable input laser power.

Data acquisition

The collection of the ringdown transients as well as the continuous monitoring of the wavelength were accomplished via a high-resolution flexible digitizer (National Instrument, NI 5922) and home-written LABVIEW [4] software. Each individual ringdown signal was digitized at a sampling rate of 10 MHz and a high vertical resolution of 18 bit for time interval extending over more than 9 ringdown decay times. The nonlinear programming solver *fmincon* implemented in MATLAB [5] has been used as a fitting routine to extract the parameters γ_1 , γ_2 , S_0 , Z^{1V} , and S_{BG} (see Eq. 7.12) as adjustable parameters, where γ_1 and γ_2 encode the gas absorption attenuation rates of the two overlapping species as

well as the empty cavity decay rate.

For LAS measurements, the same digitizer was used and the data were collected using a home-written LABVIEW code. The laser was scanned continuously with a scan rate of 10 mHz and the signals from the detectors were averaged and recorded as a function of the laser frequency.

Coupling efficiency and intracavity power

The focal configuration (50 cm in length and 1 m radius of curvature ringdown mirrors) of the commercial Fabry-Perot resonator used in our previous studies [1, 2, 3] has been slightly changed by extending the cavity length to ~ 51 cm. In this way, the previously reported [1] beating of the predominantly excited TEM₀₀ mode with the nearly degenerate higher transverse modes were suppressed. In addition, for improved spatial mode matching of the laser beam waist ω_g to the cavity mode waist ω_c , two plano-convex lenses have been used as a telescope instead of a single 50 cm focusing lens used before [1]. This resulted in an improvement in the mode matching coupling efficiency,

$$\epsilon_{\text{mode}} \approx \left(\frac{2\omega_g\omega_c}{\omega_g^2 + \omega_c^2} \right)^2 \quad (7.4)$$

estimated to be around $\epsilon_{\text{mode}} = 0.89$.

The overall ‘‘ideal’’ coupling efficiency, which determines the ultimate achievable intracavity light power, can be estimated theoretically based on (i) the ratio of the laser to cavity mode linewidth $k = \Delta\nu_{\text{laser}}/\Delta\nu_{\text{cavity}}$, (ii) the scanning speed W of the cavity relative to the cavity resonance frequencies, and (iii) the geometrical coupling efficiency ϵ_{mode} . In our experimental setup, $\Delta\nu_{\text{laser}} < 60$ kHz (500 μs timescale) $\Delta\nu_{\text{laser}} \approx 1$ MHz (80 ms timescale) and $\Delta\nu_{\text{cavity}}$ is about 10 kHz (as estimated from the measured empty cavity decay time of 15.85 μs). For a laser linewidth of 60 kHz (the minimum specified value at the short timescale), this would result in a value of $k = 6$. This together with an approximate scan speed of 15 GHz/s relative to the cavity resonance frequency should result in an injection efficiency of about 5% (see Fig.1.5 in Ref. [6]). Consequently, an ideal theoretical intracavity coupling efficiency of $\epsilon_{\text{total}} \sim 7.4 \times 10^{-3}$ is predicted. Experimentally, estimated from the detector responsivity and the signal level, the power coupling efficiency was about 7.0×10^{-4} . This significantly lower value was probably due to unidentified losses e.g., by absorption of the mirror coatings and substrate. Additionally, acoustic noise or spectral noise components resulting from the OPO seed laser may play an important role. The seed laser frequency is scanned by a piezo ramp voltage, hence any noise of the piezo amplifier would directly cause frequency noise of the light source. As a result, the effective linewidth of the laser may be actually larger than the specified 60 kHz that we have assumed for the calculation above, hence resulting in a much reduced injection efficiency.

The intracavity power can be estimated through a conversion factor $C = S/P$ that relates the measured detector signal S to the intracavity power P ,

$$C = R_D \times \frac{T(1-L)}{2} \approx R_D \times \frac{(1-R)(1-L)}{2}. \quad (7.5)$$

Here, $T = 1 - R = 1.05 \times 10^{-4}$ is the mirror transmission, with the mirror reflectivity R determined from the ringdown time $\tau_0 = 15.85 \mu\text{s}$ and $R_D = 1.29 \times 10^5$ V/W is the detector responsivity. L is an additional loss parameter to account for the extra losses experienced by the detected light (e.g., by CRD mirror substrate, absorption, surface reflections, etc.) before reaching the detector. Here, we set

$L = 0.5$ to account for the reflection losses by a focusing lens in front of the detector and undisclosed absorption/scattering by mirror coatings, which could be even larger than the mirror transmission in the mid-IR region [7]. Using Eq. 7.5, a typically measured 4.5 V detector signal intensity from 50 mW of incident power on the cavity first mirror would correspond to an intracavity power of ~ 1.30 W.

Saturation Model

For LAS measurements, Eq. 7.1 in the main text is used directly for simulating the “double-bended” absorption saturation behavior. The data were fit to Eq.1 and the corresponding fit parameters include $\alpha_0^{\text{CH}_3\text{Cl}}$, $\alpha_0^{\text{CH}_4}$ as well as the saturation powers $P_s^{\text{CH}_3\text{Cl}}$ and $P_s^{\text{CH}_4}$ were extracted.

For CRDS measurements, the evolution of the absorption saturation of two overlapping species, with sufficiently different saturation power, relative to the empty cavity decay rate can be represented as:

$$P(t) = P_0 \times \exp(-\gamma_{\text{empty}}t) \times [f_1(t, \gamma_{\text{empty}}, \gamma_{\text{gas1}}, P_s^{\text{gas1}}) + f_2(t, \gamma_{\text{empty}}, \gamma_{\text{gas2}}, P_s^{\text{gas2}})], \quad (7.6)$$

$P(t)$ is proportional to the measured signal $S(t)$ with the calibration parameter $C = S(t)/P(t)$, hence

$$S(t) = S_0 \times \exp(-\gamma_{\text{empty}}t) \times [f_1(t, \gamma_{\text{empty}}, \gamma_{\text{gas1}}, Z_{\text{gas1}}^{1V}) + f_2(t, \gamma_{\text{empty}}, \gamma_{\text{gas2}}, Z_{\text{gas2}}^{1V})] + S_{BG}. \quad (7.7)$$

Here, S_{BG} is the detector offset. As indicated elsewhere [8, 1], the saturation power P_s is related to the adjustable parameter $Z^{1V} = 1/(CP_s)$, which is corresponding to the value $P(t)/P_s$ for a signal amplitude of 1V.

Eq. 7.3 can be understood by considering the power attenuation along z axis due to gases absorption,

$$\frac{dP}{dz}(t) = -2\pi \int_0^\infty \alpha(\rho, t) I(\rho, t) \rho d\rho, \quad (7.8)$$

where $\alpha(\rho, t)$ is the effective absorption coefficient for the two absorbing species. It is given by Eq. 7.1 in the main text for homogeneously broadened absorption profiles or its variant,

$$\alpha(\nu, P) = \frac{\alpha_0^{\text{gas1}}(\nu)}{\sqrt{1 + P/P_s^{\text{gas1}}}} + \frac{\alpha_0^{\text{gas2}}(\nu)}{\sqrt{1 + P/P_s^{\text{gas2}}}}, \quad (7.9)$$

for inhomogeneously broadened absorption profiles. $I(\rho, t) = I_0(t)e^{-2(\rho^2/\omega^2)}$ is the time-dependent intensity of the TEM₀₀ mode with a beam waist ω and radial distance ρ . With the assumption that the beam waist is nearly constant along the cavity axis (this is a valid assumption since about 85% of the cavity length is within the Rayleigh range), substitution of Eq. 7.9 into Eq. 7.8 and integrating, yields the intracavity power attenuation due to absorption. After including the mirror loss decay term, an overall power attenuation within the optical cavity can be expressed as:

$$\frac{dP(t)}{dt} = - \left(\gamma_{\text{empty}} + \frac{2\gamma_{\text{gas1}}}{1 + \sqrt{1 + P/P_s^{\text{gas1}}}} + \frac{2\gamma_{\text{gas2}}}{1 + \sqrt{1 + P/P_s^{\text{gas2}}}} \right) P(t). \quad (7.10)$$

Eq. 7.10 represents a general form of the saturated-absorption model (i.e., the so-called SCAR model) which was first reported by Giusfredi et al [9, 8] for one species detection. Here simply an additional term was added for the second absorbing species.

As outlined in the main text, the major challenge to use Eq. 7.10 to extract the individual absorption (γ_{gas1} , γ_{gas2}) is that γ_{gas1} (corresponds to the decay rate due to the less saturated species) is often not temporally resolved from γ_{empty} . A more straightforward and numerically stable implementation of Eq. 7.10 for two species detection can be achieved after reducing the three decay parameters into only two γ_1 , and γ_2 , encoding the individual gas absorption decay rates γ_{gas1} , and γ_{gas2} as well as the empty cavity decay rate γ_{empty} :

$$\frac{dP(t)}{dt} = - \left(\gamma_1 + \frac{2\gamma_2}{1 + \sqrt{1 + P/P_s^{\text{gas2}}}} \right) P(t). \quad (7.11)$$

Experimentally this can be realized when (i) one of the molecules is completely saturated (e.g., gas2) and the other molecule is only partially saturated (e.g., gas1). In this scenario, $\gamma_1 = \gamma_{\text{empty}}$ and $\gamma_2 = \gamma_{\text{gas1}}$. However, in general this would require very high intracavity power and low working pressures and moreover, it would only provide a selective detection of single species while the other is essentially transparent. Therefore, under practical conditions of relatively high pressure, it is more convenient to tune the input laser power such that only one molecule is saturated (e.g., gas2 with the low saturation power) and the other one non-saturated (e.g., gas1 with the high saturation power). In that scenario, which is explored in this work, $\gamma_1 = \gamma_{\text{empty+gas1}}$ and $\gamma_2 = \gamma_{\text{gas2}}$.

Consequently, Eq. 7.7 reduces to

$$S(t) = S_0 \times \exp(-\gamma_1 t) \times f(t, \gamma_1, \gamma_2, Z^{1V}) + S_{\text{BG}}. \quad (7.12)$$

Here $S(0) = S_0 + S_{\text{BG}}$ and $f(0) = 1$. The f function describes the evolution of the intracavity power relative to the first decay rate γ_1 . Its first derivative is given by ²

$$\frac{df(t)}{dt} = -\gamma_2 \frac{2f(t)}{1 + \sqrt{1 + S_0 Z^{1V} \exp(-\gamma_1 t) \times f(t)}}. \quad (7.13)$$

Both Eq. 7.12 and 7.13 are included in the fitting routine and the integration of Eqs. 7.13 is numerically performed on-the-fly using the Runge-Kutta-Fehlberg method RK45. For the homogeneously broadened absorption profile, Eq. 7.13 would have to be replaced in the fitting routine by its equivalent:³

$$\frac{df(t)}{dt} = -\gamma_2 \frac{\ln [1 + S_0 Z^{1V} \exp(-\gamma_1 t) \times f(t)]}{S_0 Z^{1V} \exp(-\gamma_1 t)}. \quad (7.14)$$

²a detailed derivation of the origin of this first derivative is presented in Chapter 2.

³It should be noted that under real experimental conditions, the measured absorption is a combination of homogeneous and inhomogeneous broadened effects.

Supplementary Figures

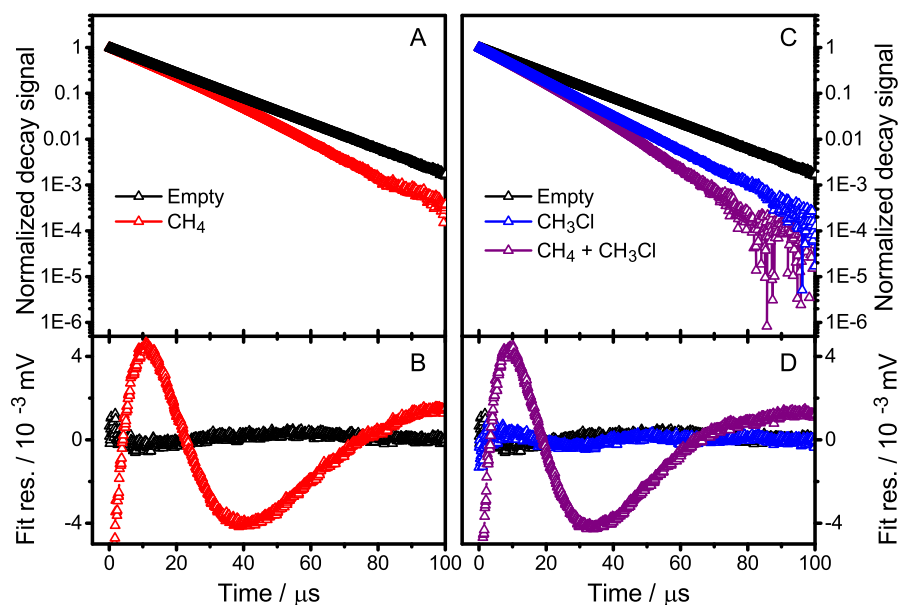


Figure 7.S3: Saturated-CRD transients around 3057.7565 cm^{-1} for the empty cavity (black) and at the top of absorption profiles of CH₄ (red), CH₃Cl (blue), and an overlapping CH₄ + CH₃Cl absorption (purple). The saturated-CRD transient for CH₄ (panel A) shows two competing decay constants (γ_{empty} and γ_{CH_4}), as indicated by the exponential fit residual (shown in panel B). The saturated-CRD transient for CH₃Cl (panel C) shows almost zero residual (shown in panel D), indicating linearly absorbing CH₃Cl. The saturated-CRD transient for a mixture of CH₄ + CH₃Cl (panel C) also shows two competing decay constants ($\gamma_{\text{CH}_3\text{Cl}+\text{empty}}$ and γ_{CH_4}), as indicated by the exponential fit residual (shown in panel D).

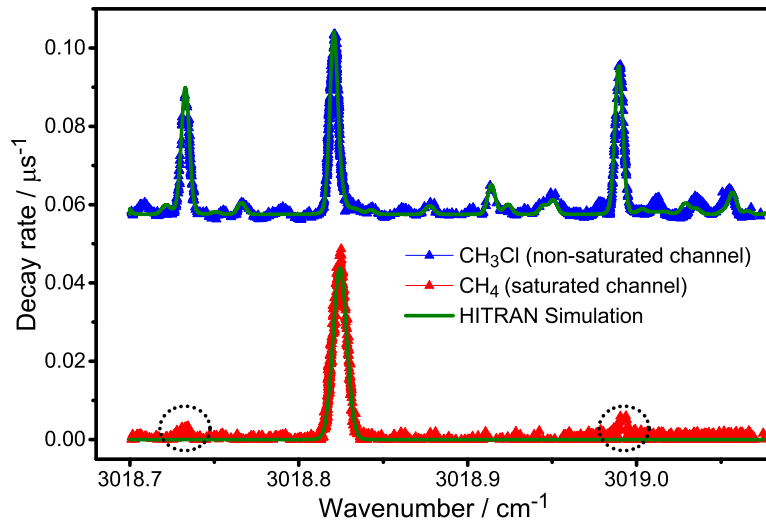


Figure 7.S4: Extracted decay rates of CH_3Cl (blue) and CH_4 (red) from saturated-CRD transients (160 nbar CH_3Cl and 45 nbar CH_4 in 2.50 mbar of Ar, intracavity power is ~ 1.6 W). The saturated-CRD transients were fit to the saturation model with $\gamma_{\text{empty}+\text{CH}_3\text{Cl}}$, γ_{CH_4} , S_0 , and S_{BG} as free parameters (Eq. 7.12 and Eq. 7.13). A very good agreement is obtained with the simulated spectra using HITRAN database [10] for CH_4 and the strong peaks of CH_3Cl . Additional small peaks visible in the non-saturated channel ($\gamma_{\text{CH}_3\text{Cl}+\text{empty}}$) are probably due to yet non-assigned CH_3Cl transitions or small sample impurities. Minor residuals in the extracted γ_{CH_4} (dotted circles) indicate imperfect decoupling of CH_4 and CH_3Cl , which is probably due to a slight saturation effect of the strong CH_3Cl absorption.

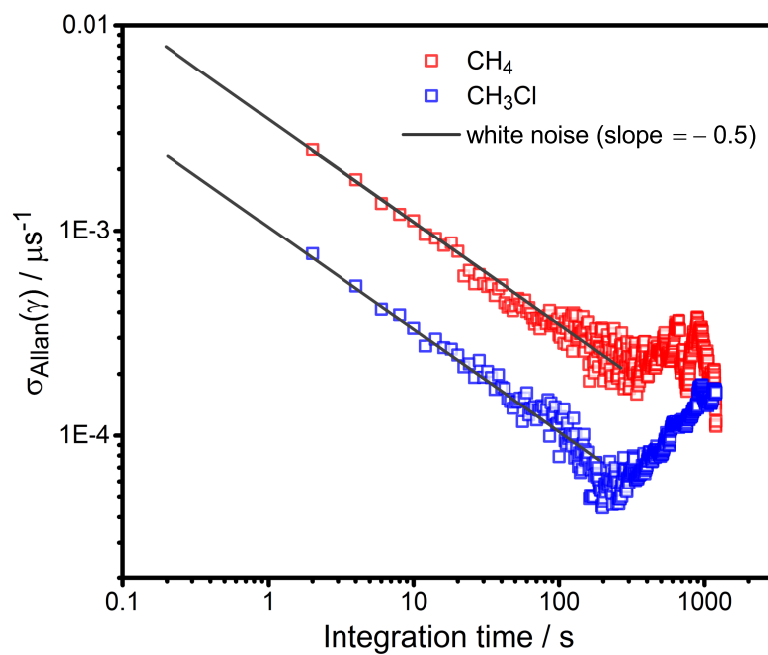


Figure 7.S5: Allan analysis for the extracted γ_{CH_4} (red) and $\gamma_{\text{empty}+\text{CH}_3\text{Cl}}$ (blue) parameters from repeatedly measured saturated-CRD transients at the top of overlapping transitions at $3057.7565 \text{ cm}^{-1}$ ($25 \mu\text{bar CH}_3\text{Cl}$, 8 nbar CH_4 , $2 \text{ mbar total cell pressure}$, buffer gas Ar, $1.2 \text{ W intracavity power}$).

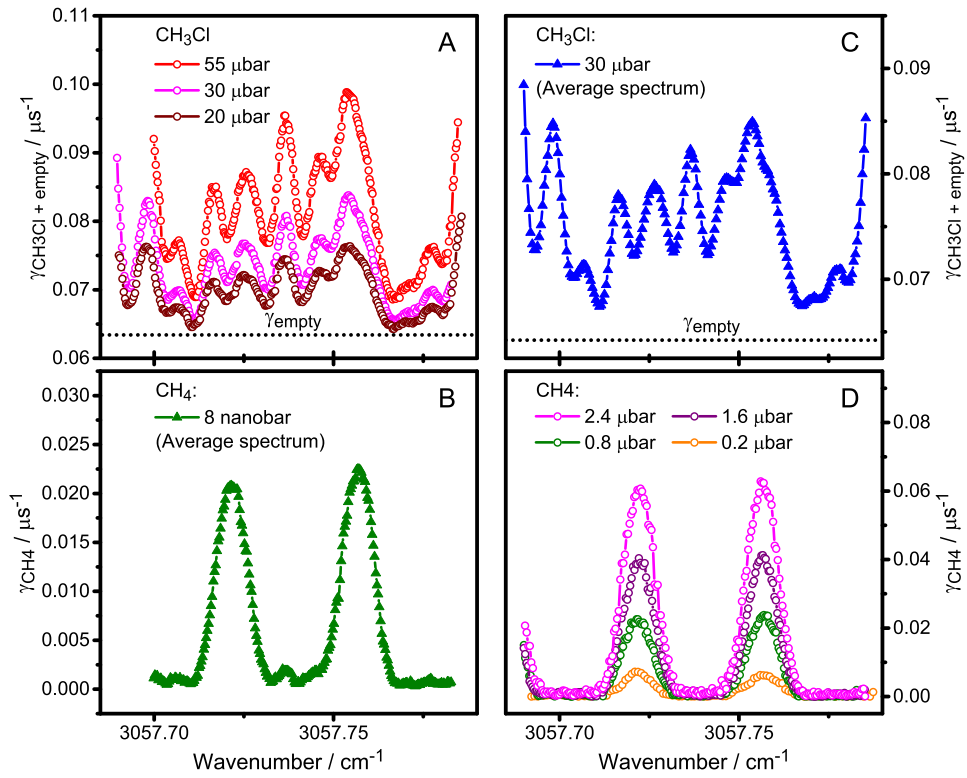


Figure 7.S6: Recorded absorption spectra from saturated CRD transients of CH_3Cl and CH_4 gas mixtures in Ar obtained for variable partial pressure of CH_3Cl and constant partial pressure of CH_4 of 8 nbar (panels A and B) and variable partial pressure of CH_4 at constant partial pressure of CH_3Cl of 30 μbar (panels C and D). All the measurements were performed at a total cell pressure of 3.0 mbar and an intracavity power of about 1.6 W. $\gamma_{\text{empty}+\text{CH}_3\text{Cl}}$, γ_{CH_4} , Z^{1V} , S_0 , and S_{BG} were used as the adjustable parameters during the fit (see Eq. 7.12 and Eq. 7.13). The linearity of corresponding γ values at $3057.7565 \text{ cm}^{-1}$ is shown in Fig. 7.3 (in the main text).

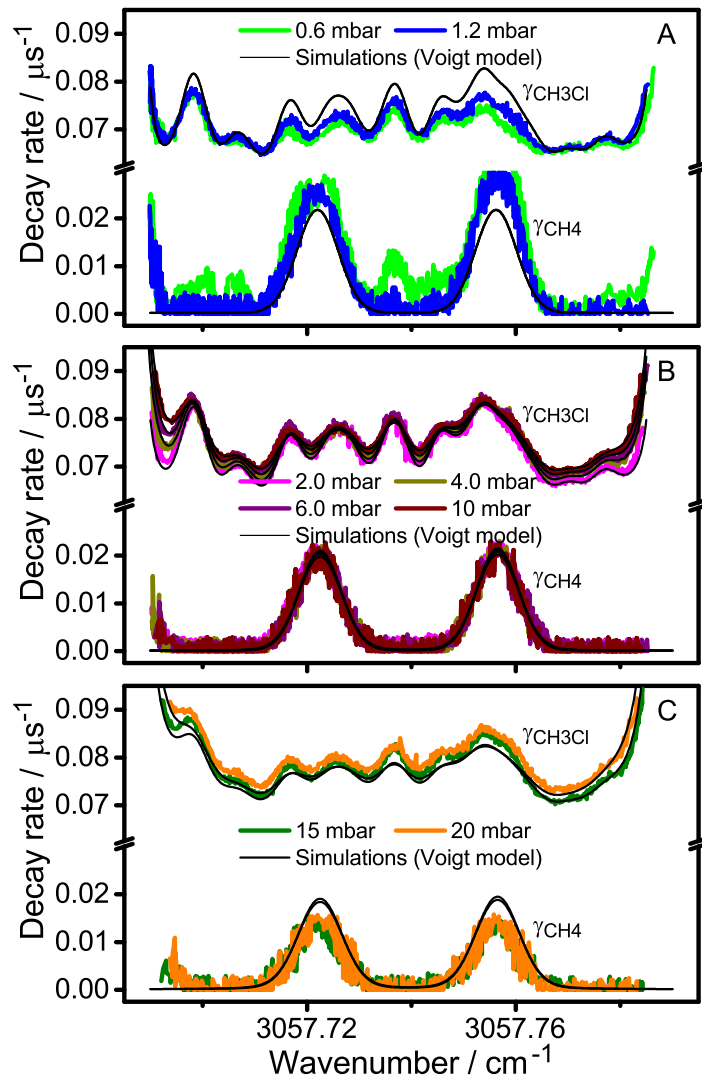


Figure 7.S7: Extracted $\gamma_{\text{empty}+\text{CH}_3\text{Cl}}$, and γ_{CH_4} decay rates for a mixture 8 nanobar of CH_4 and 30 μbar of CH_3Cl at constant intracavity power of ≈ 1.6 W and variable total cell pressure. Black solid curves refer to simulated spectra using Voigt line shape model. Panel A: For pressures less than 2 mbar, both species are saturated (to different extents), hence the decoupling of $\gamma_{\text{CH}_3\text{Cl}}$ and γ_{CH_4} in the saturated γ_2 and non-saturated γ_1 is not perfect. Panel B: For pressure range 2.0 - 10 mbar, γ_{CH_4} and $\gamma_{\text{empty}+\text{CH}_3\text{Cl}}$ are perfectly separated in the saturated and non-saturated channels, respectively. Very good agreement with the simulations is observed in this pressure range. Panel C: For pressures higher than 10 mbar, CH_4 is not strong enough saturated, hence γ_1 and γ_2 become coupled again. Part of CH_4 absorption shows up in the saturated channel.

Supplementary Text

Energy-transfer dynamics

All the deactivation processes such as spontaneous emission, diffusional deactivation (including transient-time effects) as well as the collisional excitation and deexcitation control the population relaxation of the excited states. Under the practical conditions of relatively high pressure, the collisional deactivation of the excited states prevails. Such energy transfer/relaxation dynamics in mixture of gases due to collision is very complex, however, it can be qualitatively predicted for the majority of atmospheric molecules. This energy transfer probability upon collision controls the degree of saturation of the entitled species and it is also a collider specific property.

For a mixture of gases with overlapping transitions, the absorption of laser photons excites them from ground to excited vibrational states. Molecular collisions populate and depopulate rotational sublevels within the ground and the excited state manifolds of the connected states of the two molecules. However, the deactivation of the excited states is controlled by the eventual transfer of the vibrational energy content to translational energy (i.e., the so-called vibrational-translational, V-T transfer). According to the Schwartz-Slawsky-Herzfeld (SSH) [11], this usually happens via the lowest vibrational mode after a series of vibrational-vibrational (V-V) energy transfer between the different manifolds (i.e., inter-mode V-V transfer). Alternatively, collisional deactivation can occur by a quenching mechanism initiated by collision with another relaxing molecule (i.e., near-resonant V-V transfer). In cases when vibrational energy of molecule A is transferred to another molecule B with very efficient V-T transfer, it may happen that the relaxation of molecule A becomes limited by the V-T transfer of molecule B.

Fig. 7.S8 presents a schematic of an energy-level diagram showing transitions for such a mixture of two polyatomic relaxing gases A and B (e.g., CH₄ and CH₃Cl) with overlapping vibrational bands. Since there are two vibrational transitions nearly resonant, fast intermolecular V-V transfer between vibrationally excited A* and B is very likely to occur. Now let's assume that the lowest vibrational mode of B is lower than the lowest vibrational mode of A, such that the V-T transfer of B can be assumed to be faster than that of A. This follows from the fact that, the composite relaxation rate is governed by $1/\beta = (1-x)/\beta_A + x/\beta_B$, with x being the mole fraction of the quencher B and β_A , and β_B are the relaxation times of A and B, respectively. Therefore, at sufficiently higher x and with $1/\beta_B > 1/\beta_A$ the relaxation becomes completely dominated by the quencher B. Under such conditions, a single relaxation time is observed for both interfering species and the two gases may show very similar saturation powers depending on their absorption transition probabilities. Hence, decoupling their absorption into the non-saturated channel, γ_1 and saturated channel, γ_2 may not be possible. Conversely, at very low mixing ratios, species A and B relax independently from each other. This highlights one of the advantages of using a Sat-CRDS scheme over direct LAS scheme, where the low densities of species in CRDS measurements ensure almost independent relaxation pathways of the interfering species.

A list of atmospherically important trace gases that could benefit from the optical saturation to avoid interferences are presented in Table 7.S1. In this table, the molecules are classified relative to their relaxation times β , which controls the saturation powers of interfering molecules and hence the decoupling efficiency of their absorption. For example, the measurement of ammonia in the presence of

CO₂ should be easily possible with the Two-species One-wavelength approach since the relaxation time ratio between ammonia and CO₂ is more than four orders of magnitudes. Similarly, many halogenated methanes (e.g., CH₃I, CH₂Cl₂, CHBr₂Cl,..etc.) can be measured in the presence of CH₄, CO₂, or N₂O. Even for water, it is feasible to decouple water absorption from the absorption of many greenhouse gases such as CO₂, COS, CS₂, N₂O, CH₃F. Note however that a discussion of feasible application of the Two-species One-wavelength approach merely based on relaxation times may fail since interfering transitions have different transition probabilities, which also affect their saturation powers and hence need to be considered.

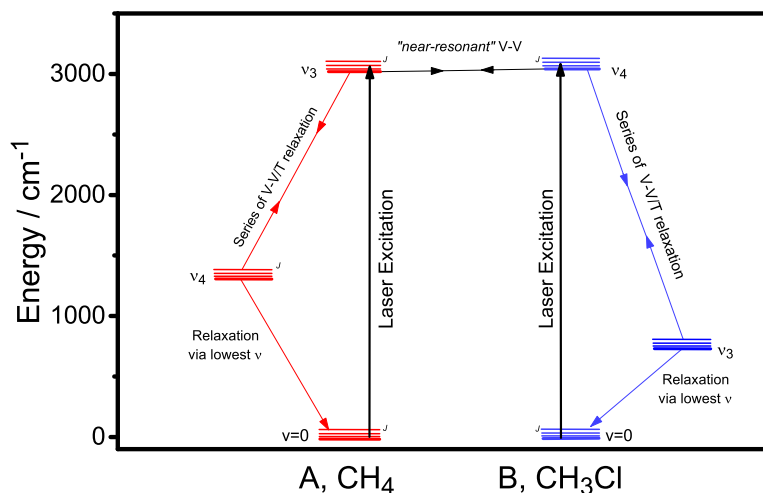


Figure 7.S8: Schematic energy-level diagram showing vibrational energy transfer pathways for two excited molecules: A and B with near-resonant vibrational-vibrational transfer. CH₄ and CH₃Cl serve as a case study. The V-V transfer within the same molecule is often a complex and fast series of transitions ending up in the lowest vibrational mode. The “near-resonant” V-V transfer between different molecules involves quenching of vibrational energy by another relaxing molecule. If the quencher (e.g., CH₃Cl) exists in high enough concentration, the near resonant V-V transfer can efficiently transfer the vibrational energy content of the whole system with relaxation time governed by the V-T transfer of the quencher.

Table 7.S1: List of atmospheric molecules grouped in terms of their relaxation times at $T = 300$ K and $p = 1$ atm [11].

> 1000 ns	1000-400 ns	400-100 ns	100-10 ns	< 10 ns
CH ₄	N ₂ O	CH ₃ Cl	H ₂ O	CH ₂ ClCH ₂ Cl
CO ₂	CS ₂	C ₂ H ₄ O	C ₂ H ₆	NH ₃
COS	CF ₄	C ₂ H ₄	CH ₂ CHBr	CH ₃ CHCl
HCl	SF ₆	CF ₃ Cl	CH ₃ I/Br	C ₃ H ₇ OH
HBr	CHF ₃		CH ₂ F ₂	CH ₂ Cl ₂
CO			SO ₂	C ₂ H ₅ OH
CH ₃ F			C ₂ H ₂	CHBr ₂ Cl
			CHCl ₃	CHBrCl ₂
			CHClF ₂	
			CHCl ₂ F	

References

- [1] I. Sadiq and G. Friedrichs. Saturation dynamics and working limits of saturated absorption cavity ringdown spectroscopy. *Phys. Chem. Chem. Phys.*, 18:22978–22989, 2016.
- [2] I. Sadiq and G. Friedrichs. Doppler-limited high-resolution spectrum and VPT2 assisted assignment of the C-H stretch of CH₂Br₂. *Spectrochim. Acta. A: Mol. Biomol. Spectrosc.*, 181:180–191, 2017.
- [3] I. Sadiq, Q. Shi, D. Wallace, and G. Friedrichs. Quantitative mid-infrared cavity ringdown detection of methyl iodide for monitoring applications. *Anal. Chem.*, 2017, Article ASAP, DOI: 10.1021/acs.analchem.7b01970.
- [4] C. Elliott, V. Vijayakumar, W Zink, and R Hansen. National Instruments LabVIEW: A programming environment for laboratory automation and measurement. *JALA*, 12(1):17–24, 2007.
- [5] *MATLAB Optimization Toolbox, Version 8.5 (R2015a)*. The MathWorks Inc., Natick, Massachusetts, 2015.
- [6] G. Gagliardi and H.-P. Loock, editors. *Cavity-enhanced spectroscopy and sensing*, volume 179 of *Springer series in optical sciences, 0342-4111*. Springer, Heidelberg, 2014.
- [7] I. Galli, S. Bartalini, R. Ballerini, M. Barucci, P. Cancio, M. de Pas, G. Giusfredi, D. Mazzotti, N. Akikusa, and P. de Natale. Spectroscopic detection of radiocarbon dioxide at parts-per-quadrillion sensitivity. *Optica*, 3(4):385, 2016.
- [8] G. Giusfredi, I. Galli, D. Mazzotti, P. Cancio, and P. de Natale. Theory of saturated-absorption cavity ring-down: Radiocarbon dioxide detection, a case study. *J. Opt. Soc. Am. B*, 32(10):2223, 2015.
- [9] G. Giusfredi, S. Bartalini, S. Borri, P. Cancio, I. Galli, D. Mazzotti, and P. de Natale. Saturated-absorption cavity ring-down spectroscopy. *Phys. Rev. Lett.*, 104(11):110801/1–4, 2010.
- [10] L. S. Rothman, I. E. Gordon, Y. Babikov, A. Barbe, D. Chris Benner, P. F. Bernath, M. Birk, L. Bizzocchi, V. Boudon, and L. R. Brown *et al.* The HITRAN2012 molecular spectroscopic database. *J. Quant. Spectrosc. Radiat. Transfer*, 130:4–50, 2013.
- [11] J. D. Lambert. *Vibrational and rotational relaxation in gases*, volume 1 of *International series of monographs on chemistry*. Clarendon Press, Oxford, 1977.

Summary and Outlook

NEW MID-IR CW-CRD SPECTROMETER. In this study a new mid-IR cw-CRD spectrometer has been setup as a *development platform* for trace gas sensors and field going instruments. In addition, it has been extensively used for investigating novel approaches based on optical saturation in order to further improve the attainable sensitivity and overcome the issue of cross-sensitivity. Halogenated volatile organic compounds (HVOCs) as a very important class of atmospheric molecules with a wide spectrum of agricultural and industrial application were targeted as a case study. A limit of detection (LOD) of $\sigma(\alpha, 1 \text{ shot}) \approx 1.5 \times 10^{-8} \text{ cm}^{-1}$ and minimum absorption coefficient $\alpha_{\text{min}} \approx 5.0 \times 10^{-10}$ (based on 100 s average time) have been achieved. The CRD decay transients were collected with a repetition frequency of 5 Hz (in worst cases) and 40 Hz (in best cases).

OUTLOOK. The first step to further improve the performance of the mid-IR CRD spectrometer is to enhance the repetition frequency. The repetition frequency can be enhanced up to two orders of magnitudes by implementing a frequency stabilization scheme (e.g., Pound-Drever-Hall locking technique), which will allow for large data averaging and hence better LOD. It will also allow for better coupling efficiency of the input laser beam to the cavity modes. Higher intracavity powers are beneficial for the saturated-CRDS approaches.

QUANTITATIVE MID-INFRARED CAVITY RINGDOWN DETECTION OF METHYL IODIDE. A quantitative detection scheme using the new mid-IR CRD spectrometer has been developed for monitoring CH₃I in industrial and agricultural workplaces as well as in the environment. The attainable LOD for CH₃I (based on the determined absorption cross section of CH₃I at 20 mbar of Ar) was ~ 15 ppb. This LOD is about two orders of magnitude below specified exposure limits of CH₃I of 0.3 - 5 ppm, while it is about three orders of magnitude too high for directly detecting CH₃I at atmospheric mixing ratio levels in the lower ppt range.

As a pre-requisite for trace gas monitoring the high-resolution spectrum of an appropriate vibrational band has been measured for the first time. The line selection procedure was based on a proper selection of a spectral window with minimum interference from trace gases. The quantitative spectroscopic parameters (e.g., absorption cross section and pressure broadening coefficients) have been determined for the selected line. A simple tank-purging experiment has been designed for comparing the temporal response of CH₃I extractions measured with the mid-IR CRD spectrometer and the well-established GC-MS/ECD system. The experiments revealed that calibration-free quantitative detection of CH₃I by mid-IR CRDS is possible with a time-resolution of several seconds and with high reproducibility.

OUTLOOK. A straightforward development of commercial analyzers for CH₃I monitoring in industrial and agricultural fields can be achieved based on the presented quantitative spectroscopic data in this study. To do so, the bulky cw-SR-OPO light source should be replaced by commercial distributed feedback laser (DFB) emitting at the selected wavelength range. For environmental field monitoring a pre-concentration scheme needs to be developed. Commercial purge-trap pre-concentration units similar to that are used for GC machines can be adopted for such purpose. However, this will increase

the measurement time (but it will still be faster than MS or ECD detectors) and calibration might be required as well.

HIGH-RESOLUTION SPECTRA AND QUANTUM-CHEMICALLY ASSISTED SIMULATIONS. The measurement of the high-resolution spectra is essential for the proper line selection for monitoring application. A major challenge for HVOCs detection is the scarcity (in some case a lack) of their high-resolution spectra. The capability of a standard CRDS systems to acquire the high-resolution spectrum is limited by the linewidth of the light source and its tuning range. Utilizing the wide tuning range of the new mid-IR cw-SR-OPO based CRD spectrometer, the Doppler limited high-resolution spectra of the ν_1 and ν_6 vibrational bands of CH_2Br_2 have been measured for the first time. The measured spectrum has been simulated and assigned using a quantum-chemistry assisted approach.

The main challenge for simulating high-resolution spectra of molecules is the availability of accurate spectroscopic constants (i.e., rotational and centrifugal distortion constants) for both ground and excited vibrational states. The ground state constants are usually available from microwave data, while the excited state constants require an *educated* guess. As an alternative, it has been demonstrated in this thesis that a quantum-chemical assisted approach based on the second vibrational perturbation theory (VPT2) provides a more reliable initial estimate for the excited state rotational constants. It turned out that an estimate relying on the calculated change in the rotational constants upon vibration excitation, which is very small, in combination with available ground state constant already yielded a very good agreement between the high-resolution spectrum of CH_2Br_2 and the simulation even without any fitting of molecular constants.

OUTLOOK. Quantum-chemically assisted simulation of the rovibrational spectra can provide absolute spectra predictions sufficiently accurate for line selection in atmospheric monitoring applications. This significantly reduces the experimental work needed to develop trace gas monitoring systems. In addition, the implementation of such approach for variety of atmospheric molecules with known high-resolution spectrum (e.g., from HITRAN database) shall provide a good validation of the different model chemistries available for anharmonicity calculations.

WORKING LIMITS AND SATURATION DYNAMICS OF SAT-CRDS. The capability of optical cavities to build-up high intracavity power suits very well for the investigation of optical saturation effects. Provided that laser light is efficiently coupled into the cavity, this even holds for low power laser sources. Saturation effects (e.g., Lamb-dip spectroscopy, two-photon spectroscopy) in optical resonators are understudied in contrast to the widely investigated quantitative spectroscopy in the linear absorption regime. This is attributed to the common practice to avoid saturation effects for quantitative monitoring applications rather than intentionally using such effects for improving the detection sensitivity.

The decay transient of an optical resonator provides a well-controlled (i.e., can be modeled) and fast (i.e., within the time scale of the decay constant) change of the intracavity power. At high intracavity power, when a saturable absorber exists inside the optical cavity, the shape of the saturated-CRD transients reflects the dynamics of the absorption saturation. The dynamics of absorption saturation nearly depends on the rate of optical pumping (i.e., depletion of the ground states) and the interactions with the surrounding gas matrix (i.e., the overall relaxation rate). The evolution of the absorption saturation within the ringdown transients, and the working limits of the new saturated-absorption

CRDS approach (Sat-CRDS), have been comprehensively investigated for inhomogeneous broadened absorption profiles in this work. The dynamics have been explored under different saturation conditions ranging from the *adiabatic* close to the *non-relaxing* limit, using methane as a test gas and argon as a buffer gas. The simultaneous extraction of multiple parameters from a single ringdown decay transient results in a strong correlations between the parameters, such that the finally achieved sensitivity of Sat-CRDS was comparable to the standard CRDS implementation in the linear absorption regime. However, the Sat-CRDS approach is advantages under experimental conditions where the determination of the empty cavity decay constant is difficult due to baseline instabilities and/or broad absorption features.

OUTLOOK. In the implemented fitting routine, the saturation model is fitted to each saturated-CRD transient and the gas absorption decay rate is determined relative to the empty cavity decay rate. Globally fitting saturated-CRD transients measured for a whole absorption profile, may better decouple the fitting parameters and hence decrease the standard error of the extracted gas absorption decay rate. In principle, such fit procedure can be easily implemented by assuming known line shape function parameters (i.e., the lines center, the Lorentzian width, the Gaussian width, and spectral area) and locally fitting only the decay transient parameters (i.e., the empty cavity decay rate, the gas absorption decay rate, the initial intensity, and the detector background).

TWO-SPECIES ONE-WAVELENGTH DETECTION. Cross-sensitivity represents a barrier for quantitative absorption measurements for many environmental monitoring applications. In this study, a fundamentally new detection concept has been worked-out utilizing the different optical saturation behavior of interfering absorptions to discriminate between them. In principle, “Two-species One-wavelength” detection can be performed holding the potential to reduce the limitations of absorption spectroscopy in terms of cross-sensitivity. The functionality of the approach relies on the fact that different molecules have different degree of saturation as the overlapping transitions have different transition probabilities. Also the different energy transfer probabilities upon collisions for each molecular species support such difference in degree of saturation. Therefore, the degree of saturation for each individual absorption in the mixture can be tuned by carefully changing the pumping power and the deactivation rates of the populated excited states (e.g., by changing the overall cell pressure). Consequently, the individual absorptions in the mixture can be decoupled.

As a proof-of-concept, direct laser absorption spectroscopy (LAS) and cavity ringdown spectroscopy (CRDS) schemes have been successfully implemented to retrieve the individual absorption of several overlapping transitions for a mixture CH_4 and CH_3Cl . For sufficiently different saturation powers of the overlapping transitions of CH_4 and CH_3Cl , a “double-bended” absorption-input laser power has been observed by the direct LAS scheme. Such double-bended profile is essential to extract the individual absorptions correctly. The low limit of detection provided by CRDS scheme enable low concentration detection of the interfering species and more importantly for the two species detection is that it minimizes the *cross-talk* of energy relaxation pathways. Moreover, the fast and controlled decay of the ringdown transients allows for fast switching between the between the limiting strong and weak saturation (i.e., within few tens of μs). Very good linearities with respect to the partial pressures of both CH_4 and CH_3Cl up to cell pressures of 10 mbar have been accomplished.

OUTLOOK. The use of optical saturation for quantitative “Two-species One-wavelength” detection is a novel approach that still requires comprehensive investigation of several aspects, including

- the cross-talk of the energy transfer and relaxation pathways of the interfering molecular systems and these effects on their quantitative detection,
- a detailed analysis and further development of the saturation model (e.g., the implementation of convoluted homogeneous and inhomogeneous saturation model),
- the development of global fitting scheme both with respect to frequency scale (i.e., global fit of the whole absorption features) and intensity scale (i.e., simultaneous fitting of Sat-CRDS profiles measured at different initial intensities) to further improve parameter decoupling,
- the implementation of the “Two-species One-wavelength” detection approach using amplitude modulated light source or broadband detection schemes, including those of novel light sources such as optical frequency combs,
- and the demonstration of the potential of “Two-species One-wavelength detection” for solving real world cross-sensitivity problems.

Curriculum Vitae

Personal Information

Name:	Ibrahim Sadiek
Born :	31 st March 1987, Egypt
Marital status:	Married
Address:	Robert-Koch-Str. 3, Kiel 24116, Germany
E-mail:	sadiek@phc.uni-kiel.de / isadiek@yahoo.com

Education and Academic Degrees

Since Dec. 2012:	<p>Ph.D. thesis title: NEW MID-IR-CRD SPECTROMETER FOR ORGANOHALOGEN DETECTION AND INNOVATIVE APPLICATIONS OF SATURATION SPECTROSCOPY, Institute of Physical Chemistry, University of Kiel (Prof. Dr. G. Friedrichs). The Ph.D. project was part of the transatlantic Helmholtz Research School for Ocean System Science and Technology (HOSST).</p> <ul style="list-style-type: none">• I was responsible for the development of the new mid-IR-OPO based CRDS spectrometer of the Cluster of Excellence Future Ocean for trace gas sensing applications.• The work also involved implementation of new detection approaches; measurements and analysis of high-resolution spectra; and benchmarking with other methods.• One of the work phases involved research visit to the laboratory of Prof. D. Wallace (University of Dalhousie, Canada).• The Ph.D. resulted in 4 peer-reviewed publications (3 accepted + 1 to be submitted), 1 newsletter, 1 patent (reported to the University), and more than 8 international conference contributions.• Since winter 2015/2016, I am working as instructor in the Institute Physical Chemistry, University of Kiel.
Jun. - Nov. 2012:	Research assistant in a joint project between Qatar Univ. And Texas A & M Univ., <i>Examination of the structure and dynamics of hydroxyl groups in the edges sites of clay minerals using DFT calculations</i> , Doha, Qatar (Prof. Dr. M. Khader).
Aug. - Sept. 2011:	Internship at the Lab of Prof. T. Bernhardt group, participated in a <i>femtosecond laser experiment for investigating the catalytic properties of Pd clusters</i> , Institute of Surface Chemistry and Catalysis, University of Ulm, Germany.
May 2011 - May 2012:	Full time as an instructor for experimental Physical Chemistry classes (Thermodynamics, Electrochemistry, and Chemical Kinetics), College of Science, University of Cairo.
Oct. 2009 - May 2011:	Time was divided 50 % for teaching experimental Physical Chemistry and 50 % for M.Sc. work, College of Science, Cairo University.

Ph.D. Publications

Full Papers

1. **I. Sadiék**, Q. Shi, D. W. R. Wallace, G. Friedrichs, Quantitative Mid-Infrared Cavity Ringdown Detection of Methyl Iodide for Monitoring Applications, **Anal. Chem.**, 2017, DOI: 10.1021/acs.analchem.7b01970.
2. **I. Sadiék**, G. Friedrichs, Doppler-Limited High-Resolution Spectrum and VPT2 Assisted Assignment of the C-H Stretch of CH₂Br₂ **Spectrochim. Acta. A**, 181: 180–191, 2017, DOI: 10.1039/c6cp01966h.
3. **I. Sadiék**, Gernot Friedrichs, Saturation Dynamics and Working limits of Saturated Absorption Cavity Ringdown Spectroscopy, **Phys. Chem. Chem. Phys.**, 18: 22978–22989, 2016, DOI: 10.1039/c6cp01966h.
4. **I. Sadiék**, G. Friedrichs, Two-species One-wavelength Detection Based on Selective Optical Saturation, **To be submitted**.

Newsletter

1. I. Sadiék and G. Friedrichs, Working limits of Saturated Absorption Cavity Ringdown Spectroscopy (Sat- CRDS), **Bunsen-Magazin** 17 (2015) 185.

Conferences

1. **I. Sadiék**, Q. Shi, D. W. R. Wallace, G. Friedrichs Towards In-Situ Organohalogen Detection by Mid-IR Cavity Ringdown Spectroscopy, *12th International User Meeting and Summer School on Cavity Enhanced Spectroscopy*, 12 - 15 Jun. 2017, Radboud University, the Netherlands (poster).
2. **I. Sadiék**, G. Friedrichs, High-Resolution Spectrum of the Asymmetric C-H Stretch of CH₂Br₂: CRDS Measurements and Simulations, *115th General Assembly of the German Bunsen Society for Physical Chemistry*, 5 - 7 May 2016, University of Rostock, Germany (poster).
3. C. Smets, **I. Sadiék**, G. Friedrichs, High-Resolution cw-IR-CRDS Measurements of the Rovibrational Spectrum of the CH₂Br₂ Symmetric C-H Stretch, *18th JCF-Frühjahrs-symposium*, 16 - 19 Mar. 2016, Kiel, Germany (poster).
4. **I. Sadiék**, G. Friedrichs, Toward in-situ Organohalogen Detection by Advanced Cavity Ringdown Spectroscopy Methods, *SOLAS Open Science Conference*, 7 - 11 Sept. 2015, Kiel, Germany (poster).
5. **I. Sadiék**, G. Friedrichs, Saturation Dynamics and Working Regimes of Saturated Absorption Cavity Ringdown Spectroscopy (Sat-CRDS), *11th International User Meeting and Summer School on Cavity Enhanced Spectroscopy*, 16 - 19 Jun. 2015, Boulder, Colorado, USA (talk).
6. **I. Sadiék**, G. Friedrichs, Ultimate Working Limits of Saturated Absorption Cavity Ringdown Spectroscopy (Sat-CRDS), *114th General Assembly of the German Bunsen Society for Physical Chemistry*, 14 - 16 May 2015, Ruhr-Universität Bochum (RUB), Germany (**PCCP poster prize**).
7. **I. Sadiék**, G. Friedrichs, Ranging the Potential of IR-CRDS Analyzers for Quantitative Detection of Organohalogen Compounds in Marine Environments, *International Marine and Atmospheric Science Symposium*, 21 - 22 May 2015, Mindelo, Cabo Verde (poster).

Workshops

1. **I. Sadiék**, I. Piller, G. Friedrichs, Advances in Evanescent-wave and Saturated absorption Cavity Ringdown spectroscopy (ew-CRDS & Sat-CRDS) for Environmental Applications, *Technical Workshop on Marine Applications and Perspectives of Cavity Enhanced Optical Detection Schemes*, 20 - 21 April 2015, Kiel, Germany (talk).
2. **I. Sadiék**, G. Friedrichs, Implementation of Saturated Cavity Ringdown Spectroscopy: First Results and Working Limits, *Technical Workshop on Marine Applications and Perspectives of Cavity Enhanced Optical Detection Schemes*, 20 - 21 April 2015, Kiel, Germany (poster).
3. **I. Sadiék**, G. Friedrichs, Ranging the Potential of IR-CRDS Analyzers for Quantitative Detection of Organohalogen Compounds in Marine Environments, *HOSST/TOSST Summer School*, 1 - 10. Oct. 2013, Halifax, Canada (poster).

Retreats

1. **I. Sadiék**, Q. Shi, D. Wallace, and G. Friedrichs, Comparative GC/CRDS Laboratory Study of Methyl Iodide Detection, *Future Ocean Retreat*, 10 - 11 Oct. 2016, Schleswig, Germany (poster).
2. **I. Sadiék**, A. Körtzinger, D. Wallace, and G. Friedrichs, Toward in-situ Organohalogen Detection by Advanced Cavity Ringdown Spectroscopy Methods, *Future Ocean Retreat*, 14 - 15 Oct. 2015, Neumünster, Germany (poster).
3. **I. Sadiék**, A. Körtzinger, D. Wallace, and G. Friedrichs, New Advances in Optical Trace Gas Detection: First Results Using Saturated Absorption Cavity Ringdown Spectroscopy, *Future Ocean Retreat*, 29 - 30 Sept 2014, Schleswig, Germany (poster).
4. **I. Sadiék**, A. Körtzinger, D. Wallace, and G. Friedrichs, Ranging the Potential of IR-CRDS Analyzers for Quantitative Detection of Organohalogen Compounds in Marine Environments, *HOSST Retreat*, 7th Feb. 2014, GEOMAR, Kiel, Germany (talk).
5. **I. Sadiék**, I. Piller, A. Körtzinger, D. Wallace, and G. Friedrichs, Enhanced CRDS Methods for Trace Gas Detection and Surface Analysis, *Future Ocean Retreat*, 9 - 10. Sept 2013, Schleswig, Germany (poster).

Computer skills

- Professional command of several software, e.g., Microsoft office, MATLAB, LabVIEW, Gaussian/GaussView and Molpro (QC calculations), GPOP/SSUMES(Chemical Kinetics), PGOPHER (high-resolution spectral simulation), Origin, Sigma plot, ChemDraw, EG&G software (corr, echem./electrochemistry package).

Recognitions and Awards

- PCCP poster prize award, Bunsentagung, 2015.
- I have been invited together with my family by the former prime minister of Schleswig-Holstein as a representative international family in the state (newspaper article: Kieler Nachrichten, 22 Sept., 2014).
- I have participated in 3 summer schools in 3 different countries (Germany, Canada, and Cape Verde), 2013/2014/2015. During Halifax, Canada summer school activities, the project idea of our team won the “Dragon’s Den” game, Oct. 2013 (Later, the project idea has been demonstrated by others, and highlighted in broadcast).
- 10 June 2013, my first daughter Masa was born. 3 Feb. 2016, my second daughter Hana has been born.
- M.Sc. “with the highest honor”/ award of “Best M.Sc. thesis” from University of Cairo, 2012.
- “Shlumberger Award” for distinguished students, 2008.

Other Publications

Full Papers

1. M. Elshakre, **I. Sadiék**, A DFT Study of the Dissociation, Ionization, and UV/Visible Spectra of Methyl Hypobromite, **Comp. Theo. Chem.**, 15:32 - 43, 2016.
2. G. A. El-Nagar, A. F. Darweesh, **I. Sadiék**, A novel Nano-palladium Complex Anode for Formic Acid Electro-Oxidation, **Electrochim. Acta.** 215:334 - 338, 2016.
3. **I. Sadiék**, M. E. Elshakre, A. M. Mohammad, M. S. El-Deab, Enhanced Electrolytic Generation of Oxygen Gas at Binary Nickel Oxide-Cobalt Oxide Nanoparticles Modified Electrodes, **J. Solid State Electrochem.**, 17:871 - 879, 2013.
4. **I. Sadiék**, A. M. Mohammad, M. E. Elshakre, M. S. El-Deab, Electrocatalytic Evolution of Oxygen Gas at Cobalt Oxide Nanoparticles Modified Electrodes, **Int. J. Electrochem. Sci.**, 7:3350 - 3361, 2012.
5. **I. Sadiék**, A. M. Mohammad, M. E. Elshakre, M. S. El-Deab, Electrocatalytic Activity of Nickel Oxide Nanoparticles-Modified Electrodes towards the Oxygen Evolution Reaction: Optimization of the Loading Level and Operating pH, **Int. J. Hydrogen Energy**, 37:68 - 77, 2012.

Conferences

1. **I. Sadiq**, M. E. Elshakre, A. M. Mohammad, M. S. El-Deab, Electrocatalytic Evolution of Oxygen Gas at Cobalt Oxide Nanoparticles Modified Electrodes, The Egyptian Conference Celebrating International Year of Chemistry, 23 -25 Oct. 2011, Cairo, Egypt (poster).
 2. **I. Sadiq**, M. E. Elshakre, A. M. Mohammad, M. S. El-Deab, Electrocatalysis of the Oxygen Evolution Reaction at Nickel Oxide Nanoparticles-Modified Electrodes 6th International Conference in Chemistry (Chem-06), 1 - 4 Mar. 2010, Cairo University, Cairo, Egypt (talk).
-

Declaration

I hereby declare that the presented work in this dissertation was entirely prepared and worked out by myself with no other help than the referenced sources, except for guidance of my supervisor Prof. Dr. Gernot Friedrichs.

This is my first dissertation and this work has neither been used as a whole nor in parts in any other dissertation attempts.

The dissertation complies to the good scientific practice rules as proposed by the German Research Foundation (DFG).

Kiel, 2017

Ibrahim Sadiek